

**LIBRARY**  
**Michigan State**  
**University**

This is to certify that the

dissertation entitled

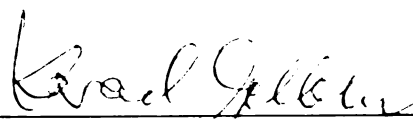
The Emission of Complex Fragments  
From Highly Excited Nuclear Systems

presented by

David James Fields

has been accepted towards fulfillment  
of the requirements for

Ph.D. degree in Physics & Astronomy

  
Major professor

Date 12-11-86



RETURNING MATERIALS:  
Place in book drop to  
remove this checkout from  
your record. FINES will  
be charged if book is  
returned after the date  
stamped below.

--	--	--

THE EMISSION OF COMPLEX FRAGMENTS  
FROM HIGHLY EXCITED NUCLEAR SYSTEMS

By

David James Fields

A DISSERTATION

Submitted to  
Michigan State University  
in partial fulfillment of the requirements  
for the degree of

DOCTOR OF PHILOSOPHY

Department of Physics and Astronomy

1986



# ABSTRACT

## THE EMISSION OF COMPLEX FRAGMENTS FROM HIGHLY EXCITED NUCLEAR SYSTEMS

by

David James Fields

The emission of complex fragments is investigated for the following reactions:  $^{12}\text{C} + ^{197}\text{Au}$  at  $E/A=15$  and 30 MeV,  $^{12}\text{C} + \text{Ag}$  at  $E/A=15$  and 30 MeV,  $^{14}\text{N} + \text{Ag}$  at  $E/A=35$  MeV, and  $^{32}\text{S} + \text{Ag}$  at  $E/A=22.5$  MeV. In all reactions, intermediate mass fragments,  $A_f > 4$ , are produced with single particle inclusive cross sections which generally decrease with increasing element number. The energy spectra and angular distributions indicate substantial non-equilibrium contributions, particularly for lighter fragments.

Measurements of light particles and target-like residues coincident with intermediate mass fragments provide information about the dynamical configuration of the fragmenting system. From these measurements it appears that intermediate mass fragments are emitted in highly damped collisions. The average fragment multiplicities are low, of the order of one. Intermediate mass fragments are typically accompanied by a significant number of nucleons, approximately 10 in the form of light particles alone, emitted prior to the attainment of full statistical equilibrium. As a consequence, only about 0.7 of the beam momentum is transferred to the fragment-residue system. Angular correlations between

light particles and intermediate mass fragments indicate enhanced emission in the entrance channel reaction plane and, therefore, that dynamical effects are important in the fragment emission mechanism. Furthermore, the angular correlations indicate that fragment emission is not restricted to central collisions.

The target residue angular distributions and the mass, isotopic, and excited state distributions indicate substantial emission of intermediate mass fragments in excited states. The effects of the sequential decay of particle-unstable states are studied in schematic statistical calculations in which the states of nuclei are assumed to be populated according to a thermal equilibrium distribution. These calculations indicate that the characteristic structures in the fragment mass spectra and the apparent suppression of excited state emission are the result of the decays of particle-unstable states.

A model is discussed in which particles are emitted at statistical rates from a source which is in the process of equilibration with the target system. The resulting calculations are discussed and compared to measured fragment multiplicities, momentum transfers, and energy spectra. The comparison indicates that descriptions of dynamical evolution and the fragment emission mechanism must be integrated in a realistic model of nuclear reactions.

I had intended to dedicate this work to my wife, Anh Phuong, and our son, Andrew David. On her suggestion, I dedicate it to her family in Viet Nam, as representatives of those against whom viscious governments have conspired and for whom there is no easy escape.

## ACKNOWLEDGMENTS

Graduate study has been both collaborative and tutorial, and at its conclusion I take some satisfaction in acknowledging the efforts of those with whom I have worked and from whom I have learned.

Dr. C. Konrad Gelbke has been the consummate thesis advisor. His advice has been excellent; his assistance, reliable; his patience, remarkable; and his attitude, thoroughly professional.

I am particularly grateful to Drs. William G. Lynch and M. Betty Tsang. Their efforts were essential to the work presented in this dissertation. I have profited from knowing them as teachers and co-workers, and take pleasure from knowing them as friends to both myself and my family.

I have benefited from the experience and efforts of a great number of other individuals. Josef Pochodzalla deserves special mention. T.C. Awes, G.R. Young, R.L. Ferguson, F. Plasil, F.E. Obenshain, R.L. Robinson, M.L. Halbert, D.C. Hensley, D.G. Sarantites, and L.G. Sobotka were instrumental in experiments at ORNL. R. Bougault and D. Horn analyzed the recoil distributions in the  $^{14}\text{N} + \text{Ag}$  experiment. I also acknowledge pleasant collaborations with V.E. Viola, Jr. and K. Kwiatkowski.

My graduate committee consisted of C.K. Gelbke, W.G. Lynch, W.W. Repko, G.F. Bertsch, and J. A. Nolen. I wish to acknowledge the early assistance H. Toki.

I can also acknowledge the graduate students with whom I have worked. Charles Chitwood, a fellow graduate of Tennessee Technological University, David Klesch, Tapan Nayak, and Hongming Xu were fellow students at MSU. Mirek Fatyga and Douglas Fields, from Indiana University, I also acknowledge as co-workers.

It is appropriate that I acknowledge the contributions of my undergraduate professors : R.L. Kozub, F.L. Culp, K. Kumar, J.F. Mateja, and J.C. Wells.

I owe a great deal to my parents, for obvious reasons. I am grateful to my family in Michigan for their help and hospitality. Finally, I am most grateful to my wife, Anh Phuong, for her continuing efforts on my behalf, and on behalf of our son.

## TABLE OF CONTENTS

LIST OF TABLES . . . . .	ix
LIST OF FIGURES . . . . .	xi
Chapter	Page
I. Introduction . . . . .	1
A. Motivation . . . . .	1
B. Scope and organization . . . . .	8
II. Experimental Methods and Analysis . . . . .	12
A. $^{12}\text{C} + \text{Ag, Au}$ at $E/A=15, 30$ MeV/A . . . . .	12
1. Experimental objectives . . . . .	12
2. Detectors and geometry . . . . .	13
3. Analysis and calibration . . . . .	13
B. $^{14}\text{N} + \text{Ag}$ at $E/A=35$ MeV . . . . .	16
1. Experimental objectives . . . . .	16
2. Detectors and geometry . . . . .	17
3. Analysis and calibration . . . . .	19
C. $^{32}\text{S} + \text{Ag}$ , $E/A=22.5$ MeV, particle-particle coincidence measurements . . . . .	22
1. Experimental objectives . . . . .	22
2. Detectors and geometry . . . . .	23
3. Analysis and calibration . . . . .	27
D. $^{32}\text{S} + \text{Ag}$ , $E/A=22.5$ MeV, particle-gamma coincidence measurements . . . . .	29
1. Experimental objectives . . . . .	29

Chapter	Page
2. Detectors and geometry . . . . .	32
3. Analysis and calibration . . . . .	36
III. Single Particle Inclusive Data . . . . .	43
A. Features of the inclusive data . . . . .	43
1. Light particle spectra . . . . .	43
2. Intermediate mass fragment spectra . . . . .	50
B. Two source parametrization of the cross sections . .	52
1. Moving source parametrizations . . . . .	52
2. Description of present parametrization . . . . .	53
3. Results of parametrization . . . . .	55
4. Limits of the parametrization . . . . .	60
C. Integrated cross sections . . . . .	61
1. Elementally resolved yields . . . . .	61
2. Isotopically resolved yields . . . . .	68
IV. Light Particle-Intermediate Mass Fragment Correlations.	71
A. Spectra of light particles coincident with intermediate mass fragments . . . . .	71
B. Angular correlations . . . . .	77
1. The correlation functions . . . . .	77
2. Azimuthal correlations . . . . .	79
3. In-plane correlations . . . . .	87
C. Discussion . . . . .	87
V. Associated Multiplicities . . . . .	93
A. Associated multiplicity defined . . . . .	93
B. Multiplicities of light particles associated with intermediate mass fragments . . . . .	95
C. Intermediate mass fragment multiplicities . . . . .	97

Chapter	Page
1. Fragment multiplicities associated with light particles . . . . .	97
2. Fragment multiplicities associated with other intermediate mass fragments . . . . .	101
D. Summary . . . . .	102
VI. Velocity Distributions of Target-Like Residues . . . . .	104
A. Velocity distributions . . . . .	104
1. General characteristics . . . . .	104
2. Dependences of the peak position . . . . .	106
3. Integrated probabilities . . . . .	112
B. Kinematic analysis . . . . .	113
1. Method of missing momentum analysis . . . . .	113
2. Quantities of interest . . . . .	114
3. Results of missing momentum analysis . . . . .	115
4. Errors and uncertainties . . . . .	122
5. Sequential decay . . . . .	122
C. Summary . . . . .	123
VII. Statistical Aspects of Fragment emission . . . . .	126
A. Introduction . . . . .	126
B. Statistical Emission and the Population of Excited States . . . . .	127
1. A schematic model . . . . .	127
2. Mass distributions . . . . .	130
3. Isotopic yields . . . . .	136
4. Excited state populations . . . . .	143
C. Comparison with $^{32}\text{S} + \text{Ag}$ data . . . . .	150
1. Isotopic ratios . . . . .	151



Chapter	Page
2. Population ratios . . . . .	155
D. Summary of results . . . . .	161
VIII. Equilibration and decay in nuclear collisions . . . . .	164
A. Model for statistical decay during equilibration . . . . .	164
1. Motivation . . . . .	164
2. Formulation of the model . . . . .	165
B. General features of the calculation. . . . .	171
1. Instantaneous emission rate . . . . .	171
2. Time evolution . . . . .	176
C. Results of the model . . . . .	182
D. Summary . . . . .	194
IX. Summary and conclusion . . . . .	196
A. Summary of present results . . . . .	196
B. Concluding remarks . . . . .	200
APPENDIX A : Kinematic bias in target velocities . . . . .	202
APPENDIX B : Gamma ray efficiency calibration . . . . .	204
APPENDIX C : Jacobian for relativistic transformation . . . . .	208
APPENDIX D : Sequential decay . . . . .	210
APPENDIX E : Quantum statistical calculations . . . . .	222
LIST OF REFERENCES . . . . .	228

# LIST OF TABLES

TABLE		PAGE
II-1	The positions and solid angles of the light particle detectors (LP) and the intermediate mass fragment detectors (IMF) used to study the $^{32}\text{S} + \text{Ag}$ system, as discussed in Section II.C. . . . .	25
II-2	The positions, solid angles, and construction of the solid state fragment detectors used in the $^{32}\text{S} + \text{Ag}$ particle - gamma coincidence experiment, as discussed in Section II.D. . . . .	33
II-3	The positions and typical efficiencies of the Compton suppressed germanium detectors, as discussed in Section II.D. The number in parenthesis next to the detector number is the parameter number for the Compton shield. The position of each detector in the ORNL Spin Spectrometer is given in the second column. The remaining columns give the absolute position with respect to the beam axis and the absolute efficiency of each detector at 300 keV. . . . .	34
III-1	The best fit parameters from the parametrization discussed in the text for fragments produced in $^{12}\text{C}$ induced reactions on Au at $E/A=30$ MeV. The estimated cross sections for the fast and slow sources are also given. . . . .	57
III-2	The best fit parameters from the parametrization discussed in the text for fragments produced in $^{14}\text{N}$ induced reactions on Ag at $E/A=35$ MeV. The estimated cross sections for the fast and slow sources are also given. . . . .	58
III-3	The best fit parameters from the parametrization discussed in the text for fragments produced in $^{32}\text{S}$ induced reactions on Ag at $E/A=22.5$ MeV. The estimated cross sections for the fast and slow sources are also given . . . . .	59

V-1	The estimated average total multiplicities, $M$ , of light particles, $p, d, t, \alpha$ , associated with intermediate mass fragments with momenta, $\langle P_x \rangle$ , emitted in $^{32}\text{S}$ induced reactions on Ag at $E/A=22.5$ MeV. $M_T$ is the total nucleon multiplicity; $\langle P \rangle$ and $\langle E \rangle$ are the average total longitudinal momentum and average total energy carried away by non-equilibrium light particles. Momenta and energies are given in units of MeV/c and MeV, respectively. The multiplicities are inferred from cross sections measured at $\theta_y = 40^\circ$ , $\theta = 27.5^\circ$ , averaged between $\Delta\phi = 90^\circ$ and $180^\circ$ . . . . .	96
VI-1	The observed and calculated kinematic properties of systems for which the peak in the distribution of heavy residue velocities, $\vec{v}_2$ , was within the experimental acceptance when detected in coincidence with an intermediate mass fragment with a momentum $\langle P_1 \rangle$ at an angle $\theta_1$ . . . . .	119
B-1	The properties of the sources used to provide absolute efficiency calibrations. The gamma ray source is given and the nucleus which emits the gamma ray is given in parenthesis, $E$ is the transition energy, $J_i^\pi$ is the initial and $J_f^\pi$ is the final spin and parity of the transition, $L$ is the multipole, $\delta$ is the multipole mixing ratio, $B$ is the number of partner gamma rays emitted in coincidence with each transition, and $A_2$ and $A_4$ are the angular correlation coefficients for the transition pairs. . . . .	207

## LIST OF FIGURES

FIGURE		PAGE
I-1	The cross sections for fragments of mass $A_f$ produced in the $p + Xe$ reaction [HIR84] are shown as solid points. A power law dependence on fragment mass is indicated by the solid curve . . . . .	5
II-1	A scatter plot of $\Delta E$ vs. $E - \Delta E$ for the reaction $^{12}C + ^{197}Au$ at $E/A=30$ MeV measured at $\theta=70^\circ$ . The solid curve represents the locus of peak kinetic energies predicted by a generalization of the systematics of fission Coulomb kinetic energies [VI085] . . . . .	15
II-2	A schematic diagram of the experimental layout for the $^{14}N + Ag$ coincidence studies. The position sensitive detector is labelled as "HR" and the ionization chamber-solid state telescopes are labelled as "IMF". . . . .	18
II-3	A schematic diagram of the triple Frisch-grid ion chamber system used in two of the experiments discussed in this thesis. The solid state detectors are contained in the gas volume. . . . .	20
II-4	A schematic diagram of the multiwire avalanche counter used in the $^{14}N + Ag$ experiment. The ionization avalanches occur about the wires in the anode planes labelled a and c. The signals induced on the wires undergo a position dependent delay before amplification. A signal induced on the foil cathode, b, is used as a time reference . . . . .	21
II-5	A schematic diagram of the $^{32}S + Ag$ particle-particle coincidence experiment. The intermediate mass fragments are labelled as "IMF", the light particle detectors, as "LP", and the position sensitive detector, as "HR". . . . .	24

FIGURE		PAGE
II-6	A schematic diagram of the Breskin design position sensitive detector. The ionization avalanches occur at the central wire anode. The signals induced on the evaporated stripes on the foil cathode undergo a position dependent delay before amplification. . . . .	26
II-7	Raw position spectra from the Breskin detector placed at the three laboratory angles from target-like fragments detected in coincidence with lithium fragments detected at $\theta=27^\circ$ . Detector originated modulations of the spectra are easily recognized . . . . .	30
II-8	Final angular distribution from the raw spectra in Figure II-7. The distribution is smooth and relatively free of spurious structures . . . . .	31
II-9	Schematic diagram of one of the Compton suppressed germanium detectors used in the particle-gamma coincidence experiment . . . . .	35
II-10	The relative efficiency curve (a) for $\gamma$ detector 1 from a $^{152}\text{Eu}$ source (circles) and $^{182}\text{Ta}$ source (squares). The solid curve indicates the analytic interpolation discussed in the text. The ratio of the source data to the interpolation is shown in the bottom part of the figure (b). . . . .	38
II-11	The spectrum of gamma rays coincident with $^{10}\text{B}$ ions, without Doppler shift, is shown in the upper part of the spectrum, (a). The bottom part of the figure, (b), shows the corrected spectrum, indicated by the histogram, and the estimated background, indicated by the solid points. The background is produced by Doppler shifting gamma rays coincident with other nuclei, as discussed in the text . . . . .	39
III-1	Differential cross sections, $d^2\sigma/dE d\Omega$ , measured at $\theta=40^\circ$ , $70^\circ$ , and $130^\circ$ , for light particles, p, d, t, and $\alpha$ , from $^{32}\text{S}$ induced reactions on Ag at $E/A=22.5$ MeV. Also, cross sections measured at $\theta=27.5^\circ$ and $52.5^\circ$ are shown for $\alpha$ particles. The solid curves are the result of the parametrization discussed in the text . . . . .	44
III-2	Differential cross sections, $d^2\sigma/dE d\Omega$ , measured at $\theta=30^\circ$ , $50^\circ$ , $70^\circ$ , and $120^\circ$ , for fragments, $5 \leq Z \leq 10$ , from $^{12}\text{C}$ induced reactions on Au at $E/A=30$ MeV. The solid curves are the result of the parameterization discussed in the text. . . . .	45

FIGURE		PAGE
III-3	Differential cross sections, $d^2\sigma/dEd\Omega$ , measured at $\theta=32.5^\circ$ , $45^\circ$ , and $57.5^\circ$ , for fragments, $4\leq Z\leq 9$ , from $^{14}\text{N}$ induced reactions on Ag at $E/A=35$ MeV. The solid curves are the result of the parameterization discussed in the text. . . . .	46
III-4	Differential cross sections, $d^2\sigma/dEd\Omega$ , measured at $\theta=32.5^\circ$ , $45^\circ$ , and $57.5^\circ$ , for fragments, $10\leq Z\leq 15$ , from $^{14}\text{N}$ induced reactions on Ag at $E/A=35$ MeV. The solid curves are the result of the parameterization discussed in the text. . . . .	47
III-5	Differential cross sections, $d^2\sigma/dEd\Omega$ , measured at $\theta=27.5^\circ$ , $40^\circ$ , and $52.5^\circ$ , for fragments, $3\leq Z\leq 8$ , from $^{32}\text{S}$ induced reactions on Ag at $E/A=22.5$ MeV. The solid curves are the result of the parameterization discussed in the text. . . . .	48
III-6	Differential cross sections, $d^2\sigma/dEd\Omega$ , measured at $\theta=27.5^\circ$ , $40^\circ$ , and $52.5^\circ$ , for fragments, $9\leq Z\leq 24$ , from $^{32}\text{S}$ induced reactions on Ag at $E/A=22.5$ MeV. The solid curves are the result of the parameterization discussed in the text. . . . .	49
III-7	Differential cross sections, $d\sigma/d\theta_{\text{cm}}$ , for various fragments, $5\leq Z\leq 18$ , from $^{12}\text{C}$ induced reactions on Au at $E/A=30$ MeV. The solid curves are drawn to guide the eye. Emission from fission would produce a flat curve. . . . .	51
III-8	Average differential cross sections, $\langle d\sigma/d\Omega \rangle$ , over the region $50^\circ\leq\theta\leq 120^\circ$ for fragments of charge, $Z$ , from $^{12}\text{C}$ induced reactions on Au at $E/A=15$ and $30$ MeV (solid and open points, respectively). . . . .	62
III-9	Average differential cross sections, $\langle d\sigma/d\Omega \rangle$ , for fragments of charge, $Z$ , from $^{12}\text{C}$ induced reactions on Ag at $E/A=15$ ( $50^\circ\leq\theta\leq 70^\circ$ , solid points ) and $30$ MeV ( $40^\circ\leq\theta\leq 70^\circ$ , open points ). The solid curve depicts a strict power law dependence, $Y\propto Z^{-2.6}$ . . . . .	63

FIGURE		PAGE
III-10	The extrapolated total cross sections, $\sigma_x$ , for fragments produced in $^{12}\text{C}$ induced reactions on Au at $E/A=30$ MeV are shown as open circles. The solid circles and open squares show the average differential cross sections, $\langle d\sigma_x/d\Omega \rangle$ , measured over the angular ranges $30^\circ \leq \theta \leq 120^\circ$ and $50^\circ \leq \theta \leq 120^\circ$ , respectively . . . . .	65
III-11	The extrapolated total cross sections, $\sigma_x$ , for fragments produced in $^{14}\text{N}$ induced reactions on Ag at $E/A=35$ MeV are shown as open circles. The solid circles show the average differential cross sections, $\langle d\sigma_x/d\Omega \rangle$ , measured over the angular range $32.5^\circ \leq \theta \leq 57.5^\circ$ . The solid curves depict a power law dependence $Y \propto Z^{-2.8}$ . . . . .	66
III-12	The extrapolated total cross sections, $\sigma_x$ , for fragments produced in $^{32}\text{S}$ induced reactions on Ag at $E/A=22.5$ MeV are shown as open circles. The solid circles show the average differential cross sections, $\langle d\sigma_x/d\Omega \rangle$ , measured over the angular range $27.5^\circ \leq \theta \leq 52.5^\circ$ . The solid curves depict a power law dependence $Y \propto Z^{-1.6}$ . . . . .	67
III-13	Relative isotopic yields for isotopes of elements, $3 \leq Z_x \leq 8$ , are shown as solid points. The solid curves represent the predictions of a simple statistical model discussed in the text. . . . .	69
IV-1	Energy spectra of protons (top of figure) and alpha particles (bottom of figure) in coincidence with Li fragments (left side of figure) and C fragments (right side of figure). The circles and diamonds correspond to the light particles being detected at $\theta=40^\circ$ and $70^\circ$ , respectively. The solid and open points correspond to relative azimuthal angles between the light particle and intermediate mass fragment of $\Delta\phi=180^\circ$ and $90^\circ$ , respectively. The inclusive spectra are shown as solid curves. . . . .	73

- IV-2 The ratio of the differential coincidence cross sections to the single particle inclusive cross sections for protons as a function of proton energy. The ratio is shown for protons detected at  $\theta_p = 40^\circ$  (left hand side) and  $\theta_p = 70^\circ$  (right hand side) in coincidence with Li nuclei (top of figure) and C nuclei (bottom of figure) detected at  $\theta_x = 27.5^\circ$  and at relative azimuthal angles of  $\Delta\phi = 180^\circ$  (solid points) and  $\Delta\phi = 90^\circ$  (open points) . . . . . 75
- IV-3 The ratio of the differential coincidence cross sections to the single particle inclusive cross sections for alpha particles as a function of alpha particle energy. The ratio is shown for alpha particles detected at  $\theta_p = 40^\circ$  (left hand side) and  $\theta_p = 70^\circ$  (right hand side) in coincidence with Li nuclei (top of figure) and C nuclei (bottom of figure) detected at  $\theta_x = 27.5^\circ$  and at relative azimuthal angles of  $\Delta\phi = 180^\circ$  (solid points) and  $\Delta\phi = 90^\circ$  (open points). . . . . 76
- IV-4 The correlation function for alpha particles detected at  $\theta_\alpha = 40^\circ$  in coincidence with fragments,  $Z_x = 2-7$ , as a function of their relative azimuthal angle,  $\Delta\phi$ . The coincidence fragments, X, are detected at laboratory angles of  $\theta_x = 27.5^\circ$  (open points) and  $\theta_x = 52.5^\circ$  (solid points). . . . . 80
- IV-5 The correlation function integrated with low and high low particle energy thresholds (open and solid points, respectively) for alpha particles detected at  $\theta_\alpha = 40^\circ$  in coincidence with fragments,  $Z_x = 2-7$ . It is shown as a function of their relative azimuthal angle,  $\Delta\phi$ . The coincidence fragments, X, are detected at  $\theta_x = 27.5^\circ$ . . . . . 81
- IV-6 The in-to-out of plane ratio,  $A_\phi$ , defined in the text, for fragments of charge,  $Z_x = 2-7$ , detected at  $\theta_x = 27.5^\circ$  and light particles,  $Y = p, d, t, \alpha$ , detected at  $\theta_y = 40^\circ$ . The solid and open points correspond to the ratio for correlations integrated for particle energies above a higher and lower low energy threshold. . . . . 83



IV-7	The in-to-out of plane ratio, $A_\phi$ , defined in the text, for fragments of charge, $Z_x=2-7$ , detected at $\theta_x=40^\circ$ and light particles, $Y=p,d,t,\alpha$ , detected at $\theta_y=40^\circ$ . The solid and open points correspond to the ratio for correlations integrated for particle energies above a higher and lower low energy threshold. . . . .	84
IV-8	The in-to-out of plane ratio, $A_\phi$ , defined in the text, for fragments of charge, $Z_x=2-7$ , detected at $\theta_x=27.5^\circ$ (open points) and $52.5^\circ$ (solid points) and light particles, $Y=p,d,t,\alpha$ , detected at $\theta_y=40^\circ$ . . . . .	85
IV-9	The in-to-out of plane ratio, $A_\phi$ , defined in the text, for fragments of charge, $Z_x=2-7$ , detected at $\theta_x=27.5^\circ$ (open points) and $52.5^\circ$ (solid points) and light particles, $Y=p,d,t,\alpha$ , detected at $\theta_y=70^\circ$ . . . . .	86
IV-10	The correlation function for alpha particles in coincidence with fragments, $Z_x=2-7$ , detected in the same plane ( $\Delta\phi=0^\circ$ or $180^\circ$ ) as a function of the polar angle, $\theta_\alpha$ , of the alpha particle. The coincidence fragments, $X$ , are detected at laboratory angles of $\theta_x=27.5^\circ$ (open points) and $\theta_x=52.5^\circ$ (solid points) . . . . .	88
V-1	The estimated average total multiplicities, $M_x$ , of particles, $Z_x=2-7$ , associated with alpha particles in $^{32}\text{S}$ induced reactions on Ag at $E/A=22.5$ MeV. The results were obtained from the correlations measured at $\theta_\alpha=40^\circ$ and $\theta_x=27.5^\circ$ at $\Delta\phi=90^\circ$ and $180^\circ$ . . . . .	98
V-2	The correlation function, $C_{xy}$ , between light particles (y) and intermediate mass fragments (x), measured at $\theta_y=40^\circ$ and $\theta_x=27.5^\circ$ , and averaged between $\Delta\phi=180^\circ$ and $90^\circ$ , is shown as a function of $Z_x$ , the charge of the coincident fragment. . . . .	100

FIGURE		PAGE
VI-1	Velocity distributions for target-like residues detected in coincidence with intermediate mass fragments detected at $\theta_1=27.5^\circ$ with momenta, $P_1$ . The left hand side shows the distribution as a function of the polar angle, $\theta_2$ , of the projections of the recoil velocity vector onto the reaction plane. The right hand side shows the measured distributions of $ \vec{v}_2 $ . The arrows show the values expected for binary reactions. . . . .	105
VI-2	Probability distributions for heavy residues as a function of recoil angle, $\theta_2$ , detected in coincidence with boron fragments of different momenta, $P_1$ , detected at $\theta_1=40^\circ$ , (upper part) and coincidence with different intermediate mass fragments gated by the same momentum bin (lower part). The arrows indicate the maxima of the distributions. . . . .	107
VI-3	The differential cross sections for heavy residues detected in coincidence with Be fragments (lefthand side) and O fragments (right hand side) of various momenta detected at $\theta_1=45^\circ$ . . . . .	109
VI-4	The value of the average recoil angle $\langle\theta_2\rangle$ for angular distributions of heavy residues detected in coincidence with O fragments detected at $\theta_1=45^\circ$ as a function of fragment momentum. The solid curves are expected values for 100% and 73% momentum transfer. . . .	110
VI-5	The results of kinematics calculations for coincidences between heavy residues and carbon nuclei detected at $\theta_1=27.5^\circ$ with an average momentum of 1448 MeV/c are shown as solid curves. The hatched area represents the estimated uncertainties. The dashed curves are obtained when the carbon nucleus is assumed to be a secondary fragment produced in the decay of a particle stable O nucleus. A detailed discussion is to be found in Section VI.B. . . . .	116

FIGURE		PAGE
VII-1	Correlations between protons and ${}^7\text{Li}$ nuclei (bottom) and between alpha particles and ${}^7\text{Li}$ nuclei (top) measured in ${}^{40}\text{Ar} + \text{Au}$ reactions at $E/A=60$ MeV as functions of the relative momenta between the two particles. Peaks in the correlations which correspond to states in ${}^{11}\text{B}$ and ${}^8\text{Be}$ are indicated in the top and bottom figures, respectively . . . . .	129
VII-2	Mass distributions calculated from Eq. VII-1 for emission from a Xe nucleus at $T=5$ MeV. Histogram : primary distribution; solid points : final distribution; dark and light shaded regions show contributions from bound ground and excited states, respectively . . . . .	131
VII-3	Mass distribution from proton induced reactions on Xe (solid points) and final distribution predicted from Eq. VII-1 (histogram). . . . .	133
VII-4	Mass distributions as a function of the emission temperature for emission from a nucleus, $A=131$ and $Z=54$ . The primary (histogram), final (solid points), and stable ground state (shaded region) distributions are shown for emission temperatures of $T=3,5,7$ , and $10$ MeV . . . . .	135
VII-5	The calculated isotopic distributions for $N$ nuclei emitted from a nucleus, $A=131$ and $Z=54$ , at $T=5$ MeV. The distribution of stable ground states is shown as squares. The primary and final distributions from calculations which include excited states are shown as the histogram and solid points, respectively. . . . .	137
VII-6	The calculated isotopic distributions of $Z_x=3-8$ from a nucleus, $A=131$ , $Z=54$ and $T=5$ MeV are shown as histograms. The solid points represent the measured isotopic ratios for $p+\text{Xe}$ reactions [HIR84] . . . . .	139
VII-7	The calculated primary isotopic distributions for $N$ nuclei emitted from a nucleus, $A=131$ and $Z=54$ , at temperatures, $T(\text{MeV})=1$ (solid diamonds), $3$ (open squares), $5$ (star) and $10$ (solid circle) . . . . .	140
VII-8	The calculated final isotopic distributions for $N$ nuclei emitted from a nucleus, $A=131$ and $Z=54$ , at temperatures, $T(\text{MeV})=1$ (solid diamonds), $3$ (open squares), $5$ (star) and $10$ (solid circle) . . . . .	142

FIGURE		PAGE
VII-9	The calculated primary isotopic distributions for the stable ground states of nitrogen nuclei emitted from a nucleus of charge, $Z=54$ , and mass, $A = 120$ (open diamonds), 130 (solid squares), and 140 (stars), at a temperature of $T= 5$ MeV . . . . .	144
VII-10	The calculated final isotopic distributions of nitrogen nuclei emitted from a nucleus of charge, $Z=54$ , and mass, $A = 120$ (open diamonds), 130 (solid squares), and 140 (stars), at a temperature of $T= 5$ MeV. . . . .	145
VII-11	Temperature dependence of population ratios, $R_p/R_\infty$ , for specific states in $^4\text{He}$ , $^5\text{Li}$ , $^6\text{Li}$ , $^8\text{Be}$ nuclei. Ratios measured [POC86p] for the $^{40}\text{Ar}+^{197}\text{Au}$ reaction at $E/A=60$ MeV are shown by hatched regions. Dotted curves : temperature dependence of primary population ratios; solid curves : final ratios predicted from Eq. VII-1; dashed and dashed-dotted curves : final ratios predicted by quantum statistical calculations for densities of $\rho/\rho_0= .05$ and $.9$ , respectively. . . . .	148
VII-12	Isotopic distributions from $^{32}\text{S} + \text{Ag}$ at $E/A=22.5$ MeV (solid points) are compared to calculations (histograms) for emission from a nucleus, $A=130$ , $Z=58$ , at a temperature of $T=2$ MeV. . . . .	152
VII-13	Isotopic distributions from $^{32}\text{S} + \text{Ag}$ at $E/A=22.5$ MeV (solid points) are compared to calculations (histograms) for emission from a nucleus, $A=130$ , $Z=58$ , at a temperature of $T=4$ MeV. The solid curves correspond to Eq. III-5 with $T=3.8$ MeV . . . . .	153
VII-14	Isotopic distributions from $^{32}\text{S} + \text{Ag}$ reactions at $E/A=22.5$ MeV (solid points) are compared to calculations (histograms) for emission from a nucleus, $A=130$ , $Z=58$ , at a temperature of $T=10$ MeV . . . . .	154
VII-15	Energy spectra (shown as histograms) of gamma rays in the regions corresponding to transitions in coincident intermediate mass fragments produced in $^{32}\text{S} + \text{Ag}$ reactions at $E/A=22.5$ MeV. The background is indicated by the solid points. . . . .	156

FIGURE		PAGE
VII-16	The fractions, $F_\gamma$ , of intermediate mass fragments undergoing specified transitions are indicated as a functions of temperature for calculations from Eq. VII-1 both with (solid curves) and without (dashed curves) the contributions from sequential decay. The observed fractions are indicated by the hatched regions. . . . .	157
VII-17	The apparent emission temperatures of intermediate mass fragments emitted in $^{32}\text{S} + \text{Ag}$ reactions at $E/A=22.5$ MeV, as discussed in the text . . . . .	158
VII-18	The fractions, $F_\gamma$ , of intermediate mass fragments undergoing specified transitions are indicated as a functions of temperature for quantum statistical calculations at $\rho/\rho_0=.1$ (solid curve) and $.9$ (dashed curve). The observed fractions are indicated by the hatched regions. . . . .	160
VIII-1	The dependence on source and fragment mass introduced by the preexponential terms in Eq. VIII-9. . . . .	173
VIII-2	The mass spectrum of the instantaneous emission rate for particle stable nuclei as a function of source size in a composite system of $a=220$ and $z=80$ . . . . .	174
VIII-3	The mass spectrum of the instantaneous emission rate of nuclei emitted in their particle stable ground states as a function of source temperature for a compound nucleus of $a=112$ and $z=56$ . . . . .	175
VIII-4	The mass spectrum of the instantaneous emission rate of particle stable nuclei calculated as a function of the Coulomb parameter, $\lambda$ , as in Eq. VIII-12. . . . .	177
VIII-5	The time evolution of compound nuclear systems with initial $a=112$ and $z=52$ starting from four temperatures . . . . .	178
VIII-6	The time evolution of the $^{12}\text{C} + ^{197}\text{Au}$ system at $E/A=30$ MeV, with four different initial source sizes. The accretion rate used in these calculations was $[da_s/dt]_a = 3$ nucleons/(fm/c) . . . . .	180
VIII-7	The time evolution of the $^{12}\text{C} + ^{197}\text{Au}$ system at four different incident energies, calculated with $a_s(t=0)=24$ and $[da_s/dt]_a = 3$ nucleons/(fm/c). . . . .	181

FIGURE		PAGE
VIII-8	The time evolution of the $^{12}\text{C} + ^{197}\text{Au}$ system at four different incident energies, calculated with $a_s(t=0)=24$ and $[da_s/dt]_a = 1$ nucleons/(fm/c). . . . .	183
VIII-9	The momentum transfer systematics [FAT85] for $^{12}\text{C}, ^{14}\text{N}$ induced reactions on $^{197}\text{Au}$ are indicated by solid points. The solid curves represent calculations for the $^{12}\text{C} + ^{197}\text{Au}$ system using three different accretion rates. . . . .	184
VIII-10	The experimental elemental cross sections for $^{12}\text{C}$ carbon induced reactions on $^{197}\text{Au}$ at $E/A=15$ and $30$ MeV, shown as solid and open points, respectively, are compared to calculations with accretion rates of $[da_s/dt]_a = 1$ (solid curve) and $5$ (dashed curve) nucleons/(fm/c). . . . .	186
VIII-11	The experimental elemental cross sections from $^{12}\text{C} + ^{197}\text{Au}$ reactions at $E/A=30$ MeV, shown as open points, are compared to the yield curves for the preequilibrium (dashed curve) and equilibrium (solid curve) stages of the reaction. . . . .	188
VIII-12	The energy spectra measured in $^{12}\text{C} + ^{197}\text{Au}$ reactions at $E/A=30$ MeV at $\theta=30^\circ, 50^\circ, 70^\circ$ , and $120^\circ$ , shown as solid points, are compared to the calculation described in the text. . . . .	190
VIII-13	The calculated energy spectra for $^{12}\text{C} + ^{197}\text{Au}$ reactions at $E/A=30$ MeV at $\theta=30^\circ$ (left) and $90^\circ$ (right), shown as solid curves, are decomposed into a preequilibrium component (dotted curve) and an equilibrium component (dashed curve) . . . . .	191
VIII-14	The calculated energy spectrum for $^{12}\text{C} + ^{197}\text{Au}$ reactions at $E/A=30$ MeV at $\theta=30^\circ$ , corresponding to the upper solid curve, is decomposed into the contributions from stable primaries (lower solid curve), neutron-unstable primary fragments (dotted curve), proton-unstable primary fragments (dot-dashed curve), and alpha-unstable primary fragments (dashed curve) . . . . .	193

FIGURE		PAGE
D-1	Transmission coefficients calculated as a function of energy with the form $T_\ell = x \cdot \exp(-2\omega)$ for three decay channels of $^{12}\text{C}$ : n(bottom), p(middle), and $\alpha$ (top). The calculations are shown as solid curves for partial waves $\ell=0$ to 8 (from left to right). . . . .	213
D-2	Transmission coefficients calculated as a function of energy with the form $T_\ell = \exp(-2\omega)$ for three decay channels of $^{12}\text{C}$ : n(bottom), p(middle), and $\alpha$ (top). The calculations are shown as solid curves for partial waves $\ell=0$ to 8 (from left to right). . . . .	215
D-3	Final mass distributions calculated for the system A=131, Z=54, and T=5 MeV using three forms of the transmission coefficients : $T_\ell = \exp(-2\omega)$ (histogram), $T_\ell = x \cdot \exp(-2\omega)$ (open circles), and a sharp cutoff approximation (solid squares). . . . .	216
D-4	The ratios of populations of levels in $^4\text{He}$ , $^5\text{Li}$ , $^6\text{Li}$ , and $^8\text{Be}$ are shown as functions of emission temperature for calculations with different transmission coefficients : $T_\ell = \exp(-2\omega)$ (solid curves), $T_\ell = x \cdot \exp(-2\omega)$ (dotted curves), and a sharp cutoff approximation (dashed curves) . . . . .	218
D-5	A comparison of the mass distributions calculated according to Eq. VII-1 using branching ratios calculated from transmission coefficients (histogram) and using branching ratios that are fixed to be equal for all allowed decay channels (solid points) for a system A=131 and Z=54 at T=5 MeV . . . . .	219
D-6	A comparison of the fractions, $F_\gamma$ , of nuclei in their excited states as calculated according to Eq. VII-1 with branching ratios calculated according to statistical rules (solid curves) and branching ratios fixed to be equal for allowed channels for a system of A=130 and Z=58. The fractions observed in $^{32}\text{S}$ induced reactions on Ag at E/A=22.5 MeV are indicated by the hashed regions. . . . .	220

FIGURE

PAGE

- E-1      The primary and final mass distributions for the fragmentation of a A=131, Z=54 system at a density of  $\rho/\rho_0=.4$  and at temperatures, T= 1,3,5, and 10 MeV, are shown as histograms and solid points, respectively . . . . . 224
- E-2      The primary and final mass distributions for the fragmentation of a A=131, Z=54 system at a temperature of T=5 MeV and at densities,  $\rho/\rho_0= .05, .3, .6,$  and  $.9,$  are shown as histograms and solid points, respectively . . . . . 225



## Chapter I

### Introduction

#### I.A. Motivation :

To understand the properties of highly excited nuclear systems, it is necessary to understand the processes by which such systems decay. Nuclei excited to sufficiently high energies are known to decay by division into two smaller nuclei. Decay by symmetric division is termed fission, while extremely asymmetric decay into a H or He nucleus and a larger residual nucleus is termed light particle evaporation. Great progress has been made in understanding these modes of decay, particularly for systems in which all internal degrees of freedom can be considered fully equilibrated.

Between these two extremes in mass asymmetry lies the emission of fragments of intermediate mass. These fragments are heavier than alpha particles but lighter than typical fission fragments. In many cases, the angular distributions of these fragments indicate that they are emitted before the composite systems reach equilibrium. The emission of intermediate mass fragments was first observed in reactions induced

by relativistic protons [STE67] [POS71] [HYD71] [WES78]. It was thereafter observed in proton induced reactions at lower energies [GRE80] and in heavy ion collisions both at relativistic [GOS77] [WAR83] and non-relativistic energies [MOR75b] [FRA81] [JAK82] [CHI83] [SOB83]. In general, the emission of intermediate mass fragments has been associated with the most violent nuclear collisions. The recent observation [GALS84] of the radioactive emission of  $^{14}\text{C}$  indicates, however, that intermediate mass fragment emission is likely a "normal" nuclear decay mode [POE85], the relative importance of which can be understood in terms of penetrabilities and binding energies.

Existing single particle inclusive data exhibit a few simple characteristics. The energy spectra are peaked at energies somewhat below the Coulomb barrier energy between the fragment and daughter nuclei. The cross sections decrease approximately exponentially with increasing fragment energy. The angular distributions of many fragments contain at least two components. One is approximately isotropic in the center-of-mass of a fusion-like (target-like) residue. The other is strongly forward peaked in the laboratory and nearly isotropic in a frame moving with a velocity between the center of mass and the projectile velocities. (Unless otherwise stated, normal kinematics are assumed, i.e. the projectile is lighter than the target.) The integrated cross sections decrease smoothly with increasing fragment mass. The total fragmentation cross section increases with increasing energy [CHI83] until it reaches a limiting value at relativistic energies [GRE80] [KAU80].

Theoretical investigations of intermediate mass fragment emission have evolved from two directions. Relativistic reactions were expected

to produce energy densities in excess of the nuclear binding energy. Nuclear systems with such excitation energies would be intrinsically unstable and would "explode" [FAI82] [BON85b]. As a result, models applied to these data are generally based on the assumption of high particle multiplicities. The relative particle yields are calculated by applying statistical partition rules.

The thermodynamical models are based on the assumption that equilibrium is effectively reached ( or, as a weaker statement, that the ensemble average of all reactions approaches the equilibrium limit ) in a uniform region of nuclear matter. This hot region is assumed to expand until it reaches a temperature and density where the interactions between fragments cease and the distribution "freezes out" [MEK78]. The fragment yields are calculated either from the microcanonical ensemble [RAN81] [FAI82] [FAI85] or from the grand canonical ensemble corresponding to a system in chemical equilibrium [STOC83] [JAC83] [HAH86]. In general, these models neglect the Coulomb interaction between particles, though it has been shown that the Coulomb interaction is important even at high energies [GR082].

Models of non-thermodynamical partitioning attribute the emission of fragments to mechanical instabilities which develop during the collision process. In some models the projectile nucleons "cleave" or "shatter" the target nucleus. In another, the interacting system develops "cracks" and "bubbles" which result in the fragmentation of the system. In the first of these (cleavage) the partition is determined solely by geometrical considerations [BOH83]. In the shattering and cracking models it is determined by the average partition of any finite set of objects (nucleons) [AIC84a] [AIC84b] [FIE84] [BON85b] [SOB85] or

by percolation calculations in a "nuclear lattice" [BAU85] [BAU86]. A more fundamental understanding can only be provided by microscopic calculations. Monte Carlo integrations of transport equations indicate that in small systems density fluctuations can persist and result in fragmentation [JEN86]. Molecular dynamics calculations [VIC85] suggest that these density fluctuations result in fragmentation only if the system expands to low densities.

The nucleon-nucleon potential is attractive at long range and repulsive at short range, analogous to the Van der Waals force. Nuclear matter may, then, exhibit liquid and gas phases [JAQ83] [GOO84] [JAQ84], much as a Van der Waals gas. Droplets formed in a classical gas near the critical point are produced with probabilities [FIS67] [SIE83]:

$$P_A \propto A^{-\tau} \exp(-b(T)A^{2/3}) \quad , \quad (I-1)$$

where  $A$  is the fragment size,  $b(T)$  is a temperature dependent parameter measuring the surface tension of the drops, and  $\tau$  is the critical exponent. At the critical point the argument of the exponential becomes zero and a pure power law dependence remains. In measurements of macroscopic systems, the critical exponent is approximately  $\tau \approx 2.5$  [KIA70]. Mass distributions in proton induced reactions on Xe and Kr [FIN82] exhibit a similar power law dependence (see Figure I-1) with  $\tau \approx 2.6$ , and from this it was inferred [HIR84] that the emitting systems had passed through the critical point for nuclear matter. The results of a systematic study [PAN84] of mass distributions in energetic collisions were interpreted to indicate a critical temperature of  $T=12$  MeV and  $\tau=1.8$ .

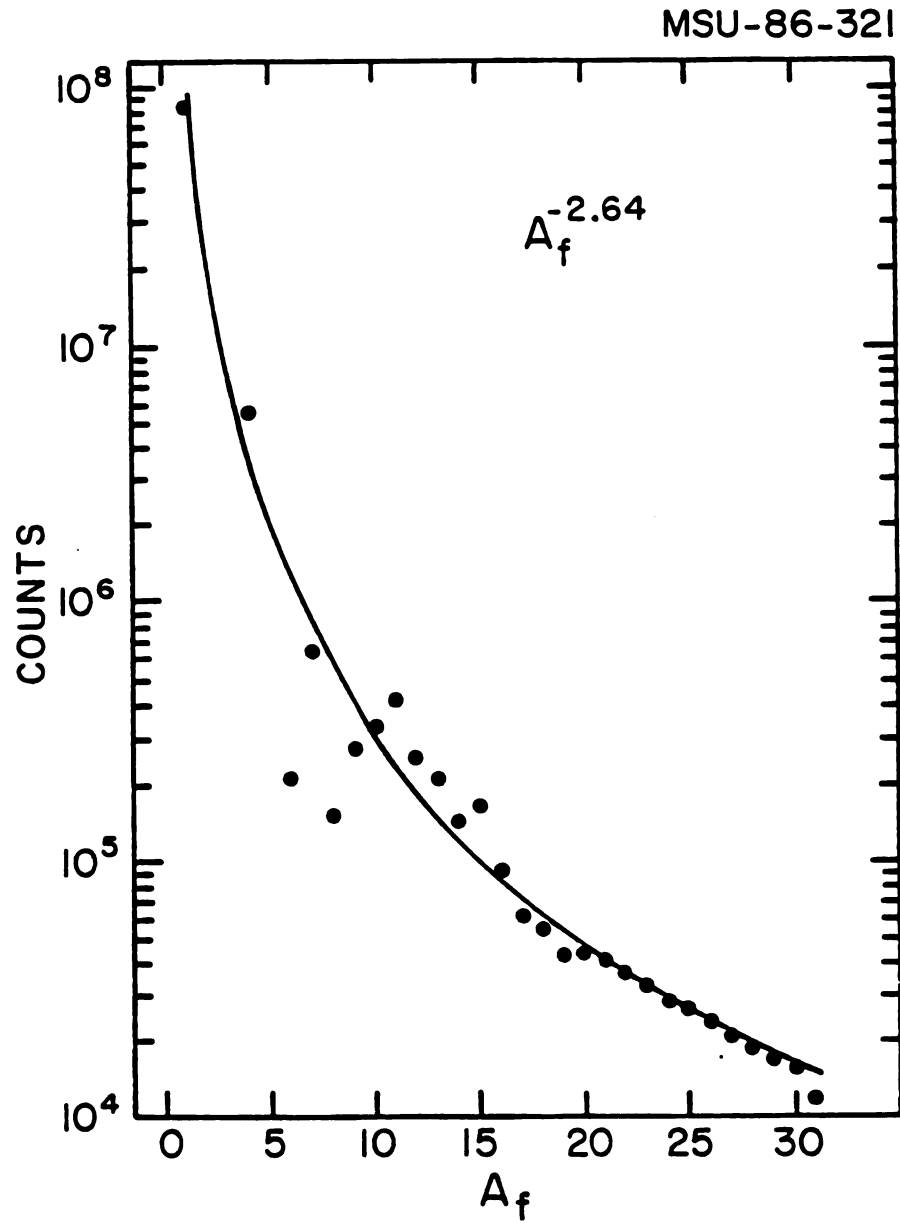


Figure I-1 The cross sections for fragments of mass  $A_f$  produced in the p + Xe reaction [HIR84] are shown as solid points. A power law dependence on fragment mass is indicated by the solid curve.

The validity of the phase transition model is vigorously debated. The analogy between small, electrically charged, quantum mechanical clusters of nucleons and macroscopic droplets is somewhat strained. A number of more specific objections have been raised. Molecular dynamics calculations indicate that fragmentation in small systems does not occur in the region of the phase diagram suggested by the phase transition theories [VIC85]. The signatures of any critical phenomenon would be seriously affected by the small number of nucleons in the experimentally accessible nuclear systems and by the properties of the nuclear surface [BOA84a] [GOO84]. In addition, the range of fragmentation data is not consistent with the single mechanism provided by the model [CUM85a].

Intermediate mass fragments may also be emitted from nuclei at much lower excitation energies. At these lower energies emission may proceed by a mechanism analogous to light particle evaporation [FRI83a] or the fission-like decay [MOR72] [MOR75a] of equilibrated nuclei. In fact, it was suggested that the study of intermediate mass fragment emission may assist in the unification of evaporation and fission into a single description [MOR75a]. These low energy mechanisms explicitly include the Coulomb interaction between the fragment and the parent system.

A statistical evaporation model [FRI83a] [FRI83c] of fragment emission based on the Weisskopf formula [WEI37] successfully described relative fragment cross sections and energy spectra from proton induced reactions [HIR84]. It also explained the relative fragment yields in  $^{12}\text{C}$  induced reactions on Ag and  $^{197}\text{Au}$  at  $E/A = 15$  and  $30$  MeV, as well as the measured dramatic rise in the cross sections between these two incident energies [CHI83].

Aspects of complex fragment emission have also been explained by transition state fission theories [MOR72] [MOR75a] for equilibrated systems. The energy spectra and angular distributions of complex fragments emitted at backward angles in  $^3\text{He} + \text{Ag}$  reactions at  $E=90$  MeV [SOB83] were consistent with equilibrium emission of fragments from compound nuclei. The energy dependence of the fragment cross sections was used to test models for fission barriers at different mass asymmetries [McM85] and to explore the target mass dependence of the shape of the fission saddle point along the mass asymmetry coordinate [SOB84].

At lower energies, up to  $E/A \approx 10$  MeV, the target and projectile may form a dinuclear system and separate without losing their identity [BAB76], a process termed deeply inelastic scattering. At energies above  $E/A=15$  MeV, the memory of the initial configuration, the defining characteristic of deeply inelastic scattering, is lost [GRA85] and the fragment mass distributions become broad.

Intermediate mass fragment emission becomes increasingly important at beam energies above  $E/A=15$  MeV [CHI83]. Cross sections for complete fusion, the other principal low energy mechanism, decline to zero with increasing bombarding energy [GAL82] [FAT85], signalling the rapid rise in pre-equilibrium processes [AWE81b] [AUB82], i.e. emission prior to the equilibration of the target-projectile system. Intermediate mass fragment cross sections clearly indicate contributions from such non-compound emission mechanisms [CHI83] [SOB83].

At the lowest energies fragments are emitted from equilibrated compound nuclei. At the highest energies, the reactions can result in a distinct division of the system into a participant region and the

projectile- and target-like spectators. At intermediate bombarding energies, there is no distinct separation between the spectator and participant components. A wide variety of emission mechanisms may contribute, including projectile fragmentation [MUR84] [MUR86], pre-equilibrium emission, and some remnant of deeply inelastic processes. It is difficult to distinguish clearly, either experimentally or conceptually, between these mechanisms.

The greater part of the experimental data has been in the form of single particle inclusive cross sections. The information content of these data is limited, since the inclusive distributions are averaged over all reaction channels, impact parameters, and orientations. They contain no direct information on particle multiplicities, collective effects, localization, or energy and momentum balance. Although several models are based on thermodynamic concepts, the inclusive data support this assumption only weakly : the energy spectra of fragments and light particles appear to be random and phase space dominated, and the relative fragment yields can be reproduced by statistical models. Yet there are non-thermal models which can reproduce these cross sections as well [AIC84d] [FIE84]. Additional information is necessary to adequately characterize intermediate mass fragment emission.

### I.B. Scope and organization :

The object of this dissertation is the characterization of fragmentation processes in intermediate energy heavy ion collisions through single and two-particle inclusive measurements. Of particular interest is the identification of non-statistical, dynamical aspects of



these reactions, as well as those aspects which can be treated with statistical theories. Useful experimental observables which can provide such information include the particle multiplicities, momentum transfer to the target, energy dissipation, and angular correlations. Of particular relevance for statistical treatments are the relative probabilities of emitting nuclei in excited states and the relative time scales for particle emission and equilibration.

This thesis addresses three issues: 1) single particle inclusive cross sections, 2) two particle coincidence cross sections, and 3) the statistical aspects of intermediate mass fragment emission at intermediate energies. The data presented here are drawn principally from experiments with the following projectile-target systems :  $^{12}\text{C} + ^{197}\text{Au}$  at  $E/A = 15$  and  $30$  MeV [CHI83] [FIE84],  $^{12}\text{C} + \text{Ag}$  also at  $E/A = 15$  and  $30$  MeV [CHI83],  $^{14}\text{N} + \text{Ag}$  at  $E/A = 35$  MeV [BOU86s], and  $^{32}\text{S} + \text{Ag}$  at  $E/A = 22.5$  MeV [FIE86] [XU87]. The experimental procedures employed to study these systems are discussed in Chapter II.

Single particle inclusive cross sections from all of these systems are presented in Chapter III. The object of this chapter is to present and characterize the single particle inclusive data and to provide a possible link between complex fragment emission from collisions at intermediate and high energies. Through the use of moving source parametrizations, the non-compound aspect of the differential cross sections is highlighted. The inclusive charge and isotopic distributions are also discussed.

The dynamics of fragment emission, as evident in the two particle coincidence data, will be the object of study in Chapters IV-VI. The data presented were obtained from the  $^{32}\text{S} + \text{Ag}$  system and , to a lesser

extent, the  $^{14}\text{N} + \text{Ag}$  system. Non-equilibrium aspects of reactions leading to intermediate mass fragment emission are established. Chapter IV addresses the cross sections for coincident light particles (p,d,t, $\alpha$ ) and intermediate mass fragments. Angle and energy dependent correlations between these particles provide clear evidence for the importance of the reaction dynamics. Associated multiplicities of light particle and intermediate mass fragments are evaluated in Chapter V. These measurements help to determine the validity of high multiplicity fragmentation models in intermediate energy reactions. In Chapter VI the velocity distributions of the target-like residues from fragment emission are studied. These provide information on the global energy and momentum balance in the projectile-target system.

In Chapters VII and VIII statistical aspects of fragment emission are addressed. Chapter VII presents calculations using a schematic model in which excited states of nuclei are populated with thermal probabilities, and compares these calculations with data to demonstrate the plausibility of such a statistical mechanism. The impact of the sequential decay of particle unbound states on the mass and isotopic distributions is investigated. Consequences of thermal populations of the excited states on measurements of excited state populations are discussed. Chapter VIII describes statistical model calculations which treat particle emission during and after the equilibration of the composite system. These calculations use a simplifying assumption, that a localized region of excitation from which particles are emitted at statistical rates is formed and evolves towards the fully equilibrated residual nucleus. They are compared to experimental charge distributions, momentum transfers, and energy spectra.

Chapter IX contains a summary of the present results and a few comments on the outlook for progress.

## Chapter II

### Experimental Methods and Analysis

In the following discussion of the experiments and their analysis, a polar coordinate system is employed. The polar axis is defined by the beam unit vector,  $\hat{b}$ , and the origin by the target. The polar angle,  $\theta$ , of a unit vector,  $\hat{v}$ , is defined as  $\theta = \cos^{-1}(\hat{v} \cdot \hat{b})$ . The azimuthal angle,  $\phi$ , is defined to be positive clockwise when facing in the beam direction.

#### II.A. $^{12}\text{C} + \text{Ag,Au}$ at $E/A=15.30$ MeV/A :

##### **II.A.1. Experimental objectives :**

At the time that the K500 cyclotron at Michigan State University became operational (Spring, 1983), little was known of intermediate mass fragment production in heavy ion collisions. The objective of this first experiment was the measurement of single particle inclusive cross sections of intermediate mass fragments in order to establish the existence of fragment production in intermediate energy heavy ion collisions, and the comparison of the results with data from low energy

heavy ion collisions and high energy proton-nucleus collisions.

### II.A.2. Detectors and geometry :

Beams of  $^{12}\text{C}$  ions accelerated to energies of 180 and 360 MeV were used to bombard self supporting Ag and Au targets with areal densities of  $0.6 \text{ mg/cm}^2$ . Fragments of  $Z=4-20$  were detected by a single telescope positioned at polar angles greater than the grazing angles of Coulomb trajectories (  $\theta_{\text{gr}} \approx 11^\circ$  and  $25^\circ$  for  $^{12}\text{C}+\text{Au}$  reactions and  $\theta_{\text{gr}} \approx 7^\circ$  and  $16^\circ$  for  $^{12}\text{C}+\text{Ag}$  reactions at  $E/A=30$  and  $15 \text{ MeV}$ , respectively). The telescope consisted of an ion chamber and two  $0.4 \text{ mm}$  thick silicon surface barrier detectors with active areas of  $450 \text{ mm}^2$ . The ion chamber was a  $10 \text{ cm}$  deep Frisch grid ion chamber [BAR75] and was operated with an  $\text{Ar}(90\%)-\text{CH}_4(10\%)$  gas mixture at a pressure of  $80 \text{ Torr}$ . The solid angle subtended by the telescope was  $5 \text{ msr}$ .

### II.A.3. Analysis and calibration :

The normalization of the absolute cross sections is calculated from the target thickness, detector solid angle, and integrated beam current according to the formula

$$\frac{d\sigma}{d\Omega} = \frac{A N Z}{\Omega \rho I} \cdot 2.66 \cdot 10^{-4} \quad , \quad (\text{II-1})$$

where  $d\sigma/d\Omega$  is the differential cross section in  $\text{mb/sr}$ ,  $A$  is the atomic weight of the target,  $N$  is the number of counts,  $\Omega$  is the solid angle of the detector in  $\text{sr}$ ,  $\rho$  is the target thickness in  $\text{mg/cm}^2$ ,  $I$  is the

integrated beam current in nanocoulombs, and  $Z$  is the charge state of the beam particles collected in the Faraday cup. The estimated uncertainty is less than 20%.

The energy calibrations for the solid state detectors were assumed to be linear over the measured energy range, i.e. of the form  $E=m(x-o)$ , where  $E$  is the particle energy,  $x$  is the ADC channel, and  $m$  and  $o$  are calibration parameters. These parameters were obtained in a two step process. Firstly, a series of known charges was injected into the input of the preamplifier to produce a linear curve of pulse height vs. energy, which determines the offset,  $o$ , of the calibration curve. Secondly, a thin, high resolution source of alpha particles was used to provide an absolute calibration point which determines the slope,  $m$ , of the pulse height vs. energy curve. The resulting energy calibration of the solid state detectors is accurate to within 3%. The energy calibration for the ionization chamber was obtained by comparing the pulse heights of signals from fragments of known element and energy with calculated energy losses for those heavy ions. The energy calibration of the gas counter is accurate to within 10%.

Particle identification was obtained from the elemental localization in a  $\Delta E$ - $E$  scatter plot, such as is shown in Figure II-1. The elemental cross sections were obtained for both Ag and Au targets at  $E/A=15$  MeV and 30 MeV. For the  $^{12}\text{C} + \text{Au}$  reaction at  $E/A=30$  MeV, the statistics were sufficient to produce differential cross sections for fragments up to  $Z=10$ . Energetic lighter fragments,  $Z \leq 4$ , were not stopped in the detector; therefore, differential energy spectra are not shown for these fragments. Integrated and average cross sections are estimated from the cross sections at larger angles, where the cross sections for

MSUX-83-176

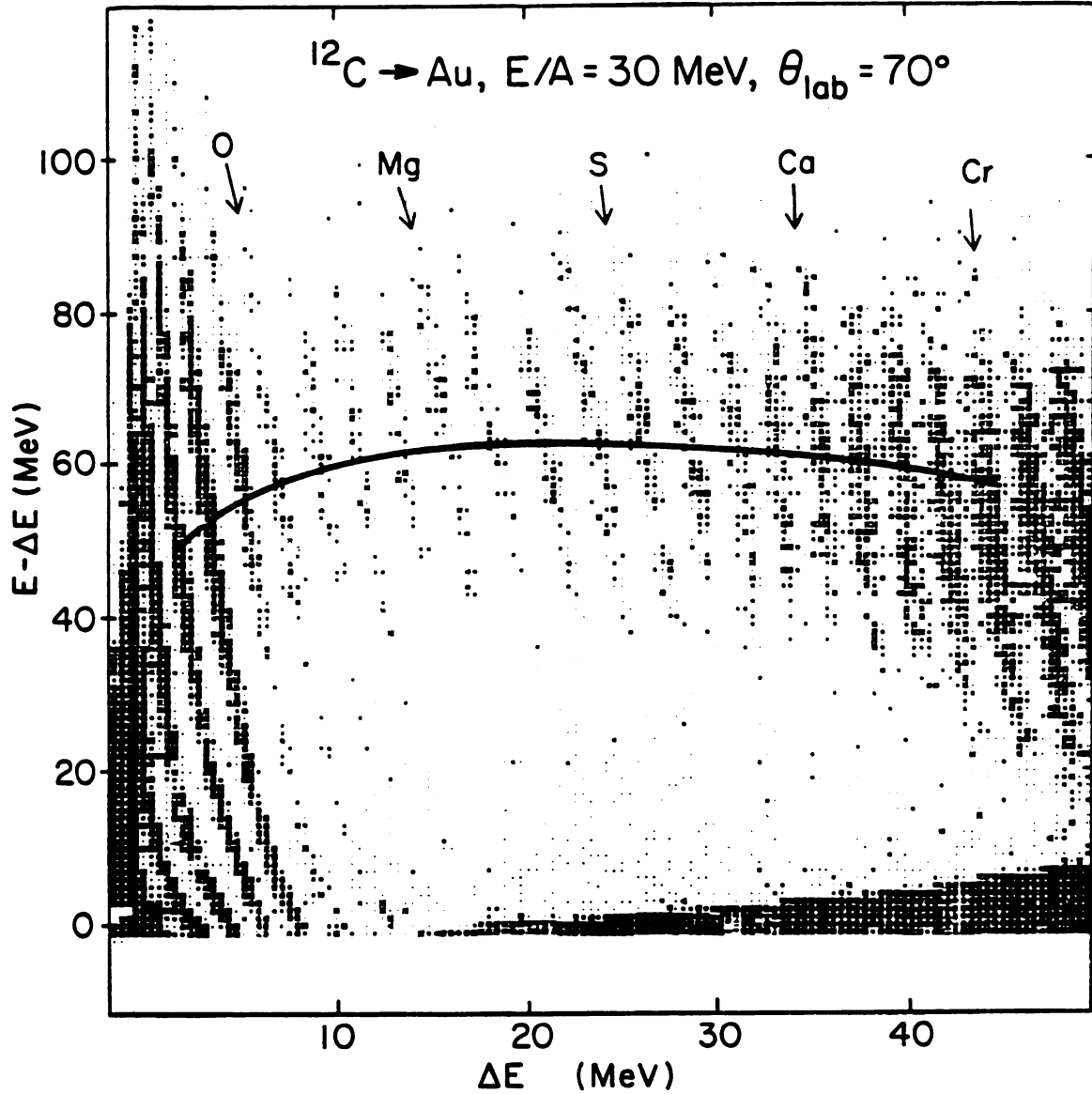


Figure II-1 : A scatter plot of  $\Delta E$  vs.  $E - \Delta E$  for the reaction  $^{12}\text{C} + ^{197}\text{Au}$  at  $E/A = 30$  MeV measured at  $\theta = 70^\circ$ . The solid curve represents the locus of peak kinetic energies predicted by a generalization of the systematics of fission Coulomb kinetic energies [VI085].

the emission of penetrating particles are small.

When more than one particle arrives in the telescope within its resolving time ( $\approx 1 \mu s$ ), the event will produce a  $\Delta E$ - $E$  signal which does not fall on a locus corresponding to one of the incident particles. Such events generate a background which is most evident at low energies and can be seen in Figure II-1 in the region between  $\Delta E=10$  and  $40$  MeV and around  $E-\Delta E=20$  MeV. The low energy thresholds of energy spectra presented in Chapter III are set at values where this background becomes small. A method for minimizing this contamination is discussed in Section II.C.3.

## II.B. $^{14}\text{N} + \text{Ag}$ at $E/A=35$ MeV :

### **II.B.1. Experimental objectives :**

This experiment was designed to measure both the single particle inclusive spectra of intermediate mass fragments and the angular distributions of target-like residues detected in coincidence with these fragments. The inclusive spectra provide information on the relative importance of equilibrium and non-equilibrium fragment emission processes. The angular distributions of coincident target residues provide information on two aspects of fragment producing reactions. Firstly, they determine whether fragments are typically produced by the complete disintegration of the target nuclei. Secondly, if heavy target residues remain, their angular distributions are related to the momentum transferred to the target system by the projectile, the relative



sequence of particle emission, and other dynamical aspects of the reaction.

The  $^{14}\text{N}$  beam at  $E/A=35$  MeV was chosen because it was the beam with the highest energy per nucleon available at the NSCL at the time. This high energy assured reasonably large fragment cross sections, as well as a sizable cross section for incomplete fusion reactions. The Ag target was chosen because it is relatively heavy and yet has a low fission cross section, somewhat simplifying the interpretation of the data. In addition, other measurements with Ag targets were available for comparison [CUR85t].

## II.B.2. Detectors and geometry :

The reactions were produced in a  $1.1 \text{ mg/cm}^2$  thick self-supporting Ag target by 490 MeV  $^{14}\text{N}$  ions. The arrangement of the detectors is depicted in Figure II-2. Intermediate mass fragments were detected in three detectors at laboratory polar angles of  $\theta=32.5^\circ$ ,  $45^\circ$ , and  $57.5^\circ$ , angles significantly larger than the grazing angle of a Coulomb trajectory,  $\theta_{\text{gr}} \approx 6^\circ$ . These detectors define the azimuthal angle  $\phi=0^\circ$ . Coincident target-like residual nuclei were detected with a position sensitive multiwire detector with a  $20 \text{ cm} \times 16 \text{ cm}$  active area. The detector was located 32 cm from the target and, in separate measurements, at polar angles of  $\theta=30^\circ$  and  $\theta=45^\circ$  on the opposite side of the beam from the intermediate mass fragment detectors ( $\phi=180^\circ$ ). Thus, coincidence measurements were performed for the range of polar angles in the reaction plane,  $12^\circ \leq \theta \leq 60^\circ$ .

The three intermediate mass fragment telescopes were contained in a

MSU-86-286

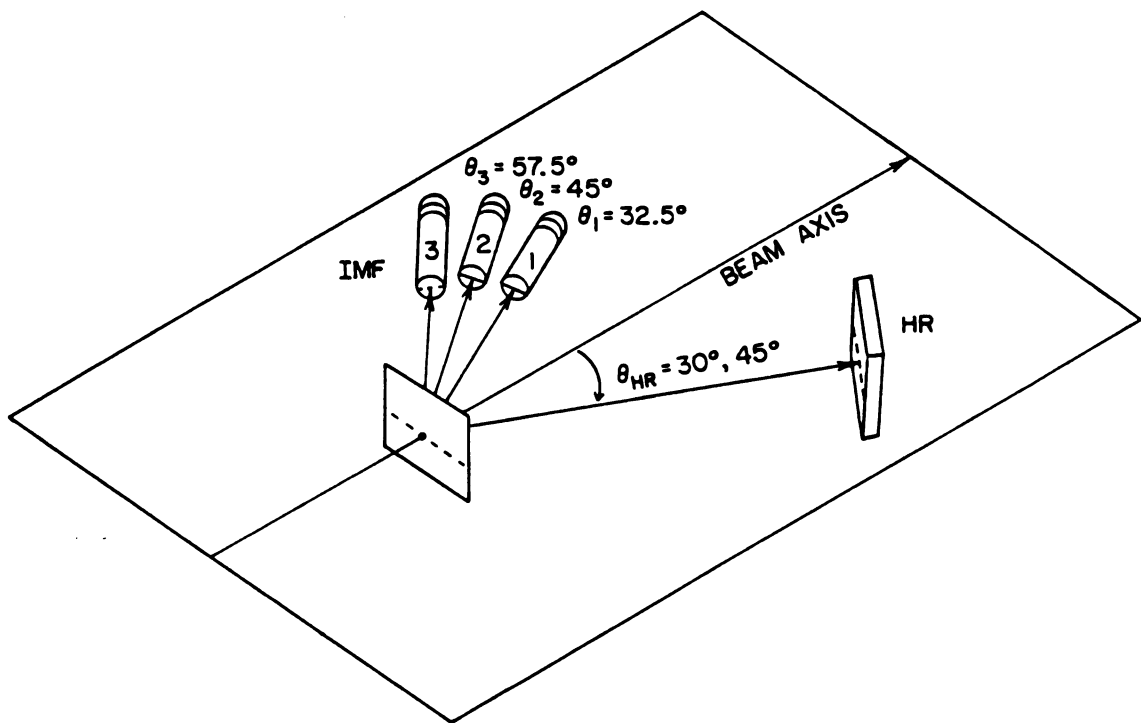


Figure II-2 : A schematic diagram of the experimental layout for the  $^{14}\text{N} + \text{Ag}$  coincidence studies. The position sensitive detector is labelled as "HR" and the ionization chamber-solid state telescopes are labelled as "IMF".

single three detector system, as shown in Figure II-3. Each telescope consisted of a 10.5 cm long Frisch grid ion chamber ( $\Delta E_1$ ), a .44 mm thick silicon surface barrier detector ( $\Delta E_2$ ), and a 5 mm thick lithium drifted silicon solid state detector (E). The ion chamber was operated with a Ar(90%)-CH<sub>4</sub>(10%) gas mixture at a pressure of 90 Torr. Each telescope subtended a solid angle of 9.1 msr.

A schematic diagram of the position sensitive detector is shown in Figure II-4. This multiwire avalanche counter consists of two planes of parallel wires which act as anodes separated by a conducting foil cathode plane. The wires in each plane are arranged in parallel and are read from a tapped delay line. The wires of each plane are perpendicular to the wires of the other. The avalanche at the anode induces a signal at the cathode foil which serves to provide a reference time signal. The relative time between the cathode time signal and the anode signal, which has a position dependent delay, is directly related to the position of the incident ion.

### II.B.3. Analysis and calibration :

The normalization for absolute cross sections and the energy calibrations were obtained as described in Section II.A.3. The normalization is accurate to 10%. The energy calibrations for the intermediate mass fragments were also obtained with uncertainties similar to the experiment in Section II.A.

The position calibration for the target recoil detector was obtained with a metal mask placed over the front face of the detector. The position of this mask with respect to the laboratory coordinate

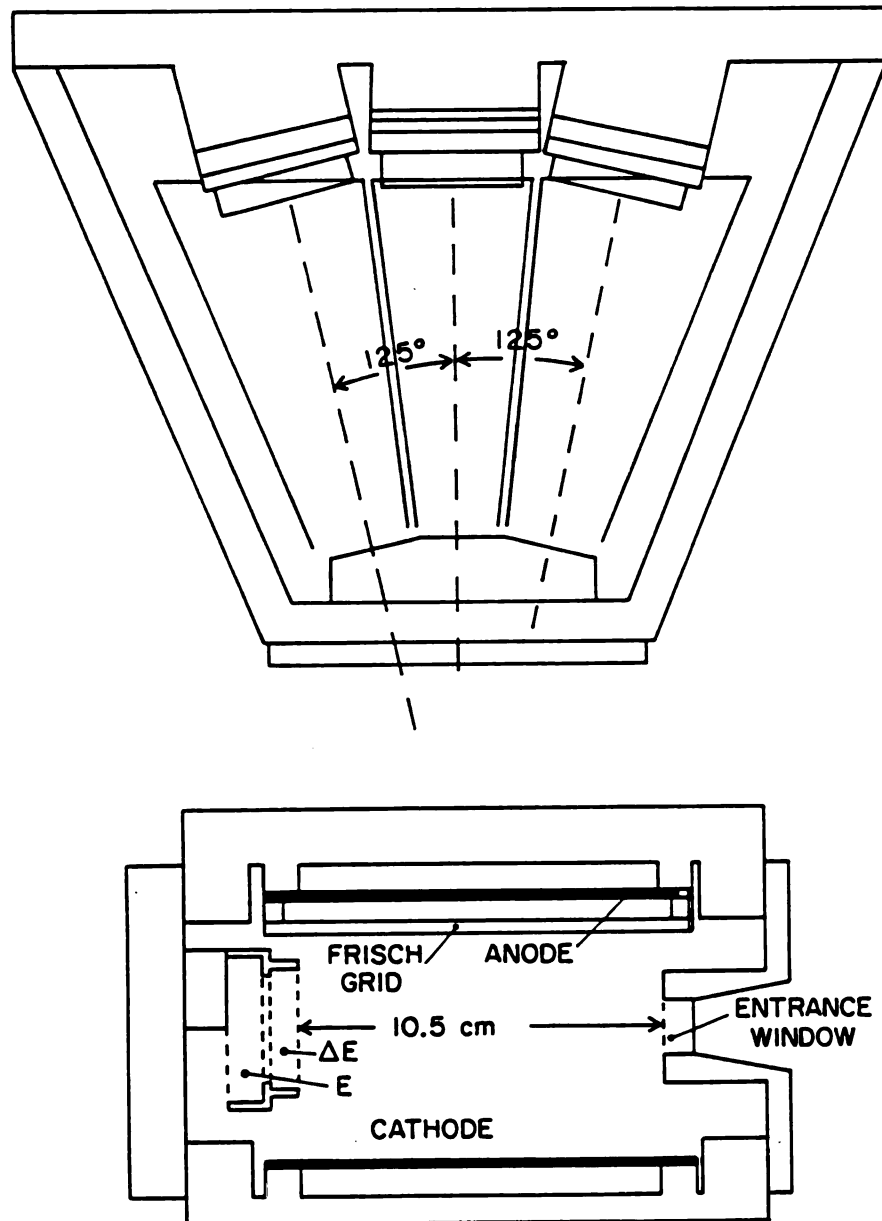


Figure II-3 : A schematic diagram of the triple Frisch-grid ion chamber system used in two of the experiments discussed in this thesis. The solid state detectors are contained in the gas volume.

MSU-86-253

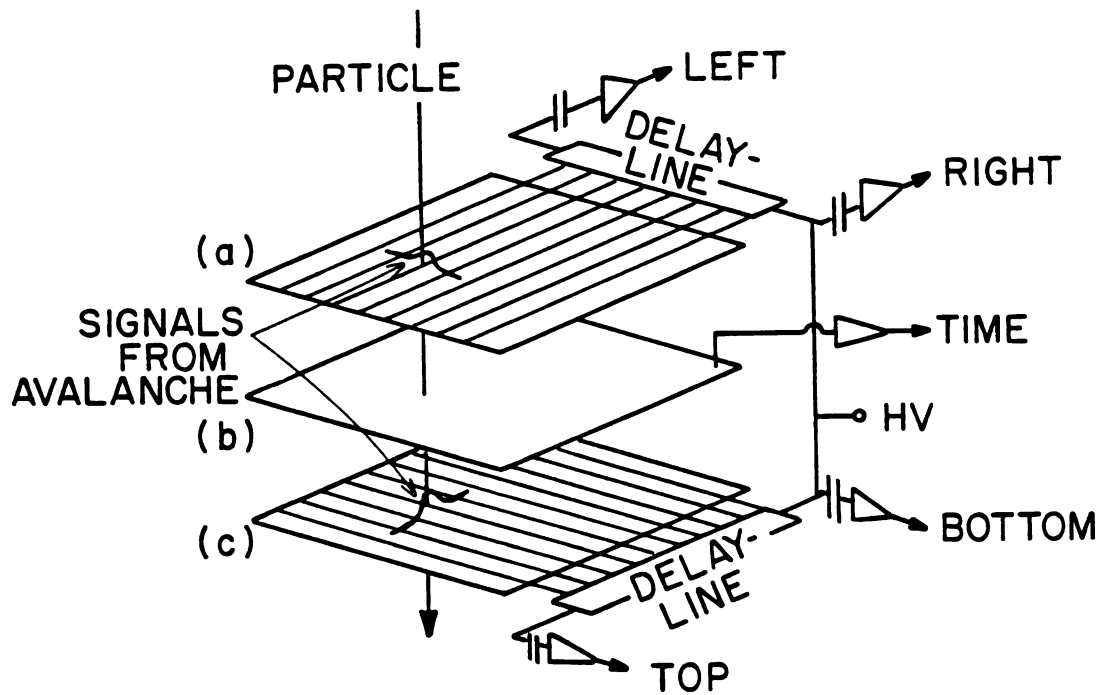


Figure II-4 : A schematic diagram of the multiwire avalanche counter used in the  $^{14}\text{N} + \text{Ag}$  experiment. The ionization avalanches occur about the wires in the anode planes labelled a and c. The signals induced on the wires undergo a position dependent delay before amplification. A signal induced on the foil cathode, b, is used as a time reference.

system was determined by optical alignment. The uncertainties are less than  $1^\circ$ .

Single particle inclusive cross sections for intermediate mass fragments were obtained in addition to angular distributions of coincident target-like nuclei. These angular distributions were analyzed as functions of fragment charge and momentum.

## II.C. $^{32}\text{S} + \text{Ag}$ , $E/A=22.5$ MeV, particle-particle coincidence measurements :

### **II.C.1. Experimental objectives :**

This experiment had two principal objectives. The first was to measure the distributions and multiplicities of non-equilibrium light particles emitted in collisions producing intermediate mass fragments. These provide information on the effects of the nuclear mean field on particle emission and on the momentum and energy transfer from the projectile to the target. The second objective was the determination of the velocity distributions of target-like residues from reactions which produce fragments.

The projectile,  $^{32}\text{S}$  at  $E/A=22.5$  MeV, was chosen because of its large total energy. The Ag target was chosen because it is heavy and non-fissile, and because other measurements with Ag targets were available for comparison. This experiment was performed at the Holifield Heavy Ion Research Facility at Oak Ridge National Laboratory.

### II.C.2. Detectors and geometry :

Two self-supporting Ag targets were used. For the light particle-intermediate mass fragment measurements, a target with an areal density of  $3.2 \text{ mg/cm}^2$  was used in order to maximize coincidence count rates. For the measurements of coincident intermediate mass fragments and heavy residues, a  $.75 \text{ mg/cm}^2$  thick target was used in order to reduce the energy loss of the heavy residues in the target. This thinner target was also used to obtain the single particle inclusive cross sections.

The experimental geometry is depicted in Figure II-5 and summarized in Table II-1. Light particles were detected at the azimuthal angle  $\phi=180^\circ$ , and the polar angles  $\theta=40^\circ$  and  $70^\circ$ , and at the azimuthal angle of  $\phi=-90^\circ$ , and the polar angles  $\theta=40^\circ$ ,  $70^\circ$ , and  $130^\circ$  ( see Figure II-5 for an illustration ). Light particle telescopes consisted of  $400 \mu\text{m}$  thick silicon surface barrier detectors as  $\Delta E$  elements and 10 cm thick NaI(Tl) scintillation detectors as E elements.

Intermediate mass fragments were detected at laboratory polar angles,  $\theta=27.5^\circ$ ,  $40^\circ$ , and  $52.5^\circ$  with respect to the beam axis and at an azimuthal angle of  $\phi=0^\circ$ . They were detected with the three telescope system described in Section II.B.2. The ion chamber was operated with an  $\text{Ar}(90\%)\text{-CH}_4(10\%)$  gas mixture at a pressure of 150 Torr.

The position sensitive detector was located 50 cm from the target and had an active area of  $11 \text{ cm} \times 11 \text{ cm}$ . It was placed at the azimuthal angle,  $\phi=180^\circ$ , and at polar angles,  $\theta=11^\circ$ ,  $16^\circ$ , and  $22^\circ$ . This detector [BRE79] [BRE84] is shown schematically in Figure II-6. It consisted of two  $50 \mu\text{g}$  polypropylene cathode foils with parallel conducting strips evaporated onto their surfaces, separated by a grid of thin wires which

MSU-85-566

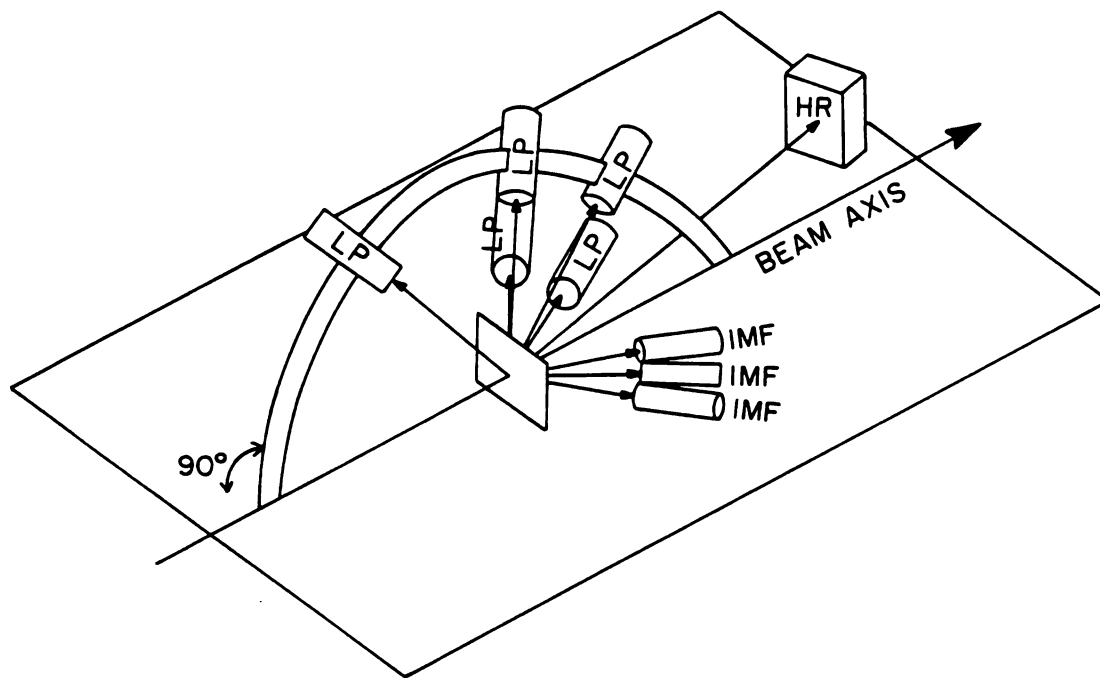


Figure II-5 : A schematic diagram of the  $^{32}\text{S} + \text{Ag}$  particle-particle coincidence experiment. The intermediate mass fragments are labelled as "IMF", the light particle detectors, as "LP", and the position sensitive detector, as "HR".



Table II-1 : The positions and solid angles of the light particle detectors (LP) and the intermediate mass fragment detectors (IMF) used to study the  $^{32}\text{S} + \text{Ag}$  system, as discussed in Section II.C.

detector	$\theta$ (deg)	$\phi$ (deg)	$\Delta\Omega$ (msr)
LP-1	40	180	27.
LP-2	40	-90	21.8
LP-3	70	180	64.6
LP-4	70	-90	34.
LP-5	130	-90	64.6
IMF-1	27.5	0	7.9
IMF-2	40	0	7.9
IMF-3	52.5	0	7.9

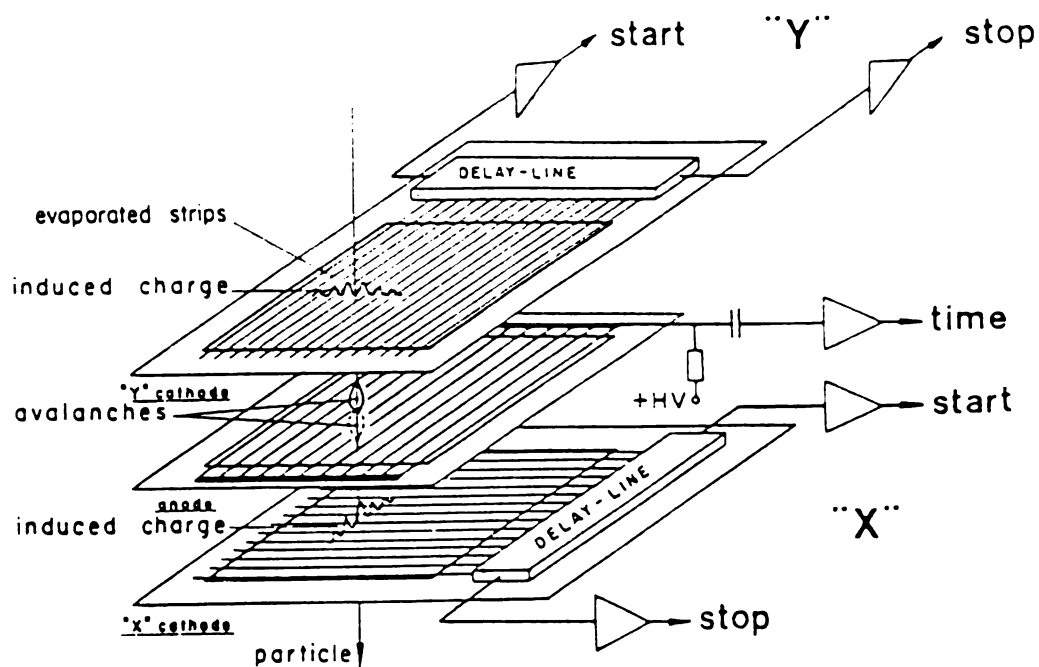


Figure II-6 : A schematic diagram of the Breskin design position sensitive detector. The ionization avalanches occur at the central wire anode. The signals induced on the evaporated strips on the foil cathode undergo a position dependent delay before amplification.

acts as the anode plane. The parallel strips in each foil are connected in parallel to a delay line. The two foils are oriented so that the evaporated strips will be mutually perpendicular. The position is calculated from the relative time of arrival of the anode signal and the signal induced on the cathode delay line.

### II.C.3. Analysis and calibration :

The normalization of the absolute cross sections, obtained as discussed previously, is accurate to 10%. The energy calibrations of the solid state detectors in the intermediate mass fragment telescopes and  $\Delta E$  elements of the light particle telescopes were obtained with a pulser and an alpha source and are accurate to 5%. The ionization chamber calibrations are accurate to 10%. The NaI(Tl) scintillation detectors were calibrated with peaks from protons emitted in the elastic scattering of  $^{32}\text{S}$  ions from a polyethylene target. The NaI(Tl) detector energy calibrations are accurate to about 5%.

Intermediate mass fragments were identified elementally using the localization of the elements in  $\Delta E$ -E scatter plots. For detectors of large solid angle, the spectra are contaminated by events in which two particles are detected simultaneously in the same telescope. Light particles may arrive with heavier fragments which deposit most or all of their energy in the gas  $\Delta E_1$  element. Such events produce a low energy contamination of the energy spectra of intermediate mass fragments consisting of misidentified particles. With a two element telescope, this contamination is impossible to eliminate. With three element telescopes, as were used here, the events which produce signals in three

elements can be rejected by double identification: particles which are identified differently in the  $\Delta E_1 - (\Delta E_2 + E)$  and  $\Delta E_2 - E$  scatter plots are rejected.

The position response of the parallel plate multiwire detector was calibrated with respect to the edges of the active area. The calibrations are accurate to one degree. The known flight times of elastically scattered beam particles provided the absolute time calibration. The period of the cyclotron beam was used to calibrate the conversion constants of the TDC. The resulting velocity determinations are accurate to within 5%.

In order to measure the velocities of target like recoil nuclei, it is necessary to measure their times-of-flight. The quantity measured was a time interval between a signal which begins the clock (supplied by the overlap coincidence between an intermediate mass fragment telescope logic signal and a logic signal generated from the anode pulse) and the signal from the anode of the position sensitive detector, which is delayed so that it stops the clock. This time interval differs from the actual time of flight by a constant, which is provided in the time calibration.

Because of energy losses in the target foil, the measured velocity spectra of the target-like residues are not the original velocities of the emitted particles. A correction for this energy degradation would increase the velocities by 5%-10%, depending on the mass and charge of the residue. These quantities were not measured. However, an additional kinematic effect connected with the finite acceptance of our detectors biases the velocity spectra towards higher velocities. This produces as much as a 10% increase in the measured velocities. A more complete

discussion of this effect is included in Appendix A. Because of the uncertainties involved in estimating the effects of either mechanism, they are assumed to cancel and no corrections to the velocity distributions have been applied.

The raw position spectra, as shown in Figure II-7, are modulated by spurious structures resulting from non-linearities in the detector response. These have been eliminated by correcting the position histogram by a factor which represents the deviation of the raw, ungated position spectra from a smooth linear dependence on angle. The position spectra from the three detector positions were corrected, normalized, and combined to produce a distribution as shown in Figure II-8. The distributions are normalized to represent the probability of detection,  $P(\theta)$ , per degree; here  $\theta$  is the polar angle of the projection of the recoil velocity onto the reaction plane.

#### II.D. <sup>32</sup>S + Ag. E/A=22.5 MeV. particle-gamma coincidence measurements:

##### **II.D.1. Experimental objectives :**

In this experiment the fractions of intermediate mass fragments emitted in their particle stable excited states were measured. This set of measurements provides information about the partition of excitation energy among the available intrinsic degrees of freedom which are represented by the excited states of fragments. Statistical models of fragment production make certain predictions concerning the relative population of these excited states. Comparisons between such calculations and measured values may indicate the applicability of

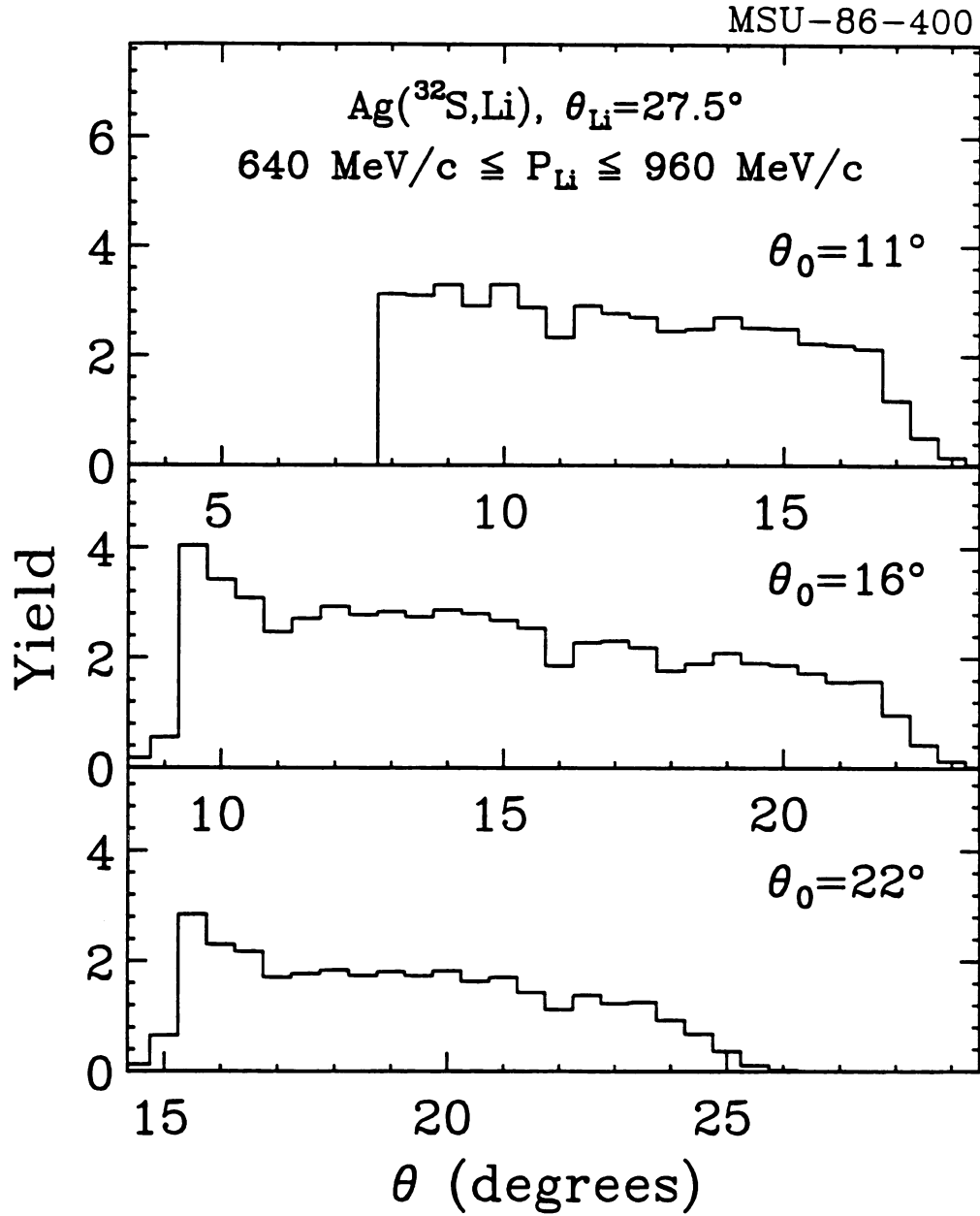


Figure II-7 : Raw position spectra from the Breskin detector placed at the three laboratory angles from target-like fragments detected in coincidence with lithium fragments detected at  $\theta = 27^\circ$ . Detector originated modulations of the spectra are easily recognized.

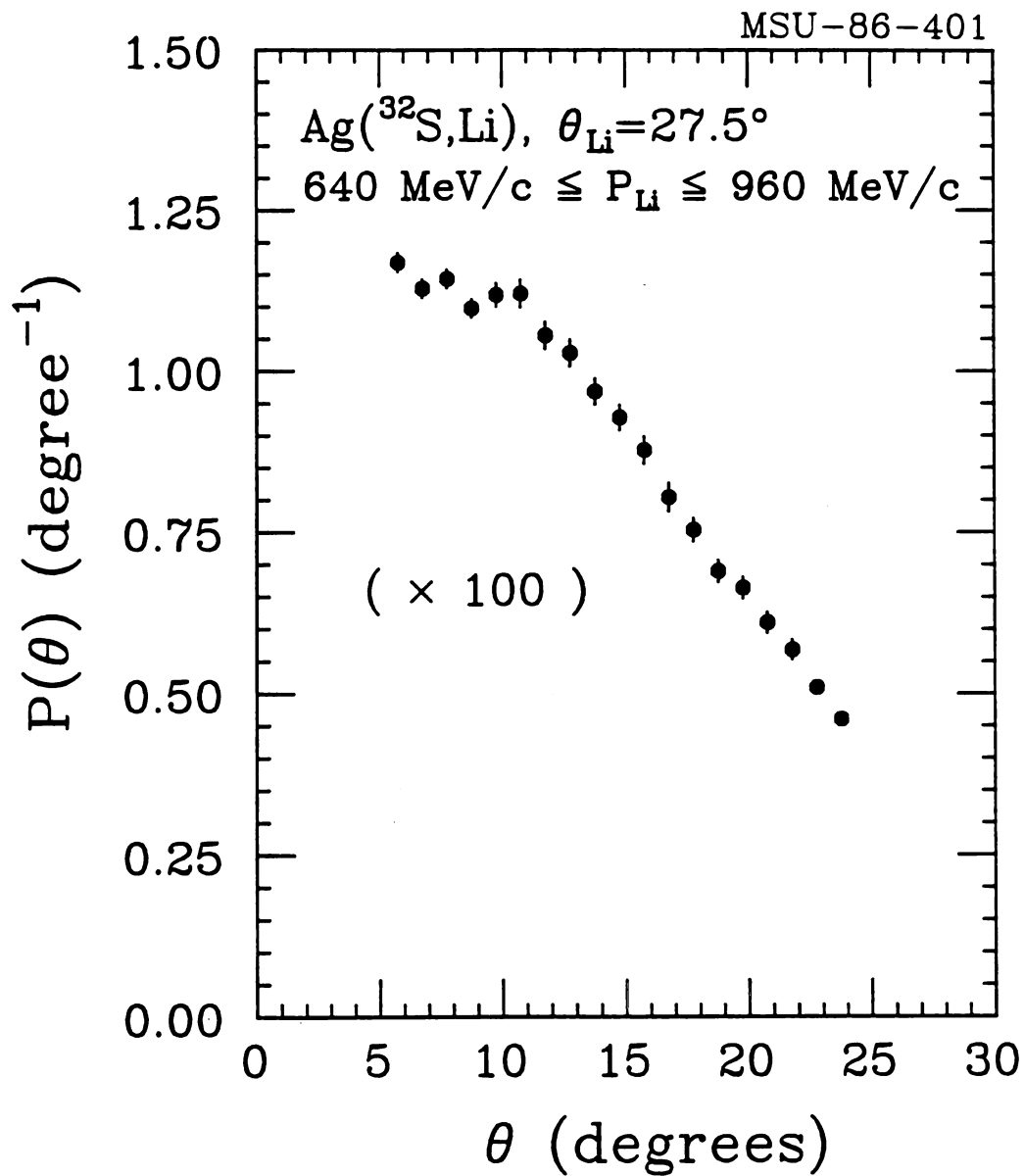


Figure II-8 : Final angular distribution from the raw spectra in Figure II-7. The distribution is smooth and relatively free of spurious structures.

statistical theories to fragment emission and the state of the systems giving rise to fragments. The  $^{32}\text{S} + \text{Ag}$  projectile-target system was chosen because of the availability of other measurements to which these results might be complementary.

#### II.D.2. Detectors and geometry :

The fragments are produced in reactions induced in a  $1.1 \text{ mg/cm}^2$  thick natural Ag target by a beam of  $^{32}\text{S}$  ions accelerated to an energy of 720 MeV at the Holifield Heavy Ion Facility.

The intermediate mass fragments were detected by solid state detector telescopes at polar angles,  $\theta = 20^\circ, 25^\circ, 30^\circ, 45^\circ$ , and  $50^\circ$ . The telescopes consisted of two transmission solid state detectors,  $\Delta E_1$  and  $\Delta E_2$ , and a solid state detector which measured the total remaining energy, E. The detector dimensions are summarized in Table II-2.

Discrete gamma rays were detected with the Oak Ridge Spin Spectrometer. The results discussed here were obtained from six Compton-shielded germanium detectors which were placed in the Spin Spectrometer. A recent version of the Compton shielded germanium detectors is shown in Figure II-9. The resolution of the detectors is of the order of 2 keV for 1 MeV gamma rays. The maximum opening angle for each detector is approximately  $12^\circ$ . Typical efficiencies for gamma rays emitted from the target position are given in Table II-3. The geometrical arrangement of the gamma ray and particle detectors is summarized in Tables II-2 and II-3.

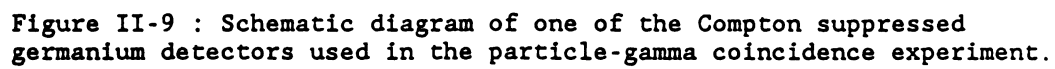


Table II-2 : The positions, solid angles, and construction of the solid state fragment detectors used in the  $^{32}\text{S} + \text{Ag}$  particle - gamma coincidence experiment, as discussed in Section II.D.

det	$\theta(\text{deg})$	$\phi(\text{deg})$	$\Delta\Omega(\text{msr})$	detector depth ( $\mu\text{m}$ )		
				$\Delta E1$	$\Delta E2$	E
1	20	90	9.75	75	100	1500
2	25	-90	10.1	75	100	1500
3	30	0	15.35	75	100	1500
4	45	90	36.0	50	75	1500
5	50	-90	28.5	44	75	1500

Table II-3 : The positions and typical efficiencies of the Compton suppressed germanium detectors, as discussed in Section II.D. The number in parenthesis next to the detector number is the parameter number for the Compton shield. The position of each detector in the ORNL Spin Spectrometer is given in the second column. The remaining columns give the absolute position with respect to the beam axis and the absolute efficiency of each detector at 300 keV.

$\gamma$ -detector	SS-pos	$\theta$ (deg)	$\phi$ (deg)	$\epsilon$ (@300 keV)
1 (18)	D0	63.4	36.0	.00105
2 (66)	L0	116.6	-72.0	.00068
3 (48)	I0	116.6	72.0	.00079
4 (30)	F0	63.4	-108.0	.00092
5 (24)	E0	63.4	-36.0	.00095
6 (12)	C0	63.4	108.0	.00101



### II.D.3. Analysis and calibration :

Cross section normalizations and particle energy calibrations were obtained as discussed previously; they are accurate to 10% and 3%, respectively. The energy calibrations of the germanium gamma ray detectors were obtained from peaks provided by a number of standard sources, and are accurate to 1 keV.

This experiment requires an accurate isotopic identification of fragments, even at the expense of detection efficiency. Instead of the particle identification method discussed previously, two different particle identification functions,

$$F_1 = (\Delta E_1 + \Delta E_2 + E)^K - (\Delta E_2 + E)^K \quad \text{and} \quad (\text{II-2})$$

$$F_2 = (\Delta E_2 + E)^K - E^K \quad , \quad (\text{II-3})$$

were generated, where K is a constant value, K=1.74. An accepted particle event was required to satisfy consistent constraints on both identification functions. Less than 4% of accepted particles are estimated to be misidentified. The resulting detection efficiency is in the range of 80%-90%.

The efficiency of the germanium detectors was determined in a two step process. In the first step, the relative efficiency of the detectors as a function of photon energy is determined by comparison of the integrated photopeak intensities from transitions from  $^{152}\text{Eu}$  and  $^{182}\text{Ta}$  sources to the known relative transition intensities. This

results in relative efficiency curves as shown as solid points in Figure II-10a. These relative efficiencies were fit to a function,

$$\bar{\epsilon} = (m \cdot E + b) \cdot \exp(a|E - E_0|^r) \cdot \left(1 - \frac{c}{(E - d)^2 + f}\right) \quad (\text{II-4})$$

for purposes of interpolation, where  $E$  is the gamma ray energy,  $\bar{\epsilon}$  is the parametrized relative detector efficiency, and the other quantities represent fitting parameters. This fit produces the solid curve shown in Figure II-10a. The ratio of the data to the fit is shown in Figure II-10b. The maximum deviation of the measured response from the fit is less than 10%.

The normalization for absolute efficiency was obtained from sources which emit two coincident photons, specifically  $^{75}\text{Se}$ ,  $^{88}\text{Y}$ , and  $^{60}\text{Co}$ . The absolute efficiency of a detector is the probability, after correcting for the angular correlations between the two photons, that one photon is detected in that detector given that the other photon in the decay is detected in another detector (see Appendix B). These measurements were then used to normalize the relative efficiencies curves to absolute efficiencies. The errors in the resulting efficiencies are of the order of 5%.

A spectrum of gamma rays measured in coincidence with  $^{10}\text{B}$  is shown in Figure II-11a. The gamma rays are Doppler shifted in the laboratory, so that

$$E_{\gamma}^* = E_{\gamma} \frac{(1 - \beta \cos \theta)}{(1 - \beta^2)^{1/2}}, \quad (\text{II-5})$$

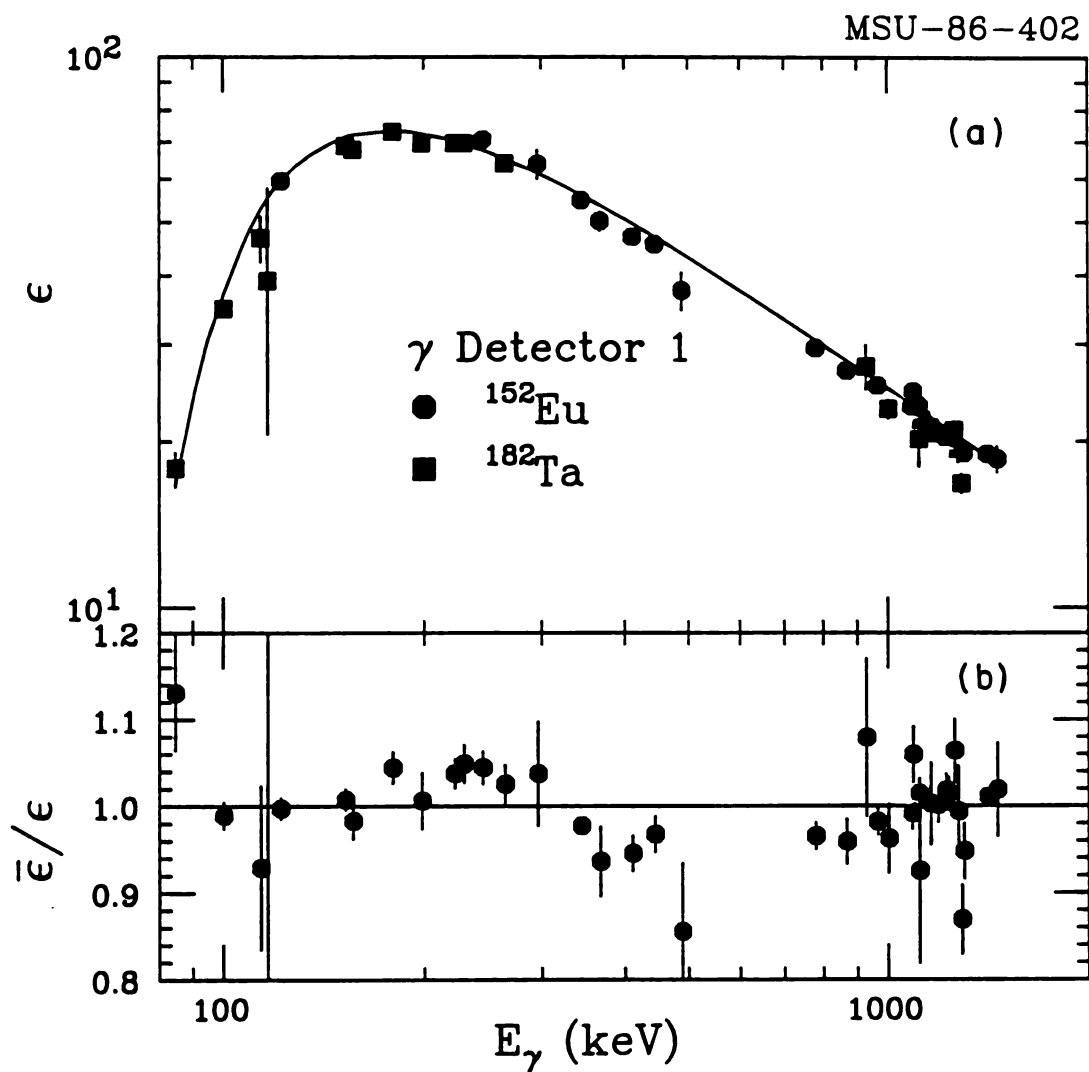


Figure II-10: The relative efficiency curve (a) for  $\gamma$  detector 1 from a  $^{152}\text{Eu}$  source (circles) and  $^{182}\text{Ta}$  source (squares). The solid curve indicates the analytic interpolation discussed in the text. The ratio of the source data to the interpolation is shown in the bottom part of the figure (b).

MSU-86-403

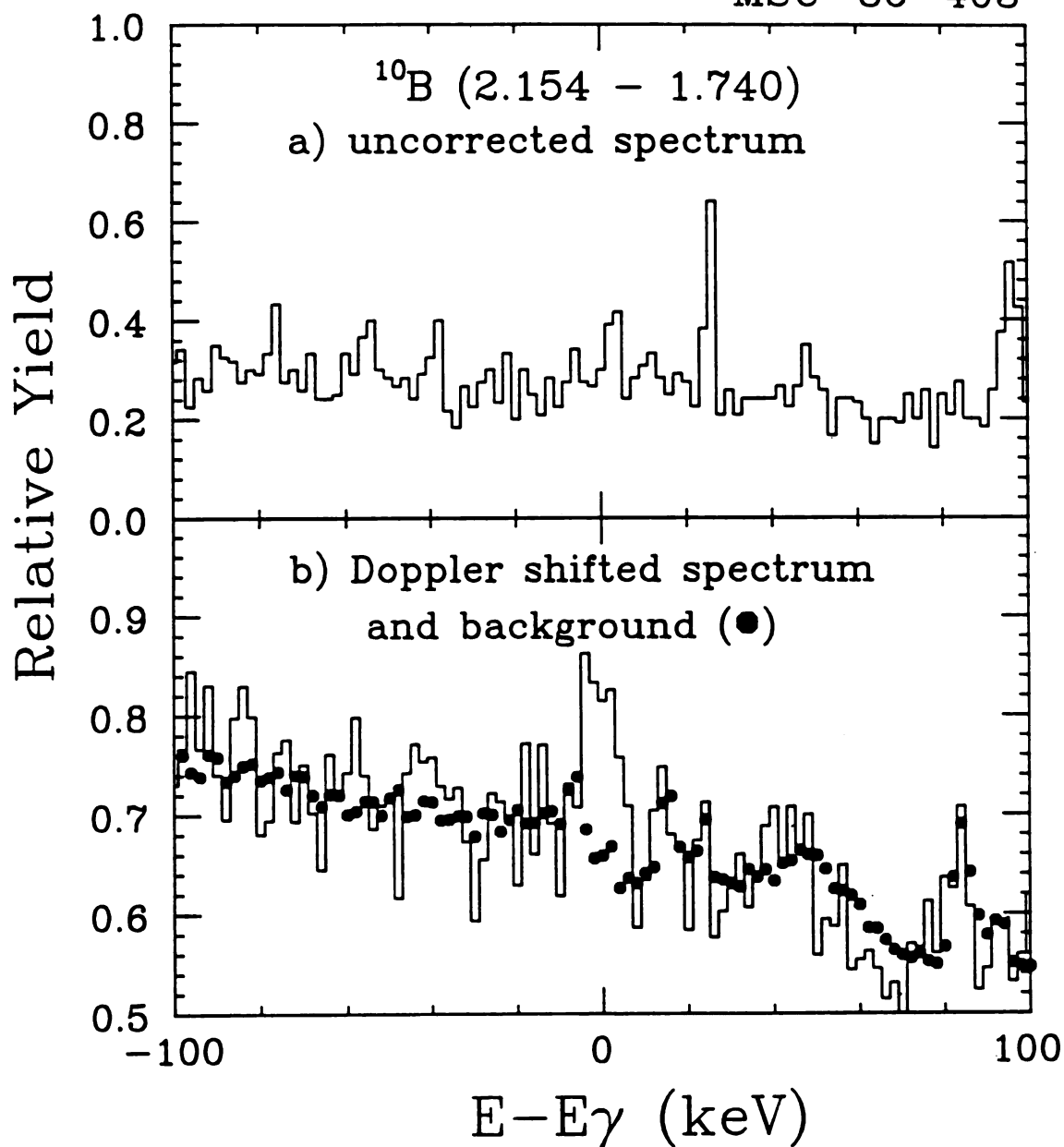


Figure II-11: The spectrum of gamma rays coincident with  $^{10}\text{B}$  ions, without Doppler shift, is shown in the upper part of the spectrum, (a). The bottom part of the figure, (b), shows the corrected spectrum, indicated by the histogram, and the estimated background, indicated by the solid points. The background is produced by Doppler shifting gamma rays coincident with other nuclei, as discussed in the text.

where  $\cos\theta = \hat{\beta} \cdot \hat{\mu}_\gamma$ ,  $E_\gamma^*$  is the transition energy,  $E_\gamma$  is the photon energy in the laboratory rest frame,  $\beta$  is the velocity in the laboratory of the nucleus from which the gamma rays are emitted,  $\hat{\beta}$  and  $\hat{\mu}_\gamma$  are unit vectors in the direction of the detected particle and photon, respectively, and  $\theta$  is the relative angle between these two vectors. Due to summations over different particle energies and detection angles, lines from discrete transitions in intermediate mass fragments are Doppler shifted and broadened. Gamma rays from transitions in the relatively slow moving target residues are not greatly Doppler shifted in the laboratory. Therefore, gamma ray energies from each event were corrected for the Doppler shift on the assumption that the photon was emitted from the detected intermediate mass fragment. The corrected spectrum is shown as the histogram in Figure II-11b. The transition from the intermediate mass fragment is well resolved, while the lines from target-like residues are broadened.

There is a change in the effective solid angle and efficiency of the photon detectors due to the relativistic Jacobian of transformation,  $|J|$ , between the solid angles in the laboratory and fragment rest frames:

$$|J| = \frac{d\Omega}{d\Omega^*} = \frac{(1 - \beta \cos\theta)^2}{1 - \beta^2}, \quad (\text{II-6})$$

where  $\Omega$  and  $\Omega^*$  are the solid angles of the gamma ray detectors in the laboratory and fragment rest frames, respectively. (See Appendix C for a derivation.) The spectra were corrected on an event by event basis for



this change in efficiency and for the difference in the detector efficiencies at the energies  $E_\gamma$  and  $E_\gamma^*$ .

The gamma rays of interest lay on top of a background which contains noticeable contributions from discrete transitions in target-like nuclei. As already mentioned, when the gamma ray spectrum is Doppler corrected for the motion of the fragment in the laboratory, the fragment gamma peak is narrowed while the target related gamma peaks are broadened into complicated structures. This background must be subtracted from the area under the fragment gamma peak, so it is necessary to identify any structures under that peak.

This target related background is only weakly dependent on the intermediate mass fragment; the laboratory background spectra can be assumed to be the same for spectra of neighboring fragments. This feature is utilized to estimate the background underneath the peak of interest. To calculate the background for gamma rays coincident with fragment A, the spectrum of gamma rays coincident with a fragment B with a similar mass and charge is utilized. The calculated background,  $B_A(E_\gamma^*)$ , is given by

$$B_A(E_\gamma^*) = N \sum_{E_\gamma} \sum_{E_A} B_B(E_\gamma) \sigma_A(E_A) \frac{d\Omega}{d\Omega^*} \frac{\bar{\epsilon}(E_\gamma^*)}{\bar{\epsilon}(E_\gamma)} \\ \times \delta(E_\gamma^*, E_\gamma \cdot \frac{(1-\beta \cos \theta)}{(1-\beta^2)^{1/2}}) \quad , \quad (\text{II-7})$$

where  $B_B(E_\gamma)$  is the gamma yield at energy  $E_\gamma$  coincident with fragment B,  $\sigma_A(E_A)$  is the cross section of fragment A at energy  $E_A$ , N is a

normalization constant,  $\beta$  is the velocity of the fragment A at the energy  $E_A$ , and  $\delta(x,y)$  is 1 when  $x=y$  and 0 otherwise. The background for the  $^{10}\text{B}$  gamma ray spectrum, generated from gamma rays in coincidence with neighboring nuclei, is indicated by the solid points in Figure II-11b.

Five gamma ray transitions of interest were analyzed. These are the transitions from the following states :  $^8\text{Li}$  ( $E^*=0.981$  MeV,  $J^\pi=2^+$ ),  $^7\text{Be}$  ( $E^*=0.429$  MeV,  $J^\pi=1/2^-$ ),  $^{10}\text{B}$  ( $E^*=2.154$  MeV,  $J^\pi=1^+$ ),  $^{12}\text{B}$  ( $E^*=0.953$  MeV,  $J^\pi=2^+$ ,  $E^*=2.621$  MeV,  $J^\pi=2^-$ ), and  $^{13}\text{C}$  ( $E^*=3.854$  MeV,  $J^\pi=5/2^-$ ). The transition from the first excited state in  $^7\text{Li}$  ( $E^*=0.477$  MeV,  $J^\pi=1/2^-$ ) was not analyzed because of contamination of the particle spectra by  $^8\text{Be}$  nuclei which, after decay into two alpha particles, are misidentified as  $^7\text{Li}$  nuclei [WOZ72]. The transition from the first excited state in  $^{10}\text{B}$  ( $E^*=0.718$  MeV,  $J^\pi=1^+$ ) was also not analyzed. Because the lifetime of this state is rather long,  $\tau=1.02$  ns, nuclei excited in this state could have travelled a significant distance from the target ( $\approx 3\text{cm}$ ), introducing a considerable uncertainty into the effective photon detection efficiency of the Compton shielded Ge detectors. This experiment yielded relative isotopic fragment cross sections in addition to coincidence gamma ray spectra.

## Chapter III

### Single Particle Inclusive Data

Single particle inclusive energy spectra,  $d^2\sigma/dEd\Omega$ , for light particles and intermediate mass fragments are shown as solid and open points in Figures III-1 through III-6.

#### III.A. Features of the inclusive data :

##### **III.A.1. Light particle spectra :**

The energy spectra for p,d,t, and  $\alpha$  particles produced in  $^{32}\text{S}$  induced reactions on Ag at  $E/A=22.5$  MeV are shown in Figure III-1. The cross sections in the forward hemisphere are dominated by products of non-equilibrium processes [AWE82a], i.e. the angular and energy distributions are inconsistent with emission from equilibrated compound nuclei. In fact, the energy thresholds in the present experiment exclude most of the contributions from equilibrium evaporation from the target. Previous studies of non-equilibrium light particle emission show that it is associated with violent nuclear collisions [AWE81b] and that it is

MSU-85-504

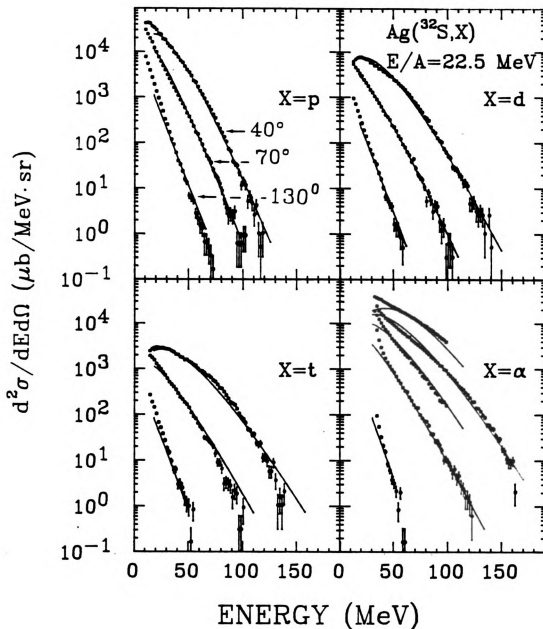


Figure III-1 : Differential cross sections,  $d^2\sigma/dEd\Omega$ , measured at  $\theta=40^\circ$ ,  $70^\circ$ , and  $130^\circ$ , for light particles, p, d, t, and  $\alpha$ , from  $^{32}\text{S}$  induced reactions on Ag at  $E/A=22.5$  MeV. Also, cross sections measured at  $\theta=27.5^\circ$  and  $52.5^\circ$  are shown for  $\alpha$  particles. The solid curves are the result of the parametrization discussed in the text.

MSU-86-404

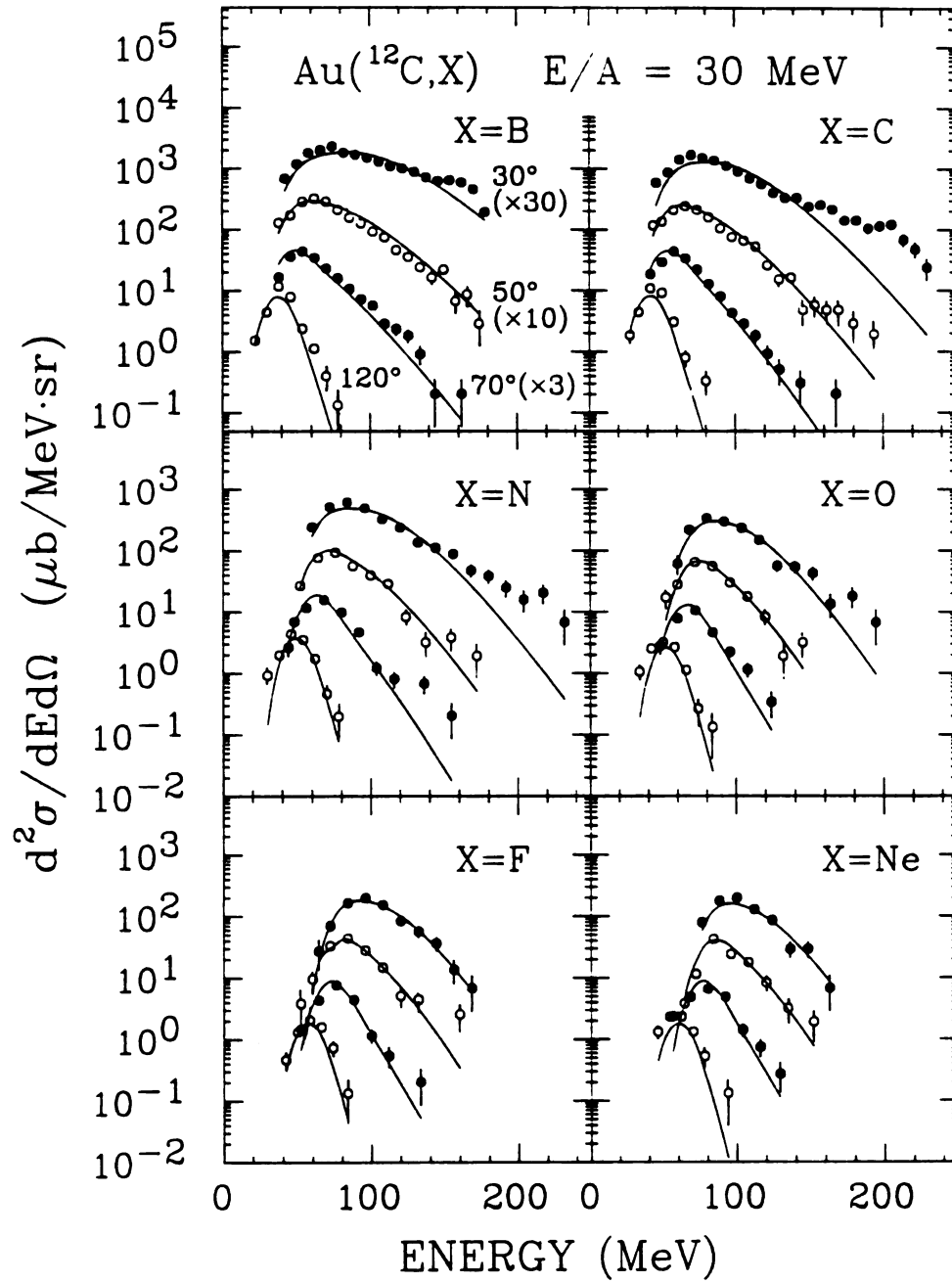


Figure III-2 : Differential cross sections,  $d^2\sigma/dEd\Omega$ , measured at  $\theta=30^\circ$ ,  $50^\circ$ ,  $70^\circ$ , and  $120^\circ$ , for fragments,  $5 \leq Z \leq 10$ , from  $^{12}\text{C}$  induced reactions on Au at  $E/A=30$  MeV. The solid curves are the result of the parameterization discussed in the text.

MSU-86-405

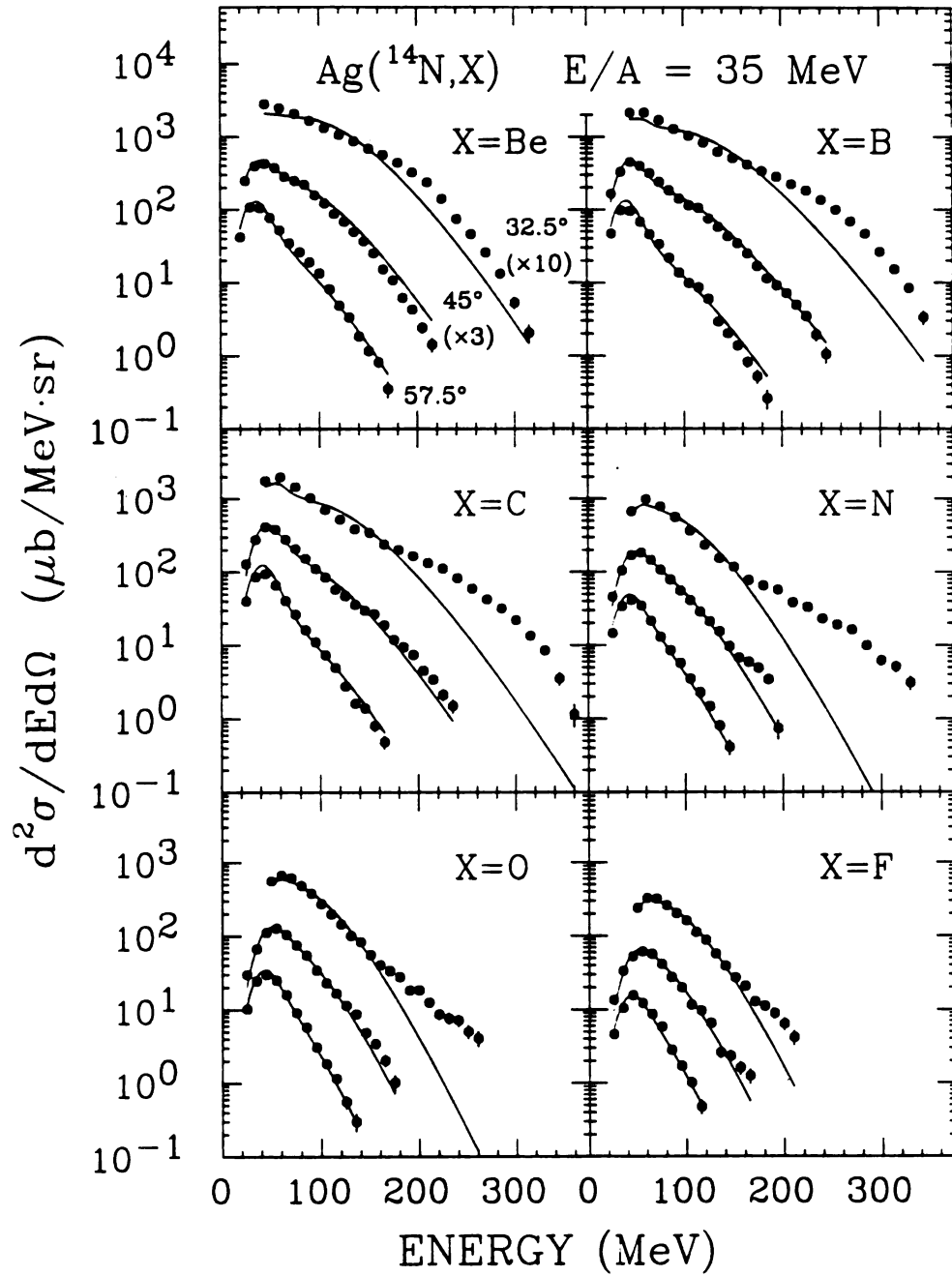


Figure III-3 : Differential cross sections,  $d^2\sigma/dEd\Omega$ , measured at  $\theta=32.5^\circ$ ,  $45^\circ$ , and  $57.5^\circ$ , for fragments,  $4 \leq Z \leq 9$ , from  $^{14}\text{N}$  induced reactions on Ag at  $E/A=35$  MeV. The solid curves are the result of the parameterization discussed in the text.

MSU-86-406

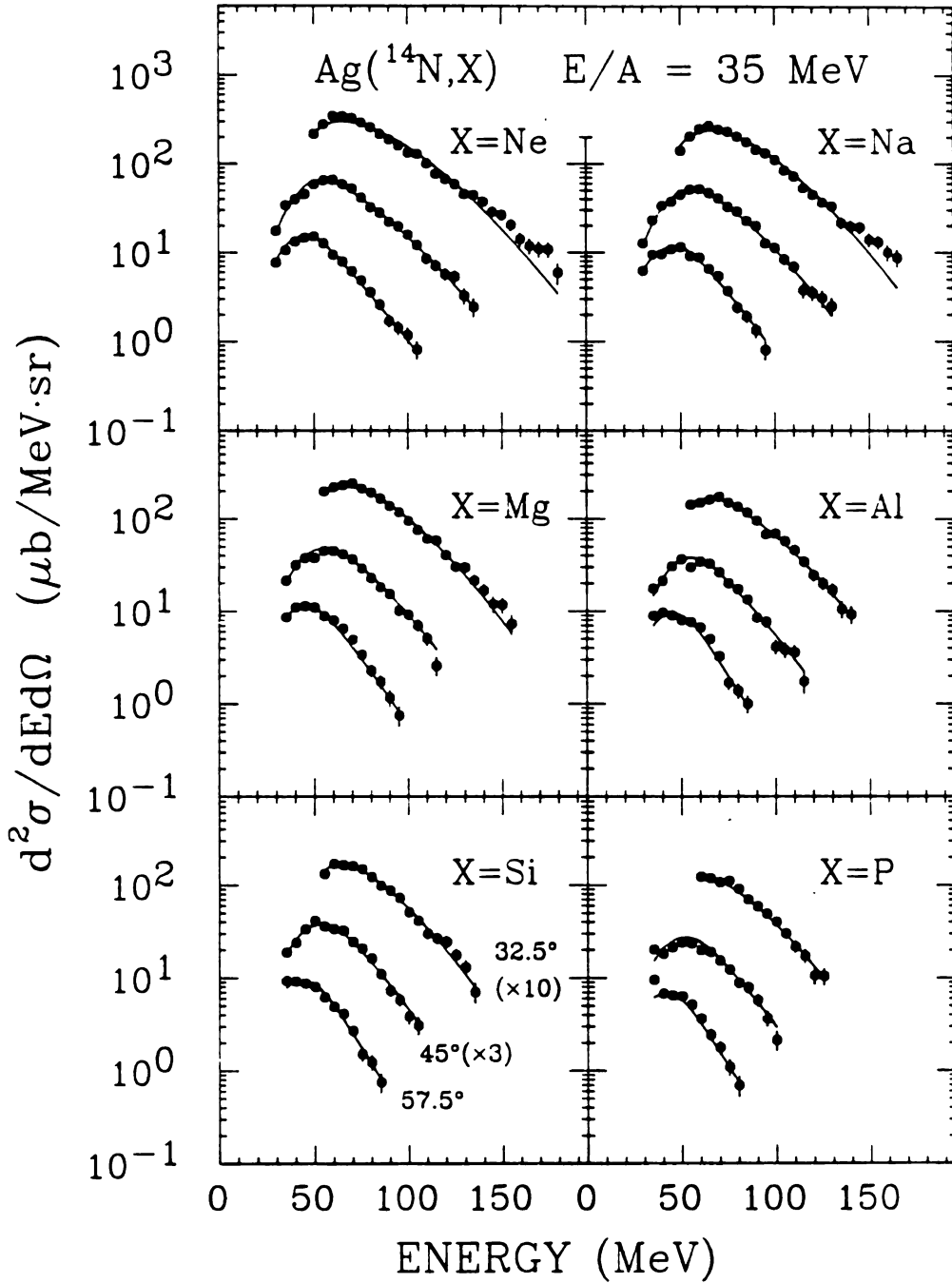


Figure III-4 : Differential cross sections,  $d^2\sigma/dEd\Omega$ , measured at  $\theta=32.5^\circ$ ,  $45^\circ$ , and  $57.5^\circ$ , for fragments,  $10 \leq Z \leq 15$ , from  $^{14}\text{N}$  induced reactions on Ag at  $E/A=35$  MeV. The solid curves are the result of the parameterization discussed in the text.

MSU-85-505

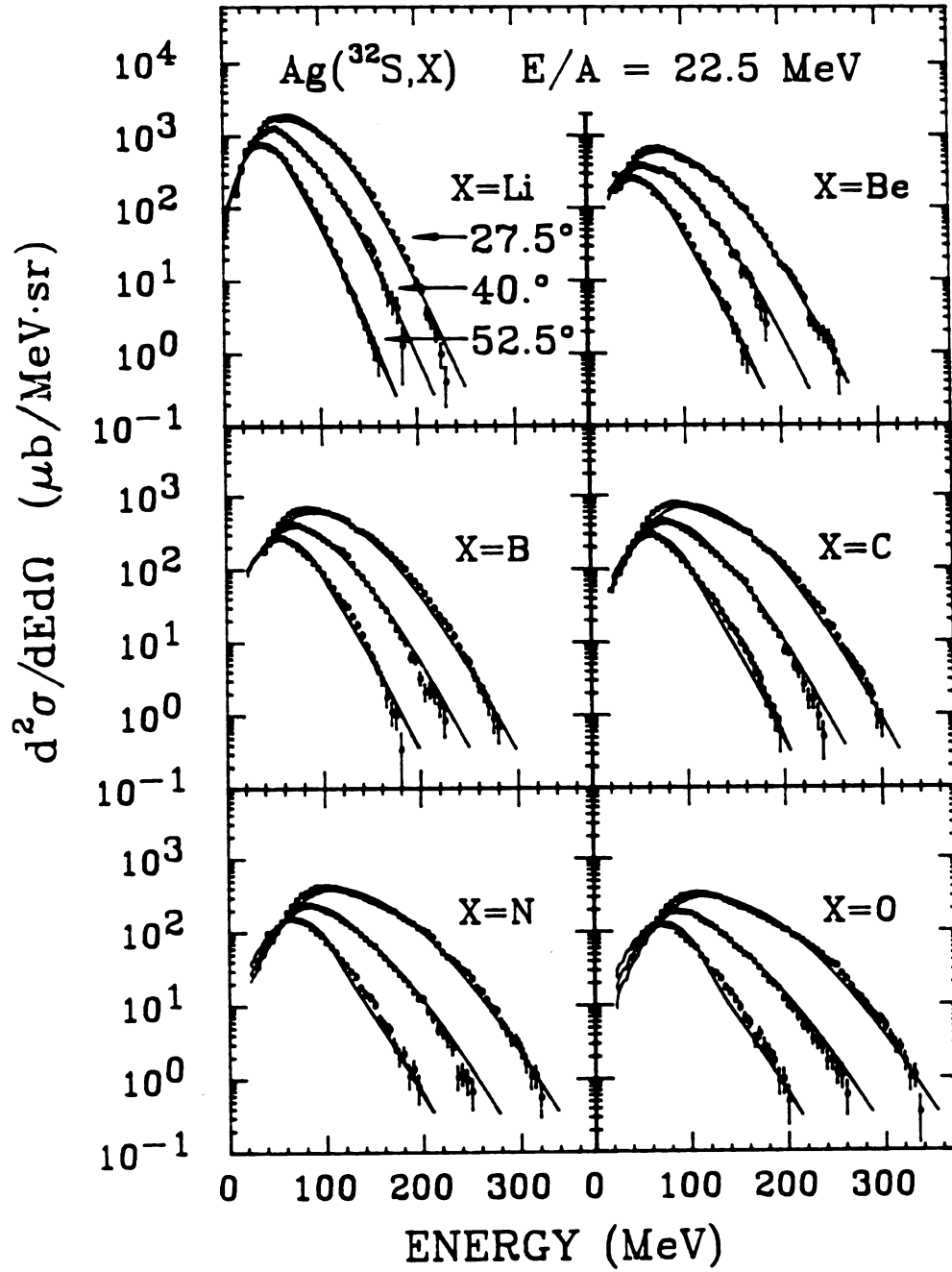


Figure III-5 : Differential cross sections,  $d^2\sigma/dEd\Omega$ , measured at  $\theta=27.5^\circ$ ,  $40^\circ$ , and  $52.5^\circ$ , for fragments,  $3 \leq Z \leq 8$ , from  $^{32}\text{S}$  induced reactions on Ag at  $E/A=22.5$  MeV. The solid curves are the result of the parameterization discussed in the text.



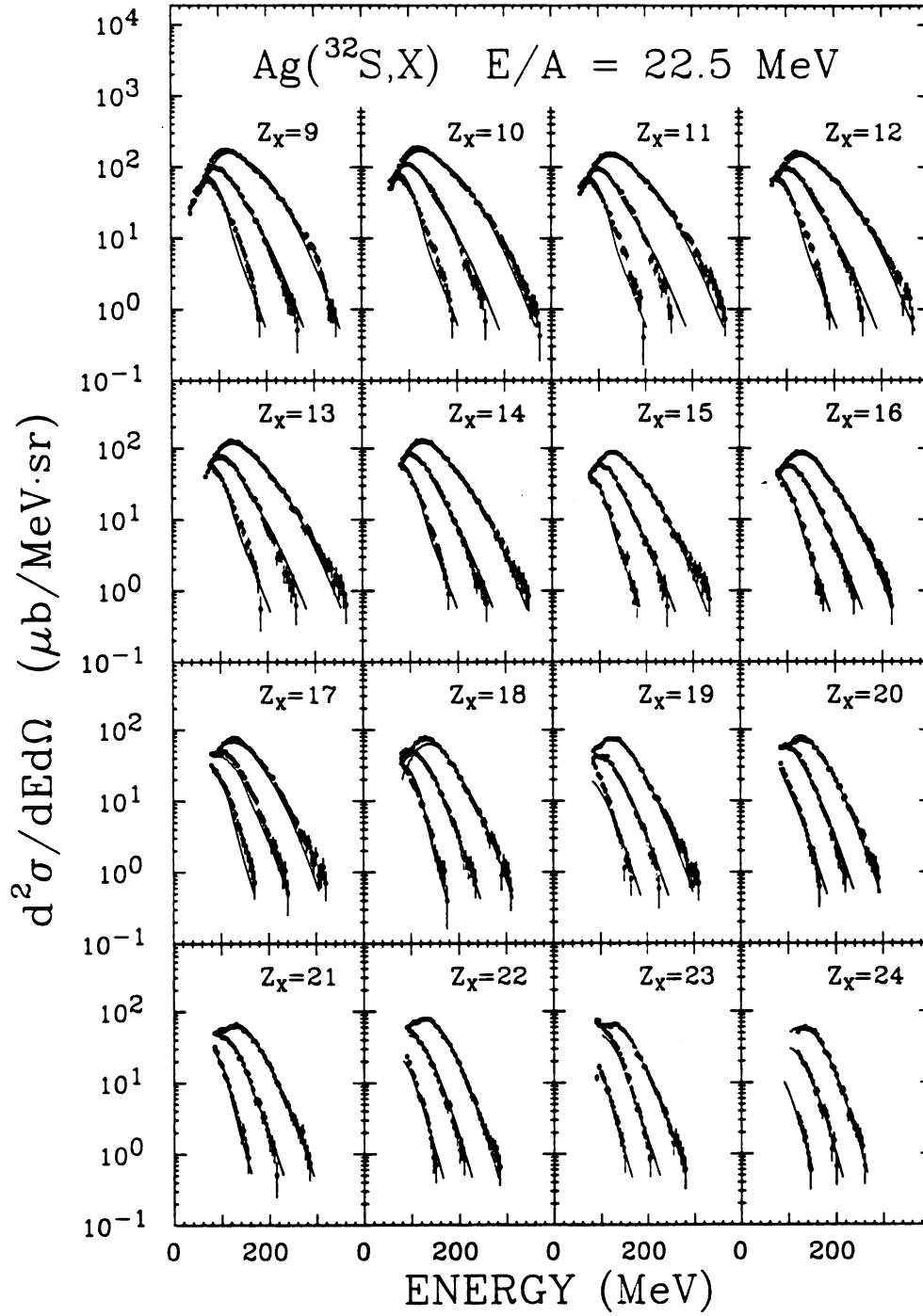


Figure III-6 : Differential cross sections,  $d^2\sigma/dEd\Omega$ , measured at  $\theta=27.5^\circ$ ,  $40^\circ$ , and  $52.5^\circ$ , for fragments,  $9 \leq Z \leq 24$ , from  $^{32}\text{S}$  induced reactions on Ag at  $E/A=22.5$  MeV. The solid curves are the result of the parameterization discussed in the text.

principally sensitive to the laboratory bombarding energy per nucleon of the reaction [WES82]. The spectra slope exponentially towards higher energies and show no particular structure.

### III.A.2. Intermediate mass fragment spectra :

The energy spectra of intermediate mass fragments display several of the characteristic features observed previously in intermediate energy heavy ion and high energy proton induced reactions [SOB83] [POS71] [HYD71] [WES78] [HIR84]. They exhibit broad maxima at energies slightly below the Coulomb energies for two touching charged spheres. At higher fragment energies the cross sections decrease exponentially with increasing energy. The slopes of the energy spectra become steeper with increasing fragment angle, changing the character of the energy spectra from Maxwellian to roughly Gaussian at very backward angles [SOB83]. The fragment spectra become increasingly Gaussian with increasing mass.

The angular distributions in the center-of-mass system,  $d\sigma/d\theta_{\text{cm}}$ , for intermediate mass fragments produced in  $^{12}\text{C}$  induced reactions on Au at  $E/A=30$  MeV are shown in Figure III-7. The cross sections are forward peaked for the case of light fragments but are approximately isotropic for the heaviest fragments.

The energy spectra of all fragments are generally smooth and structureless. In this respect, they are reminiscent of evaporation spectra of neutrons and light particles from low energy fusion reactions. These have been interpreted as the result of a fully statistical, phase-space dominated emission process [WEI37] [HAU52]. While other features of the cross sections, such as the angular

MSU-83-580

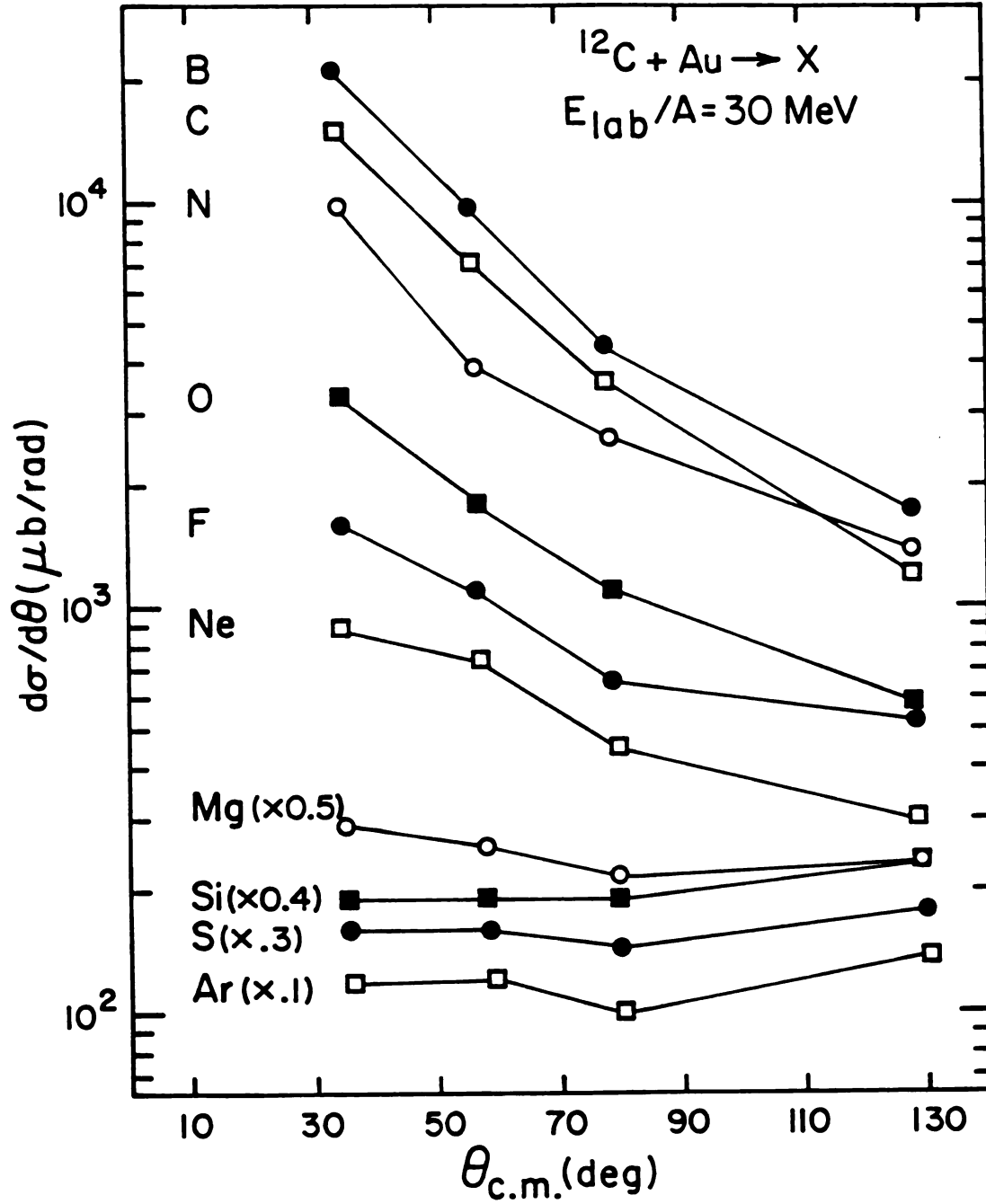


Figure III-7 : Differential cross sections,  $d\sigma/d\theta_{\text{cm}}$ , for various fragments,  $5 \leq Z \leq 18$ , from  $^{12}\text{C}$  induced reactions on Au at  $E/A=30 \text{ MeV}$ . The solid curves are drawn to guide the eye. Emission from fission would produce a flat curve.

distributions, rule out equilibrium emission from the compound nucleus as a possible production mechanism, statistical emission as a general mechanism still provides an attractive framework for understanding fragmentation.

### III.B. Two source parametrization of the cross sections :

#### **III.B.1. Moving source parametrizations :**

It was an early observation in high energy heavy ion reaction studies that particle spectra could be parametrized as isotropic thermal distributions corresponding to emission from one or more sources, moving in the laboratory with velocities different from the center-of-mass velocity [POS71]. Early work in relativistic collisions pictured three sources [WES76], clearly separated in momentum and coordinate space, corresponding to a target-like source, a projectile-like source, and an overlap, participant region with an intermediate velocity.

Parametrizations of this form are also applicable at lower energies and to heavier particles. Close examination of intermediate mass fragment differential cross sections reveals that they can be associated with either a component which is approximately isotropic in the rest frame of the composite system [SOB83] or a component which is isotropic in a frame moving with a velocity between those of the projectile and the center of mass. The forward peaked component is strongest for the lightest fragments but persists for fragments which are heavier than the projectile. This is also seen in  $^3\text{He}$  induced reactions [KWI86] where projectile fragmentation and transfer reactions would not be expected to

play a role in intermediate mass fragment production. At very forward angles, the cross sections (in  $^{40}\text{Ar} + \text{Ag}$  reactions at  $E/A=27$  MeV [BOR84], for example) contain a strong component which is approximately isotropic in the rest frame of the projectile. However, this component contributes only weakly at the intermediate angles which are the subject of discussion here. In general, the angular distributions cannot be explained by isotropic emission from the compound nucleus and/or an excited projectile remnant [BOR84].

### III.B.2. Description of present parametrization :

In order to organize the present set of data and to provide reasonable extrapolations to unmeasured scattering angles, the differential cross sections of intermediate mass fragments are fit with a two source parametrization which models emission from both a fusion-like and a non-equilibrium (intermediate rapidity) source, each of which emits isotropically with a Maxwellian energy distribution in its respective rest frame. A projectile velocity source is not included because the measurements were taken at relatively large angles, where contributions from such a source should be small. The emission of intermediate mass fragments is evidently more complicated, involving a continuum of "sources" from the quasi-elastic regime to the compound nucleus. However, the present single particle data do not justify a larger parameter space than the restricted two source space utilized here. Although the specific choice of parametrization is not unique, it may facilitate the formation of a qualitative picture of the relative time scales for particle emission and equilibration. Similar points of

view have been adopted elsewhere [TR085p], facilitating the comparison of different data sets.

This parametrization is formulated in a rest frame,  $O_{eq}$ , which moves with a velocity,  $v_{eq}$ , with respect to the laboratory frame;  $V_{eq}$  is chosen to be close to the average velocity of fusion-like residues. In this frame the cross sections are parametrized as :

$$\begin{aligned} \tilde{\sigma}'_x(\theta', E') = \frac{d^2 \tilde{\sigma}'_x}{dE' d\Omega} = \int \left[ N_{eq} \cdot (E' - V_c) \exp\left(-\frac{E' - V_c}{T_{eq} \cdot R}\right) \right. \\ \left. + N_f \sqrt{(E' - V_c) \cdot E_f} \exp\left(-\frac{E_f}{T_f}\right) \right] \\ \times (2\pi w_x^2)^{-1/2} \exp\left[-\frac{(V_c - RV_x)^2}{2 w_x^2}\right] dV_c, \quad (III-1) \end{aligned}$$

with

$$E_f = E' - V_c + E_d - 2 \cdot \sqrt{(E' - V_c) \cdot E_d} \cos \theta', \quad \text{and} \quad (III-2)$$

$$E_d = \frac{1}{2} M_x (v_f - v_{eq})^2. \quad (III-3)$$

Here, the factor  $R = (M_p + M_T - M_x) / (M_p + M_T)$  is due to momentum conservation, where  $M_p$ ,  $M_T$ , and  $M_x$  denote the masses of the projectile, target, and fragment, respectively;  $E'$  is the energy of the fragment in the frame,  $O_{eq}$ ;  $v_f$  is the velocity of the fast, non-equilibrium source with respect to the laboratory; and  $N_f$  and  $T_f$  ( $N_{eq}$  and  $T_{eq}$ ) are the normalization and "temperature" parameters which characterize the fast (slow) source. To avoid sharp cut-offs at low energies, Eq. III-1 contains a weighted average over a Gaussian distribution of Coulomb

barriers [POS71],  $V_c$ . The parameters,  $V_x$  and  $w_x$ , are the mean and the standard deviation of this distribution. Comparison to experimental data is made after transforming Eq. III-1 to the laboratory rest frame to yield the laboratory cross sections  $\tilde{\sigma}_x(\theta, E)$ . The values of  $v_{eq} = 0.79 \cdot v_0$ ,  $0.75 \cdot v_0$ , and  $0.86 \cdot v_0$  are used for  $^{12}\text{C}$ ,  $^{14}\text{N}$ , and  $^{32}\text{S}$  induced reactions, respectively, where  $v_0$  is the beam velocity. These values are consistent with the systematics for linear momentum transfer observed in measurements on fissile targets [FAT85].

We have assumed in the formulation of Eq. III-1 [GOL78] that particles are emitted from the surface of both the equilibrium and non-equilibrium sources. Temperature parameters obtained under this assumption are approximately 10% lower than those extracted from parametrizations of volume emission.

In order to reduce the number of variable parameters, the Coulomb widths of the distributions are set to fixed values. For the data from the  $^{32}\text{S}$  induced reactions on Ag, the values  $w_x = 2, 4, 11$  and  $17$  MeV for  $Z_x = 1, 2, 3$  and  $4 \leq Z_x \leq 24$ , respectively, are used. For the other fragments, the value is fixed at  $w_x = 8$  MeV. The temperature parameters of the fusion-like source were fixed at  $T_{eq} = 4.7$  MeV ( $^{12}\text{C} + \text{Au}$ ),  $6.9$  MeV

14	3	eq	f	f	f	x
----	---	----	---	---	---	---

free parameters.

### III.B.3. Results of parametrization :

The resulting fits are displayed as solid lines in the Figures III-1 - III-6,. The parametrization provides a reasonably good fit to all fragments. The fits are best for the heavier fragments ( $Z_x > 10$ ), where

the angular distributions are nearly isotropic in the rest frame  $O_{eq}$ , and for the products of the  $^{32}\text{S}$  induced reaction. There are some problems for the lighter fragments ( $Z_x < 10$ ) where fits fall more rapidly with energy than the data at forward angles, particularly at energies per nucleon close to that of the projectile. These discrepancies are likely due to contributions from peripheral processes. There is a slight inflection in the parametrized spectra at backward angles which is not duplicated in the data. Improved fits could be obtained by adding more "sources".

The fit parameters are given in Tables III-1 through III-3. The fits for all three reactions are similar in several ways. The fast source has a higher temperature than the estimated temperature for the equilibrated system. The velocity of the fast source is less than or equal to half the projectile velocity. The average velocity of the fast component decreases with fragment mass. The cross section of the fast component relative to the equilibrium component decreases with fragment mass. However, this trend is clouded by the gradual loss of distinction between the contributions from the fast and slow sources for heavier fragments.

The parameters indicate a sensitivity of the cross sections to projectile mass. For  $^{32}\text{S}$  induced reactions,  $T_f$  is relatively constant, while the values drop steadily with fragment charge for reactions with the lighter projectiles. In other studies [TRA86pc] [TRO86p], the temperatures observed for fragments produced in  $^{12}\text{C}$  ( $E/A=48$  MeV) and  $^{18}\text{O}$  ( $E/A=84$  MeV) induced reactions on Au were observed to decrease with fragment mass, while those of  $^{40}\text{Ar}$  ( $E/A=30$  MeV) induced reactions on Au are constant or slowly increasing with fragment mass [TRO86p]. The



Table III-1 : The best fit parameters from the parametrization discussed in the text for fragments produced in  $^{12}\text{C}$  induced reactions on Au at  $E/A=30$  MeV. The estimated cross sections for the fast and slow sources are also given.

X	$T_f(\text{MeV})$	$v_f/v_0$	$N_f$	$N_{eq}$	$V_x/V_s$	$\sigma_f(\text{mb})$	$\sigma_{eq}(\text{mb})$
Be	8.14	.33	18.4	10.3	.77	15.3	2.49
B	10.7	.35	8.1	9.2	.71	11.7	2.17
C	9.45	.28	6.38	9.57	.70	7.17	2.22
N	8.49	.25	2.67	4.66	.75	2.41	1.06
O	7.51	.21	1.78	3.34	.72	1.26	0.74
F	7.46	.20	1.05	2.34	.73	0.74	0.51
Ne	7.48	.17	0.91	2.37	.71	0.64	0.50

Table III-2 : The best fit parameters from the parametrization discussed in the text for fragments produced in  $^{14}\text{N}$  induced reactions on Ag at  $E/A=35$  MeV. The estimated cross sections for the fast and slow sources are also given.

X	$T_f(\text{MeV})$	$v_f/v_0$	$N_f$	$N_{eq}$	$V_x/V_s$	$\sigma_f(\text{mb})$	$\sigma_{eq}(\text{mb})$
Be	12.5	.48	24.1	63.7	.60	47.1	32.6
B	14.0	.42	13.7	68.7	.61	33.75	33.9
C	13.1	.37	10.7	67.2	.55	23.0	31.9
N	10.9	.29	8.5	21.1	.48	12.76	9.64
O	9.9	.26	6.81	14.1	.45	8.42	6.17
F	9.66	.235	4.08	5.11	.40	4.78	2.15
Ne	9.15	.22	4.17	5.54	.39	4.38	2.23
Na	8.67	.20	3.77	3.27	.36	3.56	1.26
Mg	8.38	.19	3.64	3.37	.34	3.20	1.24
Al	7.96	.19	2.29	4.52	.34	1.82	1.60
Si	7.71	.17	2.57	4.04	.30	1.91	1.37
P	7.78	.17	1.77	3.15	.27	1.35	1.02

Table III-3 : The best fit parameters from the parametrization discussed in the text for fragments produced in  $^{32}\text{S}$  induced reactions on Ag at  $E/A=22.5$  MeV. The estimated cross sections for the fast and slow sources are also given.

X	$T_f(\text{MeV})$	$v_f/v_0$	$N_f$	$N_{eq}$	$V_x/V_s$	$\sigma_f(\text{mb})$	$\sigma_{eq}(\text{mb})$
p	6.09	.53	6613.	600.	.40	3062.	367.
d	7.08	.52	1653.	320.	.40	1032.	193.
t	8.38	.50	515.	100.	.40	451.	59.
$\alpha$	7.99	.50	3318.	790.	.40	2630.	459.
Li	8.36	.55	278.	280.	.73	240.	152.
Be	8.96	.54	81.7	156.	.71	79.2	74.3
B	9.62	.50	74.1	172.	.78	84.4	84.5
C	9.30	.50	98.7	194.	.80	106.	96.9
N	10.2	.49	48.2	118.	.76	63.1	57.5
O	10.6	.49	34.4	110.	.75	48.2	52.1
F	11.2	.49	16.9	65.6	.75	26.3	30.1
Ne	11.2	.48	17.4	80.0	.69	27.5	35.3
Na	11.7	.46	13.2	70.2	.69	22.7	36.5
Mg	11.8	.43	12.5	73.8	.68	21.6	30.2
Al	12.2	.40	8.94	60.4	.62	16.7	23.7
Si	11.7	.38	9.34	64.2	.61	15.9	24.2
P	11.4	.36	7.04	43.7	.55	11.5	15.8
S	11.3	.34	6.69	45.2	.55	10.8	15.7
Cl	10.0	.34	7.49	40.0	.45	9.29	12.6
Ar	10.7	.32	6.47	38.5	.50	9.30	12.1
K	11.2	.31	5.37	40.5	.47	8.40	11.9
Ca	10.4	.29	7.60	39.7	.45	10.0	10.7
Sc	9.72	.30	5.94	46.0	.47	6.96	12.3
Ti	9.18	.27	14.0	20.0	.36	14.0	4.57
V	9.89	.26	6.24	45.9	.42	7.43	10.4
Cr	8.59	.26	13.6	5.0	.32	11.6	1.0

decrease of the spectral temperatures with increasing fragment charge observed with light projectiles have been attributed to the effects of momentum conservation [TRA86pc].

The intermediate mass fragment spectra peak at energies below the Coulomb energy for charged touching spheres, and they are quite broad. A number of different mechanisms have been proposed to explain the maxima of the fragment energy spectra in intermediate energy collisions. Reduced Coulomb barriers could be caused by emission from extended, deformed sources [ALE82]. This mechanism was suggested for fragment emission in more energetic systems [POS71] [MEY80]. On the other hand, low Coulomb barriers can also result if the emitting system has lost a significant charge through the emission of light particles [FRI83a]. If fragments are emitted in the complete fragmentation of the target-like system, then the Coulomb energy of a fragment will reflect its original position in the emitting system; the Coulomb energies for fragments emitted from the interior of the nucleus will be reduced [AIC84a] [HIR84]. An additional possibility is that the fragment spectra are influenced by sequential decay [BER84] (see also Sections VI.A.2. and VIII.C.).

#### **III.B.4. Limits of the parametrization :**

It is important to reiterate that this parametrization is not a model for fragment emission. In particular, one should not conclude that two or three well defined and physically identifiable sources moving in the beam direction are responsible for the fragment cross sections. The experimental single particle inclusive distributions,

averaged as they are over impact parameter and time, are of sufficient simplicity that they can be approximated by the superposition of a small number of Maxwellian distributions. The sources need not be spatially isolated and non-interacting nuclear entities. In addition, large azimuthal anisotropies have been experimentally observed, as is discussed in Chapter IV. Such effects have not been incorporated in this parametrization.

The parametrizations are also limited by the data. Because the light particle measurements were made with relatively high low energy thresholds, the equilibrated emission component is only poorly determined. The limited angular range over which the fragment distributions were measured makes these data less valuable as a test of the assumed emission kinematics.

### III.C. Integrated cross sections :

#### **III.C.1. Elementally resolved yields :**

In this section the elemental and isotopic cross sections for fragment production are discussed. The cross sections in Figures III-8 and III-9 correspond to the weighted average differential cross sections,

$$\langle d\sigma_x/d\Omega \rangle = \frac{\sum_i (d\sigma_x/d\Omega_i) \cdot \sin \theta_i}{\sum_i \sin \theta_i}, \quad (\text{III-4})$$

for fragments from  $^{12}\text{C}$  induced reactions on Au and Ag, respectively at

MSU-86-407

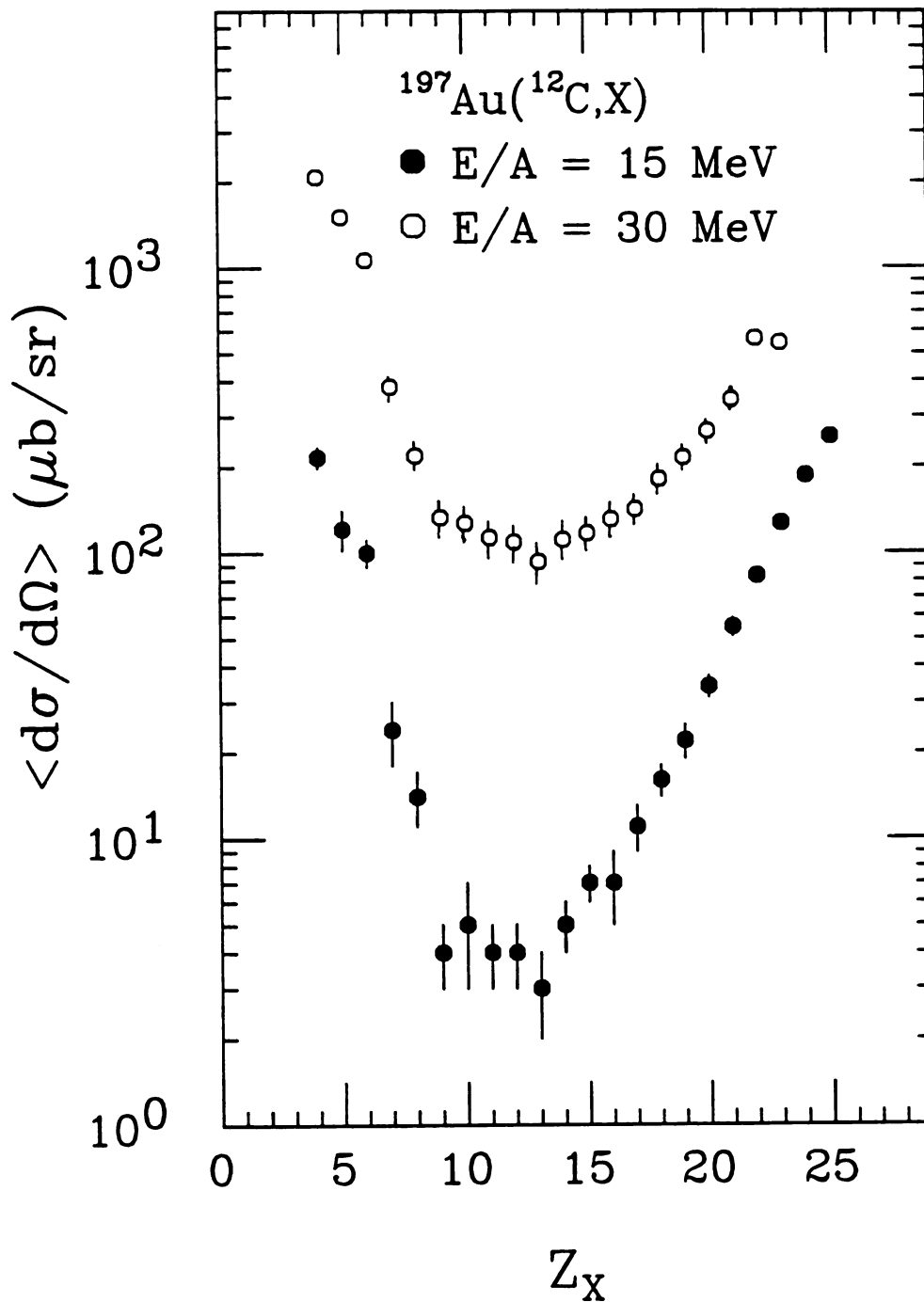


Figure III-8 : Average differential cross sections,  $\langle d\sigma/d\Omega \rangle$ , over the region  $50^\circ \leq \theta \leq 120^\circ$  for fragments of charge,  $Z$ , from  $^{12}\text{C}$  induced reactions on Au at  $E/A=15$  and 30 MeV (solid and open points, respectively).

MSU-86-408

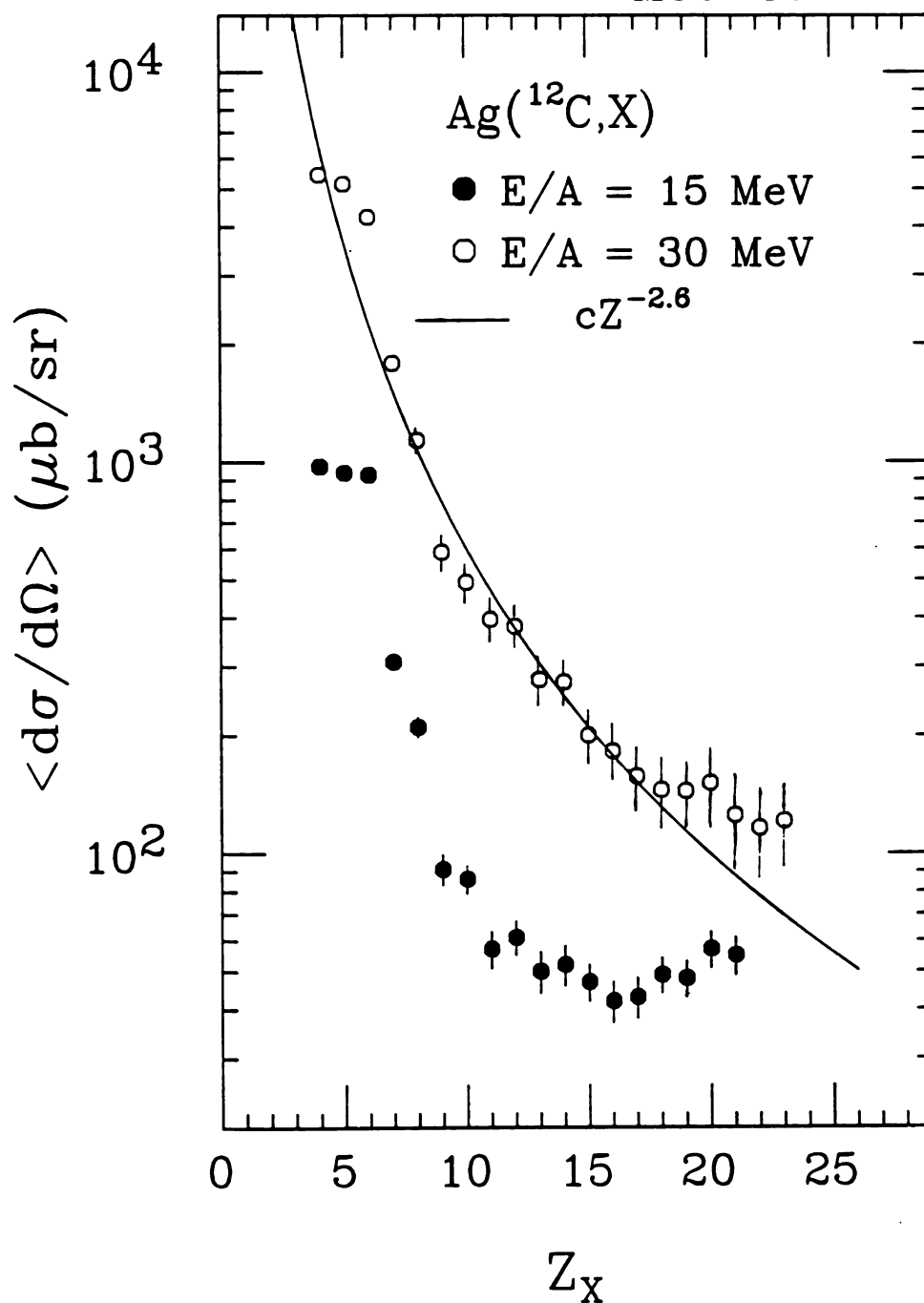


Figure III-9 : Average differential cross sections,  $\langle d\sigma/d\Omega \rangle$ , for fragments of charge,  $Z$ , from  $^{12}\text{C}$  induced reactions on Ag at  $E/A=15$  ( $50^\circ \leq \theta \leq 70^\circ$ , solid points) and 30 MeV ( $40^\circ \leq \theta \leq 70^\circ$ , open points). The solid curve depicts a strict power law dependence,  $Y \propto Z^{-2.6}$ .

$E/A = 15$  and  $30$  MeV. The cross sections exhibit a strong energy dependence, with the fragment cross sections in the  $^{12}\text{C} + \text{Au}$  reaction increasing by a factor of 10 over the energy range from 180 MeV to 360 MeV. For both targets, the cross sections decrease rapidly with increasing fragment charge up to  $Z=10$ . The cross sections for the  $^{12}\text{C} + \text{Au}$  reaction begin to increase for  $Z_x \geq 14$ . This increase is most likely due to the tails of the fission distribution, which becomes broader with increasing excitation energy and angular momentum [TSA83].

Total elemental cross sections and average differential cross sections for intermediate mass fragments from  $^{12}\text{C} + \text{Au}$ ,  $^{14}\text{N} + \text{Ag}$ , and  $^{32}\text{S} + \text{Ag}$  reactions are shown in Figures III-10, 11, and 12, respectively. The total cross sections,  $\sigma_x$ , are extrapolations from the parametrizations discussed previously and are shown as open points. Because of the limited range of angles fit by this parametrization, the estimates do not include possible contributions from projectile-like sources. For comparison, the angular average of the experimental cross sections,  $\langle d\sigma_x/d\Omega \rangle$ , as defined in Eq. III-4, is also shown in these figures as solid points and open squares. ( In Figure III-10, the averages  $\langle d\sigma/d\Omega \rangle_1$  and  $\langle d\sigma/d\Omega \rangle_2$  correspond to the average over all measured angles and over the three most backward angles, respectively.)

The elemental yield curves decrease smoothly with fragment charge. In contrast to elemental distributions measured at lower energies, where deeply inelastic processes dominate, the yields do not display an enhancement in the region of the projectile [MOR75]. The elemental yields can be approximated by a power law,  $\sigma_x \propto Z^{-\tau}$ , as have the mass distributions in high energy proton-induced fragmentation reactions [FIN82] [HIR84]. Such a power law dependence, with an exponent of



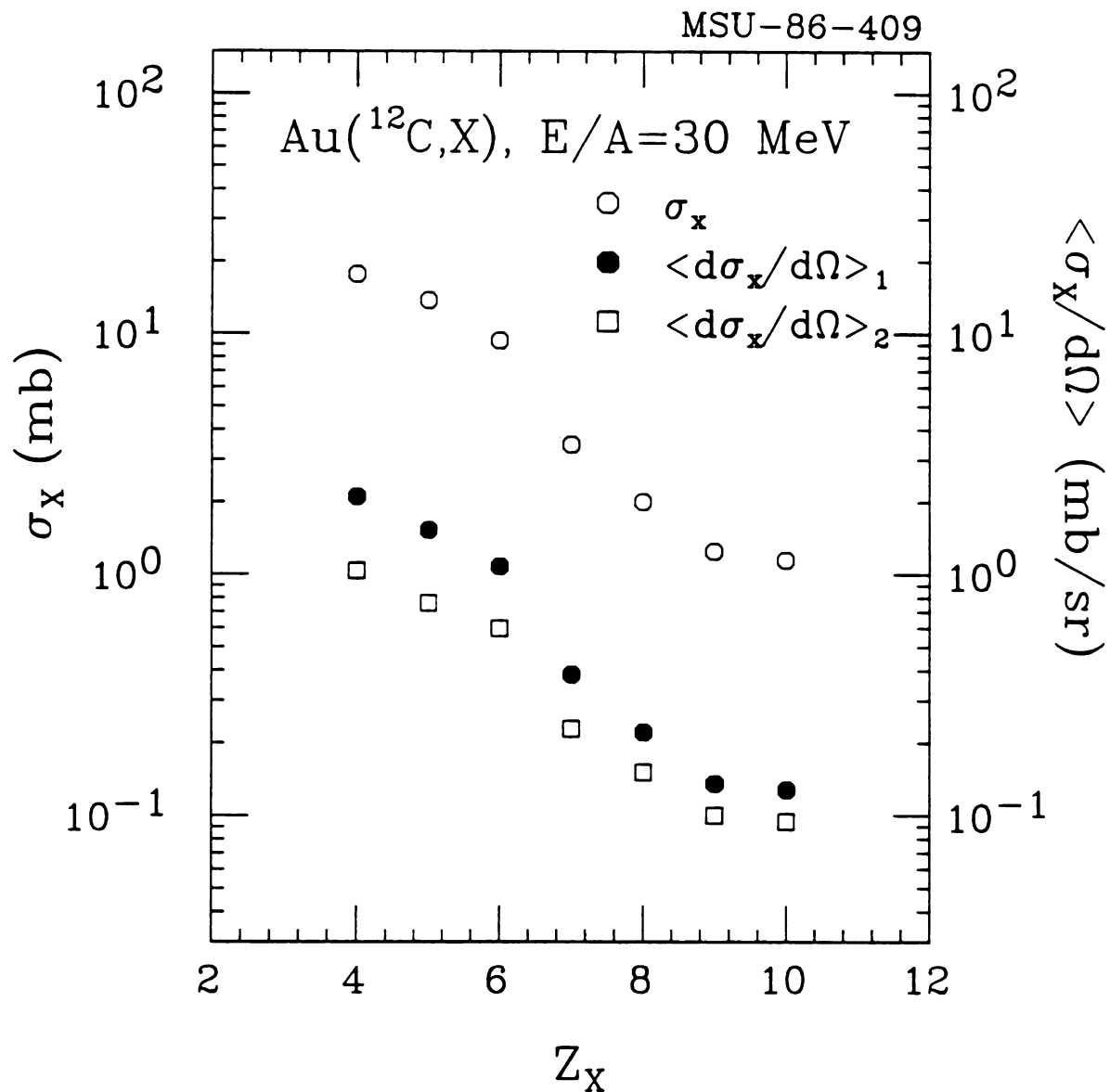


Figure III-10: The extrapolated total cross sections,  $\sigma_x$ , for fragments produced in  $^{12}\text{C}$  induced reactions on Au at  $E/A=30 \text{ MeV}$  are shown as open circles. The solid circles and open squares show the average differential cross sections,  $\langle d\sigma_x/d\Omega \rangle$ , measured over the angular ranges  $30^\circ \leq \theta \leq 120^\circ$  and  $50^\circ \leq \theta \leq 120^\circ$ , respectively.

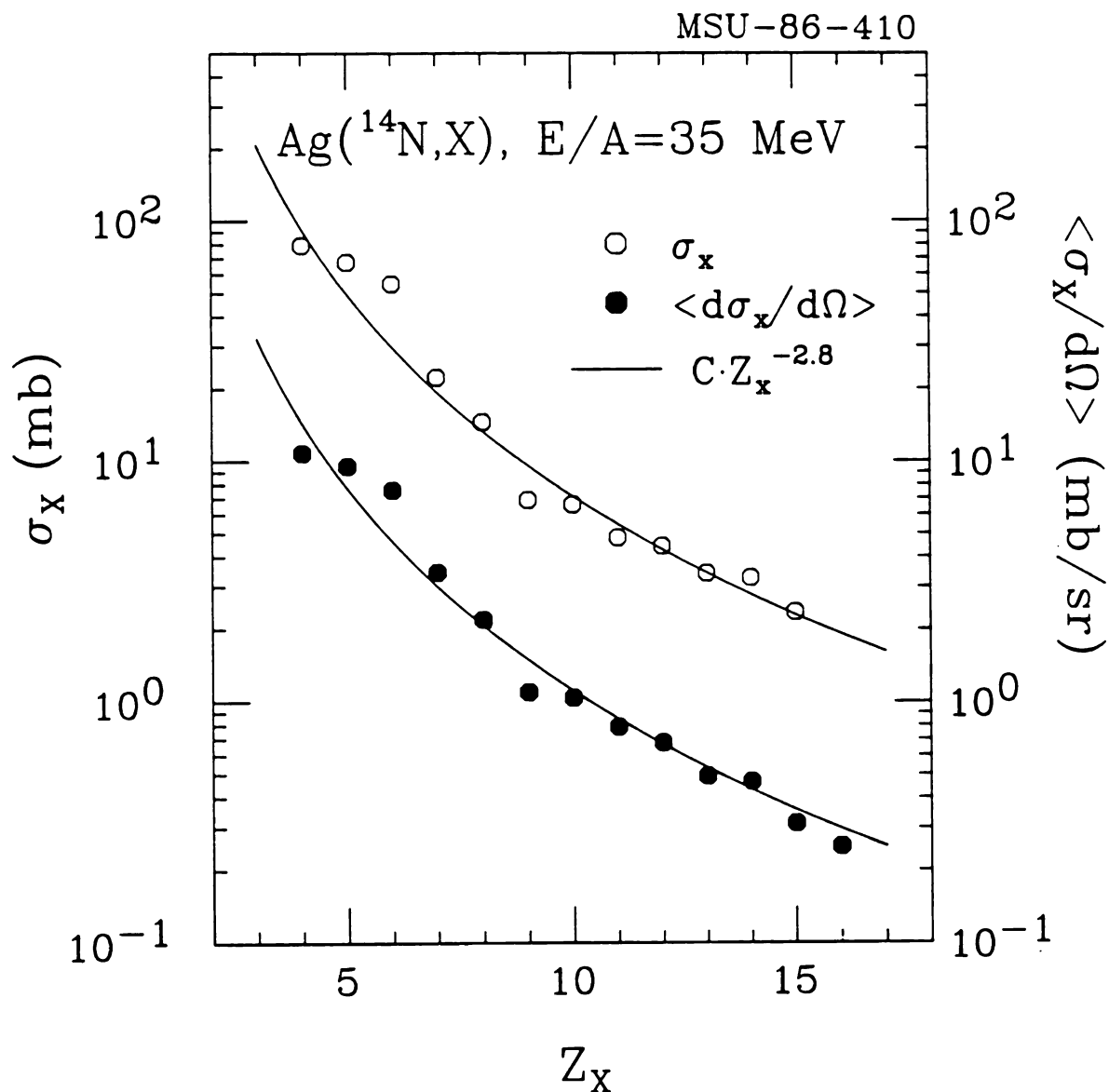


Figure III-11: The extrapolated total cross sections,  $\sigma_X$ , for fragments produced in  $^{14}\text{N}$  induced reactions on Ag at  $E/A=35 \text{ MeV}$  are shown as open circles. The solid circles show the average differential cross sections,  $\langle d\sigma_X/d\Omega \rangle$ , measured over the angular range  $32.5^\circ \leq \theta \leq 57.5^\circ$ . The solid curves depict a power law dependence  $Y \propto Z^{-2.8}$ .

MSU-85-508

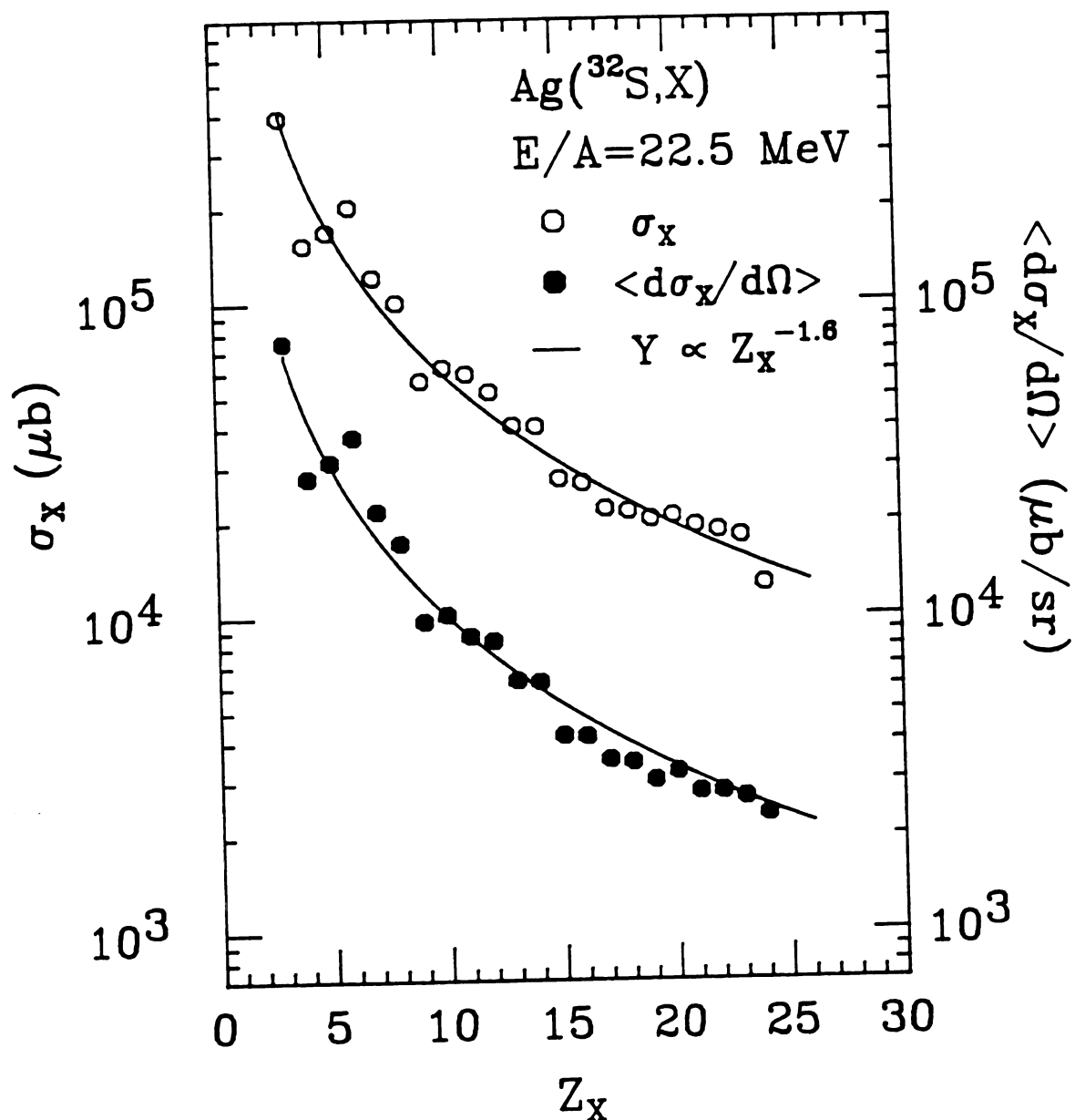


Figure III-12: The extrapolated total cross sections,  $\sigma_X$ , for fragments produced in  $^{32}\text{S}$  induced reactions on Ag at  $E/A=22.5 \text{ MeV}$  are shown as open circles. The solid circles show the average differential cross sections,  $\langle d\sigma_X/d\Omega \rangle$ , measured over the angular range  $27.5^\circ \leq \theta \leq 52.5^\circ$ . The solid curves depict a power law dependence  $Y \propto Z^{-1.6}$ .

$r=2.6$ , was interpreted as a signature of cluster formation near the critical point in the liquid-gas phase diagram of nuclear matter. If this were true then all measured fragment distributions should be steeper, i.e.  $r>2.6$ . A similar dependence ( $r=2.6$ ) was observed in the fragment cross sections resulting from  $^{12}\text{C} + \text{Ag}$  collisions at  $E/A=30$  MeV as shown in Figure III-9. However, a very different value,  $r\approx 1.6$ , describes the data from  $^{32}\text{S}$  induced reactions. A similar value ( $r\approx 1.7$ ) was observed for  $^{40}\text{Ar}$  induced reactions on Au at  $E/A=29.7$  MeV [TR086p]. The liquid-gas models do not explain this variation.

The general shape of the elemental yield curves, as well as their energy dependence, can also be understood in the framework of a statistical evaporation calculation [FRI83a]. In that model, the calculated yield curve results from a dependence on the binding energies and Coulomb barriers of the emitted fragments. Nonetheless, the dependence of the fragment cross sections on projectile mass suggests that parameters other than binding energy and Coulomb barriers, e.g. angular momentum and shape degrees of freedom, affect the fragment distributions. These dependences have, however, not yet been established quantitatively.

### III.C.2. Isotopically resolved yields :

The relative isotopic yields for intermediate mass fragments,  $3\leq Z_x\leq 8$ , emitted in the  $^{32}\text{S} + \text{Ag}$  reaction at  $E/A=22.5$  MeV, are shown as solid points in Figure III-13. These were obtained fitting the double-gated energy spectra (in the gamma ray-particle coincidence experiment described in Section II.D.) with the parameterization discussed in

MSU-86-411

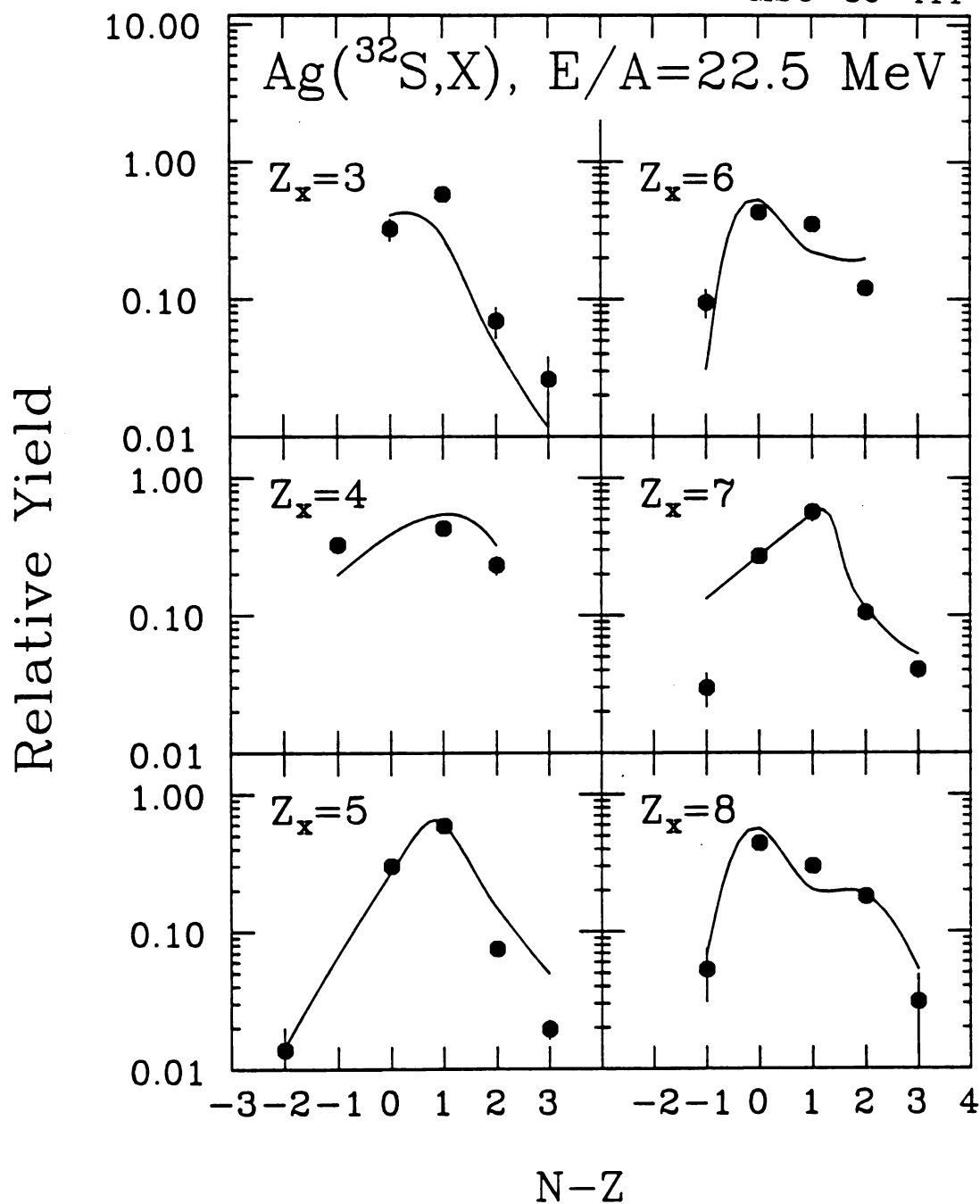


Figure III-13: Relative isotopic yields for isotopes of elements,  $3 \leq Z_x \leq 8$ , are shown as solid points. The solid curves represent the predictions of a simple statistical model discussed in the text.

Section III.B.2. All parameters except the normalizations were fixed at the values which characterize the elemental distributions (see Table III-3). The ratios of the two normalization constants,  $N_f$  and  $N_{eq}$ , were also constrained to be the same as in the elemental distributions. Thus, there is a single normalization parameter which results from this procedure. The error bars depict estimated systematic uncertainties. Additional uncertainties, of less than 20%, may also result from inefficiencies in the particle identification process. The  ${}^7\text{Li}$  yield may be over-estimated by 5-25% because of the inclusion of  ${}^8\text{Be}$  fragments in the spectra.

The solid lines are relative yields estimated with a simple statistical calculation. For each element, the relative isotopic yields,  $Y(X)$ , were assumed to be simply a function of the binding energy of the daughter system of the reaction  $A \rightarrow B + X$  [ART77]:

$$Y(X) \propto \exp( B_{sep} / T ). \quad (\text{III-5})$$

where  $B_{sep} = B_x + B_B$  are the binding energies of the fragments. The parent,  $A$ , was assumed to be  ${}^{107}\text{Ag}$ ; the binding energy for the daughter,  $B_B$ , was calculated with a liquid-drop formula; the emission temperature is  $T \approx 3.8$  MeV. The relative normalization for each element is chosen for appearance.

This simple estimation supports the assumption of statistical emission, which in turn may provide a tractable framework for understanding fragment emission.

## Chapter IV

### Light Particle-Intermediate Mass Fragment Correlations

The single particle inclusive cross sections discussed in Chapter III do not discriminate between different possible classes of reactions. More information is contained in two particle coincidence data. In this chapter, the spectra and angular distributions of non-equilibrium light particles coincident with intermediate mass fragments emitted in  $^{32}\text{S}$  induced reactions on Ag at the incident energy of  $E/A=22.5$  MeV [FIE86] will be explored. The distributions of coincident light particles provide information on the dynamical aspects of the heavy ion collisions which produce intermediate mass fragments. This type of study has been applied to relativistic nuclear collisions [MEY80] [WAR83].

#### IV.A. Spectra of light particles coincident with intermediate mass fragments :

The single particle inclusive spectra of light particles, discussed in Chapter III, exhibited rather structureless exponential slopes. It is

conceivable that such structureless spectra result from the superposition of several different mechanisms, each contributing differently to the inclusive distributions. Reactions in which intermediate mass fragments are emitted might constitute such a distinct class of reactions for which the light particle spectra differ significantly from the single particle inclusive distributions; coincidence studies may reveal such differences.

Energy spectra of non-equilibrium light particles detected in coincidence with intermediate mass fragments are compared to single particle inclusive cross sections in Figure IV-1. The single particle inclusive spectra are indicated by the solid curves. The spectra were measured at  $\theta_y = 40^\circ$  (circles) and  $70^\circ$  (diamonds) at relative azimuthal angles from the intermediate mass fragment, detected at  $\theta_x = 27.5^\circ$ , of  $\Delta\phi = 180^\circ$  (solid points) and  $\Delta\phi = 90^\circ$  (open points). The proton spectra are shown in the upper part of the figure, with the spectra coincident with Li and C on the left and right hand sides of the figure, respectively. The singles and coincidence spectra are remarkably similar. The coincidence spectra fall exponentially with increasing energy, becoming steeper at larger angles, and thus retain the essentially random, statistical character of the inclusive spectra. The slopes of the spectra are nearly unchanged by the imposition of the coincidence requirement.

The corresponding inclusive and coincidence spectra of alpha particles are displayed in the lower part of the figure. The coincidence spectra measured at  $\Delta\phi = 180^\circ$  are virtually identical to the inclusive spectra, as was true for the protons. At  $\Delta\phi = 90^\circ$ , however, the spectra possess slightly different slopes, and the coincidence cross section is



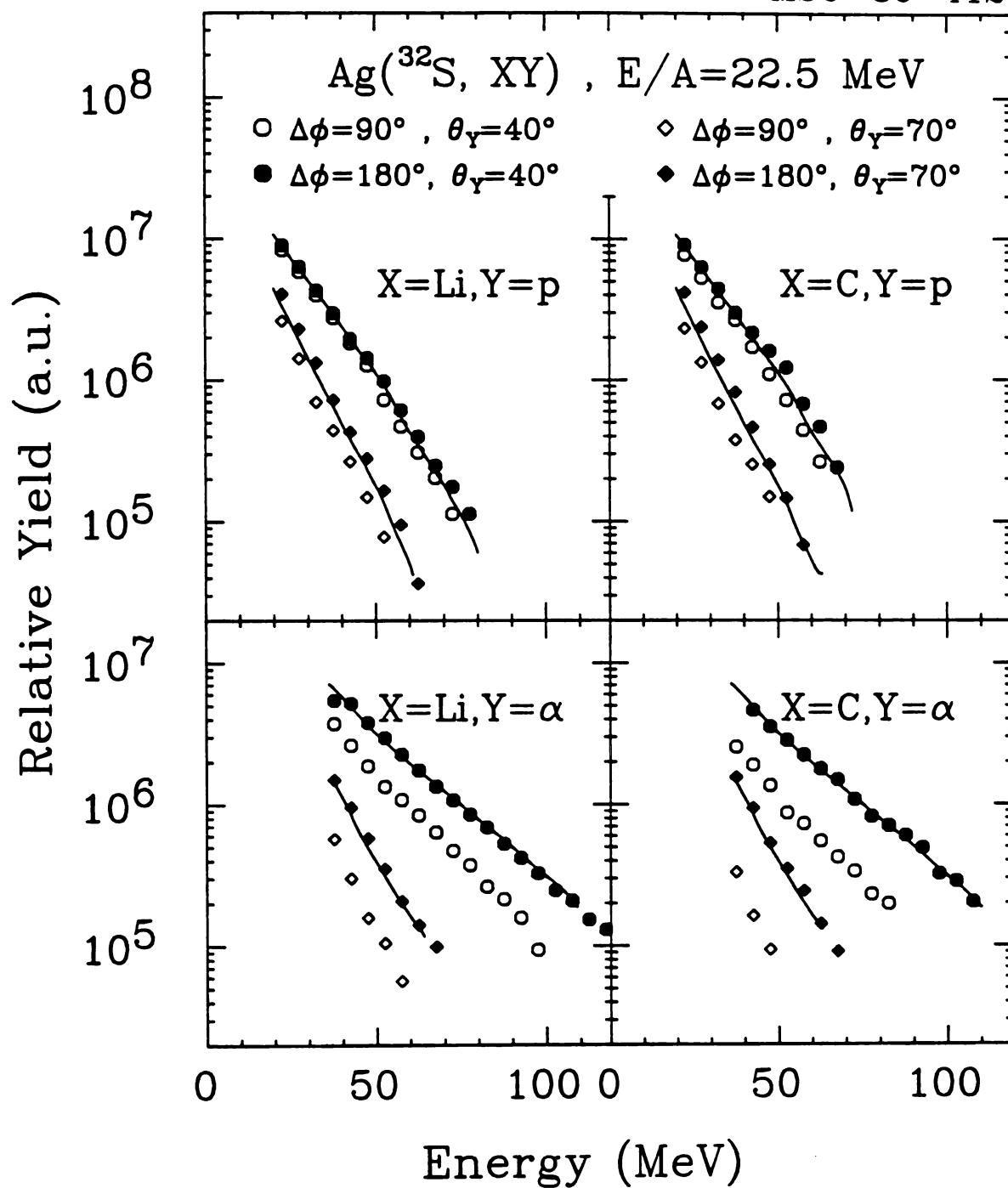


Figure IV-1 : Energy spectra of protons (top of figure) and alpha particles (bottom of figure) in coincidence with Li fragments (left side of figure) and C fragments (right side of figure). The circles and diamonds correspond to the light particles being detected at  $\theta=40^\circ$  and  $70^\circ$ , respectively. The solid and open points correspond to relative azimuthal angles between the light particle and intermediate mass fragment of  $\Delta\phi=180^\circ$  and  $90^\circ$ , respectively. The inclusive spectra are shown as solid curves.

suppressed.

The ratio of the coincidence and singles spectra can be used to display small differences between them. This ratio is defined as

$$R(E_y, \theta_y, \theta_x, \Delta\phi) = \frac{\int dE_x \sigma_{yx}(E_y, E_x, \theta_y, \theta_x, \Delta\phi)}{\sigma_y(E_y, \theta_y)} \quad (\text{IV-1})$$

where, for brevity,

$$\sigma_{yx} = \frac{d^4 \sigma_{yx}}{dE_y d\Omega_y dE_x d\Omega_x} \quad \text{and} \quad \sigma_y = \frac{d^2 \sigma_y}{dE_y d\Omega_y} \quad (\text{IV-2})$$

The ratio is calculated separately for each detector, and is less sensitive to errors in calibration than the spectra themselves. The spectrum ratios for protons are shown in Figures IV-2. Ratios for lithium and carbon coincidences are shown in the upper and lower parts of the figure. The spectrum ratios measured at  $\theta_p = 40^\circ$  (left side) and  $70^\circ$  (right side) are shown as solid and open points to indicate the relative azimuthal angles of the coincident particles,  $\Delta\phi = 180^\circ$  and  $90^\circ$ , respectively. The ratio,  $R(E_y)$ , for protons is relatively independent of energy for all angles, demonstrating the insensitivity of the proton spectra to coincidence requirements. The proton cross section is mildly suppressed in non-coplanar geometries.

The corresponding spectrum ratios for alpha particles are shown in Figure IV-3. For this heavier particle,  $R(E_y)$  measured at  $\Delta\phi = 180^\circ$  is also independent of energy. However, at  $\Delta\phi = 90^\circ$   $R(E_y)$  decreases with increasing energy, confirming that the slopes of the coincidence spectra

MSU-86-413

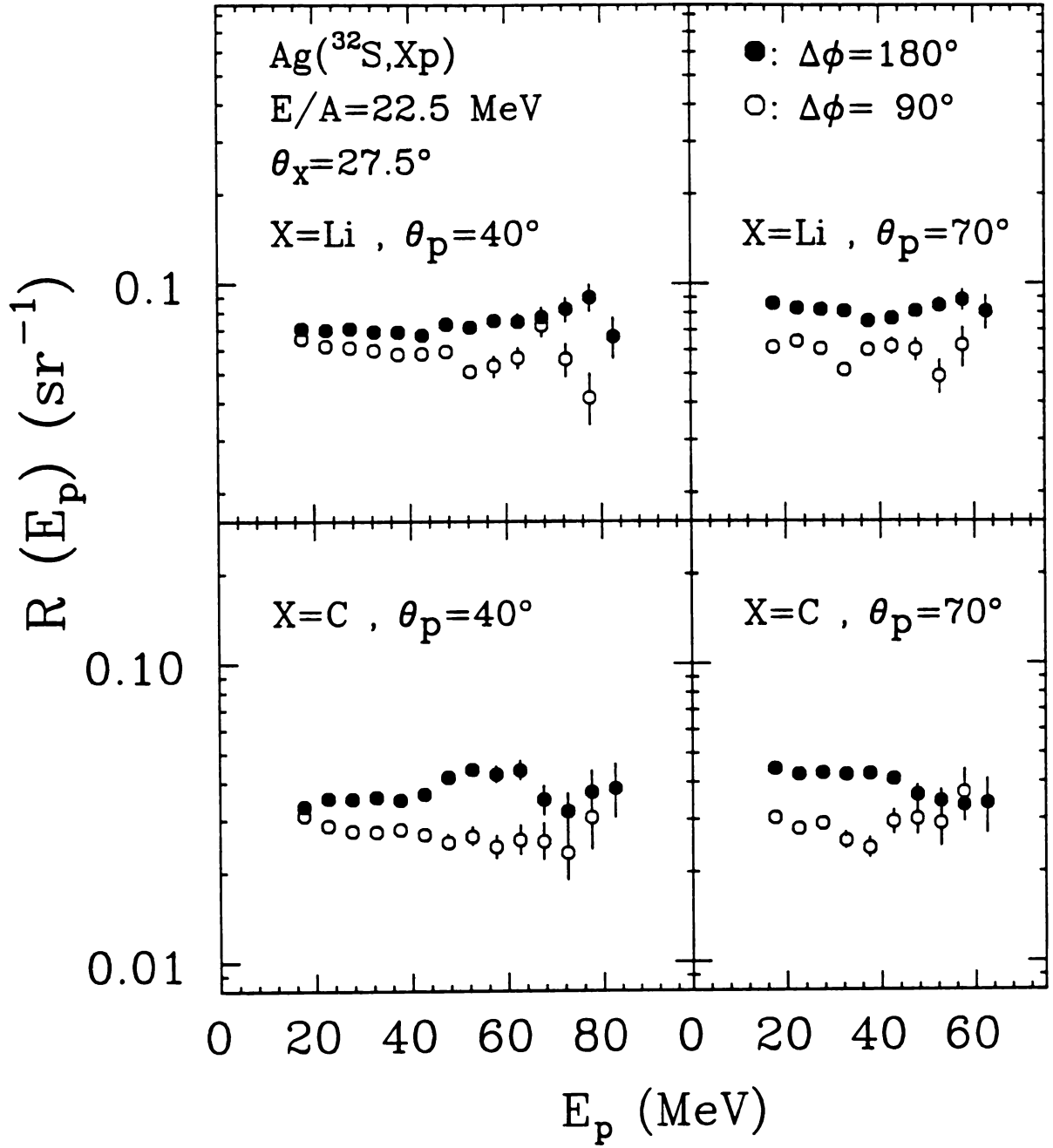


Figure IV-2 : The ratio of the differential coincidence cross sections to the single particle inclusive cross sections for protons as a function of proton energy. The ratio is shown for protons detected at  $\theta_p = 40^\circ$  (left hand side) and  $\theta_p = 70^\circ$  (right hand side) in coincidence with Li nuclei (top of figure) and C nuclei (bottom of figure) detected at  $\theta_x = 27.5^\circ$  and at relative azimuthal angles of  $\Delta\phi = 180^\circ$  (solid points) and  $\Delta\phi = 90^\circ$  (open points).

MSU-86-414

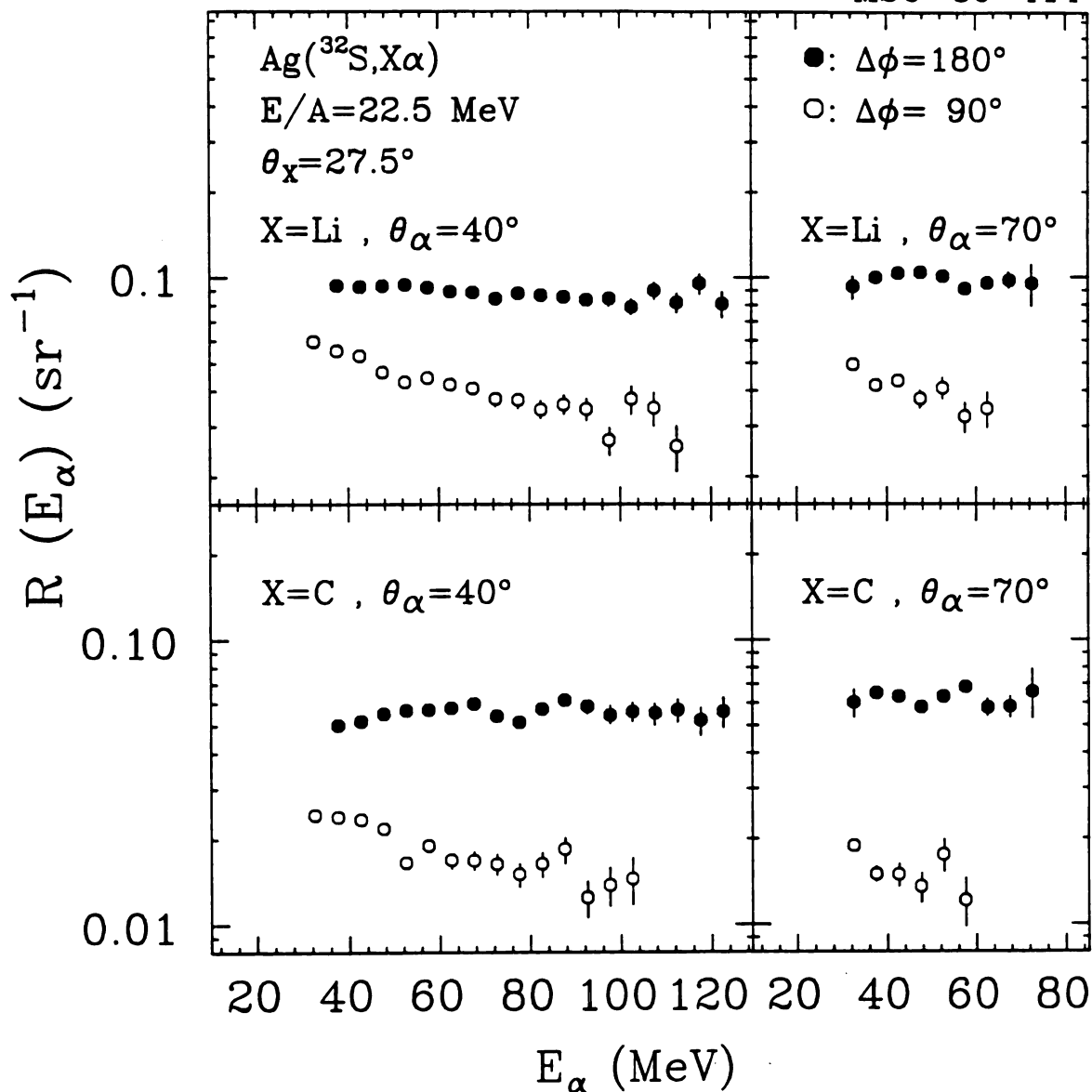


Figure IV-3 : The ratio of the differential coincidence cross sections to the single particle inclusive cross sections for alpha particles as a function of alpha particle energy. The ratio is shown for alpha particles detected at  $\theta_p = 40^\circ$  (left hand side) and  $\theta_p = 70^\circ$  (right hand side) in coincidence with Li nuclei (top of figure) and C nuclei (bottom of figure) detected at  $\theta_x = 27.5^\circ$  and at relative azimuthal angles of  $\Delta\phi = 180^\circ$  (solid points) and  $\Delta\phi = 90^\circ$  (open points).

are steeper than those of the single particle spectra. The difference in the temperature parameters which characterize the in- and out-of-plane coincidence spectra is of the order of 10%. The ratios also indicate a definite suppression of the coincidence cross sections at  $\Delta\phi=90^\circ$ .

#### IV.B. Angular correlations:

##### **IV.B.1. The correlation functions :**

The angular correlations between intermediate mass fragments and coincident light particles are explored further with the correlation function, which is defined as

$$C(\theta_y, \theta_x, \Delta\phi) = \frac{\int_y \int_x dE_y dE_x \sigma_{yx}(E_y, E_x, \theta_y, \theta_x, \Delta\phi)}{\int_y \int_x dE_y dE_x \sigma_y(E_y, \theta_y) \sigma_x(E_x, \theta_x)} \quad (\text{IV-3})$$

where the limits of the integrations can be chosen. If the coincidence cross sections are the result of independent emission of particles with their respective single particle distributions, then the correlation function is constant. The correlation function allows meaningful comparisons between angles and energies with very different coincidence and singles cross sections. The phase space acceptance of the detection system can influence coincidence observables, e.g. the coincidence cross section as a function of relative energy possesses structures which are solely functions of detector positions; such effects are not present in the correlation function. Experimental uncertainties in detector placement, solid angle, and energy calibration, also, do not influence

the correlation function since the single particle and two particle cross sections were measured simultaneously and, therefore, errors cancel in the ratio. The subtle correlations which may arise from collision dynamics [TSA84b], phase space constraints [TSA84c] [LYN82] [HAS85] [FOX86] [CHI86b], and single nucleon scattering processes [TAN80] [TAN81] can be accurately determined with this technique.

Final state interactions between particles and the decay of particle unbound states produce distinct correlations between the particles. The effects of these processes are seen in the correlation function principally at small relative momenta [BER84] [BER85] [CHI86a] [GUS85] [LYN83] [POC85a] [POC85b] [POC85c] [ZAR81]. Since dynamical effects which are independent of these processes are of interest here, the energy integrations in the correlation functions have been restricted to regions where final state interactions and sequential decay are of diminishing importance, i.e. where the relative energy between the coincident fragment and alpha particle is greater than a value,  $E_0$ , where  $E_0=6, 7, 6, 9, 11$ , and  $10$  MeV for fragment charges  $Z=2-7$ , respectively. Above these thresholds the correlation functions do not exhibit sharp structures as functions of relative energy, indicating that final state interactions and sequential decays are less important. The restriction to large relative energies influences the correlation function only at small relative angles. Because the correlation functions between intermediate mass fragments and light particles other than alpha particles were only measured at large relative angles, no similar restriction on relative energy was applied to these correlations.

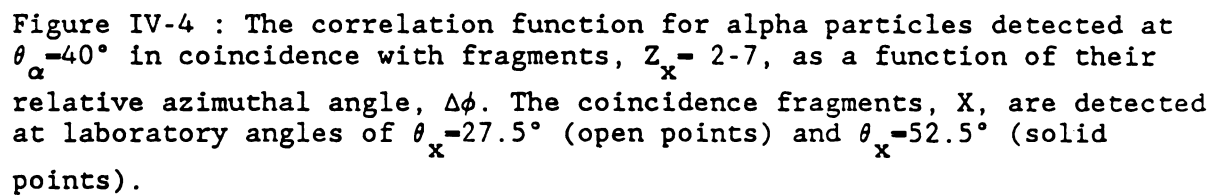
#### IV.B.2. Azimuthal correlations :

Figure IV-4 displays the correlations between alpha particles with energies,  $E_\alpha > 40$  MeV, and fragments of charge  $Z_x = 2-7$ , with energies  $E_x/A_x > 5$  MeV, except for  $E_\alpha > 40$  MeV, as a function of relative azimuthal angle,  $\Delta\phi$ . The alpha particles were detected at a polar angle of  $\theta_y = 40^\circ$ . The solid and open points represent correlations for fragments detected at  $\theta_x = 52.5^\circ$  and  $27.5^\circ$ , respectively.

For all fragments, the correlations are enhanced for coplanar particle emission, i.e. the coincidence cross sections are largest at  $\Delta\phi = 0^\circ$  and  $180^\circ$  and smallest out of the plane, at  $\Delta\phi = 90^\circ$ . An interesting feature of this azimuthal anisotropy is its symmetry about  $\Delta\phi = 90^\circ$ . While there is a modest preference for particle emission to opposite sides of the beam axis, the correlation between intermediate mass fragments and non-equilibrium light particles is only slightly sensitive to whether they are emitted to the same or to opposite sides of the beam axis.

The energy dependence of these azimuthal anisotropies is examined in Figure IV-5. The measurements were made at  $\theta_\alpha = 40^\circ$  and  $\theta_x = 27.5^\circ$  at relative angles,  $\Delta\phi = 0^\circ, 90^\circ$ , and  $180^\circ$ . Here, the open points correspond to correlations integrated with all energies,  $E_x/A_x > 5$  MeV and  $E_y > E_t$  where  $E_t = 15, 20, 20$ , and  $40$  MeV for p, d, t, and  $\alpha$  particles, respectively. The solid points correspond to correlations integrated over higher energy thresholds:  $E_x/A_x > 10$  MeV and  $E_y > E_t + 20$  MeV. This comparison demonstrates that the same side - opposite side symmetry largely persists for high energy particles.

The dependences of the in-plane enhancements of the correlation on the particle masses, angles, and energies are further demonstrated in





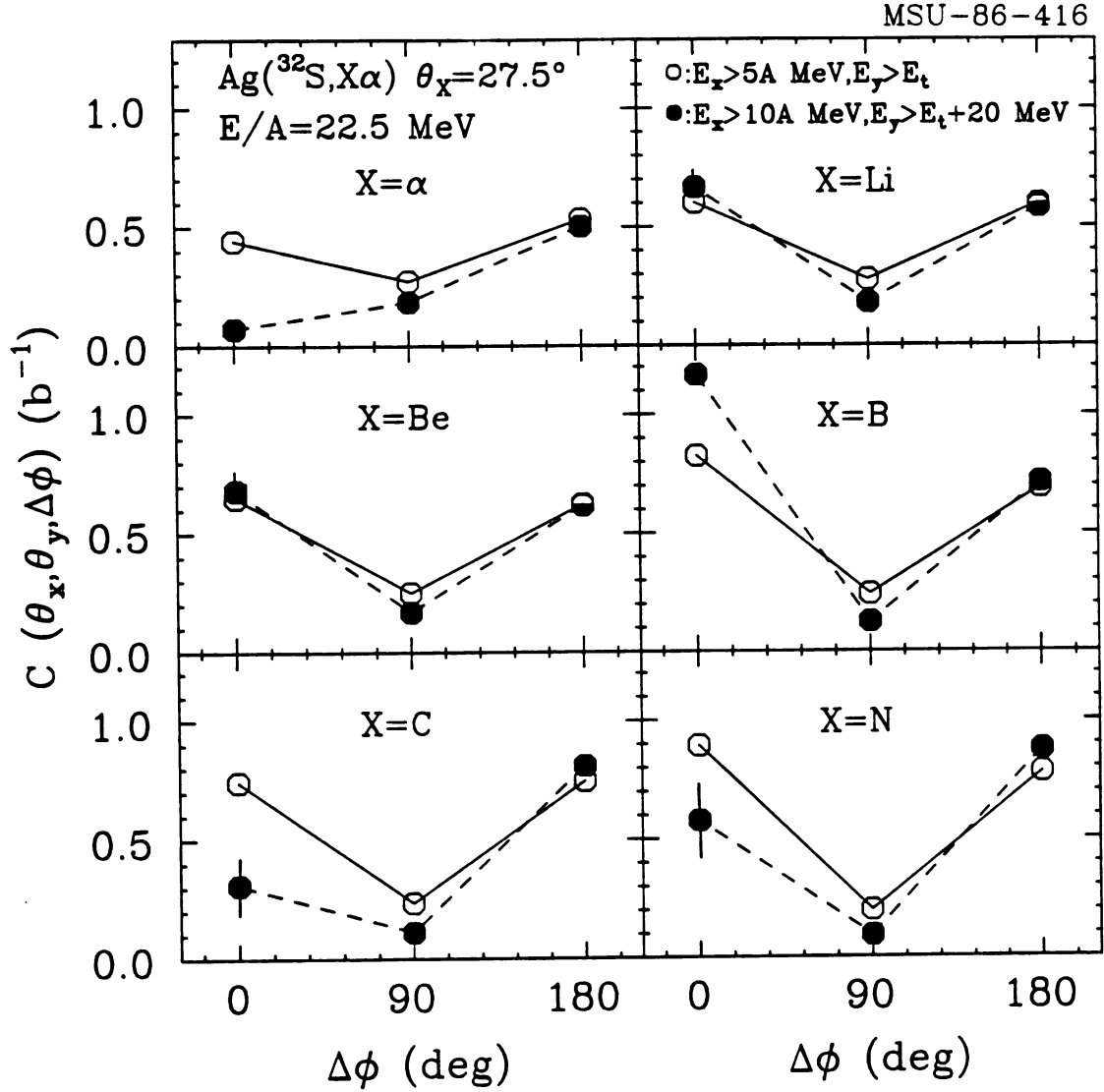


Figure IV-5 : The correlation function integrated with low and high low particle energy thresholds (open and solid points, respectively) for alpha particles detected at  $\theta_\alpha = 40^\circ$  in coincidence with fragments,  $Z_x = 2-7$ . It is shown as a function of their relative azimuthal angle,  $\Delta\phi$ . The coincidence fragments,  $X$ , are detected at  $\theta_x = 27.5^\circ$ .

Figures IV-6-9, which show the azimuthal anisotropy,

$$A_{\phi} = \frac{C(\theta_y, \theta_x, \Delta\phi=180^\circ)}{C(\theta_y, \theta_x, \Delta\phi=90^\circ)}, \quad (\text{IV-4})$$

as a function of fragment charge. In Figure IV-6, this ratio is shown for light particles,  $y=p,d,t,\alpha$ , detected at  $\theta_y=40^\circ$  and intermediate mass fragments detected at  $\theta_x=27.5^\circ$ . The solid and open points correspond to correlations integrated over particle energies above the lower and higher energy thresholds discussed with reference to Figure IV-5. A number of features are evident. The anisotropy increases with increasing mass of the intermediate mass fragment and with increasing light particle mass. The anisotropy also becomes stronger as the energy of either particle increases. This same energy and mass dependence is displayed in Figure IV-7, which shows the anisotropy measured, instead, at  $\theta_x=40^\circ$ .

In Figure IV-8, the anisotropies measured at  $\theta_x=27.5^\circ$  and at  $\theta_x=52.5^\circ$  are compared for a fixed value of  $\theta_y=40^\circ$ ; in Figure IV-9, of  $\theta_y=70^\circ$ . The anisotropy becomes larger as the polar angle of detection for either particle increases. The increase in the anisotropy with detection angle is stronger for alpha particles than for protons, though there is some suggestion that this angular dependence is less pronounced for the heavier fragments.

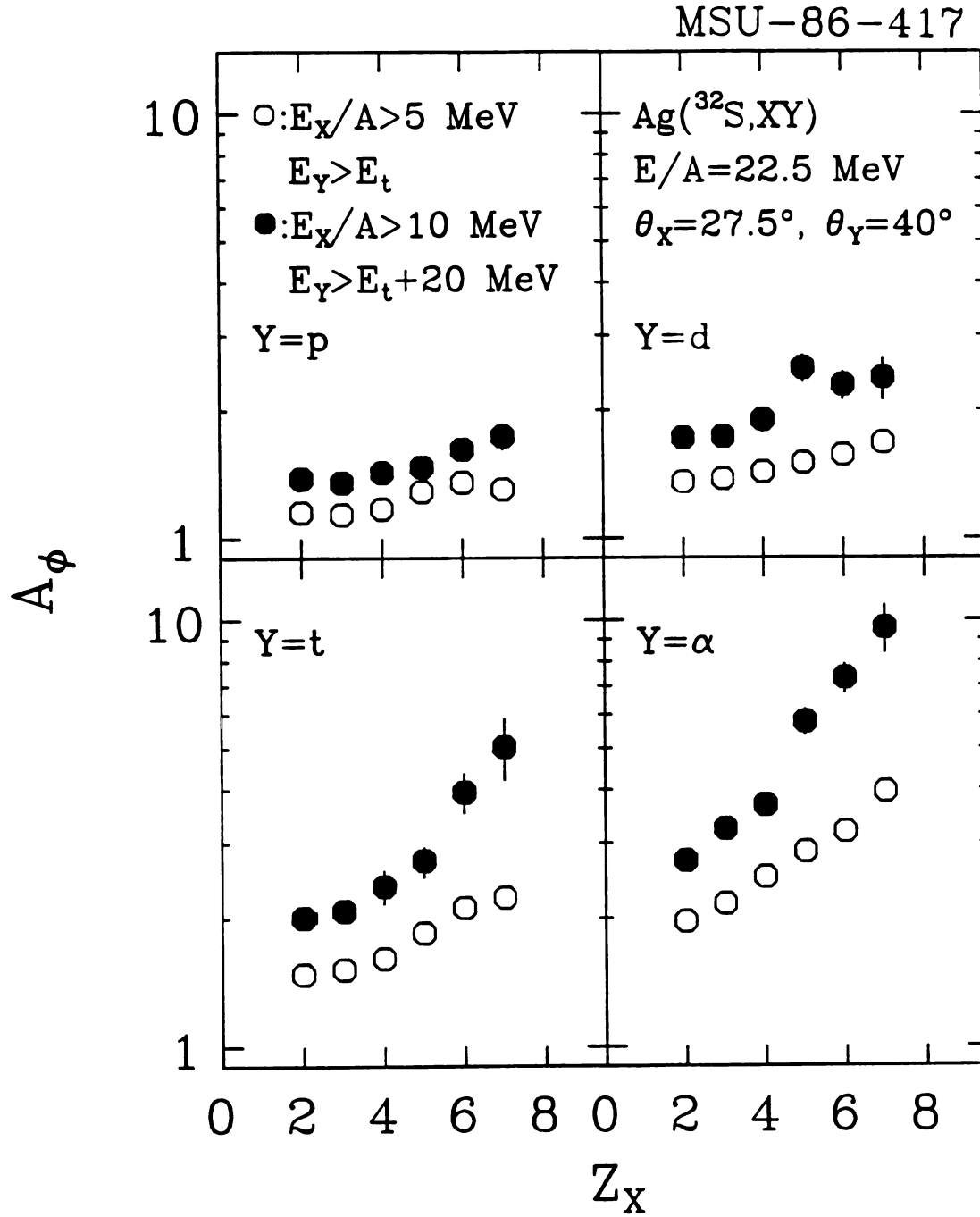


Figure IV-6 : The in-to-out of plane ratio,  $A_\phi$ , defined in the text, for fragments of charge,  $Z_x=2-7$ , detected at  $\theta_x=27.5^\circ$  and light particles,  $Y=p,d,t,\alpha$ , detected at  $\theta_y=40^\circ$ . The solid and open points correspond to the ratio for correlations integrated for particle energies above a higher and lower low energy threshold.

MSU-86-418

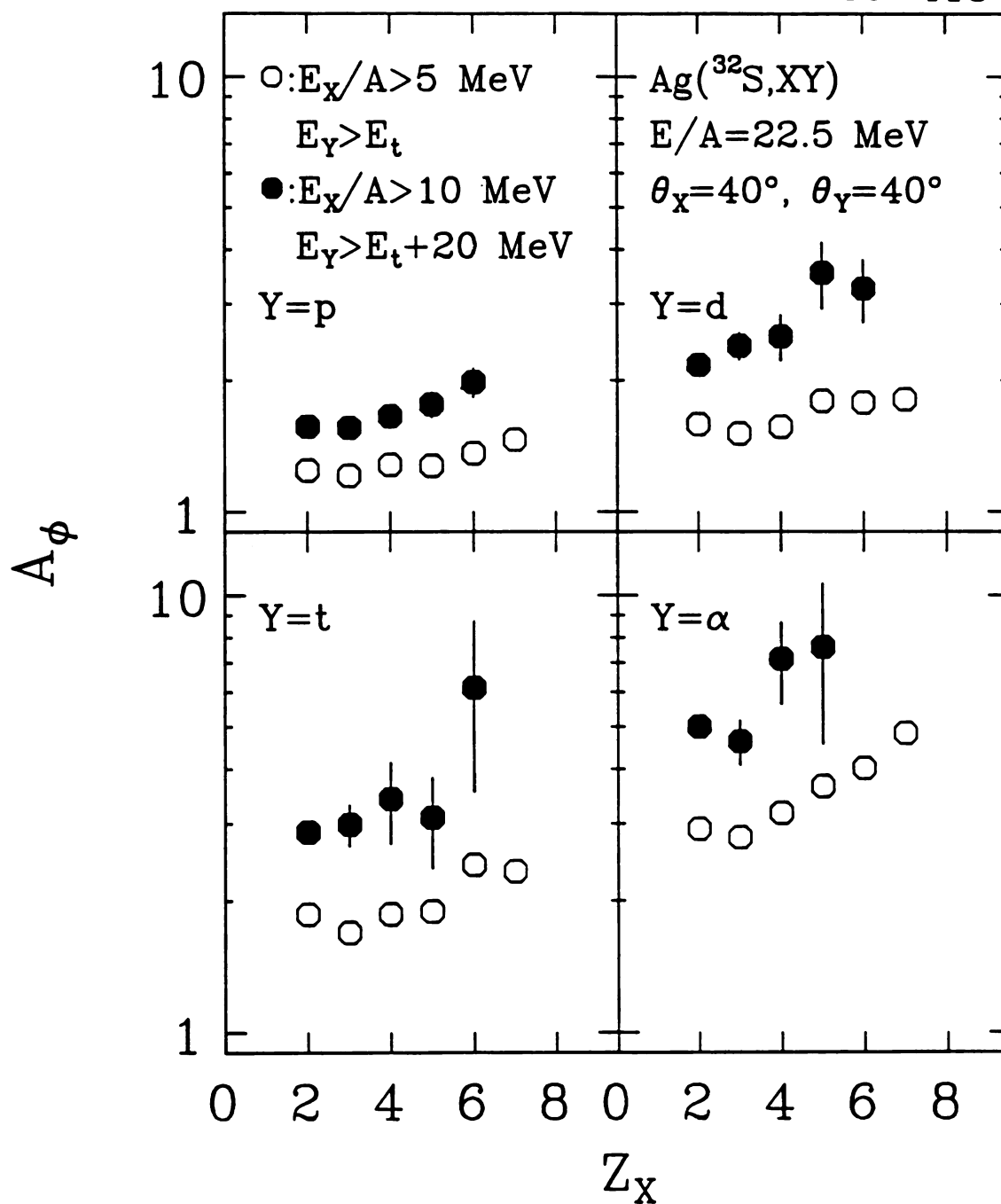


Figure IV-7 : The in-to-out of plane ratio,  $A_\phi$ , defined in the text, for fragments of charge,  $Z_X=2-7$ , detected at  $\theta_X=40^\circ$  and light particles,  $Y=p,d,t,\alpha$ , detected at  $\theta_Y=40^\circ$ . The solid and open points correspond to the ratio for correlations integrated for particle energies above a higher and lower low energy threshold.

MSU-86-419

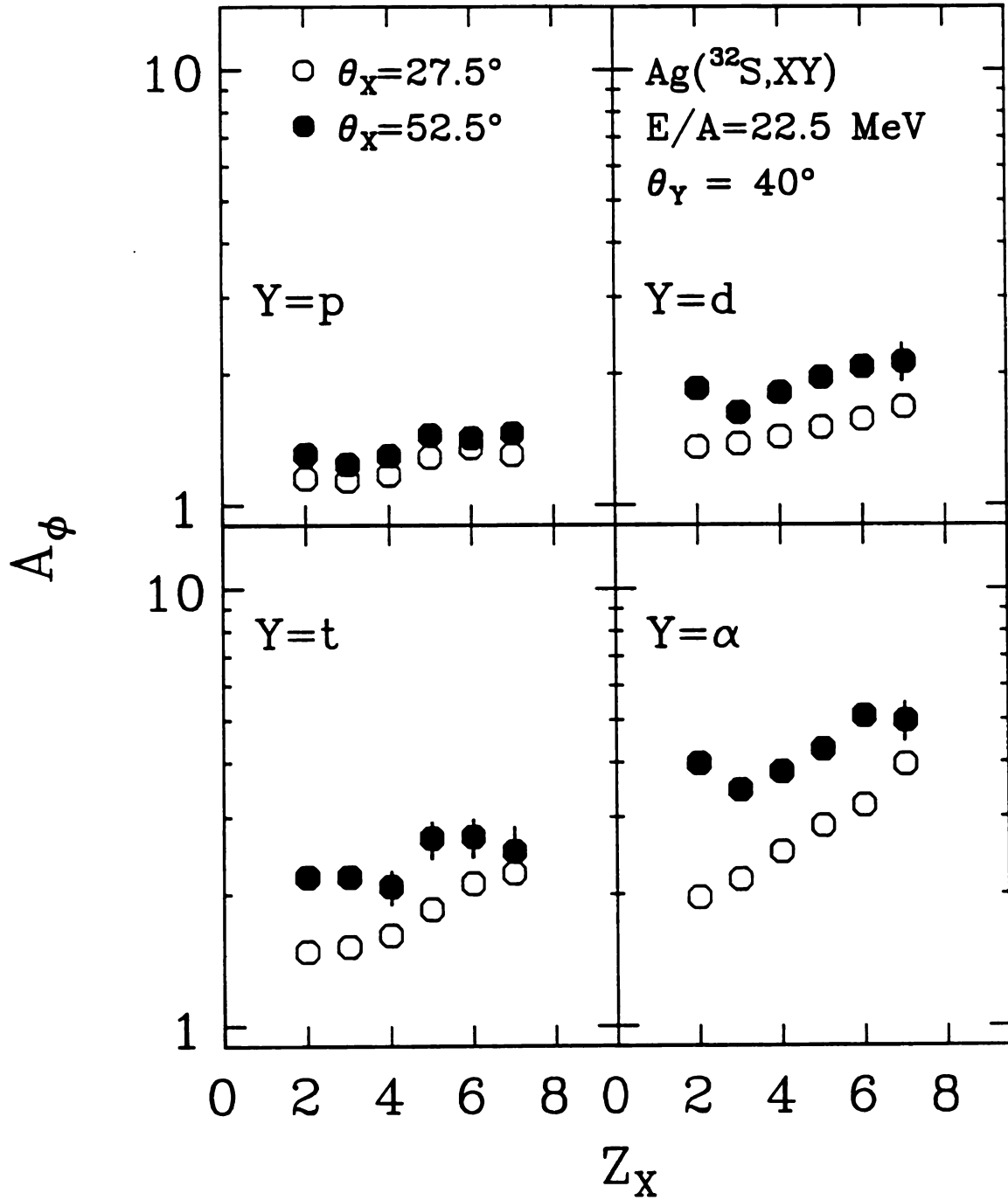


Figure IV-8 : The in-to-out of plane ratio,  $A_\phi$ , defined in the text, for fragments of charge,  $Z_x=2-7$ , detected at  $\theta_x=27.5^\circ$  (open points) and  $52.5^\circ$  (solid points) and light particles,  $Y=p,d,t,\alpha$ , detected at  $\theta_y=40^\circ$ .

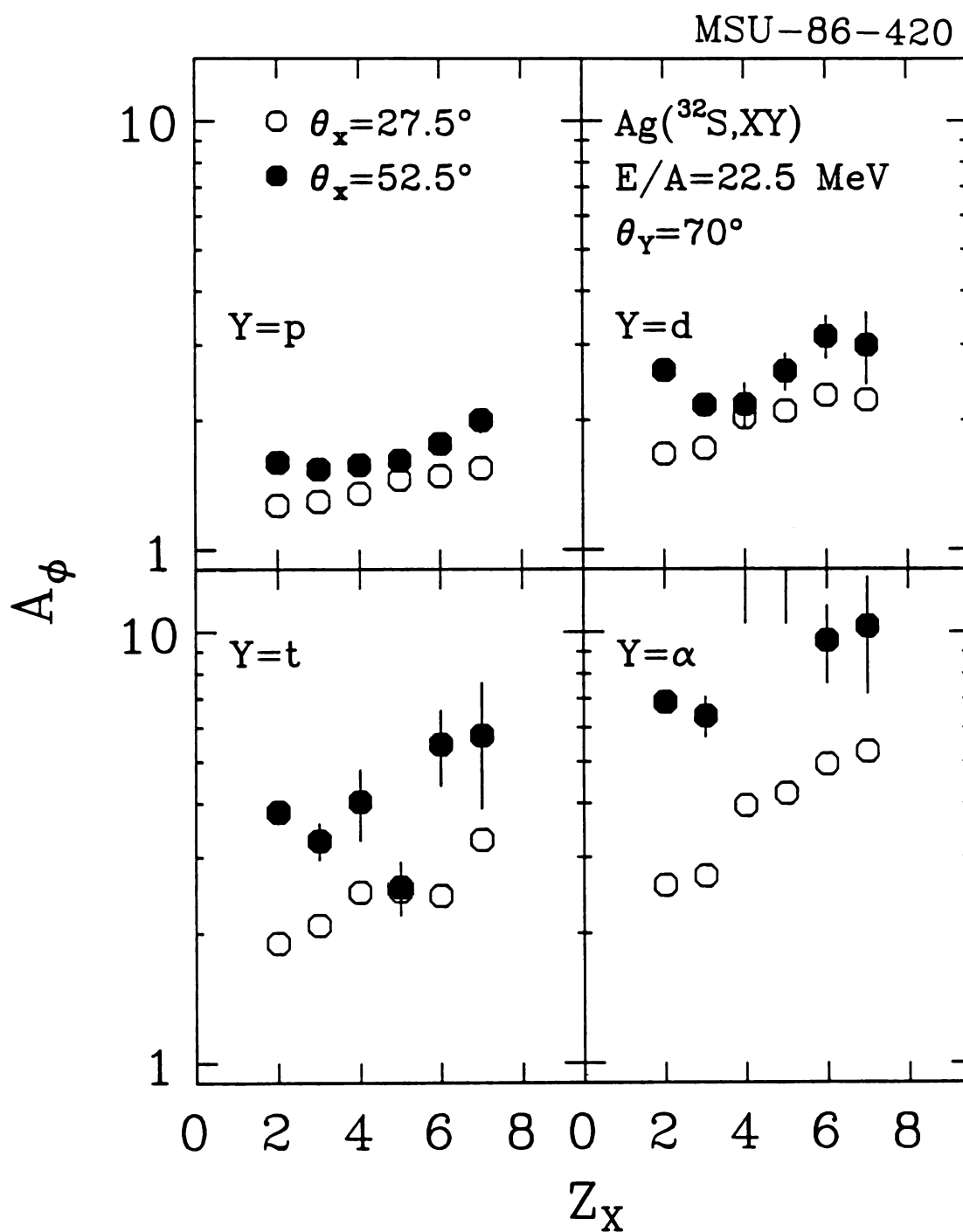


Figure IV-9 : The in-to-out of plane ratio,  $A_\phi$ , defined in the text, for fragments of charge,  $Z_X=2-7$ , detected at  $\theta_x=27.5^\circ$  (open points) and  $52.5^\circ$  (solid points) and light particles,  $Y=p, d, t, \alpha$ , detected at  $\theta_y=70^\circ$ .

### IV.B.3. In-plane correlations :

Figure IV-10 shows the correlations between alpha particles and fragments,  $Z_x=2-7$ , detected in a coplanar geometry ( $\Delta\phi=0^\circ$  or  $180^\circ$ ), as functions of the polar angle of the alpha particle,  $\theta_\alpha$ . Positive values of  $\theta_\alpha$  correspond to emission to the same side of the beam axis as the fragment. When the fragments are detected at  $\theta_x=27.5^\circ$  (open points), the measured correlations are insensitive to the polar angle of the alpha particle. When the fragment is detected at a larger angle,  $\theta_x=52.5^\circ$ , the correlations show a suppression of the correlation function at forward angles. This feature becomes clearer as the fragment mass increases.

### IV.C. Discussion :

The comparison between the coincident and single particle inclusive spectra of light particles provides no evidence for the existence of a peculiar class of fragmentation events. On the contrary, it suggests that intermediate mass fragments are associated with the rather large class of events characterized by non-equilibrium light particle emission. Such reactions have been determined to be non-peripheral, as light particle spectra gated on projectile-like fragments do not account for the inclusive spectra [HAS85]. It has been determined through the analysis of spectra gated on momentum transfer that the principal component of the non-equilibrium light particle cross sections at large angles originates in the early stages of very damped, central collisions [AWE79] [AWE81b].

Energy and angular distributions of light particles have been

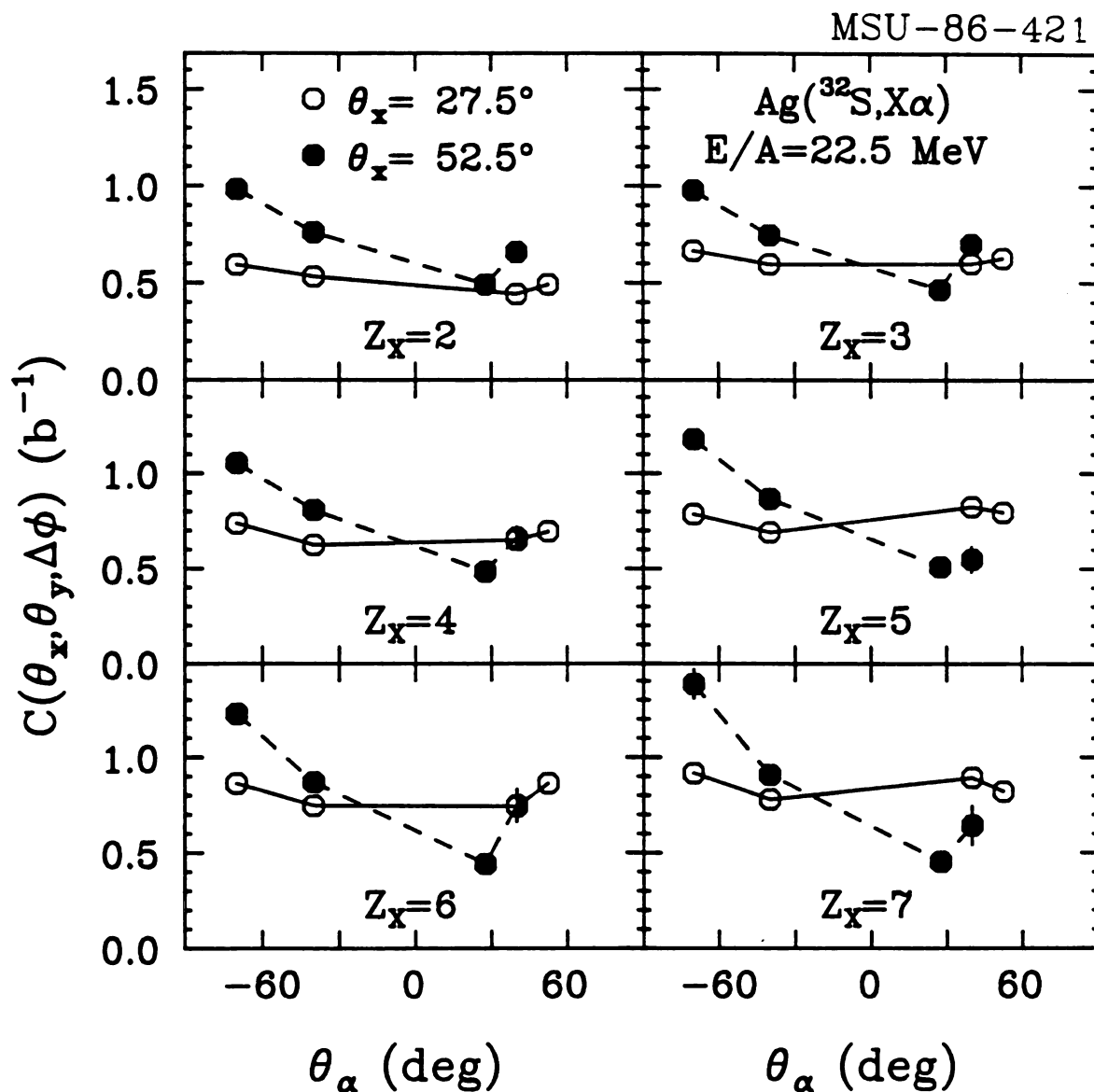


Figure IV-10: The correlation function for alpha particles in coincidence with fragments,  $Z_x = 2-7$ , detected in the same plane ( $\Delta\phi=0^\circ$  or  $180^\circ$ ) as a function of the polar angle,  $\theta_\alpha$ , of the alpha particle. The coincidence fragments, X, are detected at laboratory angles of  $\theta_x=27.5^\circ$  (open points) and  $\theta_x=52.5^\circ$  (solid points).



measured in coincidence with fission fragments in  $^{14}\text{N}$  induced reactions on  $^{197}\text{Au}$  at  $E/A=35$  MeV [TSA84b]. Like the present data, the coincidence spectra measured in the plane defined by the fission fragments were similar to the single particle distributions. Energy spectra measured out of this plane were steeper, particularly for alpha particles, and the coincidence cross sections were suppressed. It was established that non-equilibrium light particles are preferentially emitted in a plane which is perpendicular to the entrance channel orbital angular momentum [TSA84b]. Therefore, it is likely that the emission of intermediate mass fragments too, is enhanced in this plane.

The correlations are observed to be approximately the same for particle pairs of  $\Delta\phi=0^\circ$  and  $\Delta\phi=180^\circ$ . Because momentum conservation effects would produce an enhancement in the coincidence cross section at  $\Delta\phi=180^\circ$ , the approximate symmetry between same and opposite side emission indicates that the suppression of the correlation out of the plane defined by the beam and the fragment is not simply due to momentum conservation. Momentum conservation effects have been seen in in-plane enhancements in  $^{16}\text{O}$  induced reactions on light targets,  $^{12}\text{C}$  and  $^{27}\text{Al}$  [CHI86b], but they diminish with increasing target mass, while the in-plane enhancements do not diminish. Thus asymmetries [FOX85] [KRI85] evident in the ratio  $\sigma(\Delta\phi=90^\circ)/\sigma(\Delta\phi=180^\circ)$  are not sufficient to confirm the dominance of momentum conservation effects in the angular correlations between particles. The left-right symmetry also does not indicate dominant contributions from a projectile-like source [MUR85] [MUR86], which would produce increased correlations at  $\Delta\phi=0^\circ$ .

The angular correlations give a strong indication of dynamical influences in the fragment emission mechanism. Very similar correlations

have been observed in light particle-light particle coincidence measurements of  $^{16}\text{O}$  induced reactions on  $^{197}\text{Au}$  at  $E/A = 25$  MeV [TSA84c] [CHI86b]. This similarity suggests that the underlying physics of both light particle and intermediate mass fragment emission is the same. The enhancement of correlations in this reaction plane was understood in terms of a collective transverse motion in the reaction plane upon which is superimposed the random statistical motion of the light particles [TSA84c]. Such a collective motion perpendicular to the beam direction would require a substantial influence by the nuclear mean field. Microscopic calculations with the Boltzman-Uehling-Uhlenbeck theory have attributed this collective motion to the deflection of the particles in the mean field [AIC85a] which produces an enhancement of the light particle emission to negative deflection angles, i.e. to the far side of the target. This qualitative prediction was recently confirmed by measuring the circular polarization of gamma rays emitted from the target-like residue in coincidence with non-equilibrium light particles [TSA86].

A rapidly rotating system [TSA84b] is a limiting case of emission from a hot system undergoing a collective motion in the reaction plane. In such a model, the correlation with entrance channel reaction plane does indeed increase with the energy and mass of the emitted particle. Energetic particles are correlated with the plane of rotation because that is the plane where the collective velocity is most likely to contribute to the energy of the particle; out of the plane the velocities are only thermal. As the mass of the fragment increases, its thermal velocity decreases and its collective velocity remains constant, so that the collective motions become relatively more important. The

light particle and fragment distributions indicate that the emission cannot, however, be from a rotating compound nucleus. Nonetheless, the collective deflection in the mean field predicted by the Boltzman equation may play the same role in the planar emission patterns as the constant angular velocity of the compound nucleus, so that the qualitative dependence of the emission pattern on fragment mass and velocities may be the same for both descriptions.

The correlation function decreases at forward angles. This may be a result of the in-plane emission pattern observed in the azimuthal correlations. This is understood as follows: Imagine a set of rotating systems at rest, each emitting particles preferentially in a plane perpendicular to the axis of rotation, which is perpendicular to the polar axis of the observer's coordinate system. As a result of the width of the distribution out of the plane and the solid angles of the detectors, the single particle cross sections (the denominator of the correlation function) contain contributions from more than one orientation of the axis of rotation. At forward angles, many or all emission planes contribute, causing an increase in the single particle cross sections,  $d\sigma/d\Omega$ , as observed in fission fragment angular distributions [TSA83]. The plane of emission for the coincidence cross sections, on the other hand, is determined largely by the detector located at the most backward angle and is independent of the polar coordinate of the more forward detector. The single particle cross sections go up at forward angles, the coincidence cross sections are relatively unchanged, and thus the correlation decreases.

In summary, intermediate mass fragments are emitted in non-central collisions and define a plane of enhanced non-equilibrium light particle

emission. A comparison with measurements of light particles coincident with fission fragments indicates that this is the plane perpendicular to the entrance channel angular momentum. Because the correlations between light particles are similar to the light particle-intermediate mass fragment correlations, the dynamical effects that appear to influence light particle emission may similarly affect fragment emission.

## Chapter V

### Associated Multiplicities

The multiplicity of emitted particles is an important observable in fragmentation reactions. In this section, multiplicity measurements will be used to test the applicability of multifragmentation models to intermediate energy collisions, to test the statistical nature of the mechanism, and to estimate the magnitude of non-equilibrium emission.

#### V.A. Associated multiplicity defined :

Particle multiplicities are ideally measured with a array of detectors, each subtending a small solid angle, which covers a  $4\pi$  solid angle. With such a device, the inclusive and gated multiplicity distributions can be measured without ambiguity.

Lacking such a perfect detection system, one can infer the average multiplicity of a particle,  $a$ , associated with another particle,  $b$ , from the coincidence cross sections. If one assumes the particles to be emitted independently with the single particle inclusive distributions from a class of reactions with a channel cross section,  $\sigma_R$ , then the

cross section for each particle is

$$\sigma_x = \sigma_R M_x, \quad (V-1)$$

where  $M_x$  is the mean multiplicity of particle  $x$ . The coincidence cross section of particles  $a$  and  $b$  is given by

$$\sigma_{ab} = \sigma_R M_a M_b, \quad (V-2)$$

which can be used to estimate the reaction cross section :

$$\sigma_{ab}/\sigma_a \sigma_b = C_{ab} = \sigma_R^{-1}, \quad (V-3)$$

where  $C_{ab}$  is the correlation function defined in Section IV-B.1. Thus, the associated multiplicity of particle  $a$ , associated with  $b$  is

$$M_a = \sigma_a C_{ab}. \quad (V-4)$$

The total cross section,  $\sigma_a$ , can be estimated from the parametrizations discussed in Section III.B.

Alternatively, the multiplicity can be estimated as follows :

$$M_a = \frac{\int_a \int_b dE_a dE_b \sigma_{ab}(E_a, \theta_b, E_a, \theta_b)}{\int_b dE_b \sigma_b(E_b, \theta_b)} \times \frac{\tilde{\sigma}_a^{\text{tot}}}{\int_a dE_a \tilde{\sigma}_a(E_a, \theta_a)} \quad (V-5)$$

where  $\sigma_{ab}$  and  $\sigma_a$  are experimental coincidence and singles cross sections, respectively, and  $\tilde{\sigma}_a^{\text{tot}}$  and  $\tilde{\sigma}_a$  are the parametrized total and differential cross sections. The form of this expression is the same as

Eq. V-4, except that the correlation function is constructed by dividing by the parametrized cross section for particle a. The results of these methods agree within about 20%.

The uncertainties introduced in the associated multiplicities by the estimates of the channel cross section and the assumption of statistical independence are of the order of several tens of percent. The estimates of the total cross section consider only the two components of the cross section included in the parametrization of the particle spectra. Products of projectile fragmentation are not included in the estimates.

#### V.B. Multiplicities of light particles associated with intermediate mass fragments :

The average multiplicities of non-equilibrium light particles associated with the emission of Li, B, and C nuclei of average momenta,  $\langle P_x \rangle$ , detected at  $\theta_x = 27.5^\circ$  are shown in Table V-1. The estimates are deduced from the coincidence cross section at  $\theta_y = 40^\circ$  averaged between  $\Delta\phi = 180^\circ$  and  $\Delta\phi = 90^\circ$ . These results indicate that intermediate mass fragments are accompanied by an average of about 10 nucleons in the form of non-equilibrium light particles,  $A_y \leq 4$ . In light of the coincidence spectra of Section IV.A., it is reasonable to assume that these nucleons are emitted with energy distributions which are similar to the corresponding single particle inclusive distributions. Non-equilibrium light particles are estimated to remove a total longitudinal momentum of  $\approx 1100$  MeV/c from the system. This corresponds to more than 15% of the projectile momentum. The average kinetic energy carried away by these

Table V-1 : The estimated average total multiplicities,  $M$ , of light particles,  $p, d, t, \alpha$ , associated with intermediate mass fragments with momenta,  $\langle P_x \rangle$ , emitted in  $^{32}\text{S}$  induced reactions on Ag at  $E/A=22.5$  MeV.  $M_T$  is the total nucleon multiplicity;  $\langle P \rangle$  and  $\langle E \rangle$  are the average total longitudinal momentum and average total energy carried away by non-equilibrium light particles. Momenta and energies are given in units of MeV/c and MeV, respectively. The multiplicities are inferred from cross sections measured at  $\theta_y=40^\circ$ ,  $\theta=27.5^\circ$ , averaged between  $\Delta\phi=90^\circ$  and  $180^\circ$ .

	Li			B				C		
$\langle P_1 \rangle$	820.	1082.	1348.	832.	1144.	1429.	1719.	1164.	1448.	1745.
$M_{p,n}$	2.0	1.8	1.7	1.7	2.1	2.0	1.8	1.9	2.0	1.9
$M_d$	.5	0.4	0.4	0.5	0.5	0.5	0.4	0.5	0.5	0.5
$M_t$	.3	0.2	0.2	0.2	0.3	0.2	0.2	0.2	0.3	0.2
$M_\alpha$	1.2	1.1	0.9	1.0	1.2	1.2	1.1	1.2	1.3	1.2
$M_T$	10.4	9.5	8.3	9.1	10.8	10.5	9.4	10.4	11.1	10.1
$\langle P \rangle$	1170.	1073.	942.	1026.	1218.	1182.	1060.	1170.	1253.	1143.
$\langle E \rangle$	167.	152.	136.	145.	174.	168.	150.	165.	177.	161.



fast light particles is about 160 MeV, or more than 20% of the projectile laboratory energy. An energy of approximately 60 MeV is contained in the center-of-mass motion of the light particles. The remaining 100 MeV is contained in the random velocities of the light particles about their center-of-mass.

There is a perceptible dependence of the correlation function on fragment momentum. non-equilibrium light particle emission is strongest for fragments emitted near the peak in energy distributions. As the momentum of the fragment increases, the multiplicity of the light particles decreases slightly. This qualitative dependence is expected from energy conservation. The decrease in light particle multiplicity for fragment momenta lower than the maxima of the distributions is not so easily understood, and may be related to the sequential decay of excited primary fragments (see Section VI.A.2.). While this might also be related to contributions from the target-like partner of peripheral reactions, the velocity distributions of target-like residues discussed in Section VI do not indicate that low energy fragments are particularly associated with peripheral reactions.

#### V.C. Intermediate mass fragment multiplicities:

##### **V.C.1. Fragment multiplicities associated with light particles :**

The associated multiplicities of intermediate mass fragments are estimated in the same manner. Multiplicities of fragments,  $Z_x=2-7$ , associated with non-equilibrium alpha particles are shown in Figure V-1.

MSU-86-423

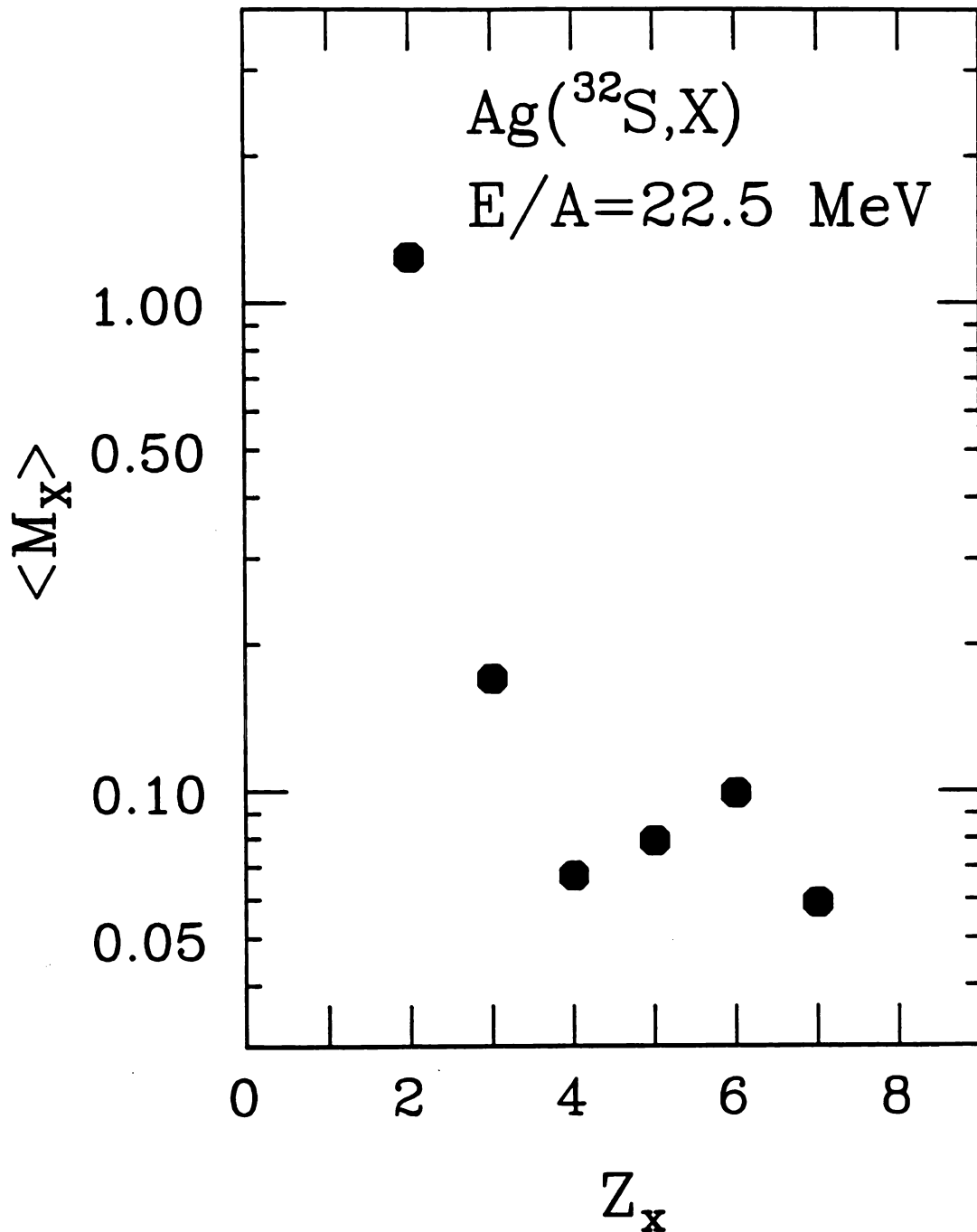


Figure V-1 : The estimated average total multiplicities,  $M_x$ , of particles,  $Z_x=2-7$ , associated with alpha particles in  $^{32}\text{S}$  induced reactions on Ag at  $E/A=22.5$  MeV. The results were obtained from the correlations measured at  $\theta_\alpha=40^\circ$  and  $\theta_x=27.5^\circ$  at  $\Delta\phi=90^\circ$  and  $180^\circ$ .

These are deduced from the correlations function measured at  $\theta_y = 40^\circ$ ,  $\theta_x = 27.5^\circ$  averaged between the two relative azimuthal angles,  $\Delta\phi = 180^\circ$  and  $90^\circ$ . The mean associated multiplicity of any one of these fragments is low, of the order of 0.1.

The azimuthally averaged correlations between light particles detected at  $\theta_y = 40^\circ$  and fragments detected at  $\theta_x = 27.5^\circ$  are shown in Figure V-2. They do not exhibit any significant dependence on fragment charge. The proportionality factor between the inclusive cross sections and the associated multiplicity is the two-particle correlation function. Thus, the coincidence cross sections scale approximately with the inclusive yields. This is very similar to result of relativistic heavy ion reactions [WAR83].

If an average value of  $C \approx 0.45$  is assumed for heavier fragments and if the particles are further assumed to be emitted independently, the value for the total associated multiplicity of fragments with charge  $3 \leq Z \leq 24$  is estimated to be 0.75. This value corresponds to the emission of about 12 nucleons in the form of complex fragments. The parametrizations of the singles cross sections indicate that there is a large non-equilibrium component in the fragment cross sections, so that energy and linear momentum are carried away prior to the attainment of full statistical equilibrium by reaction products other than light particles. This increases the momentum lost to non-equilibrium emission by about 40%. Thus, a total of about 25% of the beam momentum is carried away by pre-equilibrium emission.

These estimates have considerable uncertainties, because the correlations functions depend on particle masses and the polar angles at

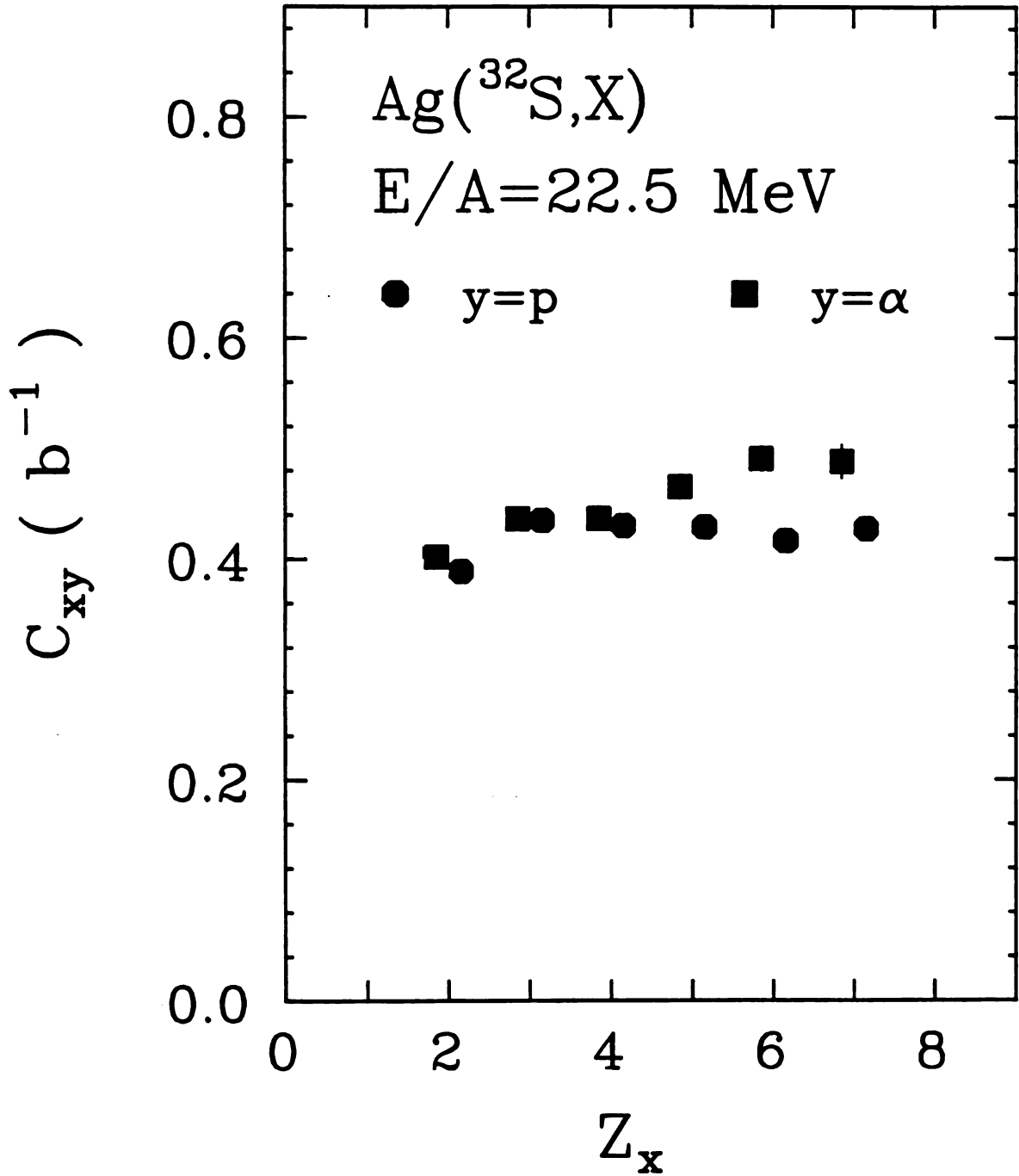


Figure V-2 : The correlation function,  $C_{xy}$ , between light particles ( $y$ ) and intermediate mass fragments ( $x$ ), measured at  $\theta_y = 40^\circ$  and  $\theta_x = 27.5^\circ$ , and averaged between  $\Delta\phi = 180^\circ$  and  $90^\circ$ , is shown as a function of  $Z_x$ , the charge of the coincident fragment.

which the fragments are detected. They vary by 10-20% between intermediate mass fragments  $Z_x=2$  and  $Z_x=7$  and between protons and alpha particles. They increase with the angle at which either particle is detected, by about 10% between  $\theta_x=27.5^\circ$  and  $\theta_x=52.5^\circ$  and by about 20% between  $\theta_y=40^\circ$  and  $\theta_y=70^\circ$ . Nevertheless, these estimates of the associated multiplicities are sufficiently accurate to establish that complex fragments are emitted with low average multiplicities and in the same class of reactions for which pre-equilibrium emission is important.

#### **V.C.2. Fragment multiplicities associated with other intermediate mass fragments :**

While the multiplicity of intermediate mass fragments associated with light particles is lower than expected for complete fragmentation of the composite nucleus, it does not necessarily preclude the dominance of high multiplicity events in the fragment production mechanism. If the emission of intermediate mass fragments occurs in a small fraction of the events producing non-equilibrium light particles, then the fragment-fragment multiplicities might still be high. The fragment-fragment associated multiplicities provide a better test.

The correlation functions between all combinations of Li and C fragment detected at  $\theta_{x1}=27.5^\circ$  and  $\theta_{x2}=52.5^\circ$  at  $\Delta\phi=0^\circ$  are  $C_{12}\approx.55b^{-1}$ . The corresponding values for light particle-intermediate mass fragment correlations are typically  $C_{12}\approx.45 b^{-1}$ . The multiplicity of intermediate mass fragments is, therefore, of the same order of magnitude ( $\approx 1$ ) as those indicated by fragment-light particle coincidence data.

One must exercise caution in interpreting this result since the estimates are deduced from measurements taken over a very restricted angular range. They are, therefore, subject to the effects of momentum conservation and final state interactions between coincident particles. In addition, the azimuthal and mass dependence of the two particle correlations suggests that there will be large in-plane enhancements in the coincidence cross sections.

Nonetheless, these associated multiplicities suggest that intermediate mass fragments do not originate from a peculiar class of reactions with high fragment multiplicities, such as the complete shattering of the target nucleus. Instead, intermediate mass fragments produced in this reaction are emitted with low probability. The fragment multiplicities exhibit little memory of prior emission.

#### V.D. Summary :

The multiplicity data indicate that intermediate mass fragments are emitted with low probability from a class of reactions with a total cross section on the order of  $C^{-1} \approx 2b$ . The geometric cross section for nuclear radii,  $r = 1.2 \cdot A^{1/3} \text{ fm}$ , is 2.8 b. If fragment emission is associated with central collisions, then the fragmentation cross section corresponds to all impact parameters of 8 fm or less. This is consistent with the conclusion of Chapter IV, made on the basis of the azimuthal correlations, that fragment production was not restricted to central collisions covering only a small range of impact parameters.

This class of reactions is characterized by substantial pre-equilibrium light particle emission, with over 10 nucleons being

emitted in that manner. These particles carry a significant part of the beam momentum and energy. In addition, about the same number of nucleons are emitted in the form of heavier fragments, with the average multiplicity of these fragments being slightly less than one. Apart from the enhanced angular correlations, the two particle correlations are approximately constant. This indicates that intermediate mass fragments are emitted statistically (with a Poisson-like distribution) with probabilities which are independent of prior particle emission.

There is some evidence that higher multiplicity events may be selected by heavier fragments emitted at larger angles. However, the increase in multiplicity is marginal. Violent multifragmentation, with fragment multiplicities much larger than 1, can be excluded as a dominant process.

## Chapter VI

### Velocity Distributions of Target-Like Residues

In this section, the velocity distributions of target-like residues coincident with intermediate mass fragments are investigated. These distributions provide information on the overall dynamics of the reactions producing fragments by determining the momentum and energy balance. One may infer from these distributions the characteristics of the particle emission in the forward direction, in the absence of direct measurements. Unless otherwise stated the data presented are taken from  $^{32}\text{S}$  induced reactions on Ag at  $E/A=22.5$  MeV [FIE86]. These data are supplemented with data from  $^{14}\text{N}$  induced reactions on Ag at  $E/A=35$  MeV [BOU86s].

#### VI.A. Velocity distributions:

##### **VI.A.1. General characteristics :**

On the left hand side of Figure VI-1, are shown angular distributions of target-like residues coincident with lithium and carbon



MSU-85-503

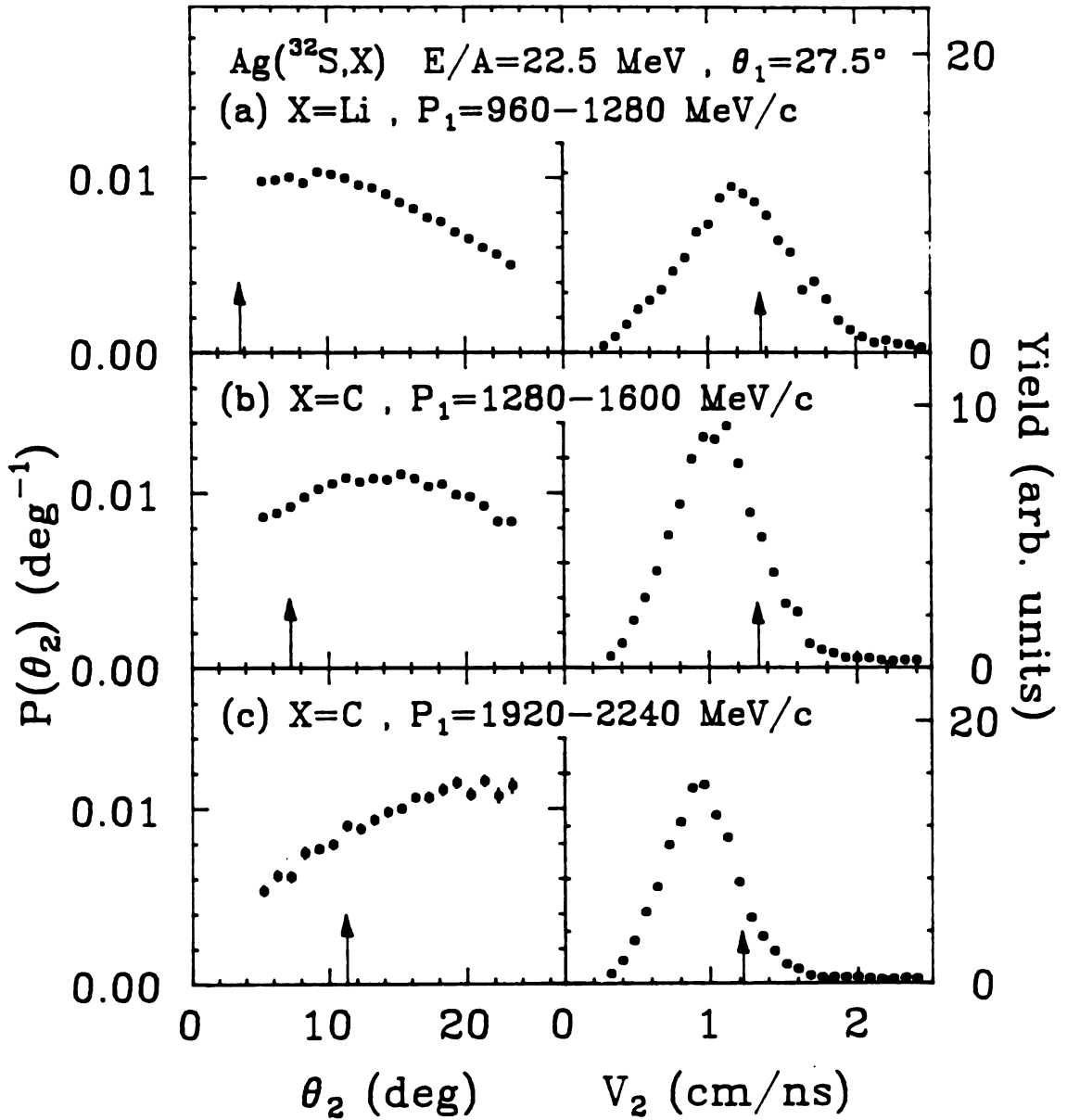


Figure VI-1 : Velocity distributions for target-like residues detected in coincidence with intermediate mass fragments detected at  $\theta_1 = 27.5^\circ$  with momenta,  $P_1$ . The left hand side shows the distribution as a function of the polar angle,  $\theta_2$ , of the projections of the recoil velocity vector onto the reaction plane. The right hand side shows the measured distributions of  $|\vec{v}_2|$ . The arrows show the values expected for binary reactions.

nuclei detected at  $\theta_1=27.5^\circ$  in  $^{32}\text{S}$  induced reactions on Ag at  $E/A=22.5$  MeV. The residues are detected in coincidence with fragments with momenta,  $P_1$ , in the ranges (a)  $P_{\text{Li}}=960\text{-}1280$  MeV, (b)  $P_{\text{C}}=1280\text{-}1600$  MeV/c, and (c)  $P_{\text{C}}=1920\text{-}2240$  MeV/c. The distributions are shown as functions of  $\theta_2$ , the polar angle of the projection of the residue velocity vector,  $\vec{v}_2$ , onto the reaction plane defined by the fragment and the beam axis. They are normalized to represent the probability per degree that a heavy residue will be detected with the coincident intermediate mass fragment. The distributions exhibit broad maxima, which have widths of about  $25^\circ$ . The peak positions expected for complete fusion followed by a binary decay into a fragment and heavy residue are indicated with arrows. They are located at angles smaller than the those of the measured maxima, indicating that a substantial part of the projectile momentum is carried away by other particles emitted into the forward direction.

Velocity distributions of heavy residues coincident with intermediate mass fragments are shown in the right hand side of Figure VI-1. They, too, are inconsistent with a fusion-fission process where 100% of the projectile momentum is transferred to the composite system. (The velocities expected for purely binary reactions are indicated by arrows.)

#### VI.A.2. Dependences of the peak position :

The location,  $\theta_2^{\text{max}}$ , of the maximum in the angular distribution of the coincident target-like residues depends both on the momentum,  $P_1$ , and the mass,  $M_1$ , of the coincident fragment. This is illustrated in Figure VI-2. The upper part of the figure shows angular distributions of

MSU-85-577

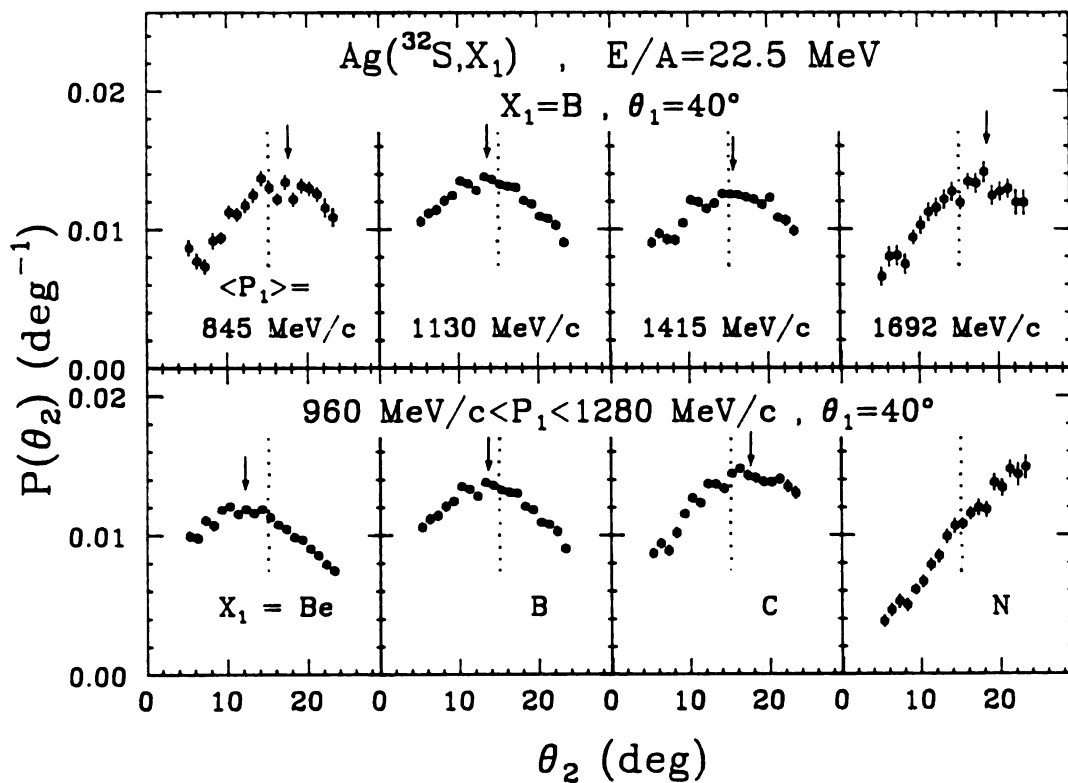


Figure VI-2 : Probability distributions for heavy residues as a function of recoil angle,  $\theta_2$ , detected in coincidence with boron fragments of different momenta,  $P_1$ , detected at  $\theta_1 = 40^\circ$ , (upper part) and coincidence with different intermediate mass fragments gated by the same momentum bin (lower part). The arrows indicate the maxima of the distributions.

recoiling residual nuclei coincident with boron nuclei of different momenta. The arrows indicate the position of the maxima,  $\theta_2^{\max}$ . For emission above the Coulomb barrier, i.e. for energies above the maximum in the fragment inclusive spectra ( $P_1 > 1000$  MeV/c),  $\theta_2^{\max}$  increases with increasing values of  $P_1$ , qualitatively consistent with momentum conservation. However, as  $P_1$  decreases below the Coulomb barrier,  $\theta_2^{\max}$  increases again;  $\theta_2^{\max}$  is smallest for fragment energies near the maximum in the energy spectra.

Similar observations were made for  $^{14}\text{N}$  induced reactions on Ag at  $E/A=35$  MeV. Figure VI-3 shows the angular distributions of target-like residues measured in coincidence with beryllium and oxygen fragments from this reaction. They share many characteristics with reactions induced by  $^{32}\text{S}$ . The angular distributions have broad maxima at angles somewhat larger than expected for binary reactions. They also show a similar dependence on fragment momentum, with the positions of the centroids,  $\langle\theta_2\rangle$ , increasing with increasing fragment momenta above the barrier, reaching a minimum around the barrier, and increasing again for momenta below the barrier. Figure VI-4 demonstrates this dependence over a broad range of oxygen fragment momenta. The minimum of  $\langle\theta_2\rangle$  is seen at the momentum corresponding to the peak of the inclusive fragment spectra, which is indicated by the arrow.

Fragment energies less than the Coulomb energy can be generated by the sequential particle decay of heavier particle unstable nuclei which were originally emitted at or above the Coulomb barrier energy [BER84]. For the example presented in Figure VI-4, it may be assumed that the primary fragment, a  $^{20}\text{Ne}$  nucleus, is emitted at  $\theta=45^\circ$  with the barrier energy ( $E=55$  MeV,  $P=1440$  MeV/c) and an excitation of about 8 MeV. The

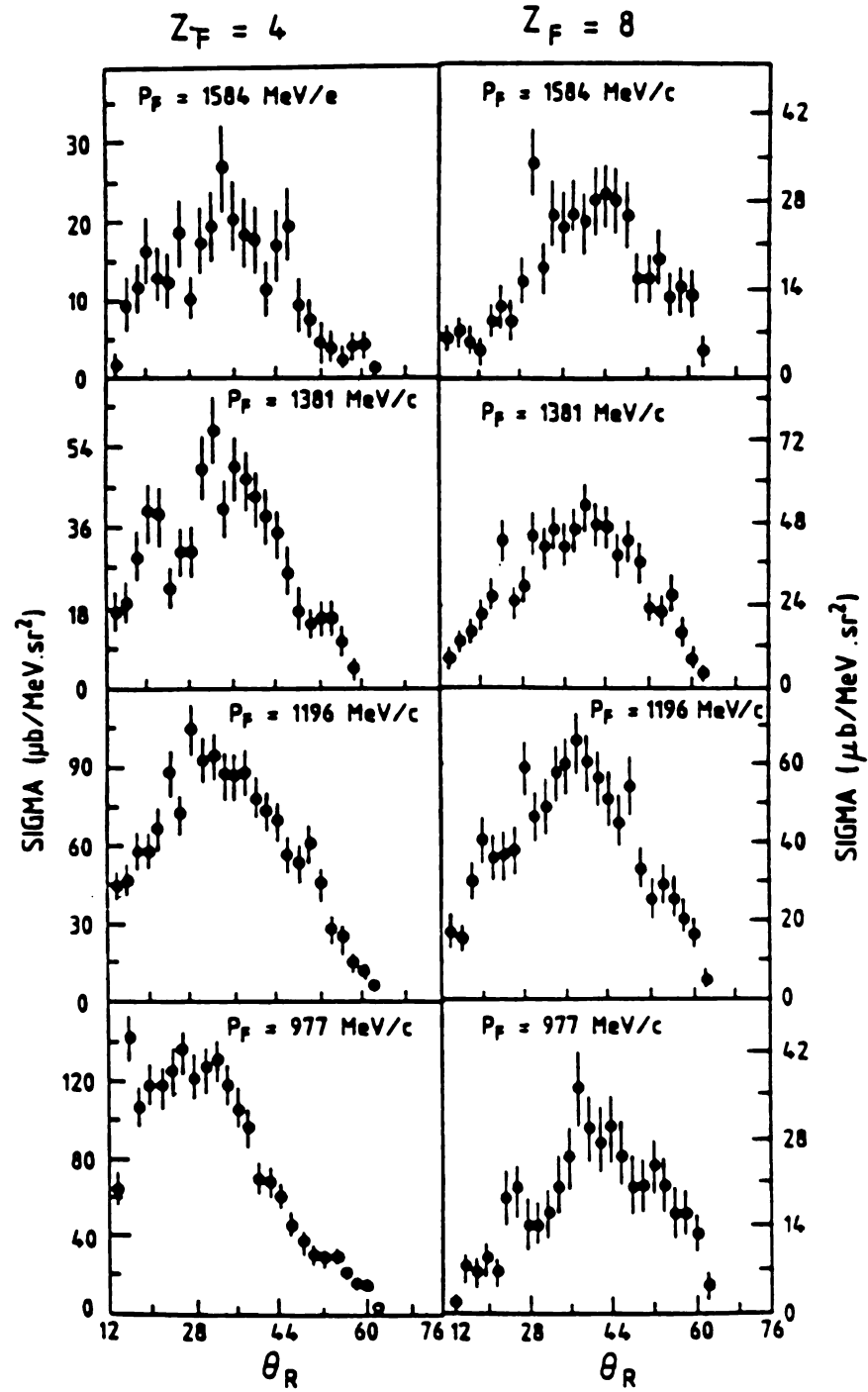


Figure VI-3 : The differential cross sections for heavy residues detected in coincidence with Be fragments (lefthand side) and O fragments (right hand side) of various momenta detected at  $\theta_1 = 45^\circ$ .

MSU-86-425

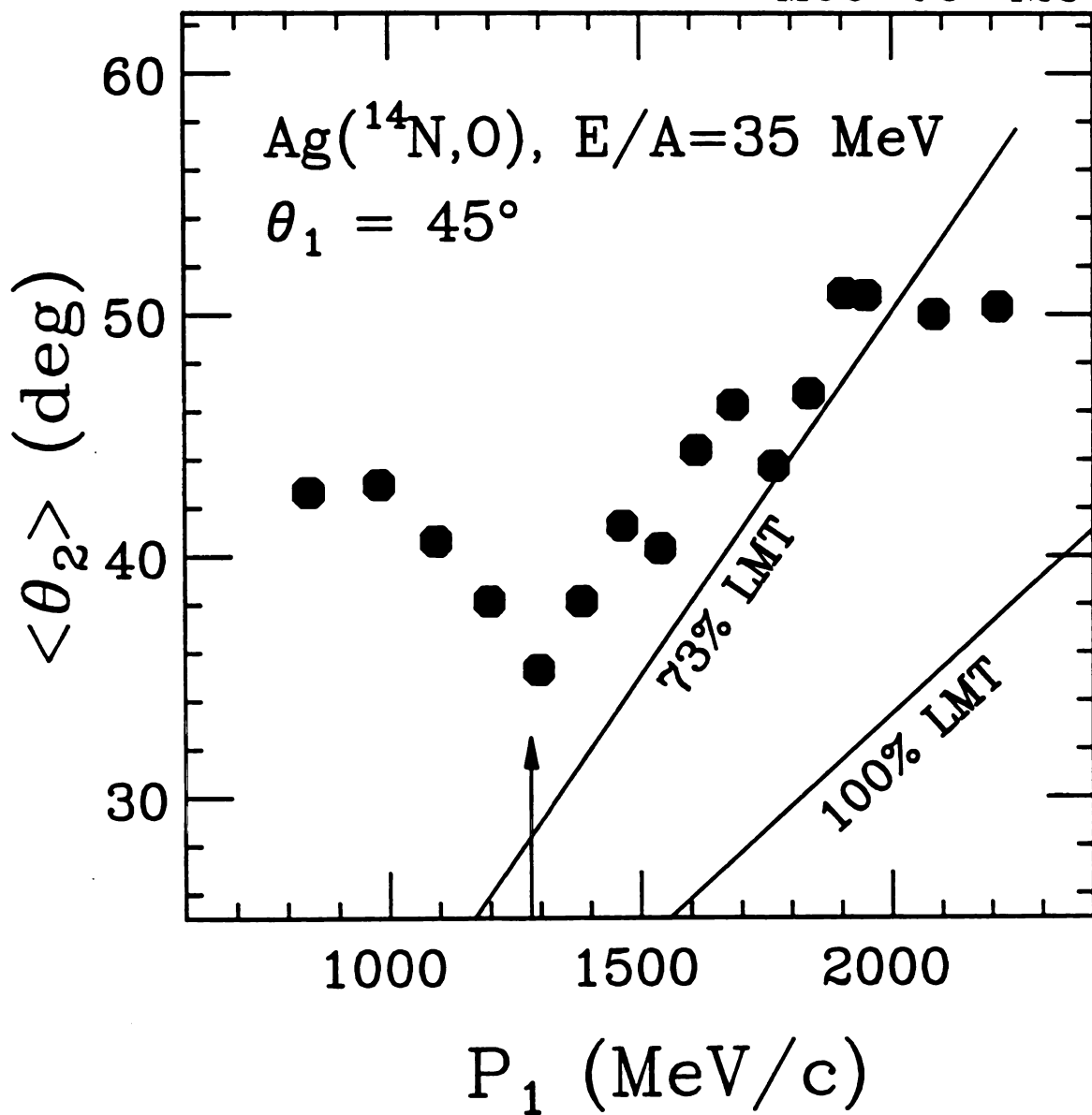


Figure VI-4 : The value of the average recoil angle  $\langle \theta_2 \rangle$  for angular distributions of heavy residues detected in coincidence with 0 fragments detected at  $\theta_1 = 45^\circ$  as a function of fragment momentum. The solid curves are expected values for 100% and 73% momentum transfer.

alpha decay energy to  $^{16}\text{O}$  is about 5 MeV. After the decay, the remaining oxygen fragment will have a momentum between 950 and 1330 MeV/c, corresponding to energies between 30 and 60 MeV, all at or below the peak of the oxygen spectrum.

Such a mechanism has been discussed with respect to the spectra of light particles emitted from unstable resonances [BER84]. Two-particle correlations at small relative angles [POC85c] suggest that the sequential decay of excited primary fragments does occur (see Chapter VII). This mechanism may be a major factor determining the energy spectra about the Coulomb barrier (see Section III.B.4). Model calculations which include this effect are discussed in Chapter VIII.

Low energy fragments might originate from the target-like partners of peripheral reactions. The residues move with low velocities, and fragments emitted from them will have small velocity boosts compared to fragments emitted in full momentum transfer events (see Section VI.B.3.).

The bottom section of Figure VI-2 shows the angular distributions for residues coincident with different nuclei of similar momenta. The values of  $\theta_2^{\text{max}}$  depend not only on the momenta of the outgoing fragments but also on their mass:  $\theta_2^{\text{max}}$  increases with the mass of the coincident fragment. This behavior is also displayed in the residue angular distributions in  $^{14}\text{N}$  induced reactions as shown in Figure VI-3. Part of this behavior may be related to the energy dependence of the angular distributions. A fixed momentum will be at positioned differently relative to the peak of the distribution for different fragments, so the behavior about the barrier may influence the mass dependence. The angular distributions for heavier fragments in the  $^{32}\text{S}$  induced reaction,

$Z_f \geq 9$ , do not exhibit maxima within the angular acceptance of the detector, presumably because the distributions are peaked at angles beyond the detector acceptance.

### VI.A.3. Integrated probabilities :

We can extrapolate the measured angular distributions to estimate the probability that a heavy residue accompanies an intermediate mass fragment. For this purpose, the distribution is assumed to be a Gaussian function of angle, and the widths in- and out-of-plane are assumed to be the same. For the case of carbon nuclei detected at  $\theta_x = 27.5^\circ$  with momenta between 1280 and 1600 MeV/c, the width of the distribution in the reaction plane is approximately  $25^\circ$ . This narrow distribution argues against any high multiplicity fragmentation process. The emission of an additional carbon nucleus from the decaying residue of 100 nucleons would result in a final angular width of  $\approx 50^\circ$ , considerably larger than the observed distributions. Additional emission would widen this further. The integrated probability for detecting a residue over the measured angular range  $\theta = 9.5^\circ - 21.5^\circ$  is about 0.13. Extrapolation over the full angular range gives approximately unit probability for the detection of a coincident heavy residue; there is a single target-like residue remaining after the emission of, at most, a few fragments.



VI.B. Kinematic analysis:**VI.B.1. Method of missing momentum analysis :**

In order to provide a more quantitative analysis of the data, a kinematic analysis has been performed using the most probable values of the heavy residue velocity distributions. For this analysis the mass number,  $M_1$ , of an intermediate mass fragment of charge,  $Z_1$ , is taken to be  $M_1 = 2Z_1$ . The momentum of the intermediate mass fragment is given by the expression:

$$\vec{P}_1 = \hat{P}_1 \cdot \sqrt{2M_1 E_1} \quad , \quad (\text{VI-1})$$

where  $\hat{P}_1$  is the unit vector of the fragment momentum and  $E_1$  is the measured energy of the fragment. The momentum of the heavy residue is given by

$$\vec{P}_2(M_2) = \vec{v}_2 \cdot M_2 \quad , \quad (\text{VI-2})$$

where  $\vec{v}_2$  is the measured velocity of the residue and  $M_2$  is the mass of the residue, which is not measured. The mass is treated as a parameter in the kinematics calculations. For each assumed value of  $M_2$ , the "missing mass",

$$M_3 = M_0 - M_1 - M_2 \quad , \quad (\text{VI-3})$$

and the "missing momentum",

$$\vec{P}_3 = \vec{P}_0 - \vec{P}_1 - \vec{P}_2 , \quad (\text{VI-4})$$

carried away by undetected particles in the reaction are calculated.

Here,  $M_0$  and  $\vec{P}_0$  denote the total mass and momentum in the reaction.

### VI.B.2. Quantities of interest :

We define the "sum kinetic energy",

$$E_k = \frac{\vec{P}_1^2}{2M_1} + \frac{\vec{P}_2^2}{2M_2} + \frac{\vec{P}_3^2}{2M_3} , \quad (\text{VI-5})$$

as the sum of the kinetic energies of the two detected fragments and the kinetic energy corresponding to the motion of the center-of-mass of the missing mass. The difference between the projectile energy and the sum kinetic energy may be associated with the energy dissipated into other, "internal", degrees of freedom, i.e. degrees of freedom different from the nine translational degrees of freedom represented by  $\vec{P}_1$ ,  $\vec{P}_2$ , and  $\vec{P}_3$ . Small values of  $E_k$  correspond to violent collisions in which a large amount of energy is converted to excitations of these "internal" degrees of freedom. For example, complete fusion followed by symmetric binary fission would result in  $E_k = E_1 + E_2 \approx 250$  MeV.

Another quantity of interest is the magnitude of the center-of-mass velocity of the missing mass,  $v_3 = |\vec{P}_3/M_3|$ . For example, values of  $v_3$  close to the projectile velocity would indicate that the missing

momentum is carried away by projectile fragments, as might be expected for a breakup-fusion process. Information about the linear momentum transfer is provided by  $(P_3)_z$ , the component of the missing momentum along the beam axis. Finally, the polar angle of the missing momentum,  $\theta_3 = \cos^{-1}[(P_3)_z/P_3]$ , is evaluated. In this sign convention positive values of  $\theta_3$  indicate that the missing momentum is directed to the same side of the beam axis as  $\vec{P}_1$ .

### VI.B.3. Results of missing momentum analysis :

As a specific example, the kinematics of coincidences between heavy recoil nuclei and carbon nuclei detected at  $\theta_1=27.5^\circ$  with momenta between 1280 and 1600 MeV/c are discussed. The energy of the fragment corresponds to laboratory energies of about 90 MeV. The experimental distributions for this case are shown in Figure VI-1b. The maxima of the target-like residue angular and velocity distributions are located at  $\theta_2^{\max} = 14^\circ$  and  $v_2^{\max} = 1.05$  cm/ns, respectively. Calculations of the kinematic quantities defined above were performed as functions of  $M_2$ ; they are shown as solid curves in Figure VI-5.

The mass of the total system must be considered in order to interpret the results of the calculations. Undetected light particles evaporated from the heavy residue may be considered as part of the mass  $M_2$ . The velocities and emission angles of these particles are, on the average, the same as those of the heavy residue, so that  $v_2$  is the velocity of the residue both before and after evaporation. If  $M_2$  is defined in this manner, the "missing momentum" is not associated with undetected particles originating from equilibrium emission from the

MSU-85-506

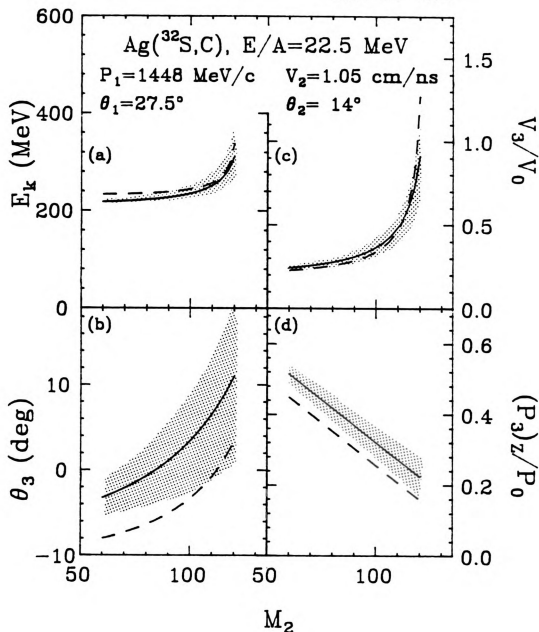


Figure VI-5 : The results of kinematics calculations for coincidences between heavy residues and carbon nuclei detected at  $\theta_1=27.5^\circ$  with an average momentum of 1448 MeV/c are shown as solid curves. The hatched area represents the estimated uncertainties. The dashed curves are obtained when the carbon nucleus is assumed to be a secondary fragment produced in the decay of a particle stable O nucleus. A detailed discussion is to be found in Section VI.B.

target-like residue.

Limits on the mass of the target residue system restrict the range of possible kinematic solutions. In Section V, it was shown that non-equilibrium light particle emission carries away about 10 mass units. Furthermore, there is a non-negligible probability for non-equilibrium emission of nucleons in the form of heavier particles. The average value of  $M_2$  should, therefore, be smaller than 120 by several mass units. Inclusive residue mass and velocity distributions from  $^{40}\text{Ar}$  induced reactions on Ag at  $E/A=27$  MeV [BORp85] suggest that the distribution probably peaks in the mass region  $M_2 \approx 70-110$  after evaporation. The present discussion is confined to values of  $75 < M_2 < 110$ .

The sum kinetic energies,  $E_k$ , extracted from the kinematics analysis are shown in Figure VI-5a. The values of  $E_k \approx 200-300$  MeV indicate that, typically, energies between 400 and 500 MeV are dissipated into degrees of freedom other than the nine translational degrees of freedom which are included in the definition of the sum kinetic energy. The multiplicity studies of Chapter V indicate that approximately 100 MeV is associated with the random motion of non-equilibrium light particles. A comparable amount of energy could be carried away by additional intermediate mass fragment emission. Thus, between 200 and 400 MeV is deposited as internal excitations of the residual nucleus or emitted fragments: intermediate mass fragments are emitted in highly inelastic collisions with temperatures of  $T \approx 4-7$  MeV.

The direction of the missing momentum vector is shown in Figure VI-5b. The missing momentum is directed close to the beam axis. The velocity of the missing mass, shown in Figure VI-5c, is less than or equal to the beam velocity. A value of about half the beam velocity,

characteristic of pre-equilibrium light particle emission, is consistent with a pre-evaporation residue mass of about 110 mass units and the emission of 15-20 nucleons at the early stages of the reaction. This number is consistent with the estimates of the associated particle multiplicities discussed in Section V.

The magnitude of the missing momentum is between 20% and 40% of the projectile momentum; see Figure VI-5d. This value of the missing momentum is larger than the value of the missing momentum,  $\approx 15\%$ , expected from the systematics of linear momentum transfer measurements for fusion-like reactions [FAT85]. Non-equilibrium light particle and fragment emission account for a major fraction of this momentum, about 25% of the beam momentum. Any remaining momentum may be the result of forward focussed emission not included in the multiplicity estimates of Chapter V.

Analyses of the coincidence measurements for other intermediate mass fragments or for different fragment momenta lead to similar conclusions. Table VI-1 shows measured recoil momenta and directions for which a value of  $\theta_2^{\max}$  could be determined. Also, values are provided for the inferred kinematic quantities assuming that  $M_2=110$ .

The total kinetic energy ranges from  $E_k = 200$  to 300 MeV. The value of  $E_k$  generally increases with increasing fragment momentum. The missing momentum ranges from 1300 MeV/c to 2300 MeV/c, averaging 1600 MeV/c. The missing momentum decreases with increasing fragment energy. While low energy fragments do show larger missing momenta than high energy fragments, there is nothing to indicate contributions from peripheral contributions : the energy losses are largest for lowest energy fragments. The very lowest energy fragments indicate the missing mass is

Table VI-1 : The observed and calculated kinematic properties of systems for which the peak in the distribution of heavy residue velocities,  $\vec{v}_2$ , was within the experimental acceptance when detected in coincidence with an intermediate mass fragment with a momentum  $\langle P_1 \rangle$  at an angle  $\theta_1$ .

$Z_1$	$\langle P_1 \rangle$ (MeV/c)	$v_2^{\max}$ (cm/ns)	$\theta_2^{\max}$	$P_3$ (MeV/c)	$\theta_3$	$E_k$ (MeV)
<u><math>\theta_1 = 27.5^\circ</math></u>						
Li	820.	1.20	-5.50	1739.	0.56	209.
Li	1082.	1.20	-9.50	1554.	6.71	240.
Li	1348.	1.20	-12.50	1376.	11.35	286.
Be	836.	1.10	-8.50	2098.	4.74	223.
Be	1113.	1.10	-8.50	1846.	1.41	234.
Be	1404.	1.10	-12.50	1644.	5.96	266.
Be	1685.	1.15	-15.00	1283.	11.04	305.
B	832.	1.10	-17.50	2352.	18.69	254.
B	1144.	1.10	-11.50	1866.	6.96	232.
B	1429.	1.05	-13.00	1794.	4.88	258.
B	1719.	1.05	-15.50	1579.	6.23	287.
B	2009.	1.05	-16.50	1333.	4.22	326.
C	1164.	1.10	-16.00	1971.	14.86	245.
C	1448.	1.05	-14.00	1797.	6.55	252.
C	1745.	1.00	-17.00	1749.	6.56	283.
N	1457.	1.10	-17.50	1737.	15.53	251.
N	1756.	1.05	-17.50	1596.	9.92	265.
N	2056.	0.95	-17.50	1634.	1.16	302.
O	1766.	1.05	-19.50	1650.	13.67	271.
O	2069.	1.00	-20.00	1523.	8.34	288.

Table VI-1 (continued) :

$Z_1$	$\langle P_1 \rangle$ (MeV/c)	$v_2^{\max}$ (cm/ns)	$\theta_2^{\max}$	$P_3$ (MeV/c)	$\theta_3$	$E_k$ (MeV)
<u><math>\theta_1 = -40^\circ</math></u>						
Li	801.	1.25	-9.00	1721.	5.26	212.
Li	1061.	1.25	-12.00	1570.	7.75	244.
Li	1336.	1.30	-15.00	1267.	13.62	291.
Be	833.	1.20	-11.50	1913.	8.64	217.
Be	1105.	1.20	-12.00	1697.	5.00	234.
Be	1380.	1.20	-17.00	1602.	11.51	272.
B	845.	1.25	-17.50	1974.	22.31	232.
B	1130.	1.20	-13.50	1712.	7.96	229.
B	1415.	1.15	-15.50	1685.	5.02	258.
B	1692.	1.15	-18.50	1536.	6.26	291.
C	1155.	1.25	-17.50	1682.	19.10	233.
C	1433.	1.20	-17.00	1556.	10.58	245.
C	1728.	1.10	-20.00	1705.	6.17	288.
N	1441.	1.25	-19.50	1506.	19.75	244.
N	1741.	1.15	-21.00	1576.	10.91	274.
O	1463.	1.25	-21.00	1560.	22.63	254.
O	1750.	1.20	-23.00	1515.	18.78	272.



Table VI-1 (continued) :

$Z_1$	$\langle P_1 \rangle$ (MeV/c)	$v_2^{\max}$ (cm/ns)	$\theta_2^{\max}$	$P_3$ (MeV/c)	$\theta_3$	$E_k$ (MeV)
<u><math>\theta_1 = 52.5^\circ</math></u>						
Li	777.	1.25	-9.50	1863.	2.87	220.
Li	1036.	1.30	-15.50	1677.	12.85	255.
Be	820.	1.25	-11.00	1862.	5.23	218.
Be	1083.	1.20	-14.00	1915.	4.17	250.
Be	1362.	1.25	-18.00	1675.	8.52	281.
B	848.	1.35	-15.00	1659.	18.59	216.
B	1109.	1.25	-14.00	1735.	5.30	235.
B	1393.	1.20	-18.00	1809.	5.40	273.
C	1136.	1.30	-16.50	1637.	13.01	234.
C	1415.	1.25	-18.00	1637.	7.23	258.
N	1154.	1.40	-20.00	1533.	28.50	241.
N	1421.	1.30	-20.00	1560.	14.93	255.
O	1445.	1.45	-23.00	1364.	36.01	261.
O	1731.	1.35	-21.00	1221.	13.77	261.

directed toward the fragment, as discussed in Section VI.A.2. At higher energies, the missing mass is directed between  $5^\circ$  and  $15^\circ$  from the beam direction.

#### **VI.B.4. Errors and uncertainties :**

In order to assess the sensitivity of the extracted quantities to uncertainties of the input parameters, three of the input parameters have been varied separately : the direction of the residue was varied by  $\pm 4^\circ$ , corresponding to the uncertainty in the most probable recoil angle; the velocity was varied by  $\pm 10\%$ , corresponding to the uncertainty in the most probable recoil velocity; the mass of the carbon ion was varied by  $\pm 2$  amu. The shaded regions in Figure VI-5 indicate the range of values of the calculated quantities which result from these variations. The direction of the missing momentum varies by from  $5^\circ$  to  $10^\circ$ , and the momentum transfer varies by  $\pm 0.05 P_0$ . These variations do not significantly affect the conclusions of this analysis.

#### **VI.B.5. Sequential decay :**

It is possible that the detected intermediate mass fragments are the decay products of highly excited primary fragments. The dependence of the position of the peak of the residue angular distribution on the fragment momenta indicates that contributions from such sequential decays are expected to be particularly large for fragment energies below the Coulomb barrier. In fact, the missing momenta for low energy fragments of  $Z=5-8$  indicate the preferential emission of matter to the

side of the beam axis on which the fragments are detected. Studies of small angle correlations between charged particles also support the existence of such a sequential decay process [POC85a] [POC85b] [POC85c]. This will be dealt with at greater length in Chapter VII.

In order to determine the effects of such a correlated emission on the kinematic analysis, the momenta of the undetected products of sequential decay may be excluded from the missing momentum,  $\vec{P}_3$ , by including them in the definition of  $\vec{P}_1$ , which is then interpreted as the momentum of the primary fragment prior to its particle decay. As a specific example of the effect of sequential decay on the total missing momentum, the undetected sequential decay products are assumed to be emitted in the decay of primary oxygen fragments into detected carbon nuclei, with the velocities of the decay products remaining the same as the velocities of the primary fragments.

The dashed curves in Figure VI-5 represent the kinematic analysis in this scenario. The sequential decay has a negligible effect on the sum kinetic energy,  $E_k$ , and the velocity,  $v_3$ , of the missing momentum. The direction of the missing momentum is pushed closer to the beam direction. The missing momentum along the beam direction is reduced by about  $0.1P_0$ , bringing the estimated momentum transfer more in line with the pre-equilibrium particle multiplicities and the systematics from inclusive studies of momentum transfer to fissile target nuclei [FAT85].

#### VI.C. Summary :

Studies of intermediate mass fragments and coincident target-like residues provide general information about the energy and momentum

balance in fragment producing reactions. In fact, they allow several conclusions about the fragment production mechanism. The velocity distributions of the heavy residues indicate that intermediate mass fragments are produced with low multiplicities from highly damped reactions. For the  $^{32}\text{S} + \text{Ag}$  reaction at  $E/A=22.5$  MeV, a total energy between 200 and 400 MeV is dissipated into internal degrees of freedom in the target-residue and primary intermediate mass fragment.

Significant particle emission occurs prior to full equilibration. More than 20% of the projectile momentum is carried away by particles emitted during the early non-equilibrium stages of the reactions. The mean velocity of these particles is directed close to the beam axis and is somewhat less than half of the beam velocity. This qualitative picture is consistent with the single particle inclusive and coincidence distributions of light particles and intermediate mass fragments.

Finally, the residue velocity distributions suggest that the portions of the energy spectra corresponding to emission at energies below the exit channel Coulomb barriers contain substantial contributions from the sequential decay of particle unstable primary fragments.

Thus, the number of candidates for the principal mechanism for intermediate mass fragment production can be reduced. One may conclude from both the measured fragment multiplicities and the angular distributions of the target residue that fragments are not produced in reactions with large fragment multiplicities. Peripheral or quasi-elastic collisions can be excluded as an important source of intermediate mass fragments at large angles because the observed energy losses are too large. The fragments do not primarily result from binary

emission processes after full momentum transfer to the compound system. This conclusion differs from the interpretations of recent results [MIT85] from  $^{84}\text{Kr} + ^{12}\text{C}$  reactions at  $E/A=35$  MeV which were supposed to proceed by complete fusion followed by binary fragment emission. For the present reactions, the peaks in the angular distributions of the recoiling residues never occur at the angles expected for such reactions. This general observation includes reactions producing fragments with masses comparable to the mass of the projectile. It is possible, however, that composite systems in some fraction of the reactions reach equilibrium without significant preequilibrium emission. Some recent studies indicate that this is possible, and that the detection of an intermediate mass fragment in the backward hemisphere is an excellent signature for such reactions [FAT86pc].

## Chapter VII

### Statistical Aspects of Fragment Emission

#### VII.A. Introduction :

In previous sections, the importance of dynamics in defining the character of the fragment production mechanism has been emphasized. In this section certain statistical aspects of intermediate mass fragment production will be discussed, specifically the emission of nuclei in particle-stable and unstable excited states. The inclusion of these states in calculations of fragment emission will influence the final distributions both through the increased number of final states available for intermediate mass fragment emission and through the sequential decay of particle-unstable nuclei.

A simple statistical formulation which includes excited states of nuclei is presented in Section VII.B. Using this schematic model, the observable effects of the emission of excited nuclei on the mass distributions, relative isotopic yields, and the relative population of excited states are discussed. A comparison of the model calculation with experimental findings will suggest that the emission of nuclei in their

excited states does have considerable impact on the final distributions of nuclei and nuclear states [FIE86p].

In section C, two distinct measurements of the  $^{32}\text{S} + \text{Ag}$  system at  $E/A=22.5$  MeV [XU87] will be compared to the calculations.

## VII.B. Statistical emission and the population of excited states :

### **VII.B.1. A schematic model :**

In order to investigate the general effect of the emission of excited nuclei, we will use a schematic calculation of statistical emission of charged particles from a compound nucleus. For simplicity, we assume that each available state,  $i$ , is initially populated with the weight,  $P_i$ , given by

$$P_i \propto P_0(A_i, Z_i) (2S_i + 1) \exp(-E_i/T) \quad , \quad (\text{VII-1})$$

where  $P_0(A_i, Z_i)$  denotes the population per spin degree of freedom of the ground state of a fragment of mass and charge numbers  $A_i$  and  $Z_i$ , respectively;  $S_i$  and  $E_i$  denote the spin and excitation energy of state  $i$ ;  $T$  is the emission temperature which characterizes the statistical population of states of a given nucleus. This temperature is not necessarily the same as the temperature which characterizes the energy spectra of emitted fragments. In order to evaluate the effect of the decay of particle-unstable states one has to specify the relative populations  $P_0(A_i, Z_i)$ . Because it is reasonably transparent, the parametrization [MAS81] used is

$$P_0(A_i, Z_i) \propto \exp ( -V_C/T + Q/T) , \quad (\text{VII-2})$$

where  $V_C$  is the Coulomb barrier for emission from a parent nucleus of mass and atomic numbers  $A_p$  and  $Z_p$ , and  $Q$  is the ground state  $Q$ -value:

$$V_C = e^2 Z_i \cdot (Z_p - Z_i) / [r_0 (A_i^{1/3} + (A_p - A_i)^{1/3})] , \quad (\text{VII-3})$$

$$Q = (B(A_p - A_i, Z_p - Z_i) + B_i) - B(A_p, Z_p) . \quad (\text{VII-4})$$

The radius parameter is  $r_0 = 1.2$  fm. The binding energies,  $B(A, Z)$ , of heavy nuclei are calculated from the Weizsäcker mass formula [MAR69]:

$$B(A, Z) = C_0 A - C_1 A^{2/3} - C_2 \frac{Z^2}{A^{1/3}} - C_3 \frac{(A - 2Z)^2}{A} , \quad (\text{VII-5})$$

where  $C_0 = 14.1$  MeV,  $C_1 = 13.0$  MeV,  $C_2 = .595$  MeV, and  $C_3 = 19.0$  MeV. For the emitted light fragments we use the measured binding energies,  $B_i$ .

We restrict our discussion to primary fragments of mass numbers  $A_i \leq 20$ . For these nuclei, all tabulated [AJZ86] states with widths smaller than 3 MeV are included in the calculations. The exclusion of broader states was motivated by the necessity that a state live long enough for the nucleus to separate itself from the parent system [FAI82].

Both particle-stable and unstable states are treated explicitly in this calculation. Recent experimental results have demonstrated that nuclei are, in fact, emitted in their excited states. Figure VII-1 depicts the correlation function between two pairs of particles, the  $\alpha$ -



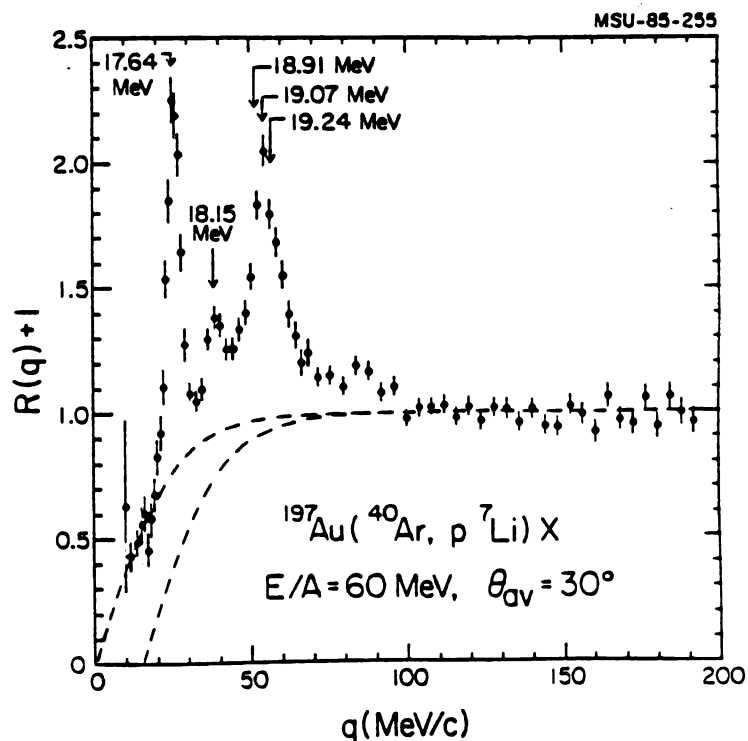
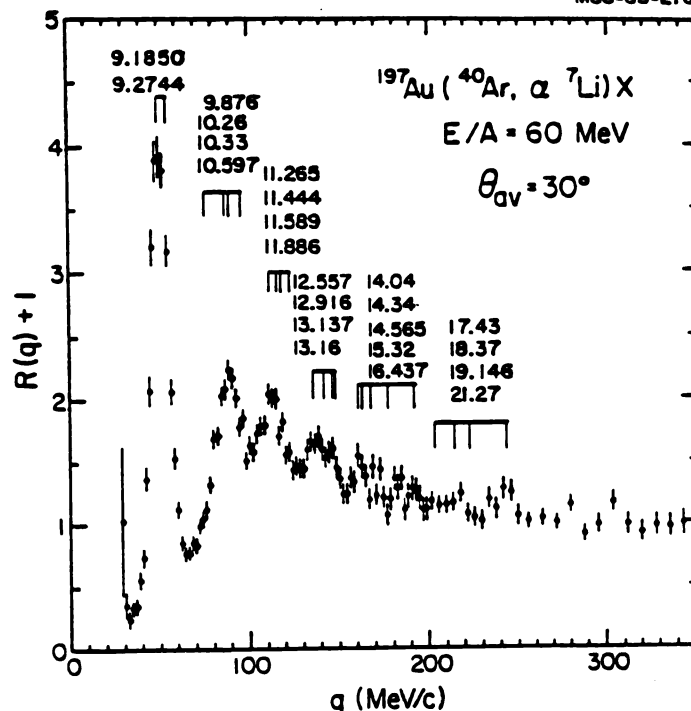


Figure VII-1 : Correlations between protons and  $^7\text{Li}$  nuclei (bottom) and between alpha particles and  $^7\text{Li}$  nuclei (top) measured in  $^{40}\text{Ar} + \text{Au}$  reactions at  $E/A=60$  MeV as functions of the relative momenta between the two particles. Peaks in the correlations which correspond to states in  $^{11}\text{B}$  and  $^8\text{Be}$  are indicated in the top and bottom figures, respectively.

$^7\text{Li}$  system (top) and the  $p$ - $^7\text{Li}$  system (bottom), as a function of the relative momentum between the two particles [POC86p]. The resonant structures correspond to the excited states of  $^{11}\text{B}$  and  $^8\text{Be}$  nuclei.

In our model calculation, particle unstable states are assumed to decay to available final states through the emission of light particles ( $n, p, d, t, ^3\text{He}$ , and  $\alpha$  particles). The relative rates to the final states are determined by the statistical model [HAU52] [STO84]

$$r(\epsilon, J, j, s) \propto \sum_{S=|j-s|}^{j+s} \sum_{\ell=|J-S|}^{J+S} T_{\ell}(\epsilon) \quad , \quad (\text{VII-6})$$

where  $s$  is the spin of the evaporated particle,  $j$  is the spin of the daughter nucleus,  $S$  is the channel spin,  $J$  is the spin of the parent nucleus,  $\ell$  is the orbital angular momentum of the emitted particle, and  $\epsilon$  is the decay energy.  $T_{\ell}$  is the parametrized transmission coefficient for the  $\ell^{\text{th}}$  partial wave. (See Appendix D for details of the decay calculations.)

### VII.B.2. Mass distributions :

Figure VII-2 shows the primary and final mass distributions for emission calculated according to Eqs. VII-1-6 from a moderately excited xenon nucleus ( $A_p=131$ ,  $Z_p=54$ , and  $T=5$  MeV). The histogram represents the total primary mass distribution including both bound and unbound states. The dark and light shaded regions represent the contributions from ground and excited particle-stable states, respectively. It is apparent from the figure that at this temperature the contribution to the

MSU-86-292

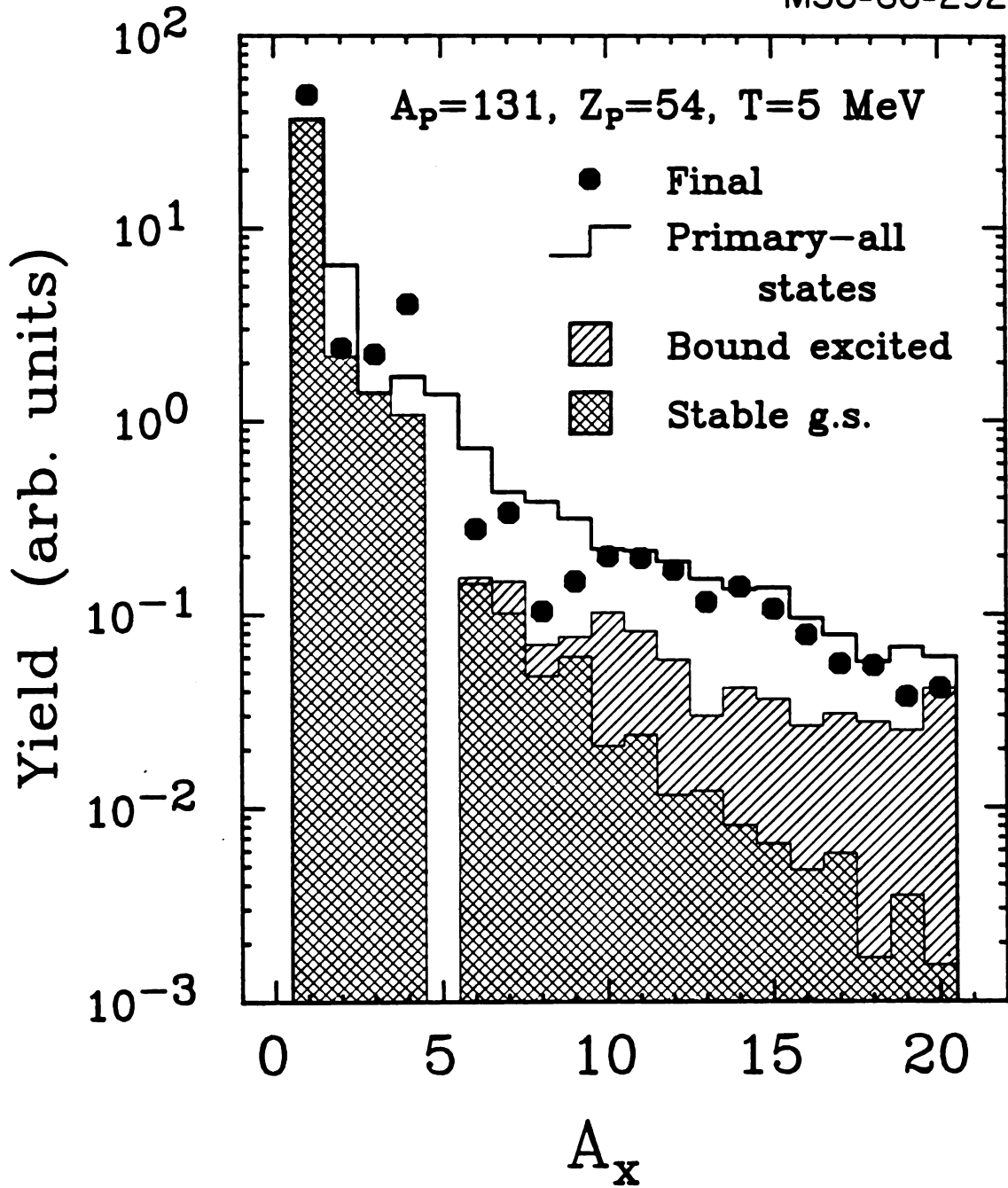


Figure VII-2 : Mass distributions calculated from Eq. VII-1 for emission from a Xe nucleus at  $T=5 \text{ MeV}$ . Histogram : primary distribution; solid points : final distribution; dark and light shaded regions show contributions from bound ground and excited states, respectively.

intermediate mass fragment yield from emission of particle-stable states is substantial and is dominant for heavier fragments. The contribution from particle-unstable states is roughly half of the total yield. The primary distributions are relatively smooth with little structure resulting from variations in level density and binding energies. The solid points in the figure show the final mass distribution after the decay of particle-unstable states. These decays enhance the light particle yields, doubling the  ${}^4\text{He}$  yield. The relative yields for the light particles have been used to infer the entropy generated in nuclear reactions [BERT81] [DOS85]. The contribution from sequential decay alters the relative yields for the light particles, and therefore must influence such interpretations of the light particle cross sections [STO83] [HAH86]. The yields of heavier fragments,  $A > 4$ , are depleted by sequential decays. However, they generally remain significantly larger than the primary yields of bound nuclei. Secondary decay products constitute approximately half of the resultant fragment yield.

Figure VII-3 compares the calculated final mass distribution (histogram) with the mass distribution measured for proton-induced reactions on xenon at  $E_p = 80\text{-}350$  GeV [HIR84] (solid points). (The calculated mass distribution includes only nuclei for which cross sections were published in [HIR84], and differs from the final distribution in Figure VII-2 primarily by the exclusion of  ${}^6\text{He}$ . The other nuclei not included are  ${}^8\text{He}$ ,  ${}^{14}\text{Be}$ ,  ${}^{8,17}\text{B}$ ,  ${}^{9,10,18-20}\text{C}$ ,  ${}^{12}\text{N}$ ,  ${}^{13,14}\text{O}$ , and  ${}^{17,18}\text{Ne}$ .) This particular mass distribution has been noted previously [FIN82] [HIR84] for its close approximation to a power law dependence (see section I.A). However, a power law dependence determined by the distribution for heavier fragments significantly over-

MSU-86-291

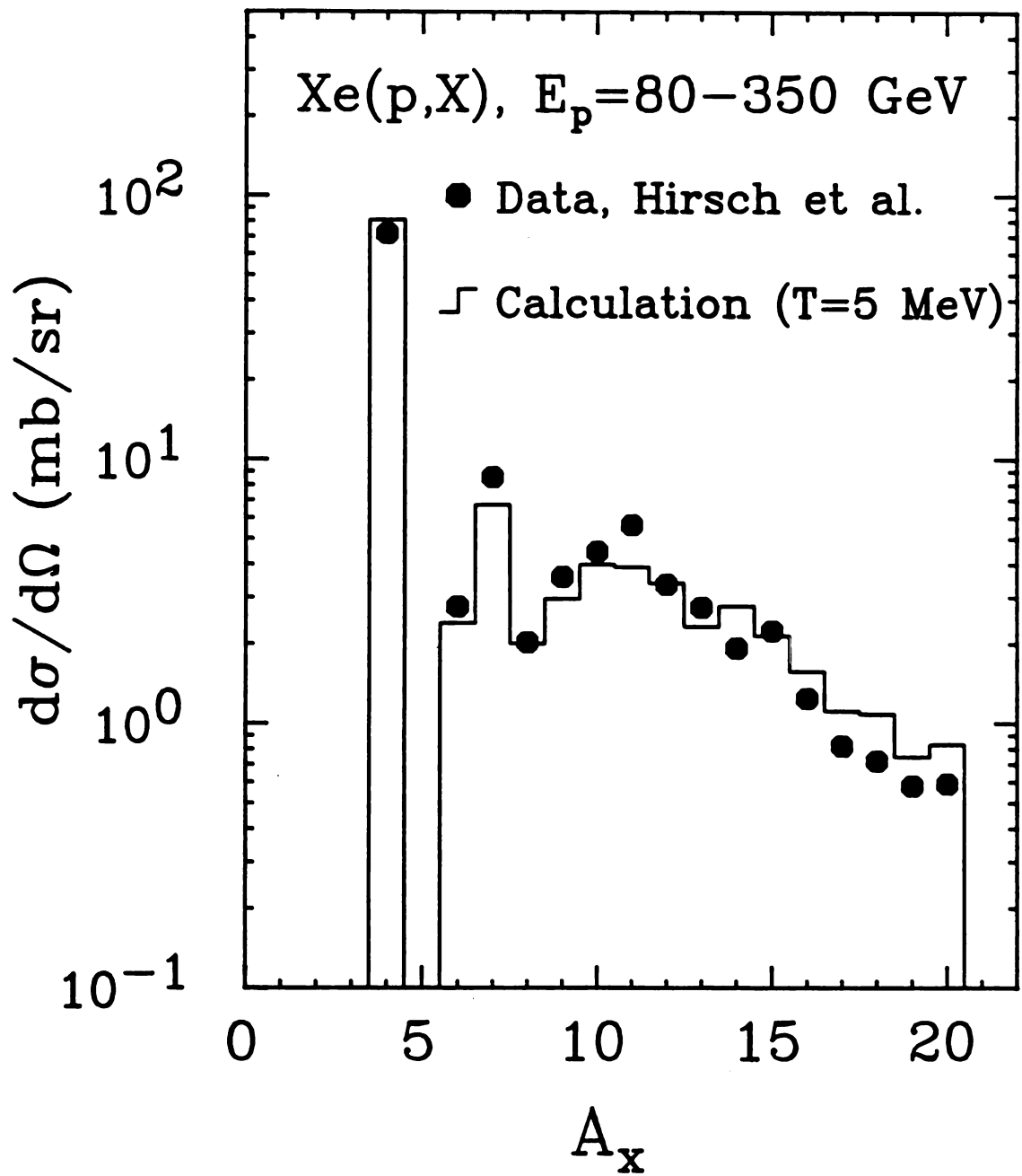


Figure VII-3 : Mass distribution from proton induced reactions on Xe (solid points) and final distribution predicted from Eq. VII-1 (histogram).

estimates the observed cross section in the region from  $A=6$  to 12. The failure of the thermal liquid-drop calculations [HIR84] [MAC85b] to predict this structure was attributed to the inadequacy of the Weizsäcker mass formula for light nuclei. However, calculations of ground state yields which use correct masses (dark shaded area in Figure VII-2) do not reproduce the data either. A similar, though less distinct, structure was produced in a statistical calculation [RAN81] which included only particle-stable states, though it became evident only at high intrinsic excitation energies of about 40 MeV/nucleon. The authors of that work estimated that the inclusion of unstable states would wash out the structure. Alternatively, the detailed structure of the mass distributions has been attributed to in-medium effects, specifically to Pauli blocking during thermal freeze-out [ROE83] [ROE85].

The present simple calculation reproduces the average slope, as well as the characteristic structures in the experimental mass distribution, using a temperature of  $T=5$  MeV. The detailed structure of the mass distributions could, therefore, be the result of the emission and decay of particle-unbound excited nuclei. This phenomenon is independent of the actual emission mechanism so long as there are significant populations of the particle-unstable states.

From the form of Eq. VII-1 it is obvious that the yields of heavier fragments increase with increasing temperature, both because of the behavior of  $P_0(A_1, Z_1)$  and because the excited state yields increase with temperature. Figure VII-4 illustrates this temperature dependence of the mass distribution and the contribution from excited states from emission from the  $A=131$ ,  $Z=54$  system at temperatures,  $T=3, 5, 7$ , and 10 MeV. The

MSU-86-426

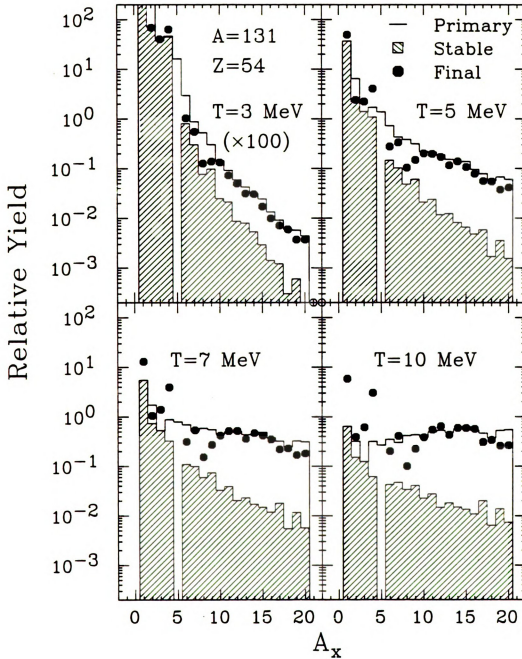


Figure VII-4 : Mass distributions as a function of the emission temperature for emission from a nucleus,  $A=131$  and  $Z=54$ . The primary (histogram), final (solid points), and stable ground state (shaded region) distributions are shown for emission temperatures of  $T=3, 5, 7$ , and  $10$  MeV.

total primary mass distributions are indicated by the histograms, the mass distributions of nuclei emitted in their ground states are shown by the shaded regions, and the final distributions are shown by the solid points. All mass distributions become less steep at higher temperatures. As the temperature increases, contributions from the primary population of stable ground states become increasingly inconsequential. At the same time the effects of sequential decay on the fragment yields (for instance, the light particle ratios) increases. The sequential decay of the particle-unstable states significantly alters the mass distribution, specifically in the mass region,  $A=6-11$ .

It is important to note that the temperature dependence of this parametrization does not agree with the behavior of more complete compound nucleus calculations. These calculations predict that at high temperatures the mass yield curve should become steeper with increasing temperature. Thus, while the present parametrization predicts that the effects of sequential decay become more important with increasing temperature, they will in reality be moderated by more steeply falling mass distributions. ( See Chapter VIII. )

### **VII.B.3. Isotopic yields :**

Relative isotopic yields from statistical calculations are also affected by the inclusion of excited nuclear states. Figure VII-5 shows the relative yields of nitrogen isotopes for the calculation shown in Figures VII-2 and VII-3. The distributions are normalized so that the yield of the most abundant isotope is one. The squares represent the relative yields corresponding to the primary population of the stable



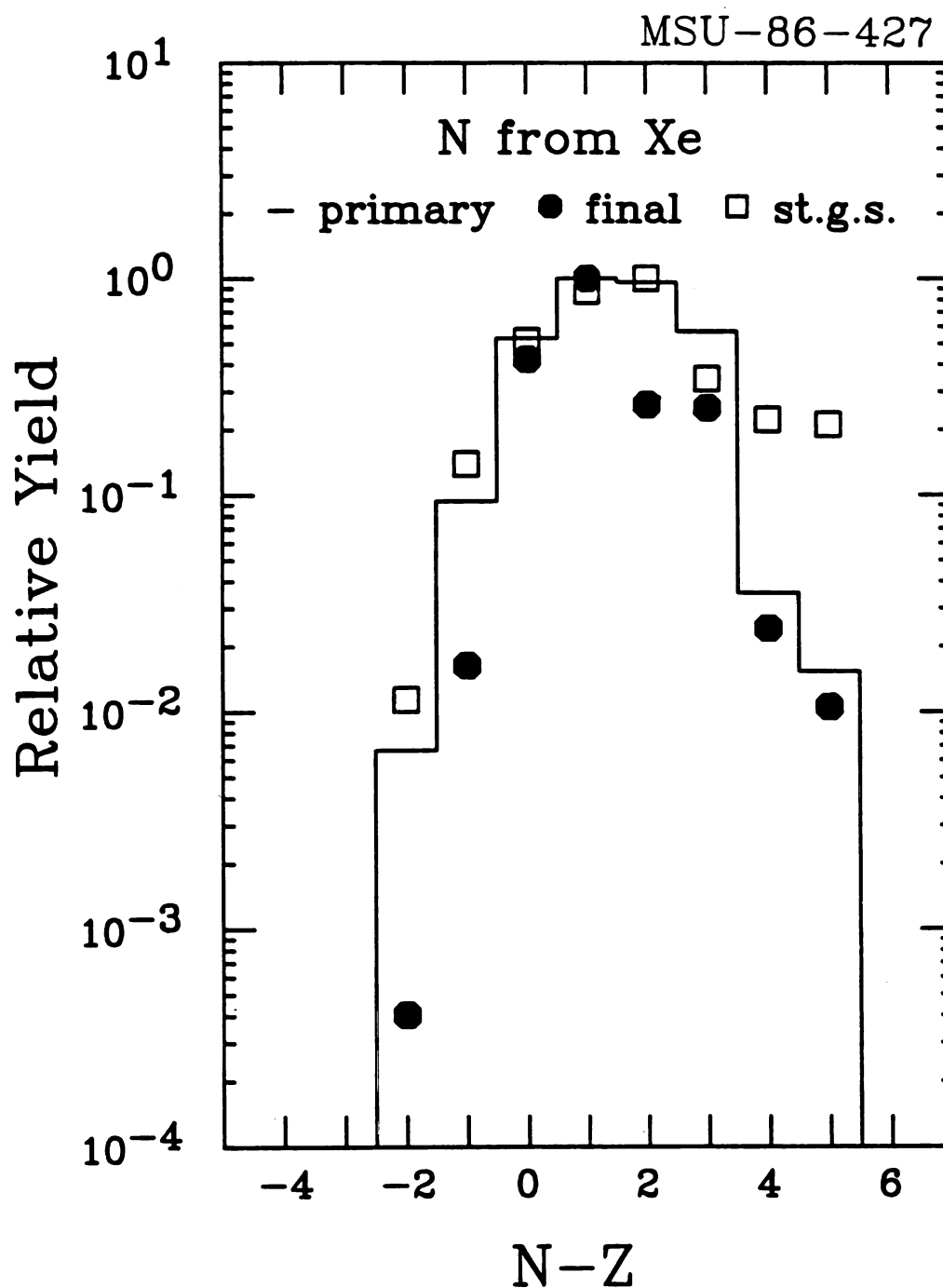


Figure VII-5 : The calculated isotopic distributions for N nuclei emitted from a nucleus,  $A=131$  and  $Z=54$ , at  $T=5$  MeV. The distribution of stable ground states is shown as squares. The primary and final distributions from calculations which include excited states are shown as the histogram and solid points, respectively.

ground states of nitrogen isotopes. The isotopic distribution of primary fragments of all states is shown by the histogram. The larger number of available states around the valley of stability produces a distribution which is narrower than the primary isotopic distributions of the ground states. The sequential decay of particle-unstable states results in a distribution (solid points) which is even more narrowly distributed about the valley of  $\beta$  stability.

Figure VII-6 compares isotopic distributions (histogram) calculated at  $T=5$  MeV with the measured distributions (solid points) for elements,  $Z=3-8$ , from proton-induced reactions on xenon [HIR84]. While the calculated isotopic distributions are slightly broader than the measured distributions, the general behavior of the data is described by the statistical calculation.

The effect of sequential decay on isotopic distributions has been pointed out previously with respect to distributions from projectile fragmentation [VIY79] [MORR79] and deeply inelastic scattering [BAR78] [BRA78] [LOC82]. It was observed that the decay of proton- and neutron-rich primary fragments towards the valley of  $\beta$  stability destroyed significant differences between proposed primary distributions. This can be seen in the calculated temperature and isospin dependence of the isotopic distributions.

The temperature dependence of the isotopic distribution results, in this model, from the competition between two effects. As the temperature increases the primary distribution becomes broader. Figure VII-7 shows the primary isotopic distributions for nitrogen nuclei emitted at temperatures of  $T(\text{MeV})=1$  (solid diamonds), 3 (open squares), 5 (stars), and 10 (solid circles). The distribution becomes broader with increasing

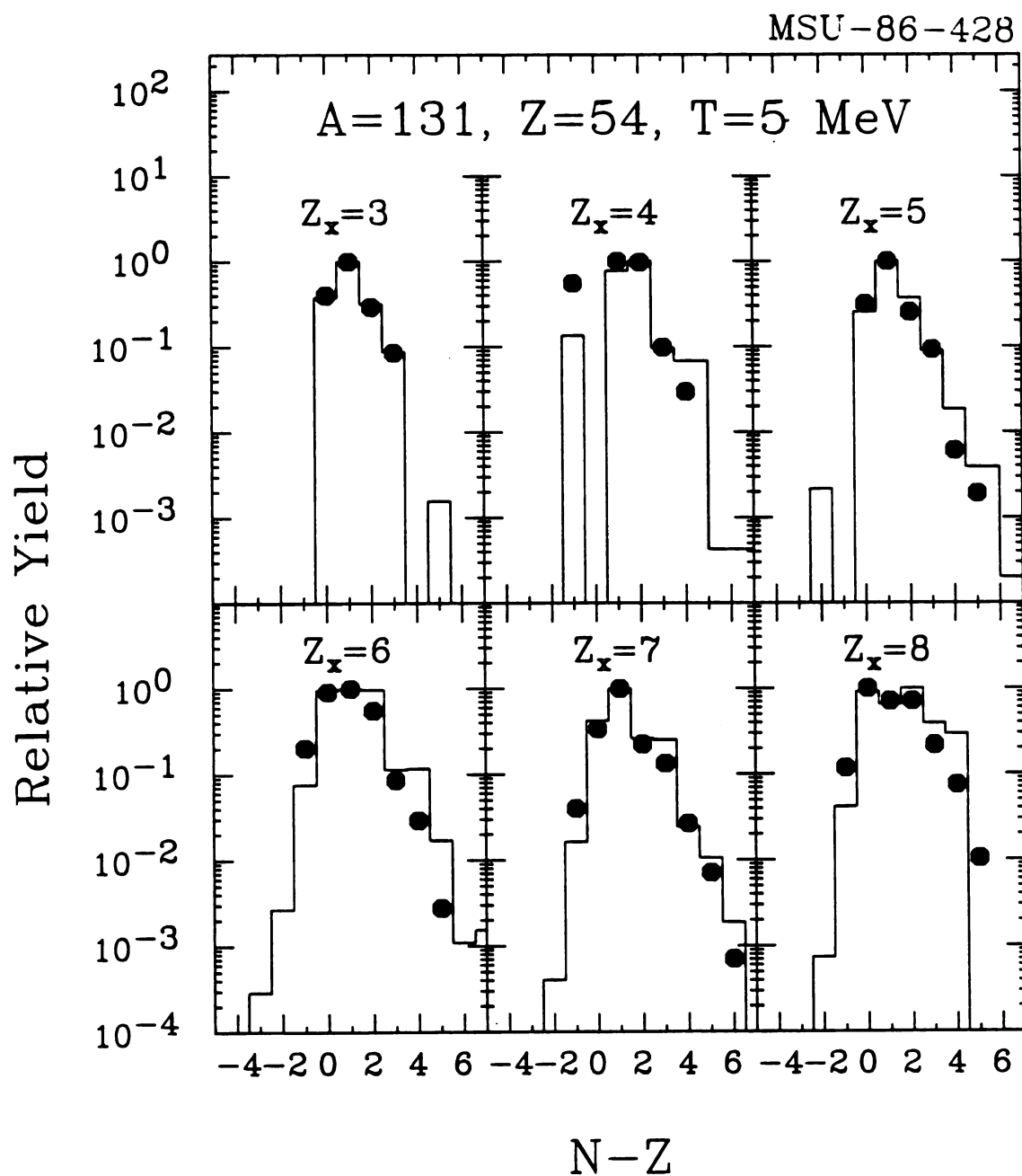


Figure VII-6 : The calculated isotopic distributions of  $Z_x=3-8$  from a nucleus,  $A=131$ ,  $Z=54$  and  $T=5 \text{ MeV}$  are shown as histograms. The solid points represent the measured isotopic ratios for  $p+Xe$  reactions [HIR84].

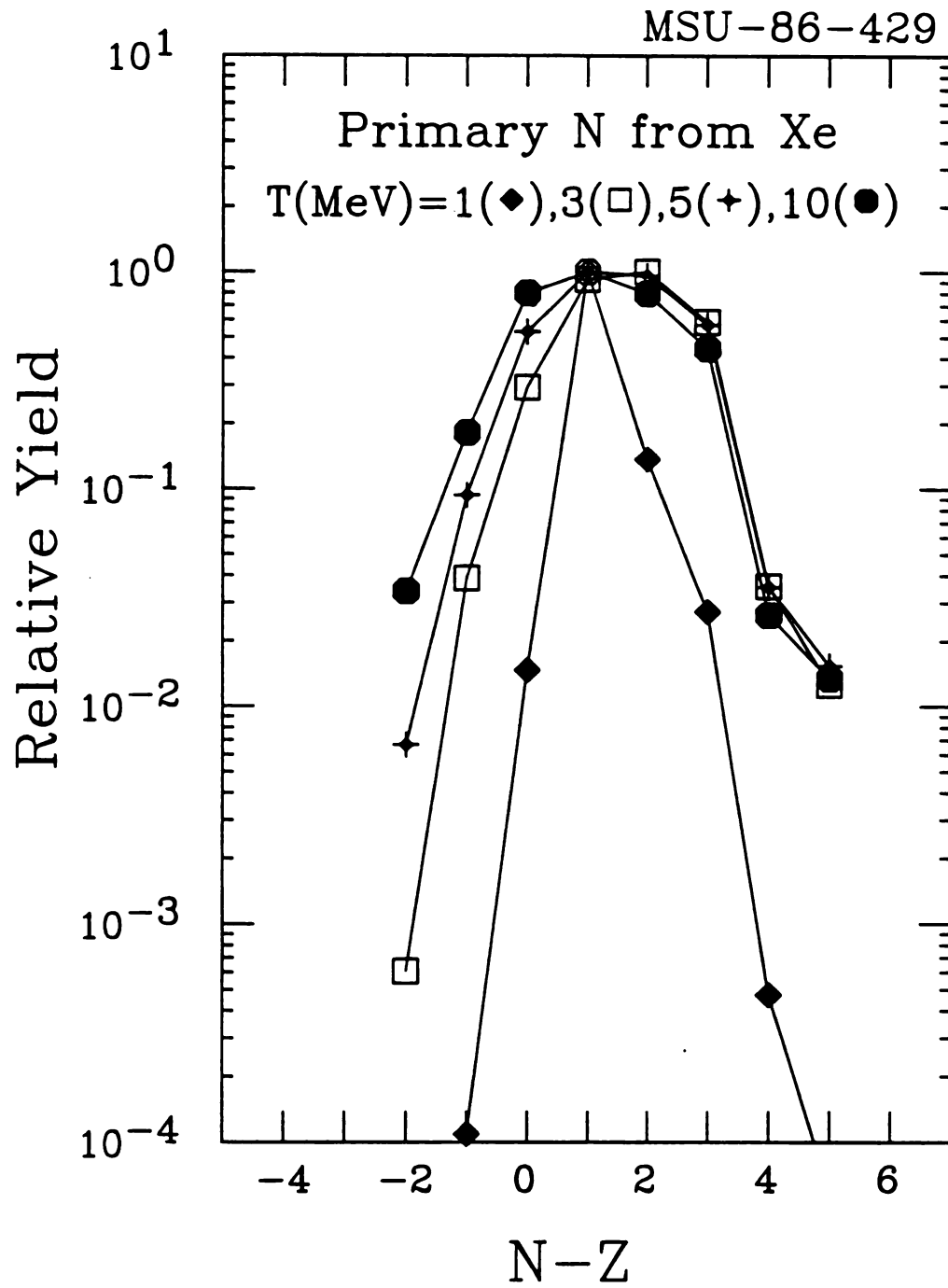


Figure VII-7 : The calculated primary isotopic distributions for N nuclei emitted from a nucleus,  $A=131$  and  $Z=54$ , at temperatures,  $T(\text{MeV})=1$  (solid diamonds), 3 (open squares), 5 (star) and 10 (solid circle).

temperature, and the centroid shifts slightly towards the proton-rich isotopes.

The primary distribution at higher temperatures is principally the result of the population of particle-unstable states. However, the decays of these particle-unstable nuclei strongly influence the final distributions. Neutron-rich nitrogen isotopes decay towards stable isotopes, other unstable nitrogen nuclei decay to other elements, and heavier elements decay towards stable nitrogen nuclei. This decay of the unstable nuclei narrows the final distributions.

The final isotopic distributions for nitrogen at the four temperatures are displayed in Figure VII-8. At low temperatures ( $T=1$  MeV) the distribution, dominated by the emission of nuclei in their ground states, is very narrow and is nearly identical to the primary distribution. As the temperature increases ( $T=3$  MeV), the distribution becomes broader. However, the width of the distribution ceases to change significantly as the temperature increases further ( $T=5,10$  MeV). This follows from the temperature independence of the particle branching ratios. Once the particle unstable states become the dominant contributions to the yields, increases in their populations relative to lower lying states do not alter their patterns of decay to lighter nuclei and thus the final distributions. Note, again, that the behavior of  $P_0(A_i, Z_i)$  at high temperatures is different from what is expected for real nuclei, so that the effect of sequential decay at  $T=10$  MeV may be somewhat smaller than calculated.

This saturation behavior has also been seen in the energy loss dependence of the isobaric charge distributions of projectile-like

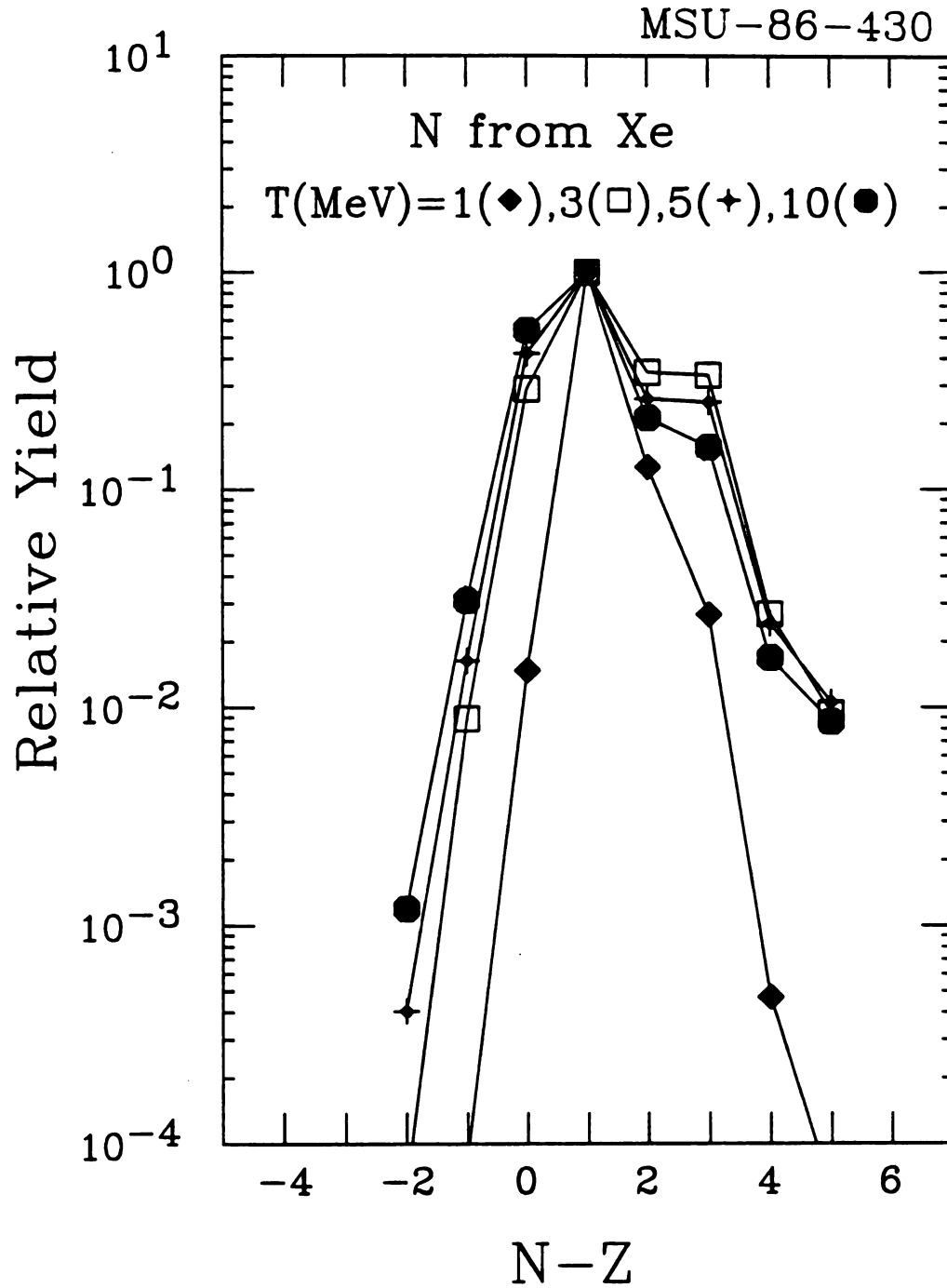


Figure VII-8 : The calculated final isotopic distributions for N nuclei emitted from a nucleus,  $A=131$  and  $Z=54$ , at temperatures,  $T(\text{MeV})=1$  (solid diamonds), 3 (open squares), 5 (star) and 10 (solid circle).

fragments from deeply inelastic collisions [MIG80] [LOC82]. The energy loss of the projectile-like fragment is directly related its excitation energy. At low energy losses the widths of the isobaric charge distributions increase with increasing energy loss. The widths cease to increase, however, for energy losses above a modest value of 30-50 MeV [MIG80]. In projectile fragmentation reactions, the isotopic distributions do not change significantly between  $E/A=20$  MeV and 2 GeV [BUE76] [GEL78]. In each of these cases, sequential decays may render the initial state of the primary system irrelevant to the final distributions.

Figure VII-9 shows the isotopic distributions for the stable ground states of nitrogen nuclei from emitting nuclei of charge,  $Z=54$ , and  $A=120$  (open diamonds), 130 (solid squares), and 140 (stars) at a temperature of  $T=5$  MeV. The distributions demonstrate a significant sensitivity to the neutron-to-proton ratio of the emitting nucleus. However, previous arguments have indicated that the final isotopic distributions are strongly influenced by sequential decay. Figure VII-10 shows the predicted final isotopic distributions when unstable states are included. The distributions are narrower than the primary stable ground state populations and exhibit only a modest sensitivity to the neutron-to-proton ratio of the emitting nucleus.

#### **VII.B.4. Excited state populations :**

The mass and isotopic distributions are sensitive to the total population of unstable states, rather than the population of each state. It is, therefore, not possible to conclude from the analysis of the

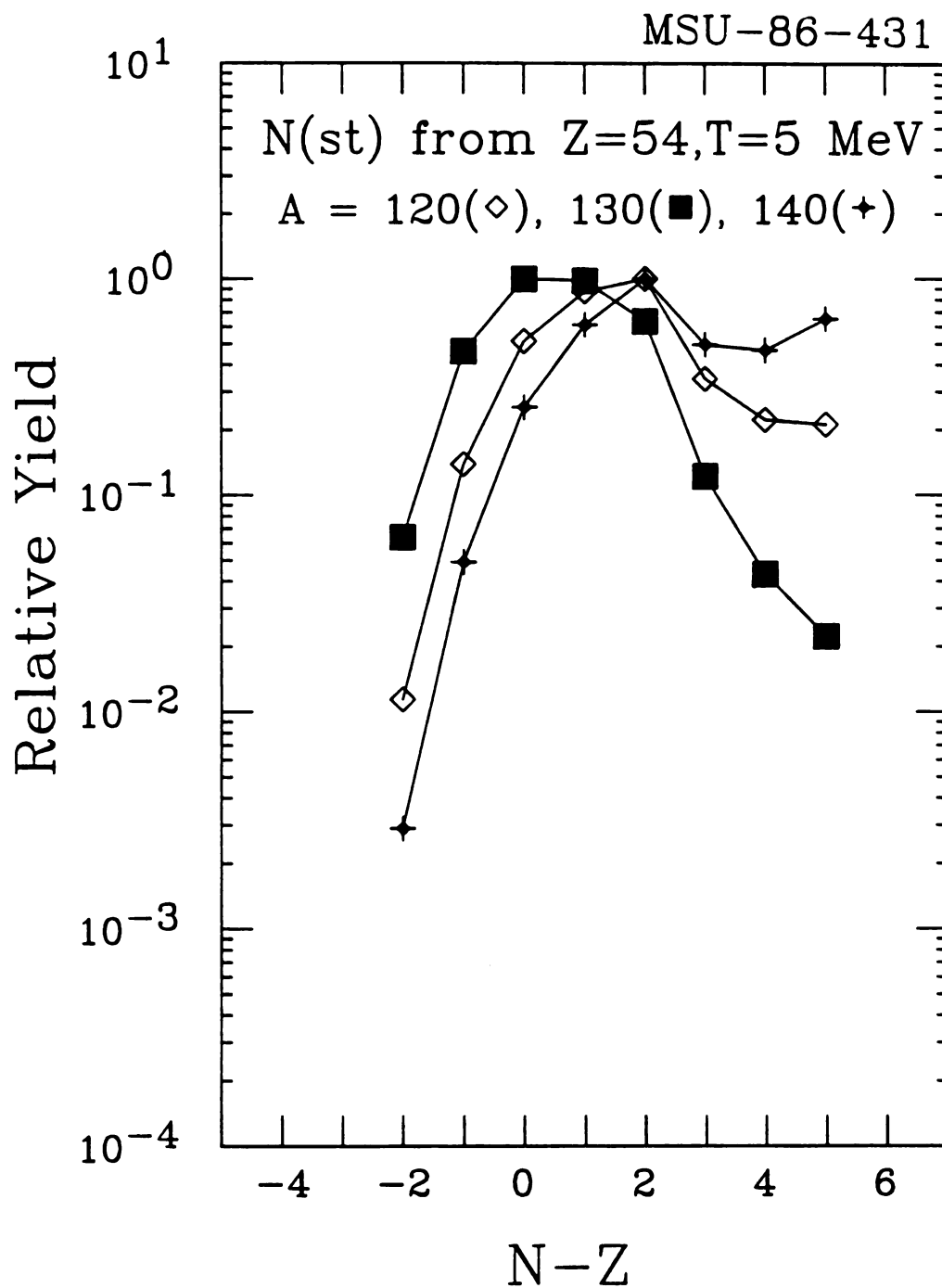


Figure VII-9 : The calculated primary isotopic distributions for the stable ground states of nitrogen nuclei emitted from a nucleus of charge,  $Z=54$ , and mass,  $A = 120$  (open diamonds),  $130$  (solid squares), and  $140$  (stars), at a temperature of  $T=5$  MeV.



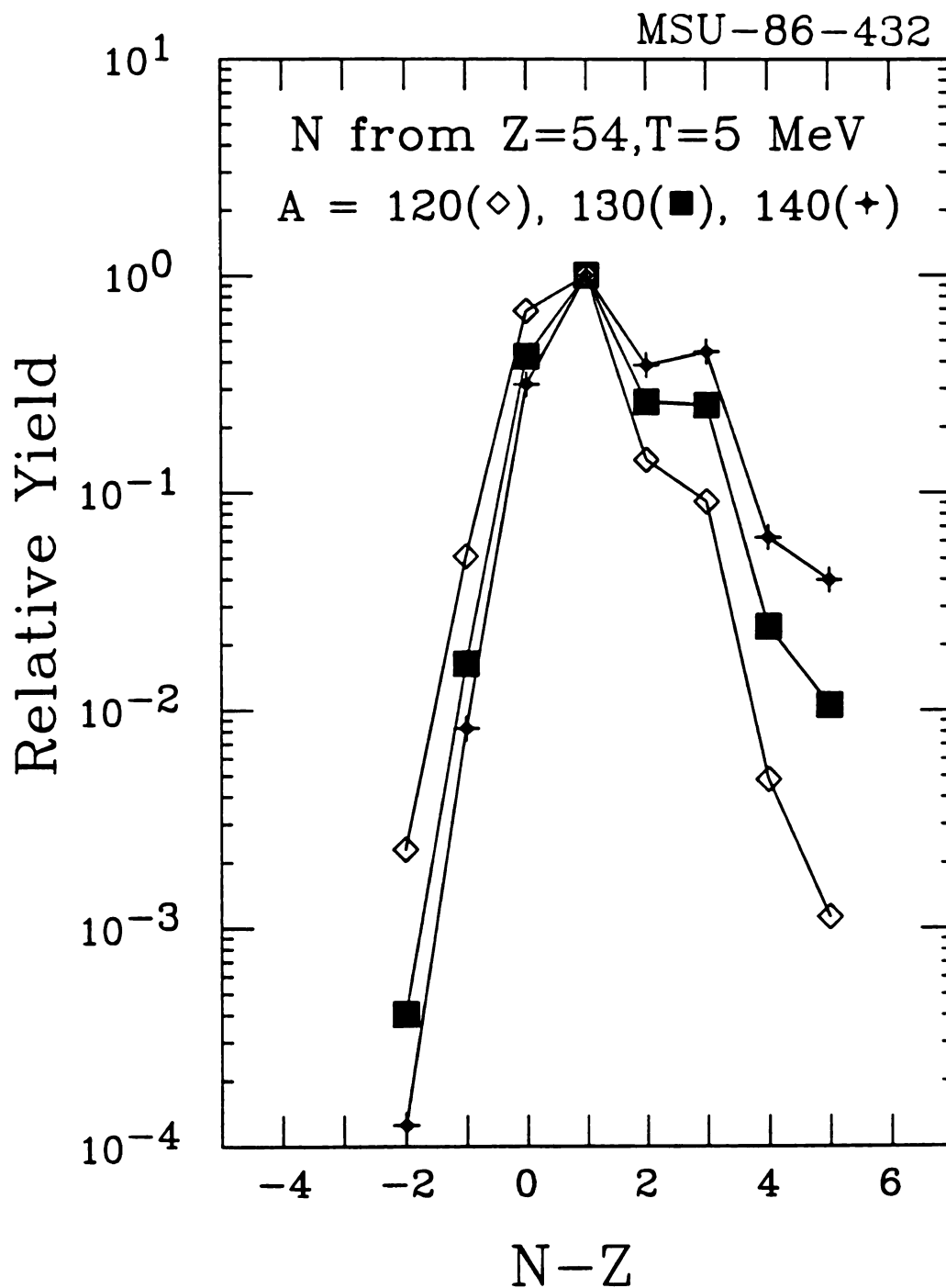


Figure VII-10: The calculated final isotopic distributions of nitrogen nuclei emitted from a nucleus of charge,  $Z=54$ , and mass,  $A = 120$  (open diamonds),  $130$  (solid squares), and  $140$  (stars), at a temperature of  $T=5$  MeV.

previous sections that nuclear excited states are populated precisely according to equilibrium thermodynamical probabilities. Direct measurements of the populations of excited nuclear states would constitute more definitive tests of statistical theories of fragmentation distributions. In thermal models, the ratio of the primary populations of two narrow states in a given nucleus is given by

$$R_p = \frac{P_i}{P_j} = R_\infty \exp(-\Delta E/T) = \frac{(2s_i+1)}{(2s_j+1)} \exp(-\Delta E/T) , \quad (\text{VII-7})$$

where  $\Delta E$  is the difference in the level energies and  $R_\infty$  is the high temperature limit. This expression was used to extract the effective emission temperatures from the measured relative populations of excited states [MORR84] [MORR85] [POC85a] [POC85c] [CHI86a] [POC86p]. The populations of low lying particle-stable levels relative to the respective ground states were interpreted [MORR84] [MORR85] in terms of unexpectedly low emission temperatures,  $T < 1$  MeV, and non-equilibrium primary populations. Measurements of populations of particle-unstable levels [POC85a] [POC85c] [CHI86a] indicated higher average emission temperatures of about 5 MeV. It has been suggested [POC85a] [CHI86a] [POC86p] that sequential decay is responsible for discrepancies between these measurements. Furthermore, mean temperatures extracted from unstable levels are not significantly different for 490 MeV  $^{14}\text{N}$ -induced and 2400 MeV  $^{40}\text{Ar}$ -induced reactions on  $^{197}\text{Au}$ , which suggests that excited state populations are insensitive to excitation energy; the sequential decay of unstable nuclei may also be origin of this property.

In order to assess the effects of secondary decays on the relative populations of states, we have calculated the primary and final population ratios,  $R_p$ , for several previously analyzed [POC85a] [POC85c] [CHI86a] [POC86p] particle-unbound levels in  $^4\text{He}$ ,  $^5\text{Li}$ ,  $^6\text{Li}$ , and  $^8\text{Be}$  nuclei. The dotted curves in Figure VII-11 show the temperature dependences of the primary population ratios as given by Eq. VII-7. The solid curves indicate the final population ratios when one includes the sequential decays of excited primary fragments populated according to Eq. VII-1. At low emission temperatures,  $T \leq 1$  MeV, few unbound states are populated; the primary and final population ratios are equivalent, and Eq. VII-7 can be used to determine emission temperatures. At higher temperatures, however, the final populations do not follow the thermal relation of Eq. VII-7. Instead, they reflect the feeding from higher lying levels. None of the population ratios reaches the saturation values expected from the simple relation of Eq. VII-7 ( $R/R_\infty = 1$ ). The calculations corroborate the qualitative arguments given in [POC85a] that Eq. VII-7 can only be used to determine emission temperatures when  $\Delta E/T \ll 1$ . However, even in such cases problems can arise; see, for example, the predicted strong perturbation of the ratio of the 3.04 and 17.6 MeV levels in  $^8\text{Be}$ . Of the six examples shown in Figure VII-11, the  $^5\text{Li}$  population ratio is the only case which is predicted to be relatively unperturbed by secondary decays for temperatures up to  $T \leq 10$  MeV.

The effects of sequential decay are influenced by two aspects of the primary distribution: the relative populations of excited states for each nucleus and the relative populations of different nuclei. When the populations of the excited states are small, then the influence of

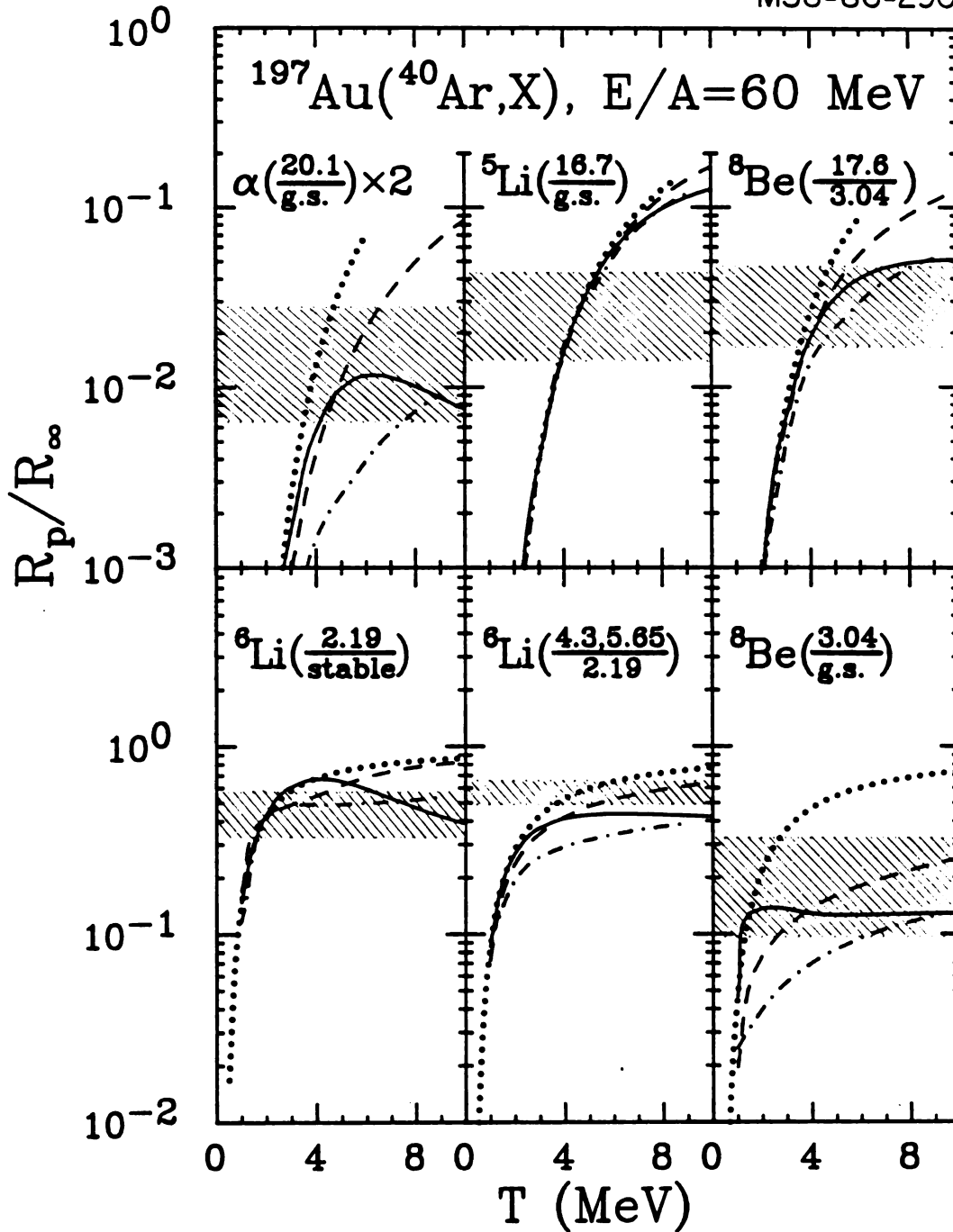


Figure VII-11 : Temperature dependence of population ratios,  $R_p/R_\infty$ , for specific states in  ${}^4\text{He}$ ,  ${}^5\text{Li}$ ,  ${}^6\text{Li}$ ,  ${}^8\text{Be}$  nuclei. Ratios measured [POC86p] for the  ${}^{40}\text{Ar}+{}^{197}\text{Au}$  reaction at  $E/A = 60$  MeV are shown by hatched regions. Dotted curves : temperature dependence of primary population ratios; solid curves : final ratios predicted from Eq. VII-1; dashed and dashed-dotted curves : final ratios predicted by quantum statistical calculations for densities of  $\rho/\rho_0 = .05$  and  $.9$ , respectively.

sequential decay will be small; when they are large, then the influence will be large. The relative populations of nuclei determine the balance between the decay of states in a given nucleus and feeding from neighboring nuclei. For steeply falling primary mass distributions, the population ratios will be less modified by sequential decay processes than for flat primary mass distributions, because the populations of heavier nuclei cannot significantly influence the larger primary yields of the lighter nuclei.

Mass distributions calculated from Eq. VII-1 become flatter at higher temperatures, as demonstrated in Figure VII-4. This means the relative contributions from heavier nuclei also increase. In fact, at high temperatures,  $T \approx 10$  MeV, the distributions should become steeper with increasing temperature. In order to assess the differences which exist for different statistical distributions of primary fragments, we also show results of quantum statistical calculations [STO83] [JAC83] [HAH86] which are described in Appendix E. The quantum statistical model describes the mass distribution of fragments in infinite nuclear matter which is in thermal and chemical equilibrium at a fixed temperature, density, and isospin. The long range Coulomb interaction, which has a significant effect on the mass distribution in Eq. VII-1, is neglected in the quantum statistical model. The mass distributions become steeper with increasing temperature and with decreasing breakup density,  $\rho$ . The dashed and dashed-dotted curves in Figure VII-11 show final population ratios predicted for breakup densities of  $\rho/\rho_0 = 0.05$  and  $0.9$ , respectively, where  $\rho_0$  is the ground state nuclear matter density. The detailed behavior of these calculations differ somewhat from the

previous calculations, but the general conclusions concerning the effect of excited state emission remain valid.

The shaded areas in Figure VII-11 give the relative populations of states measured [POC86p] for  $^{40}\text{Ar}$  induced reactions on  $^{197}\text{Au}$  at  $E/A=60$  MeV. The measurements are below the values for saturation predicted in Eq. VII-6. Using this relation, the emission temperatures for the resonances are approximately 4 MeV and less than 5 MeV, except for the ratios of the excited states to ground states, which indicate lower temperatures. The calculations indicate that population ratios cannot be used to determine temperatures above 5 MeV, with the possible exception of the  $^5\text{Li}$  population ratio.

Further specification of the primary distribution is possible only with additional constraints provided by mass, charge, and isotopic distributions. A comprehensive comparison of the  $^{40}\text{Ar} + ^{197}\text{Au}$  system with the quantum statistical calculations [POC86p] results in a best fit of the mass and excited state distributions with a temperature,  $T \approx 5.5$  MeV, and a density,  $\rho/\rho_0 = .05$ . However, considerable uncertainties remain concerning the properties and decay branching ratios of the available states.

#### VII.C. Comparison with $^{32}\text{S} + \text{Ag}$ data :

In this section the relative isotopic yields and the relative populations of excited and ground states of intermediate mass fragments from the  $^{32}\text{S} + \text{Ag}$  system at an incident energy of  $E/A=22.5$  MeV [XU86p] are presented and discussed in terms of the schematic statistical calculation introduced above.

### VII.C.1. Isotopic ratios :

In Figures VII-12, VII-13, and VII-14, the measured relative isotopic distributions for elements,  $Z_x=3-8$ , from  $^{32}\text{S}$  induced reactions on Ag at  $E/A=22.5$  MeV are shown as solid points. They are compared to calculations, shown as histograms, for emission according to Eq. VII-1. These are calculated for a system of  $A=130$  and  $Z=58$ , corresponding to the  $^{32}\text{S} + \text{Ag}$  system less non-equilibrium light particles, at three temperatures. The distribution calculated at a temperature,  $T=2$  MeV, is shown in Figure VII-12. The calculations predict distributions which are evidently narrower than the experimental distributions.

Figure VII-13 shows the distributions at  $T=4$  MeV. At this temperature, the experimental and calculated distributions are very similar. The solid curves in the figure are the same as in Figure III-13, and are determined according to Eq. III-5 by a Boltzman factor with the separation energies and a temperature of  $T=3.8$  MeV. The inclusion of the excited states improves the general agreement with the data, notably with  $^7\text{Li}$ ,  $^{13}\text{B}$ , and  $^{13}\text{N}$ .

As was pointed out in previous sections, the isotopic distributions become less sensitive to temperature changes above a few MeV. Figure VII-14 shows the calculations for  $T=10$  MeV. The differences between isotopic distributions from the  $T=4$  and  $T=10$  MeV calculations are insignificant. Thus while the calculations discriminate against emission temperatures significantly lower than 4 MeV, they do not rule out somewhat higher temperatures.

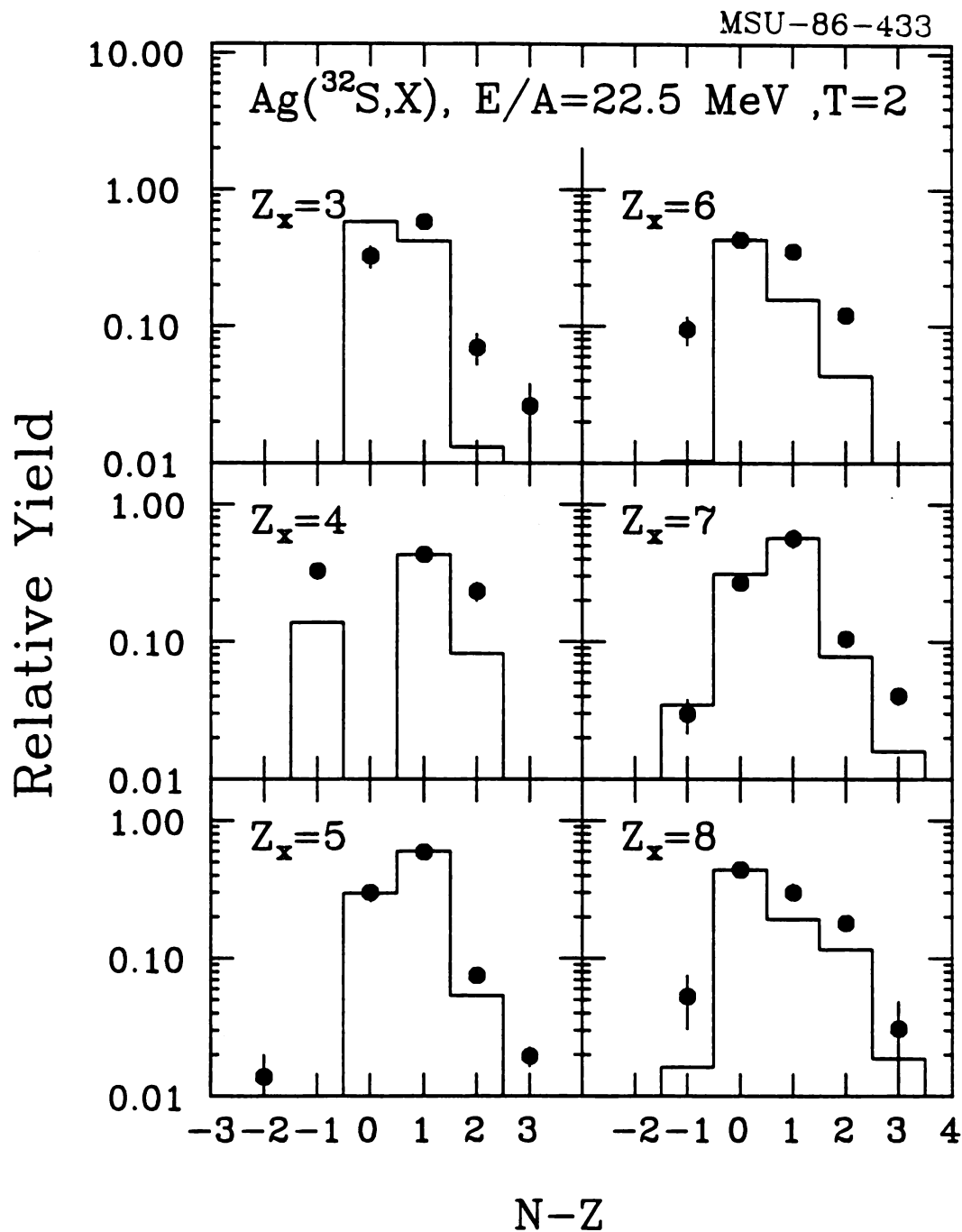


Figure VII-12: Isotopic distributions from  $^{32}\text{S} + \text{Ag}$  at  $E/A=22.5 \text{ MeV}$  (solid points) are compared to calculations (histograms) for emission from a nucleus,  $A=130$ ,  $Z=58$ , at a temperature of  $T=2 \text{ MeV}$ .



MSU-86-434

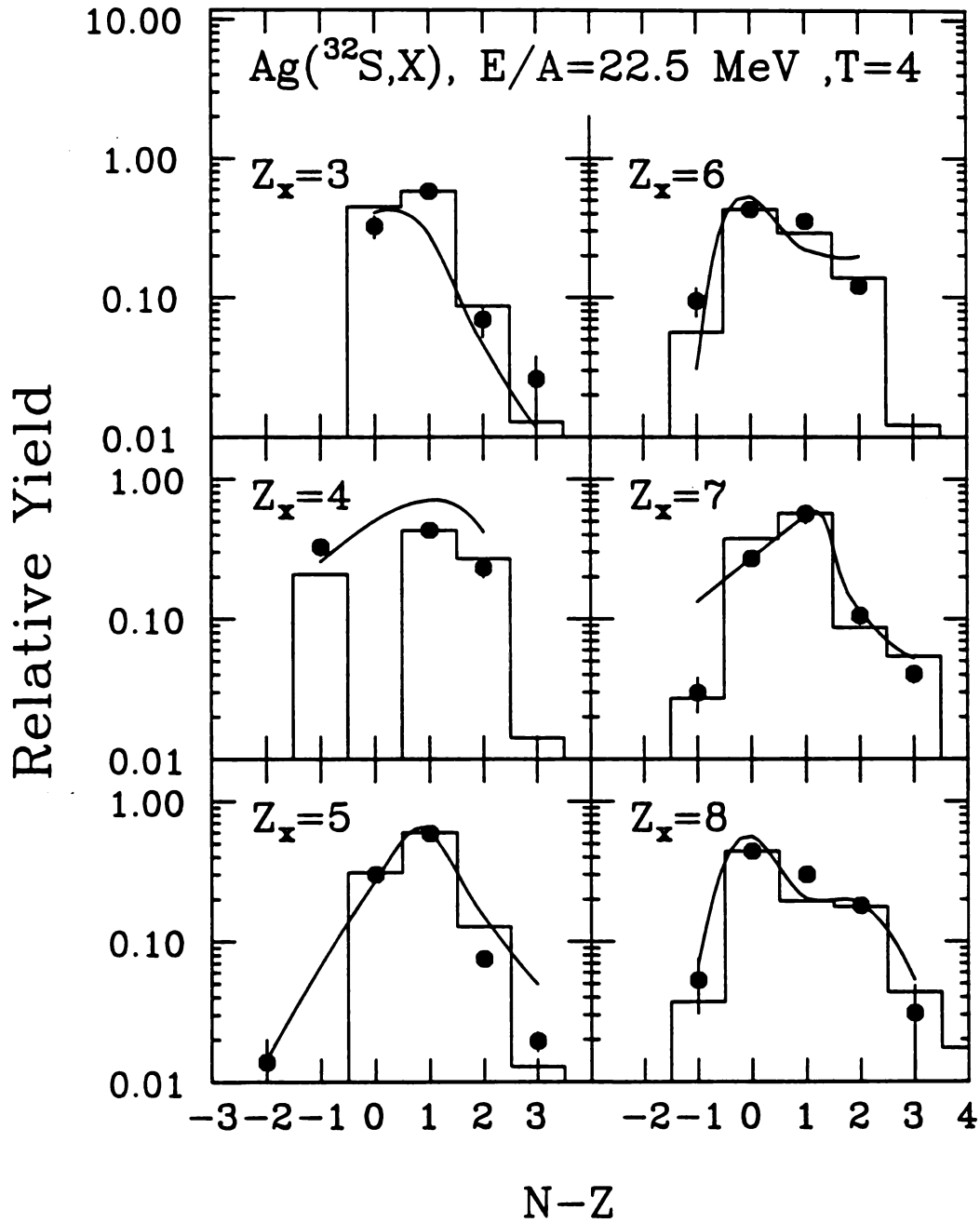


Figure VII-13: Isotopic distributions from  $^{32}\text{S} + \text{Ag}$  at  $E/A=22.5$  MeV (solid points) are compared to calculations (histograms) for emission from a nucleus,  $A=130$ ,  $Z=58$ , at a temperature of  $T=4$  MeV. The solid curves correspond to Eq. III-5 with  $T=3.8$  MeV.

MSU-86-435

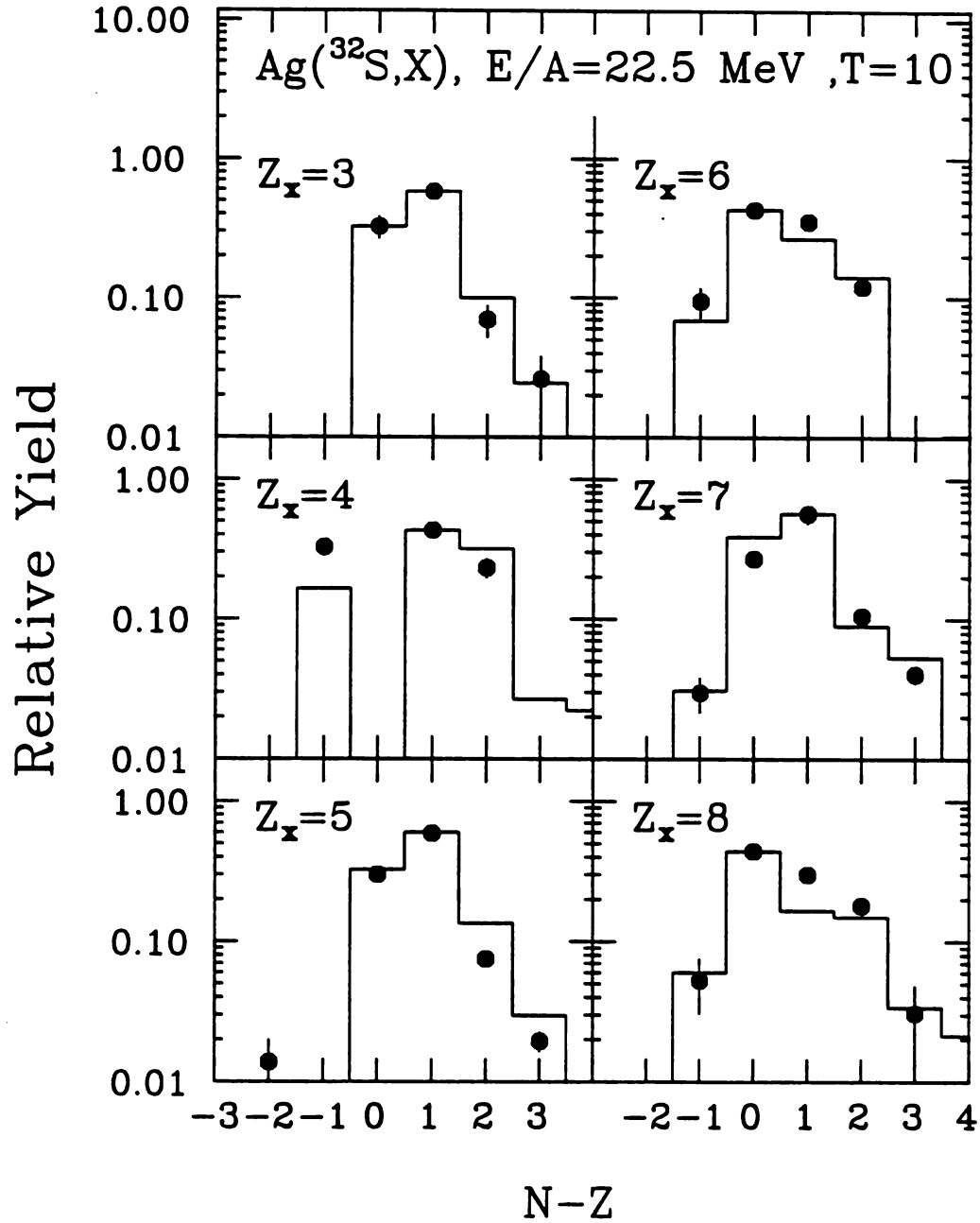


Figure VII-14: Isotopic distributions from  $^{32}\text{S} + \text{Ag}$  reactions at  $E/A=22.5$  MeV (solid points) are compared to calculations (histograms) for emission from a nucleus,  $A=130$ ,  $Z=58$ , at a temperature of  $T=10$  MeV.

### VII.C.2. Population ratios :

Spectra of gamma rays detected in coincidence with five different intermediate mass fragments produced in the  $^{32}\text{S} + \text{Ag}$  system are shown as histograms in Figure VII-15. The peaks corresponding to the specified transitions in the coincident intermediate mass fragments are clearly evident. The solid points correspond to the backgrounds estimated from a mixed event analysis for each nucleus. The fraction,  $F_\gamma$ , of nuclei emitting that particular gamma ray is given by the integrated number of counts above background in each peak divided by the product of the detection efficiency for the gamma ray and the number of detected intermediate mass fragments.

The measured values for these fractions are indicated by the hatched regions in Figure VII-16. The ratios expected for the primary distribution, as given in Eq. VII-7, are indicated by the dashed curves. The emission temperatures can be estimated from a comparison of this relationship and the measured values, except for the case of  $^{12}\text{B}$ . Because of significant feeding from higher lying particle stable states, the  $^{12}\text{B}$  ratio is consistent with the entire range of temperatures between 1 and 10 MeV and cannot unambiguously determine an emission temperature.

The temperatures estimated using Eq. VII-6 and neglecting sequential decay are shown in Figure VII-17. The temperature estimates for the first excited states in  $^7\text{Be}$  ( $E^* = 429 \text{ keV}$ ) and  $^8\text{Li}$  ( $E^* = 981 \text{ keV}$ ) are consistent with measurements made with the  $^{14}\text{N} + \text{Ag}$  system at  $E/A=35 \text{ MeV}$  [MORR84] [MORR85]. The temperatures estimated from measurements of  $^{10}\text{B}$  ( $E^* = 2154 \text{ keV}$ ) and  $^{13}\text{C}$  ( $E^* = 3854 \text{ keV}$ ) are somewhat higher,  $T \approx 1.5$ -

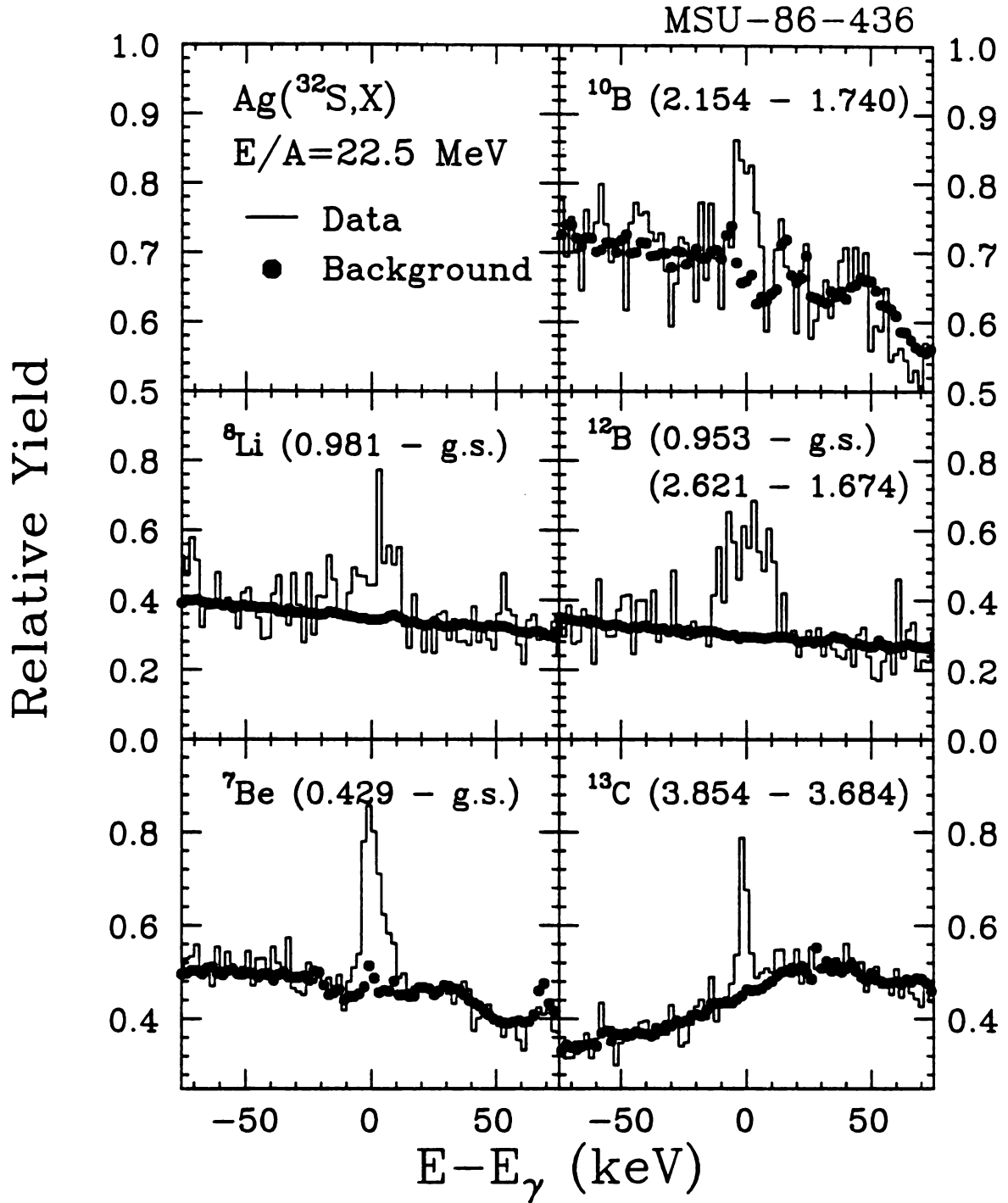


Figure VII-15: Energy spectra (shown as histograms) of gamma rays in the regions corresponding to transitions in coincident intermediate mass fragments produced in  $^{32}\text{S} + \text{Ag}$  reactions at E/A=22.5 MeV. The background is indicated by the solid points.

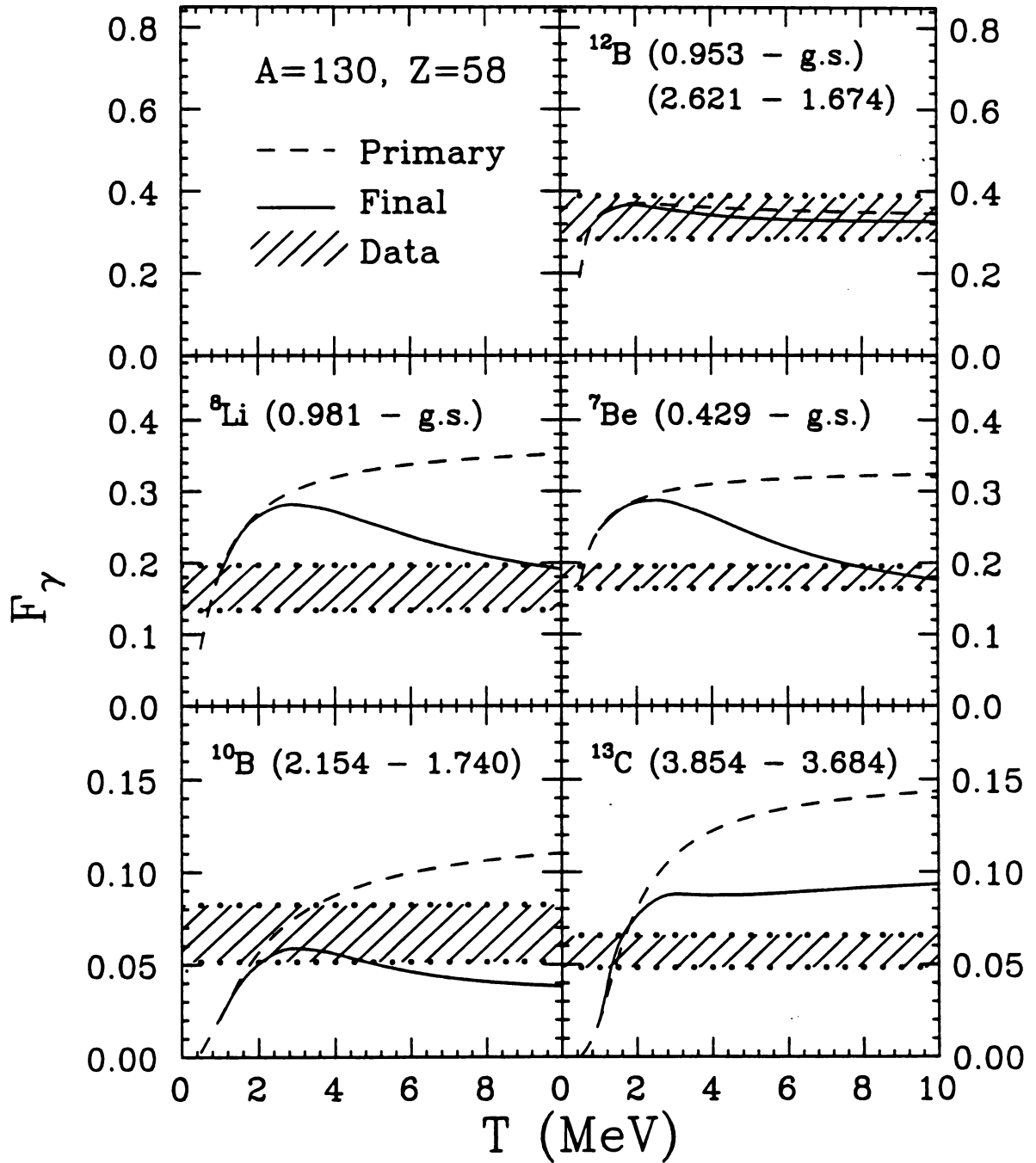


Figure VII-16: The fractions,  $F_\gamma$ , of intermediate mass fragments undergoing specified transitions are indicated as a functions of temperature for calculations from Eq. VII-1 both with (solid curves) and without (dashed curves) the contributions from sequential decay. The observed fractions are indicated by the hatched regions.

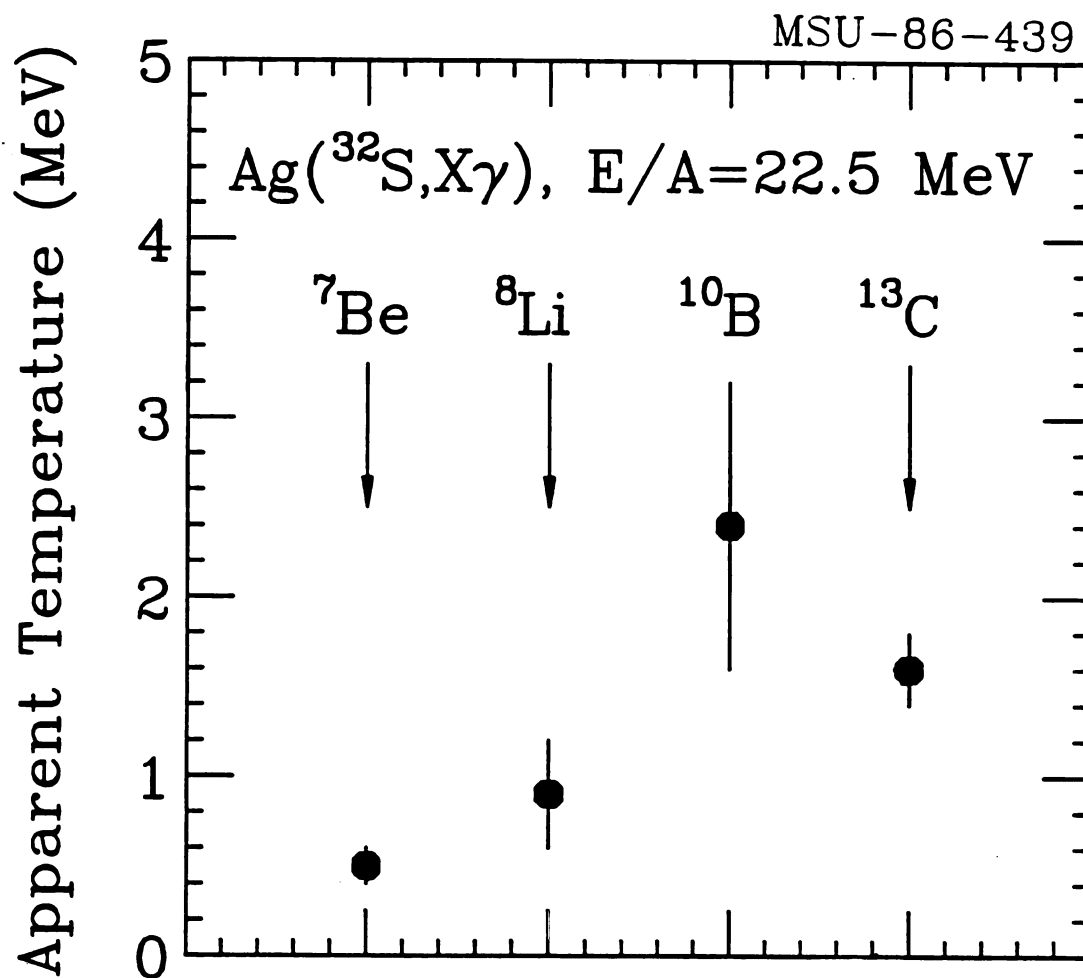


Figure VII-17: The apparent emission temperatures of intermediate mass fragments emitted in  $^{32}\text{S} + \text{Ag}$  reactions at  $E/A=22.5 \text{ MeV}$ , as discussed in the text.

2.5 MeV. The transitions in these nuclei are from levels with higher excitation energies than in  ${}^7\text{Be}$  and  ${}^8\text{Li}$ . This type of relation between the temperature estimates and the level separations was suggested in [POC85a]; it is difficult to measure temperatures higher than the level separation of the states from which the temperatures are inferred.

The solid curves in Figure VII-16 correspond to calculations which include sequential feeding from statistically populated unbound resonances. Feeding from particle-unstable states lowers the observed fraction of the nuclei which undergo the specified transitions. In fact, because the relative yield of heavier unstable nuclei increases in this model, the calculated values of  $F_\gamma$  can actually reach a maximum at some temperature and decline with increasing temperature. As was the case with the calculations for unstable states, the observed final populations of excited states relative to the ground states is predicted to be significantly less than for the primary distribution. The inclusion of the decay of particle-unstable states brings the calculation into better agreement with the data at higher temperatures.

In order to examine the importance of the shape of the mass distribution on  $F_\gamma$ , calculations with the quantum statistical model are shown in Figure VII-18 as solid and dashed curves for  $\rho/\rho_0=0.1$  and 0.9, respectively. The calculation at  $\rho/\rho_0=0.1$  produces the steepest mass distribution, and in that case the relative populations of states is least affected by sequential decay. Because the primary population of excited states increases with temperature as the number of heavier nuclei which may populate states in lighter nuclei decrease, the quantum statistical calculations show a less dramatic dependence on temperature than the calculations of Figure VII-16. The general behavior of the

MSU-86-440

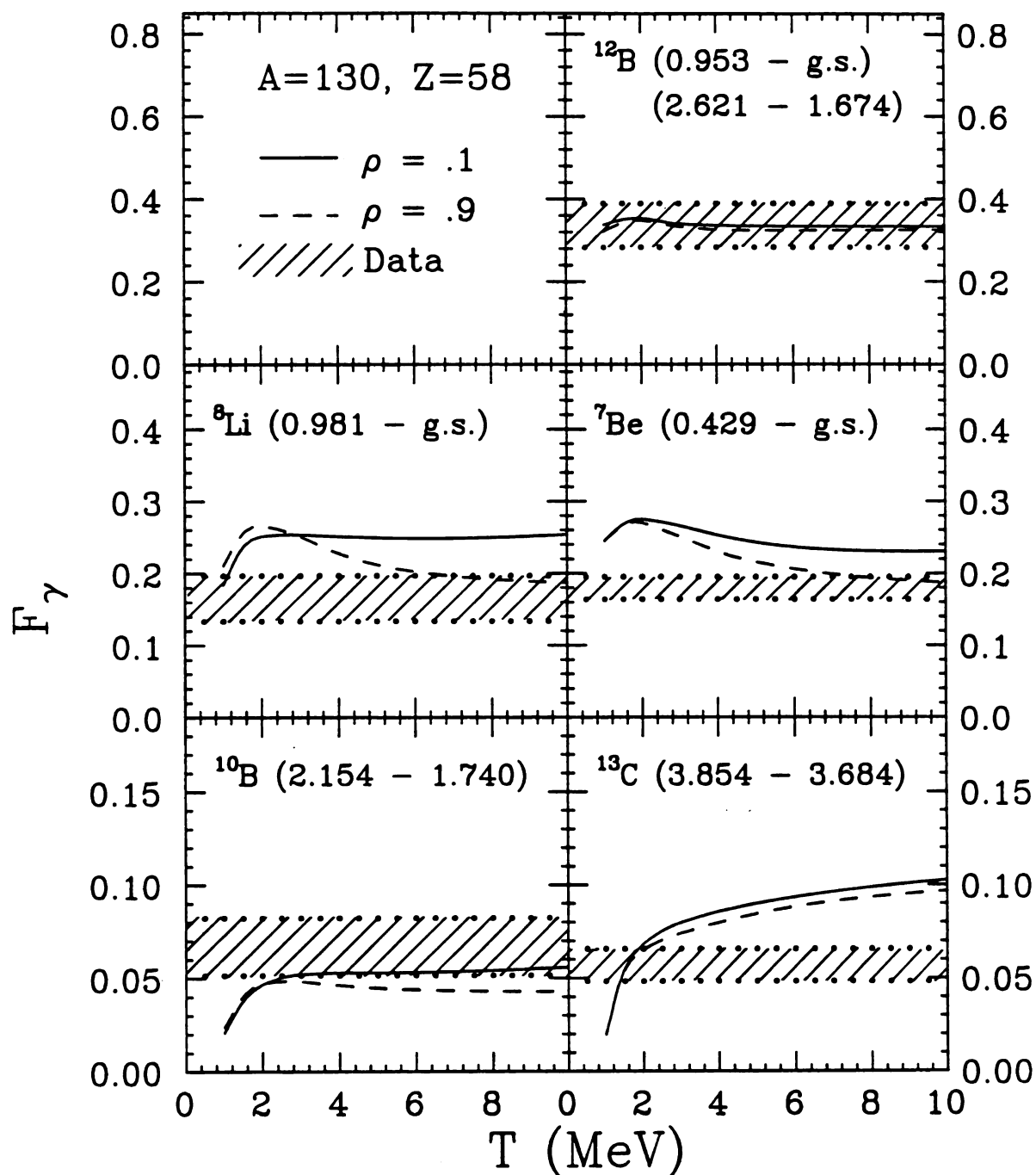


Figure VII-18: The fractions,  $F_\gamma$ , of intermediate mass fragments undergoing specified transitions are indicated as a functions of temperature for quantum statistical calculations at  $\rho/\rho_0=.1$  (solid curve) and  $.9$  (dashed curve). The observed fractions are indicated by the hatched regions.



calculations is similar to that of the calculation from Eq. VII-1.

#### VII.D. Summary of results :

In this chapter, the manifestations of equilibrium populations of excited states in the measured mass, isotopic, and excited state distributions have been investigated. These distributions, when calculated in schematic statistical models, were shown to be influenced by the decay of unstable fragments, and the experimental distributions were shown to confirm the existence of these effects.

The detailed shape of the final mass distribution is strongly influenced by the population of excited states in the primary distribution. Factors which determine the overall shapes of the mass and elemental distributions are the number of available states, the Q-values of the fragment emission, and the Coulomb barriers. Although Coulomb effects are neglected in the quantum statistical model, which can also describe aspects of the data, the experimental data clearly indicate the influence of the Coulomb energies. The particle decays of unstable states introduce a characteristic structure in the mass distributions in the region  $A=6-12$ , where the yield is suppressed compared to an interpolation of the cross sections between the heavier fragments and light particles. This structure arises from the decay of particle-unstable states. There are relatively few stable nuclear states in that particular region of the mass spectrum, leading to the particle decay of a large fraction of the primary fragments. In addition, heavier fragments decaying into this region will, with a high probability, decay

further into light particles, contributing to the diminution of the yields.

The general features of the isotopic distributions largely reflect the binding energies of the stable nuclei in their ground states. Calculations of statistical emission which include unstable states provide better agreement with the data than calculations using ground state binding energies alone. The  $^{32}\text{S} + \text{Ag}$  data appear to require that the effective emission temperature be greater than or equal to 3 MeV; distributions calculated for lower temperatures are more narrow than the observed distributions. The calculated distributions are not very sensitive to increases in temperature above 4 MeV. This is a result of the decay of unstable particles towards the valley of  $\beta$  stability. Thus, isotopic distributions provide only a lower limit for the emission temperature. This insensitivity to changes in emission temperature has also been observed in fragmentation [BUE76] [GEL78] and deeply inelastic reactions [MIG80] [LOC82].

Statistical calculations predict that the observed relative populations of nuclear states are significantly affected by feeding from the decay of unstable nuclei. The present schematic calculations indicate a preferential feeding to lower lying states, reducing the observed relative populations of higher excited states. This feeding from sequential decay leads to considerable complications in attempts to determine the emission temperatures from the relative populations of states. This problem is particularly serious when only low lying particle-stable states are investigated. At higher temperatures, however, similar problems arise for particle-unstable states, with the notable exception of states in  $^5\text{Li}$ . The present calculations may serve

as useful guides to elucidate the magnitude of the influence of sequential decay, but uncertainties in of the calculations prevent precise determinations of these effects.

The relative populations of states are sensitive to the charge and mass dependences of the primary yields. This was illustrated in the comparisons between the present calculations, in which difference in the mass spectra were reflected in the temperature dependences of the population ratios. The present parametrizations are inadequate. Improvements in theoretical treatments of the mass and charge dependences of the primary populations of states must also eventually address the angular momentum dependence of fragment production, possible in-medium corrections, and other details of the emission mechanism.

In addition, the detailed populations of final states are sensitive to the precise particle decay branching ratios. We have addressed the problem of the particle decay of unstable states in terms of a purely statistical treatment of the branching ratios. The spins, parities, and isospins of many of the tabulated states used in this analysis are poorly determined or unknown; the treatment of their decays is, therefore, not very reliable. Furthermore, nuclear structure effects are expected to affect the branching ratios. These effects have not yet been incorporated, largely because of the information is not available. Nonetheless, the general success of the calculations should encourage further refinements to such models, as well as additional experimental work.

## Chapter VIII

### Equilibration and Decay in Nuclear Collisions

#### VIII.A. Model for statistical decay during equilibration :

##### **VIII.A.1. Motivation :**

In prior chapters several features of the data were described as statistical, and in Chapter VII the relative cross sections of intermediate mass fragments and their excited states were calculated with equilibrium statistical formulations. However, both the angular distributions and energy spectra of intermediate mass fragments give clear evidence that particles are emitted prior to, as well as after, the complete equilibration of the composite system. This demands that descriptions of intermediate mass fragment emission encompass the early non-equilibrium stages of the reaction and the evolution of the system towards the fully equilibrated composite nucleus. While this process can be crudely approximated by a two source model, as in Section III.B., the details of the energy spectra and angular distributions can be expected

to contain information concerning the time scales and mechanisms for particle emission and equilibration.

In this chapter a schematic model is presented which attempts to reconcile the equilibrium and non-equilibrium aspects of the data by assuming local equilibrium in a dynamically evolving composite system [FIE84]. In this picture the initial source of emission is assumed to be a localized region of high excitation in the target-projectile system at the overlap of the projectile and the target. It is assumed to be in local equilibrium, to the extent that particles are emitted with equilibrium statistical probabilities. The local region of excitation evolves towards the fusion-like system by accreting nucleons from the cold target spectator. As a result of this accretion, the velocity and temperature of this "hot spot" decrease with time. The assumption of localization is supported by two-particle correlation experiments which indicate emission sources smaller than the compound nucleus [LYN83] [CHI86a] [POC86a].

#### VIII.A.2. Formulation of the model :

The formulation presented here follows closely the model of Friedman and Lynch [FRI83a], which calculates the time evolution of the compound nucleus and its emission products. The present model calculates the average number,  $N_i$ , of particles of species,  $i$ , with mass, charge, and neutron numbers,  $a_i$ ,  $z_i$ , and  $n_i$ , emitted from a source with momentum,  $P_s(t)$ ; mass, charge, and neutron numbers,  $a_s(t)$ ,  $z_s(t)$ , and  $n_s(t)$ ; and an excitation energy of  $E_s^* = \epsilon_p^* z_s(t) + \epsilon_n^* n_s(t)$ , where  $\epsilon_n^*$  and  $\epsilon_p^*$  are the intrinsic excitation energies of the neutrons and protons,

respectively. This source is a subset of the total system which has mass, charge, and neutron numbers,  $a(t)$ ,  $z(t)$ , and  $n(t)$ ; the sizes of both the source and the total system are functions of time,  $t$ , and, implicitly, temperature,  $T$ . The differential emission rate,  $d^2N_i/dEdt$ , for the  $i^{\text{th}}$  particle type with an energy  $E$  is determined by a statistical prescription.

The system initially consists of a hot participant region and a cold spectator. The initial size of the participant region is a parameter, which for small projectiles is usually fixed at twice the projectile mass. For initial source sizes less than or equal to twice the projectile mass, the source consists of equal numbers of target and projectile nucleons. For larger initial sources the source includes all of the projectile plus additional nucleons from the target. The source is assumed have an excitation energy determined by the conservation of the projectile momentum and energy. It is assumed to be in thermal equilibrium at the temperature calculated for a nuclear Fermi gas at normal nuclear matter density. From this initial stage, the source evolves by particle emission and accretion. The source accretes spectator nucleons at a rate  $[da_s/dt]_a$ , thus slowing and converting its kinetic energy into excitation energy. The system reaches equilibrium at a time  $t_e$  with a temperature  $T_e$  when  $a_s(t_e) = a(t_e)$ . After this time, the system continues to emit particles until the excitation energy of the residue falls below the threshold for particle emission.

The evolution of the temperature with time is contained in the cooling relation,  $dt/dT$ , which is derived from the statement of energy conservation,

$$\frac{dE_s^*}{dt} + \sum_i \left( \frac{dN_i}{dt} \right) B_{iD} + \sum_i \frac{d(E_k)_i}{dt} - \frac{dE_a}{dt} = 0 \quad (\text{VIII-1})$$

The change in the intrinsic excitation of the source is given by differentiation of  $E_s^*$ ,

$$\begin{aligned} \frac{dE_s^*}{dt} = \frac{dz_s}{dt} \epsilon_p^*(T) + \frac{dn_s}{dt} \epsilon_n^*(T) + \\ [n_s C_n + z_s C_p] \cdot \frac{\partial T}{\partial t} \end{aligned} \quad (\text{VIII-2})$$

where

$$\begin{aligned} \frac{dz_s}{dt} = \frac{Z}{A} \left( \frac{da_s}{dt} \right)_a - \sum_i \frac{dN_i}{dt} z_i \quad \text{and} \\ \frac{dn_s}{dt} = \frac{Z}{A} \left( \frac{da_s}{dt} \right)_a - \sum_i \frac{dN_i}{dt} n_i . \end{aligned} \quad (\text{VIII-3})$$

The heat capacity,  $C$ , is defined by  $\partial \epsilon^* / \partial T$  and is calculated for the protons and neutrons independently. The separation energies,  $B_{iD}$ , is given by

$$B_{iD} = B(a, z) - (B(a - a_i, z - z_i) + B_i) , \quad (\text{VIII-4})$$

where the binding energies are defined as in Eq. VII-4 and VII-5. The emission rates as a function of time are given by the integral over the particle energy,  $E$ ,

$$\frac{d N_i}{dt} = \int_0^{\infty} \frac{d^2 N_i}{dE dt} dE . \quad (\text{VIII-5})$$

The rate of energy loss due to the kinetic energy of  $i^{\text{th}}$  particle

$$\frac{d(E_k)_i}{dt} = \int_0^{\infty} \frac{d^2 N_i}{dE dt} E dE . \quad (\text{VIII-6})$$

During accretion, the source momentum is distributed among an increasing number of nucleons, and the source slows. Thus, the kinetic energy of the source is converted into excitation energy at the rate

$$\frac{dE_a}{dt} = \frac{p_s^2}{2m_0 a_s^2} \cdot \left[ \frac{d a_s(t)}{dt} \right]_a , \quad (\text{VIII-7})$$

where  $m_0$  is the rest nucleon mass. Solving for the cooling relation results in the expression

$$\frac{dT}{dt} = - \frac{\sum_i \left[ \frac{dN_i}{dt} (B_{iD} - z_i \epsilon_p^* - n_i \epsilon_n^*) + \frac{d(E_k)_i}{dt} \right] - \frac{dE_a}{dt} + \frac{\epsilon_p^* z + \epsilon_n^* n}{a} \frac{da_s}{dt}}{n_s C_n + z_s C_p} \quad (\text{VIII-8})$$

The differential emission rate for the  $i^{\text{th}}$  species is given by the Weisskopf formula [WEI37],



$$\frac{d^2 N_i}{dE dt} = \frac{2s_i + 1}{\pi^2 h^3} E M \sigma_{i+D \rightarrow P} \exp(\Delta S) \quad , \quad (\text{VIII-9})$$

where  $s_i$  is the spin of the emitted particle, and  $M$  is its mass. The cross section for the inverse, fusion reaction  $i+D \rightarrow P$ ,  $\sigma_{i+D \rightarrow P}$  is parametrized as

$$\sigma_{i+D \rightarrow P} = \pi R_{iD}^2 \left( \frac{E-V}{E} \right) \theta(E-V) \quad (\text{VIII-10})$$

where  $\theta(x)$  is 1 if  $x > 0$  and 0 if  $x \leq 0$ , the radius is given by

$$R_{iD} = \begin{cases} [(a_s - a_i)^{1/3} + a_i^{1/3}] r_0, & \text{for } a_i \geq 2 \\ r_0 (a_s - 1)^{1/3}, & \text{for } a_i = 1 \end{cases} \quad (\text{VIII-11})$$

with  $r_0 = 1.2$  fm, and the Coulomb barrier is given by

$$V_{iD} = \frac{\lambda e^2 z_i (z - z_i)}{r_C [a_i^{1/3} + (a - a_i)^{1/3}]} \quad (\text{VIII-12})$$

The Coulomb radius parameter is  $r_C = 1.44$  fm. The parameter  $\lambda$  is adjustable, and can be used to reduce the Coulomb barrier from the value for touching spheres, as reduced Coulomb barriers are observed in fragment energy spectra ( see Section III.B.3. ).

The change in the entropy of the system resulting from emission,  $\Delta S$ , is given in a constant density approximation by

$$\Delta S = - \frac{1}{T} \left[ E + B_{iD} - [z_i(\epsilon_p^* - T\sigma_p) + n_i(\epsilon_n^* - T\sigma_n)] \right. \\ \left. + \frac{(z_i\epsilon_p^* + n_i\epsilon_n^* - E - B_{iD})^2}{2T [C_p(z_s - z_i) + C_n(n_s - n_i)]} \right], \quad (\text{VIII-13})$$

where  $\sigma_p$  and  $\sigma_n$  are the intrinsic entropies for the protons and neutrons, respectively, so that  $S = \sigma_p n_p + \sigma_n n_n$ .

The time evolution of the parameters is treated in an integral approach. The mass of the source, for example, is given by

$$a_s(t) = a_s(0) + \int_0^t \left[ -\sum_i \frac{dN_i}{dt} a_i + \left( \frac{da_s}{dt} \right)_a \right] dt \\ a_s(t \rightarrow \infty) = a_s(0) + \int_0^{t_e} \left[ -\sum_i \frac{dN_i}{dt} a_i + \left( \frac{da_s}{dt} \right)_a \right] dt \\ + \int_{T_e}^0 \left( -\sum_i \frac{dN_i}{dt} a_i \right) \left( \frac{dt}{dT} \right) dT \quad (\text{VIII-14})$$

The kinematics of the emission is determined in this model by the source momentum, which is given by

$$P_s(t) = P_s(0) + \int_0^t \frac{dP_s}{dt} dt, \quad (\text{VIII-15})$$

where

$$\frac{dP_s(t)}{dt} = - \frac{P_s(t)}{a_s(t)} \cdot \sum_i \frac{dN_i}{dt} a_i \quad . \quad (\text{VIII-16})$$

### VIII.B. General features of the calculation :

This formulation of a statistical emission model differs from the schematic model presented in Section VII.B. both in its calculation of the instantaneous emission rate and in its inclusion of the time evolution of the emitting system.

#### **VIII.B.1. Instantaneous emission rate :**

The Weisskopf formula is derived from the principle of detailed balance. This is that in equilibrium the transition rate from state 1 to state 2 is the same as the rate from 2 to 1. The rate of decay from 1 with an energy  $E = mv^2/2$  in the interval  $dE$  is expressed as

$$R_1 = (\sigma_{i+D \rightarrow P}^v) \left( \frac{(2s+1)mpdE}{\pi^2 h^3} \right) \left( \frac{\omega(1)}{\omega(2)} \right) . \quad (\text{VIII-17})$$

The first term on the right hand side represents the rate at which the inverse reaction can take place for specific quantum states of 1 and 2, i.e. the flux times the cross section. The second term represents the phase space represented by the momentum of the free emitted particle. The third term is the ratio of the number of microstates in states 1 and 2.

The instantaneous emission rate differs from Eq. VIII-1 in three ways. The preexponential term in Eq. VIII-9 has no counterpart in Eq. VII-1. This preexponential term, consisting of the mass,  $m$ , of the emitted fragment and the inverse cross section,  $\sigma_{i+D \rightarrow p}$ , introduces a weak fragment mass dependence. The dependence of this term on  $a_i$  is depicted in Figure VIII-1. This preexponential term strengthens the yield of heavier fragments, particularly for large sources.

The second order,  $1/T^2$ , term of Eq. VIII-13, also makes the mass spectrum sensitive to the size of the source. The mass spectra of the instantaneous emission rate of particle stable nuclei from three different sources in the same composite system,  $a=220$ ,  $z=89$ , at  $T=8$  MeV are shown in Figure VIII-2. The spectra are shown as a solid curve for  $(a_s, z_s)$  of  $(24, 12)$ , as a dashed curve for  $(80, 35)$ , and as a dotted curve for  $(200, 80)$ . The spectra for the two larger sources are nearly the same, indicating that the mass spectrum is independent of source size when  $a_s \gg a_i$ . The mass spectrum of the smaller source exhibits a steeper slope than those of much larger sources. Thus, the  $1/T^2$  term in Eq. VIII-13 inhibits the emission of fragments which are not small compared to the source. In practice, the requirement that  $a_i < .5a_s$  is imposed in the calculation.

The other term in the argument of the exponential is of the form of  $a_i f^*/T$ , where the free energy is  $f^* = \epsilon^* - T\sigma$ . This term strongly favors the emission of light particles from a hot system, resulting in a relative suppression of the heavy fragment yields. The mass spectrum is shown in Figure VIII-3 as a function of temperature for a system of  $a=112$  and  $z=52$ . The instantaneous emission rate of particle stable ground states is plotted as a function of the atomic mass,  $a_i$ , of the

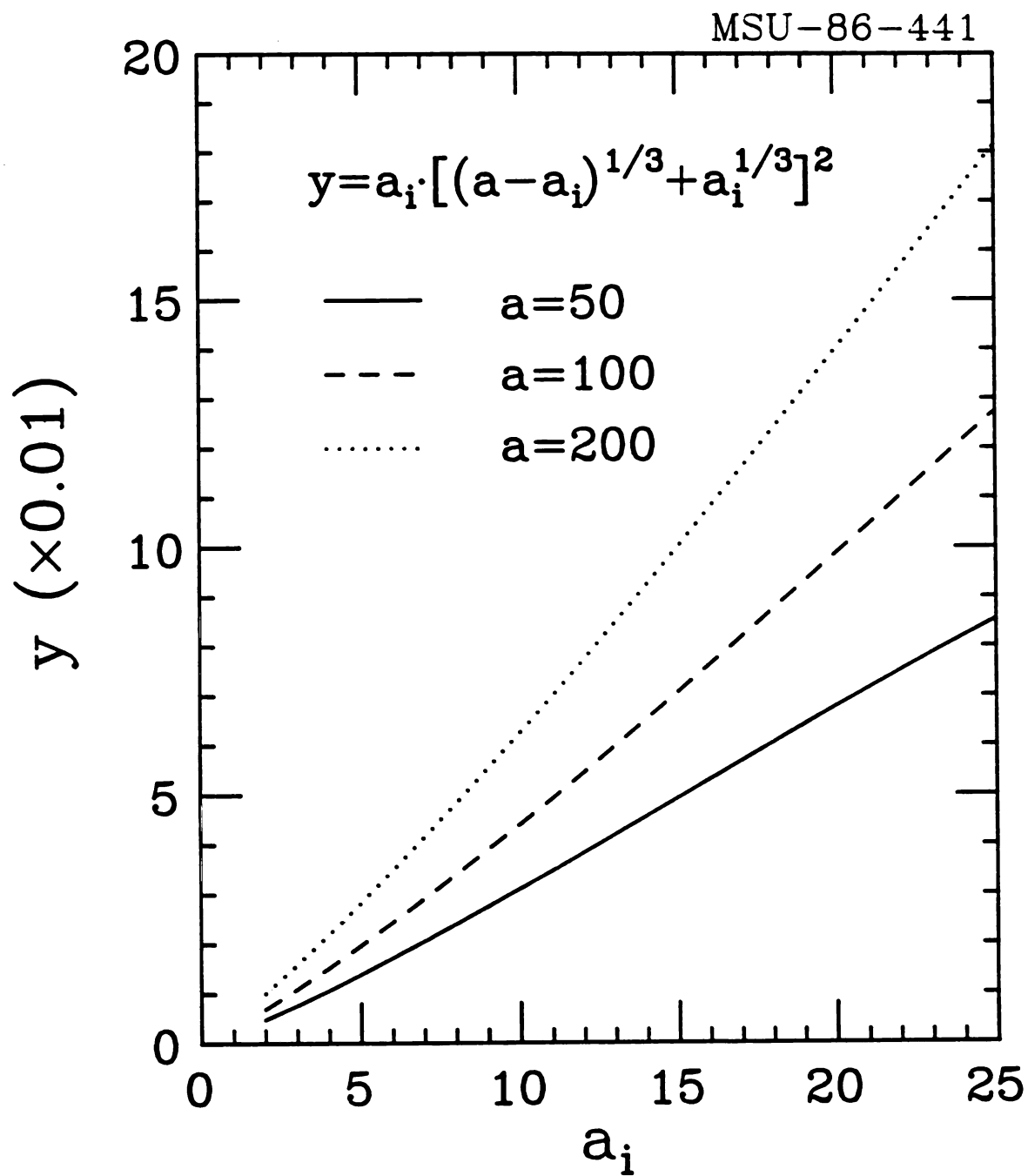


Figure VIII-1 : The dependence on source and fragment mass introduced by the preexponential terms in Eq. VIII-9.

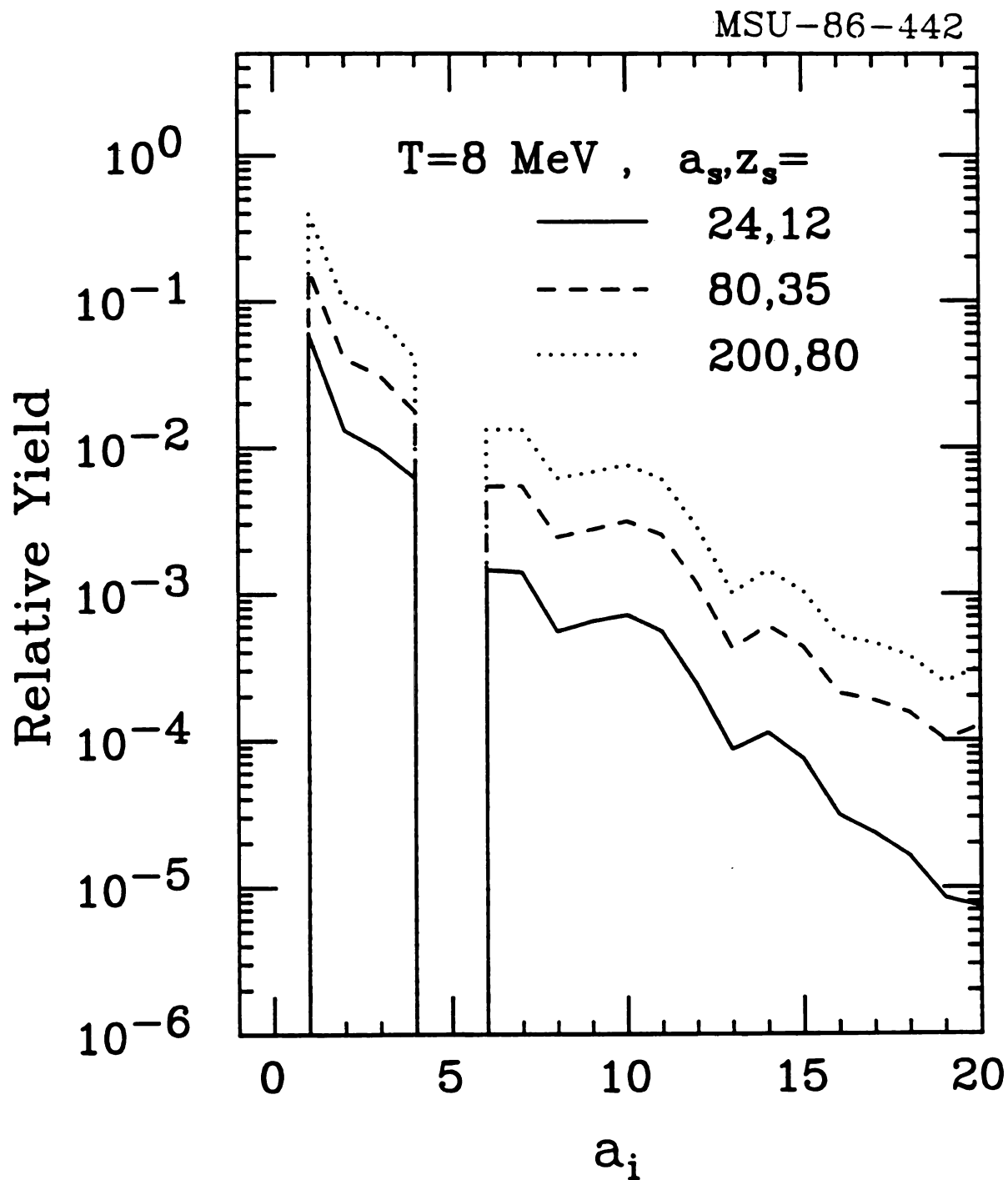


Figure VIII-2 : The mass spectrum of the instantaneous emission rate for particle stable nuclei as a function of source size in a composite system of  $a=220$  and  $z=80$ .

MSU-86-443

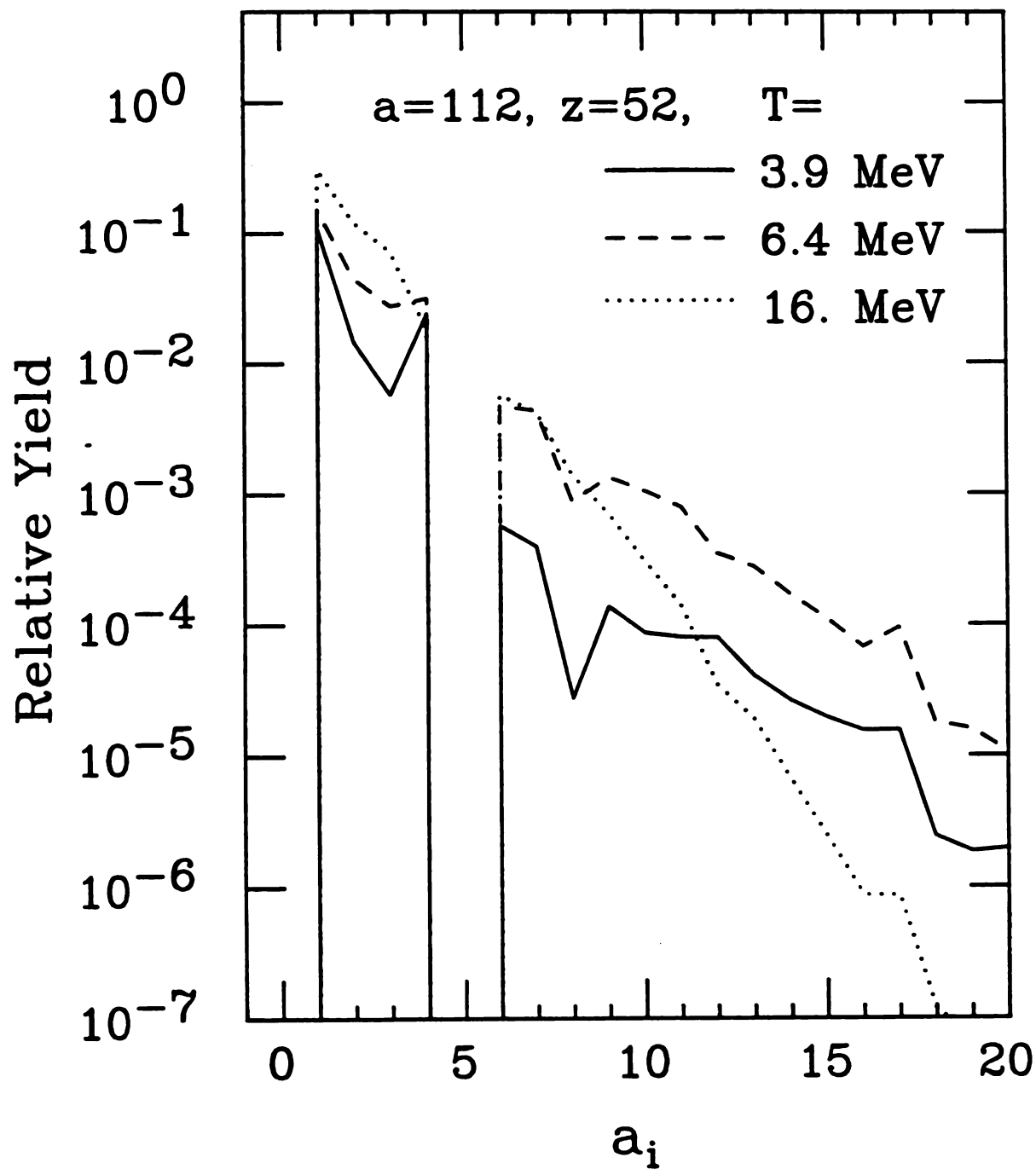


Figure VIII-3 : The mass spectrum of the instantaneous emission rate of nuclei emitted in their particle stable ground states as a function of source temperature for a compound nucleus of  $a=112$  and  $z=56$ .

emitted particle. The distribution at the lowest temperature,  $T=3.9$  MeV, shown as the solid curve, falls with increasing particle mass, principally under the influence of the Coulomb barrier. At a temperature,  $T=6.4$  MeV, the mass distribution (dashed curve) is somewhat less steep. At a higher temperature,  $T=16$  MeV (dotted curve), the free energy term becomes important, so that the mass yield drops much more rapidly with fragment mass. As the early stages of the reaction are presumably the "hottest", the non-equilibrium component of the energy spectra should be strongest for the lightest fragments.

The mass spectrum is sensitive to the Coulomb barriers for particle emission. If the effective barrier is reduced, for example, by the deformation of the composite system, then the mass spectrum will reflect this change. In Figure VIII-4, the mass spectrum for the instantaneous emission rate of particle stable nuclei from a system,  $a=200$ ,  $z=87$ ,  $T=8$  MeV, is shown for calculations with  $\lambda = 1.0$ ,  $0.8$ , and  $0.6$  by solid, dashed, and dotted curves, respectively. High Coulomb barriers inhibit the emission of heavier fragments. As the barriers are reduced, the heavy fragment yields are greatly enhanced.

#### VIII.B.2. Time evolution :

The other principal feature which distinguishes the present model from Eq. VII-1 is the time evolution of emitting nuclei. In Figure VIII-5 the time evolution of a compound nuclear system,  $a_s(t=0)=a=112$ ,  $z_s(t=0)=z=52$ , is depicted as trajectories in plots of  $a(t)$  vs.  $T(t)$ . These begin at different temperatures, as indicated by the open points, corresponding to incident energies in the Fe+Fe system of  $E/A=3$ ,  $10$ ,  $20$ ,



MSU-86-444

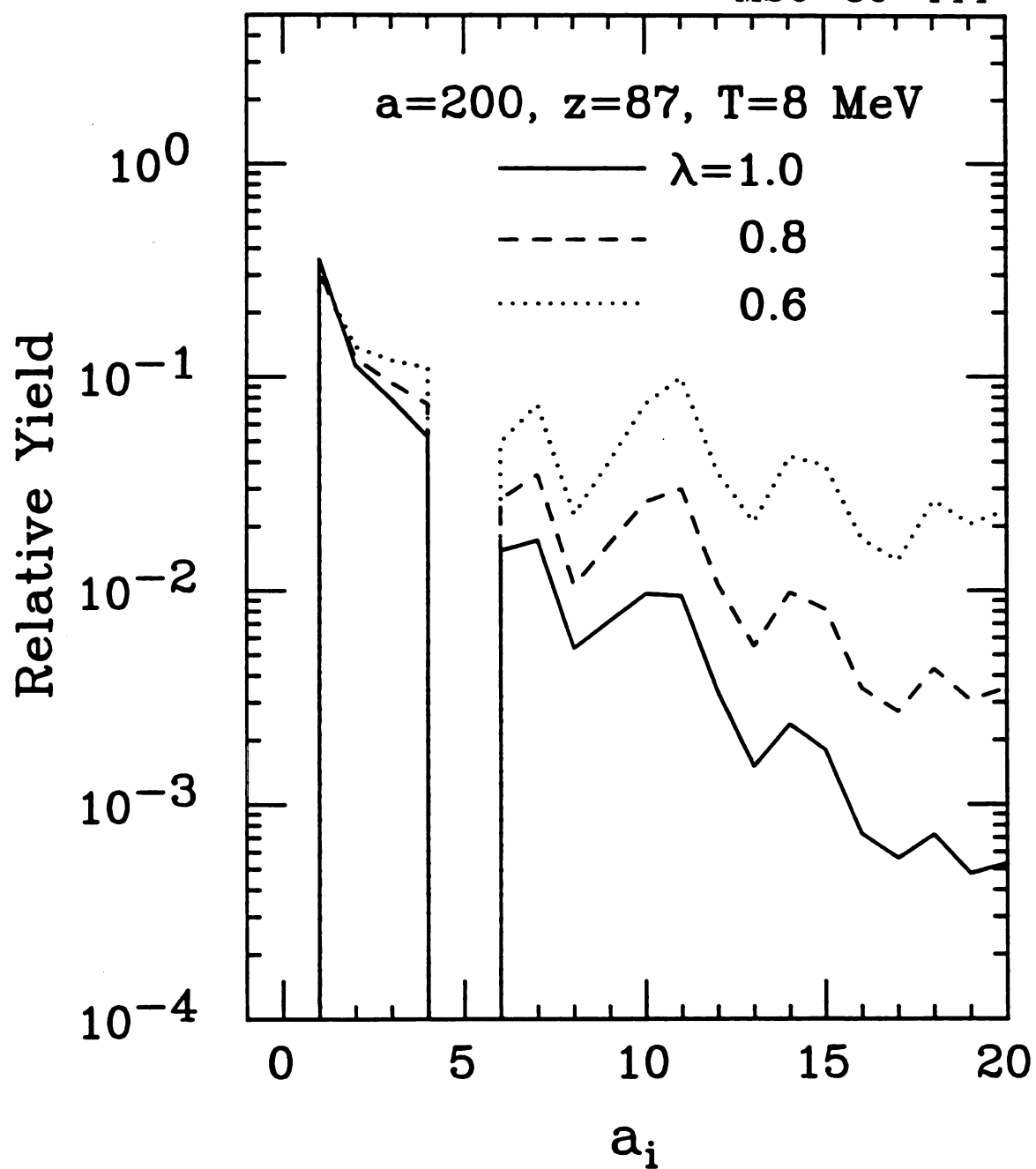


Figure VIII-4 : The mass spectrum of the instantaneous emission rate of particle stable nuclei calculated as a function of the Coulomb parameter,  $\lambda$ , as in Eq. VIII-12.

MSU-86-447

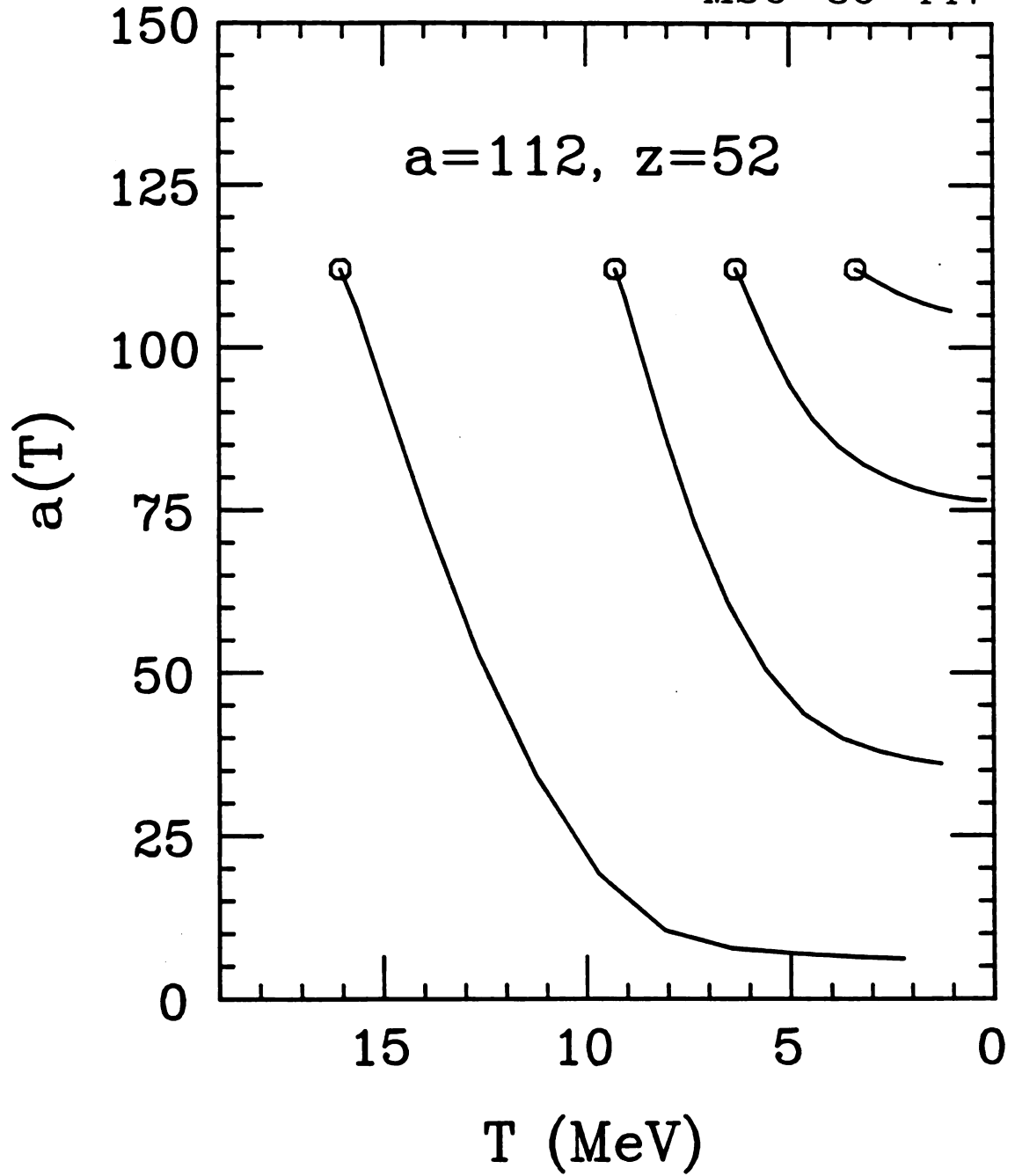


Figure VIII-5 : The time evolution of compound nuclear systems with initial  $a=112$  and  $z=52$  starting from four temperatures.

and 50 MeV. The slope of the trajectories in the early stages are steep, with large mass losses per temperature change. This follows from the energy dependence of the temperature,  $T \propto E^{1/2}$ , as the energy loss is proportional to mass loss. As the initial excitation energy increases the total mass loss increases.

The trajectories of Figure VIII-5 are calculated for equilibrated compound nuclei. A major point of this schematic model was to incorporate pre-equilibrium emission into the time evolution of the system. In Figure VIII-6, trajectories for the  $^{12}\text{C} + ^{197}\text{Au}$  system at  $E/A=30$  MeV are shown for initial source sizes of  $a_s(t=0) = 24, 50, 100$ , and 209, as indicated in the figure. The accretion rate of the source was fixed to be a constant  $[da_s/dt]_a = 3$  nucleons/(fm/c). This corresponds roughly to the number of spectator nucleons ( $\approx 180$ ) divided by the transit time of the projectile across the target ( $2r(\text{Au})/v_p \approx 50$  fm/c, where  $r$  is the radius of the nucleus and  $v_p$  is the projectile velocity). A comparison of Figures VIII-5 and VIII-6 demonstrates that emission prior to the attainment of full statistical equilibrium reduces the total particle emission during the history of the system. Particles emitted prior to equilibration are more energetic, as they carry away the energy associated with the source momentum. As a result, less energy is left for particle emission.

In Figure VIII-7, the time evolution of the  $^{12}\text{C} + ^{197}\text{Au}$  system at incident energies of  $E/A = 10, 30, 50$ , and 100 MeV is demonstrated. The accretion rate was fixed to be a constant  $[da_s/dt]_a = 3$  nucleons/(fm/c). Once again, the higher incident energies result in lighter residual systems. However, the ten-fold change in incident energies results in only a 20% change in the residue mass. This is a result of the removal

MSU-86-448

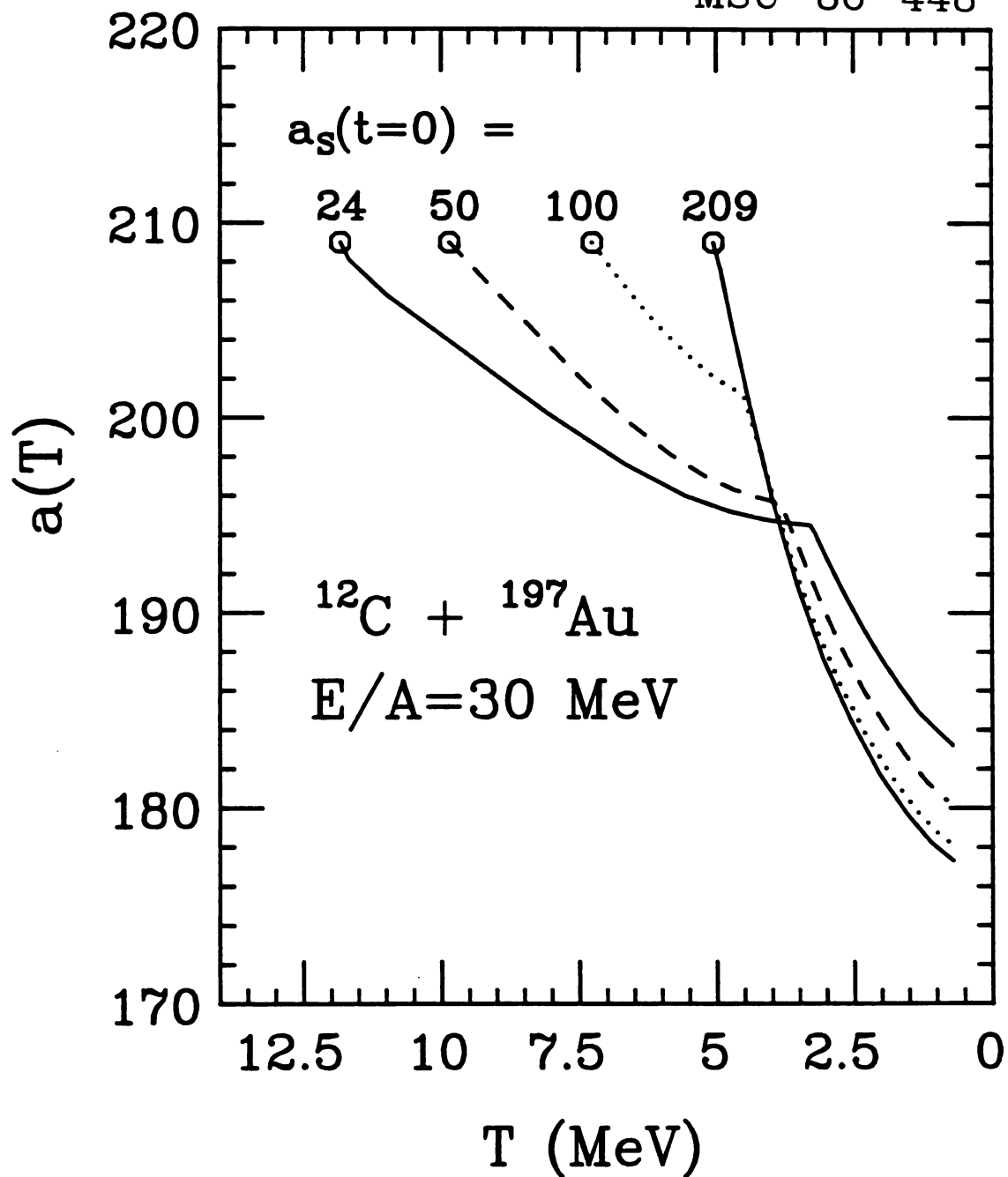


Figure VIII-6 : The time evolution of the  $^{12}\text{C} + ^{197}\text{Au}$  system at  $E/A=30$  MeV, with four different initial source sizes. The accretion rate used in these calculations was  $[da_s/dt]_a = 3 \text{ nucleons/(fm/c)}$ .

MSU-86-449

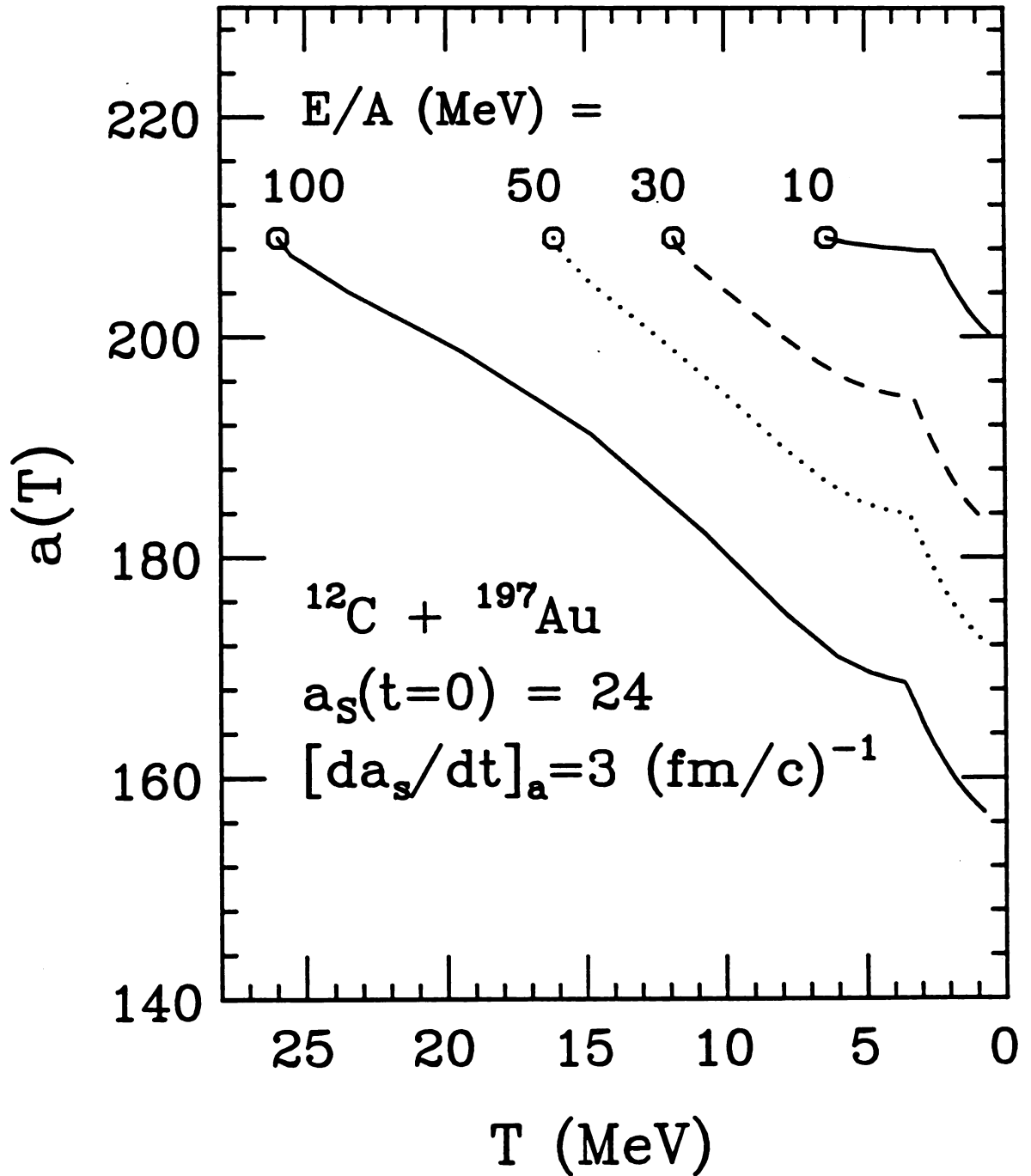


Figure VIII-7 : The time evolution of the  $^{12}\text{C} + ^{197}\text{Au}$  system at four different incident energies, calculated with  $a_s(t=0)=24$  and  $[da_s/dt]_a=3$  nucleons/(fm/c).

of a great deal of the available kinetic energy by pre-equilibrium emission.

If the accretion rate is changed to  $[da_s/dt]_a = 1$  nucleon/(fm/c), the duration of non-equilibrium emission is extended. The saturation behavior becomes even more evident, as demonstrated in Figure VIII-8, where the trajectories using this slower accretion rate are shown. The emission products are dominated by pre-equilibrium products.

#### VIII.C. Results of the model :

As demonstrated above, the accretion rate,  $[da_s/dt]_a$ , is an important parameter in this model. While, in general, this would be a time dependent quantity, it is assumed to be a constant in the present calculations. This parameter balances the contributions from equilibrium and pre-equilibrium emission. A calculated quantity which can be used to test whether the chosen parameters achieve the proper balance between post- and pre-equilibrium emission is the momentum transferred to the equilibrated residue. The systematics for momentum transfer [FAT85], as deduced from  $^{12}\text{C}$  and  $^{14}\text{N}$  induced reactions on  $^{197}\text{Au}$  are presented in Figure VIII-9 as solid points. The velocity of the equilibrated system,  $v_{eq}$ , as a fraction of the center of mass velocity,  $v_{cm}$ , is displayed as a function of the velocity of the projectile above the Coulomb barrier,  $V$ . Calculations of the  $^{12}\text{C} + ^{197}\text{Au}$  system using three different values of the accretion rate ( $[da_s/dt]_a = 1, 3$ , and  $5$  nucleons/(fm/c) ) are shown as solid curves. An accretion rate of  $[da_s/dt]_a = 3$  nucleons/(fm/c) corresponds approximately to equilibration in the transit time of the projectile across the target. The calculation with  $[da_s/dt]_a = 1$ /(fm/c)

MSU-86-450

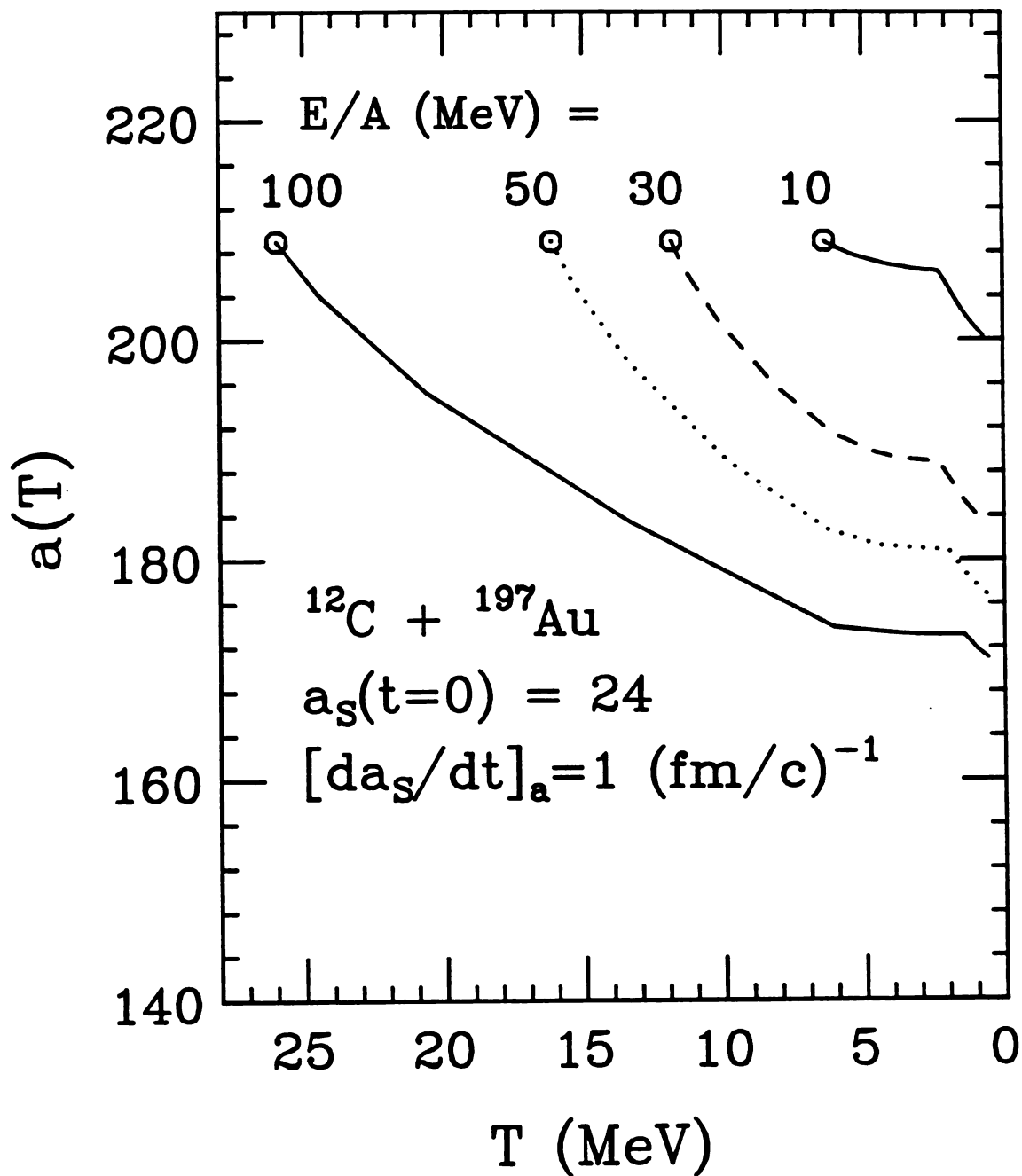


Figure VIII-8 : The time evolution of the  $^{12}\text{C} + ^{197}\text{Au}$  system at four different incident energies, calculated with  $a_s(t=0)=24$  and  $[da_s/dt]_{a=1} = 1$  nucleons/(fm/c).

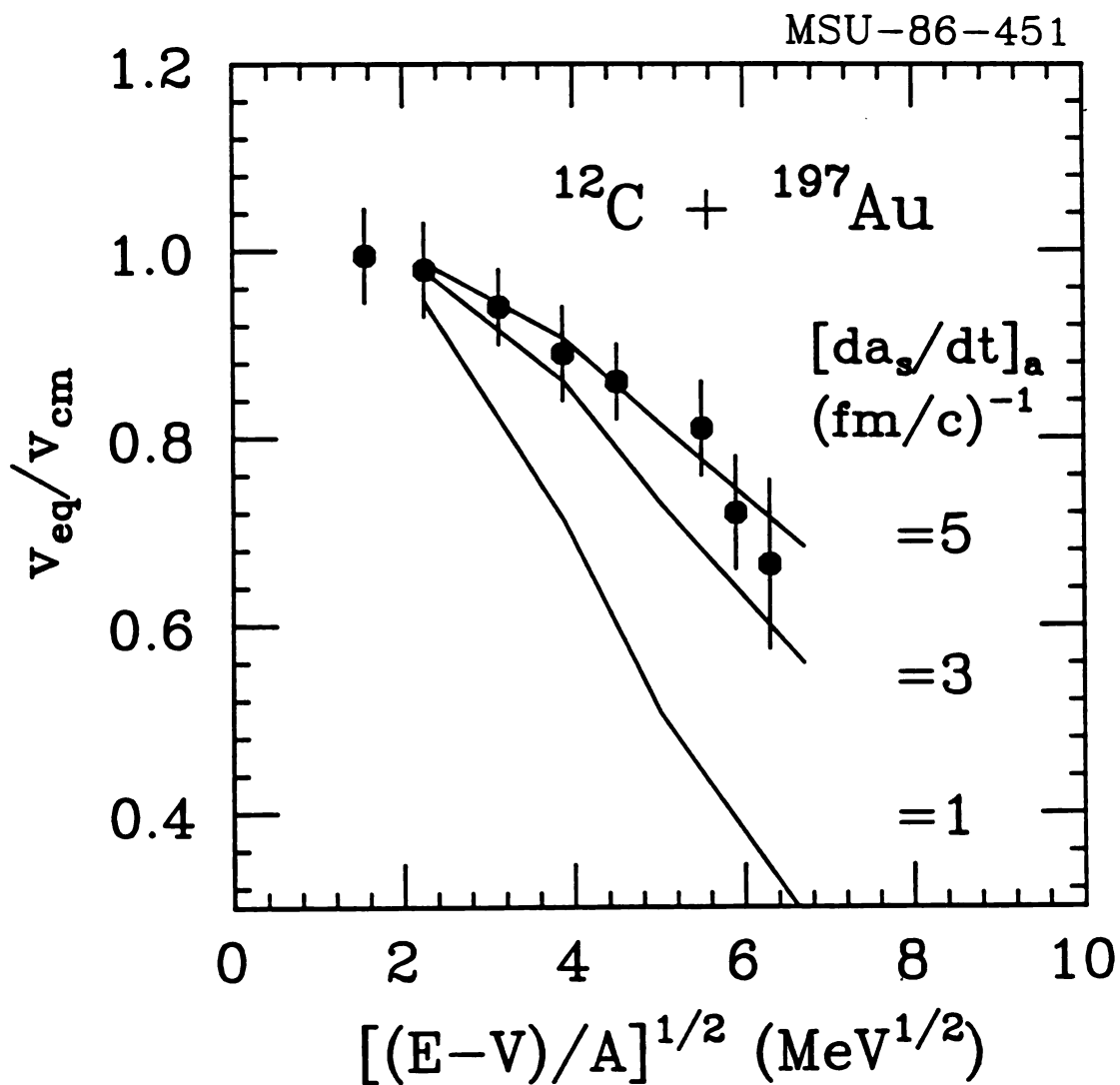


Figure VIII-9 : The momentum transfer systematics [FAT85] for  $^{12}\text{C}$ ,  $^{14}\text{N}$  induced reactions on  $^{197}\text{Au}$  are indicated by solid points. The solid curves represent calculations for the  $^{12}\text{C} + ^{197}\text{Au}$  system using three different accretion rates.



is inconsistent with the data. The time to equilibration is too long, allowing for excessive pre-equilibrium emission. The calculations at  $[da_s/dt]_a = 3$  and  $5 \text{ /(fm/c)}$  are more consistent with the experimental data.

The elemental cross sections predicted by these calculations are shown in Figure VIII-10 for the  $^{12}\text{C} + ^{197}\text{Au}$  system at  $E/A = 15$  and  $30$  MeV. The calculations using  $[da_s/dt]_a = 1 \text{ /(fm/c)}$  are shown as the upper and lower solid curves for  $E/A = 30$  and  $15$  MeV, respectively, using the same normalization between them, so that apart from the factor of 2 for separating the curves, the energy dependence of the calculated cross sections is preserved. While the  $15$  MeV curve is generally consistent with the data, the  $30$  MeV curve falls much too steeply with increasing fragment charge. As a result, the energy dependence for the heavier fragments is not well described. The dashed curves correspond to calculations using the accretion rate  $[da_s/dt]_a = 5 \text{ /(fm/c)}$  at the two incident energies. The description of both the charge distributions and the energy dependence is improved, though the energy dependence is still not well predicted. The disagreement may be the result of the absence of angular momentum effects in the calculation or of the very simple approximation used to describe the evolution of the system.

The normalizations for the case  $[da_s/dt]_a = 3 \text{ /(fm/c)}$  at  $E/A = 30$  MeV is about  $.5 \text{ b}$ . This is approximately a fifth of the total reaction cross section. The calculated multiplicities are low, with only about  $.03$  carbon ions being emitted per reaction.

It has been observed in the inclusive data that the cross sections for lighter fragments appear to have stronger non-compound contributions than those of heavier fragments. The pre-equilibrium and equilibrium

MSU-86-445

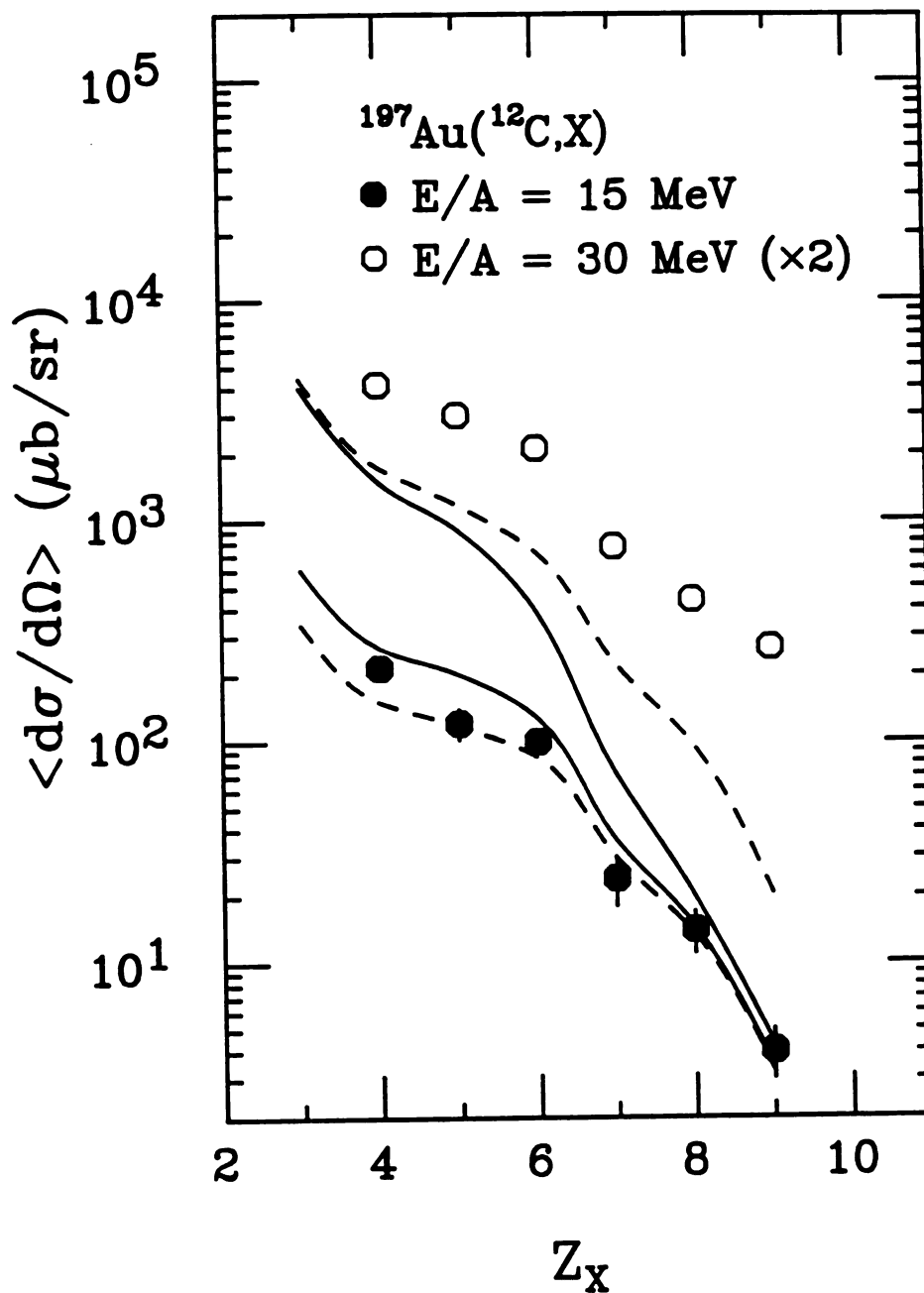


Figure VIII-10: The experimental elemental cross sections for  $^{12}\text{C}$  carbon induced reactions on  $^{197}\text{Au}$  at  $E/A=15$  and  $30$  MeV, shown as solid and open points, respectively, are compared to calculations with accretion rates of  $[da_s/dt]_a = 1$  (solid curve) and  $5$  (dashed curve) nucleons/(fm/c).

charge distributions are compared in Figure VIII-11. The equilibrium distribution is taken as the sum of the entire emission after equilibrium is reached and is shown as a solid curve. The dashed curve represents the mass spectrum of particles emitted while the source is moving faster than 0.15 of the beam velocity, i.e. during the early pre-equilibrium stages of the reaction. The pre-equilibrium contributions are stronger for lighter fragments.

Energy spectra are calculated according to Eq. III-1 with a Coulomb width of  $w_x = 8$  MeV. The emission temperature that is used to calculate the energy spectra includes a contribution from the Fermi velocities of nucleons which make up the source. While the sum of the Fermi momenta of all the target nucleons is zero, the sum of the momenta of any subset, e.g. the nucleons accreted by the source, is not. As a result, the effective temperature,  $T_{\text{eff}}$ , is given by

$$T_{\text{eff}} = T + \frac{k_F^2}{2m_0} a_i \frac{a_{st}(a - a_{st})}{(a-1) a_s^2}, \quad (\text{VIII-18})$$

where  $a_{st}$  is the number of spectator nucleons accreted by the source,  $k_F$  is the Fermi momentum, and  $m_0$  is the rest mass of the nucleon. Some fragments are emitted in unstable states which decay by particle emission. While some nuclei decay by emitting more than one particle in sequence, it is assumed here that the decay terminates after the first particle is emitted. The energy spectra for these fragments are calculated by generating the energy spectrum of the primary fragment according to Eq. III-1 and transforming this spectrum to that of the detected fragment by

MSU-86-446

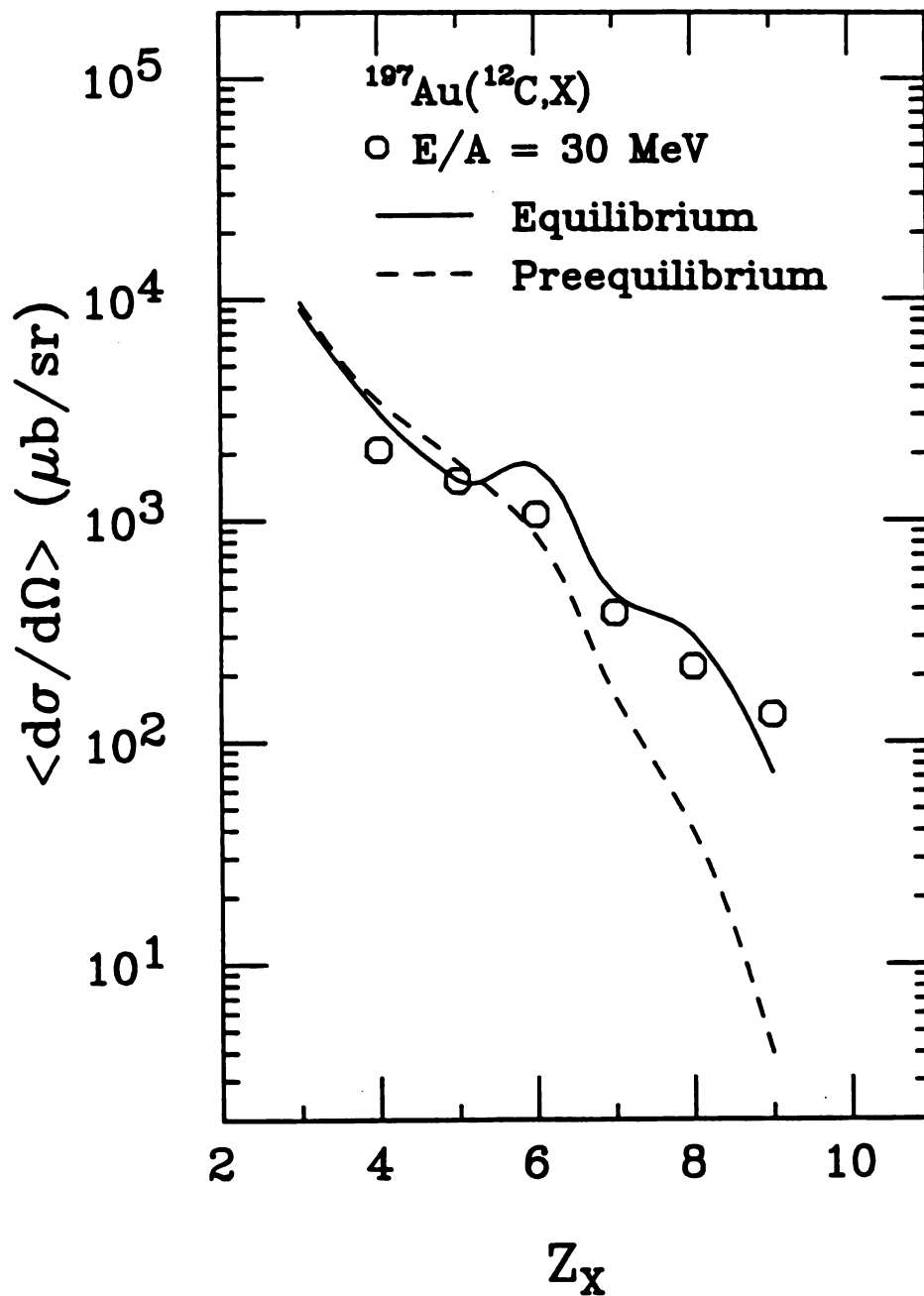


Figure VIII-11: The experimental elemental cross sections from  $^{12}\text{C} + ^{197}\text{Au}$  reactions at  $E/A=30$  MeV, shown as open points, are compared to the yield curves for the pre-equilibrium (dashed curve) and equilibrium (solid curve) stages of the reaction.

$$\frac{dN}{dE} = \frac{dN}{dE_p} \left( \frac{a_p}{a_i} \right) \quad \text{and} \quad E = E_p \left( \frac{a_i}{a_p} \right), \quad (\text{VIII-19})$$

where  $a_p$  and  $E_p$  are the mass and energy of the primary fragment. The effect of this transformation is to lower the fragment energies and thus make the energy spectra steeper.

The energy spectra for carbon nuclei  $^{12}\text{C} + ^{197}\text{Au}$  reactions at  $E/A = 30$  MeV measured at  $\theta = 30^\circ, 50^\circ, 70^\circ$ , and  $120^\circ$  are shown in Figure VIII-12 as solid points. Several important features of the energy spectra are reproduced by the calculations. The calculated differential cross sections exhibit a forward peaking in the laboratory. The energy spectra are characterized by approximately exponential slopes towards higher energies, which become steeper with increasing laboratory angle. The cross sections are somewhat over predicted for the  $50^\circ$  and  $70^\circ$  spectra. In addition, the calculated position of the peak in the distributions are at larger energies than in the observed spectra.

When the spectra are decomposed into the contributions from different stages of the collision, it is observed that different laboratory angles are sensitive to different stages of the reactions. Such a partial decomposition of the energy spectra of  $^{12}\text{C}$  fragments calculated at laboratory angles of  $\theta = 30^\circ$  and  $90^\circ$  is shown in Figure VIII-13. At  $\theta = 30^\circ$ , the pre-equilibrium contribution ( $v_s > 0.15 v_0$ ), shown as a dotted curve, are dominant, particularly at high fragment energies. The equilibrium contribution, shown as a dashed curve, is a small fraction of the total spectrum, shown as a solid curve, and contributes only at low energies. At  $\theta = 90^\circ$ , the equilibrium and

MSU-86-452

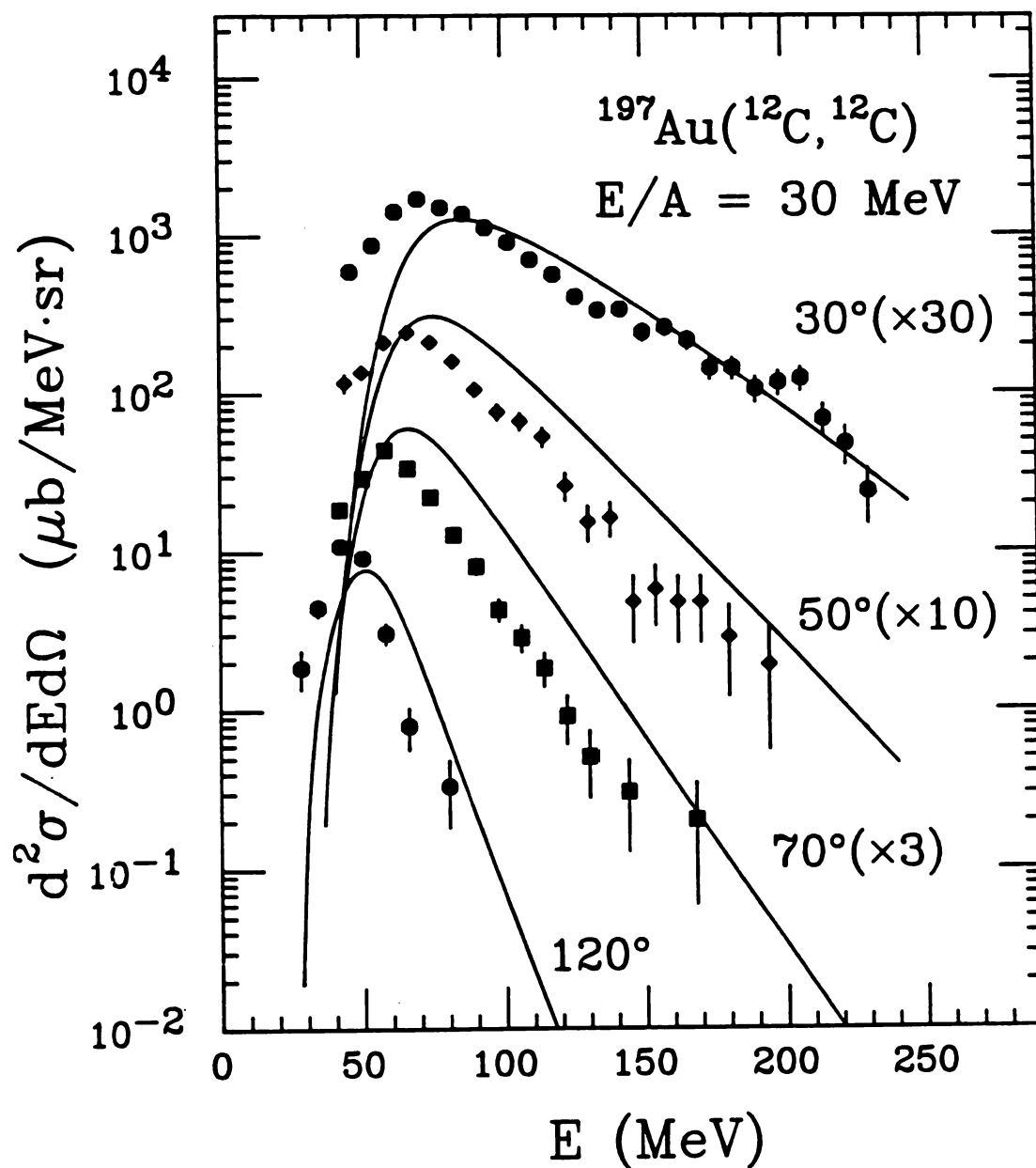


Figure VIII-12: The energy spectra measured in  $^{12}\text{C} + ^{197}\text{Au}$  reactions at  $E/A=30$  MeV at  $\theta=30^\circ$ ,  $50^\circ$ ,  $70^\circ$ , and  $120^\circ$ , shown as solid points, are compared to the calculation described in the text.

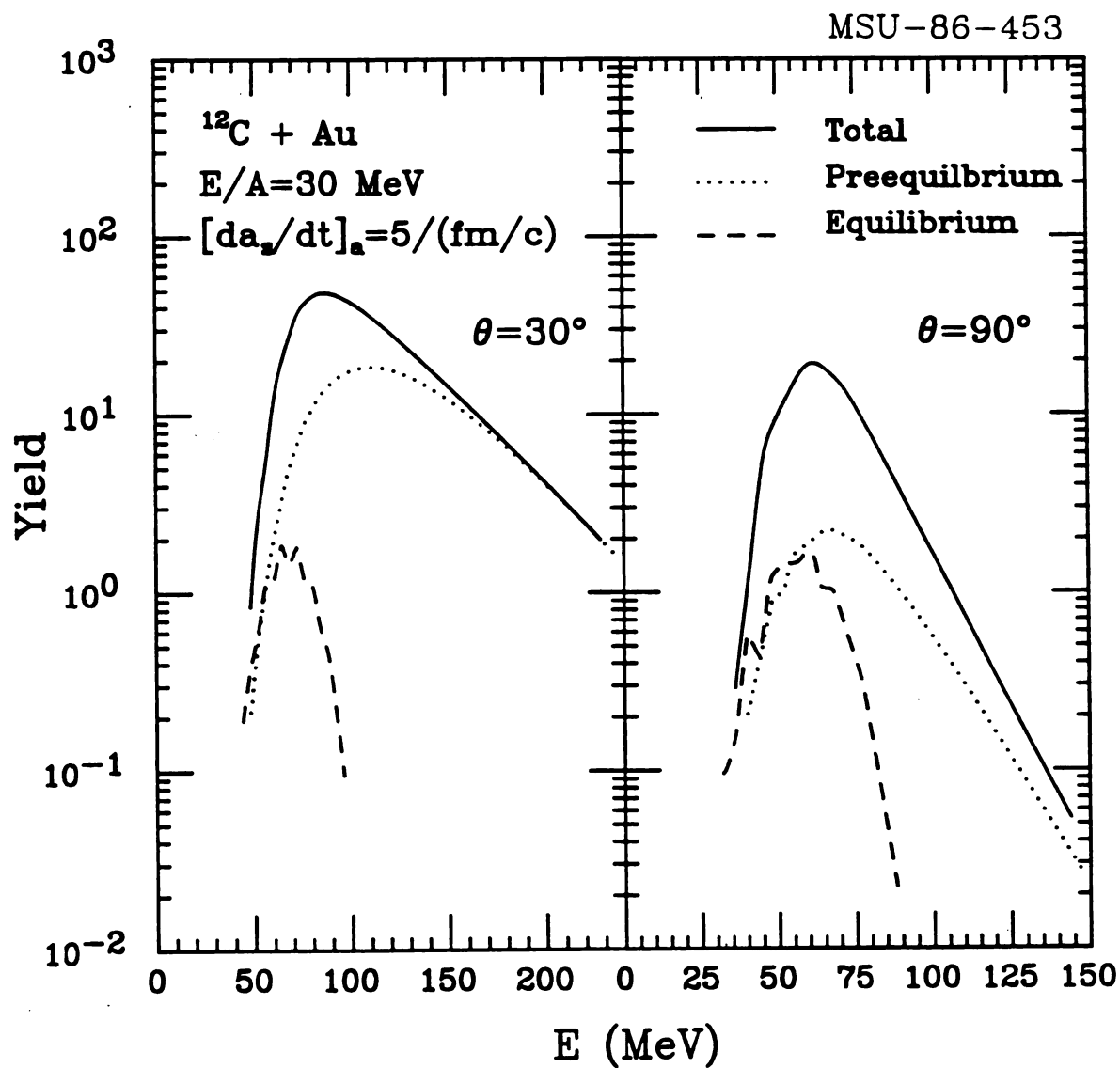


Figure VIII-13: The calculated energy spectra for  $^{12}\text{C} + ^{197}\text{Au}$  reactions at  $E/A = 30 \text{ MeV}$  at  $\theta = 30^\circ$  (left) and  $90^\circ$  (right), shown as solid curves, are decomposed into a pre-equilibrium component (dotted curve) and an equilibrium component (dashed curve).

pre-equilibrium contributions are comparable, but both are dominated by contributions during the late stages of equilibration. This kinematic effect allows for a certain selectivity on the part of the experimenter as to the stage of the collision to be studied.

A decomposition of the energy spectra into the contributions from different primary fragments is shown in Figure VIII-14, for a spectrum calculated for  $\theta=30^\circ$ . The total distribution is shown as the upper solid curve. The lower solid curve represents the primary spectrum of particle stable fragments. Contributions from the n, p, and  $\alpha$  decays of primary  $^{13}\text{C}$ ,  $^{13}\text{N}$ , and  $^{16}\text{O}$  fragments are represented by the dotted, dot-dashed, and dashed curves, respectively. As observed in Section VI.A.2., the sequential decay of primary fragments ought to lower the energy of the maximum in the energy spectrum. The calculations shown in Figure VIII-12 do not show the maxima in the observed locations. However, the spectra in Figure VIII-14 do show that the n and  $\alpha$  decay contributions do exhibit maxima at energies below the maxima for the stable fragments. However, because the unstable primary nuclei are produced predominantly during the hot, pre-equilibrium stages of the reaction, their contributions to the spectra have a kinematic boost to higher energies, obscuring the lowering of the Coulomb barrier. In addition, the full touching spheres Coulomb barrier was used in the calculation, which is an extreme assumption, and effects from the recoil of the fragment may need incorporation into the calculation. The differences in the slopes between the spectra are largely the result of the transformation of Eq. VIII-19, as well as differences in the time dependence of the emission rates.



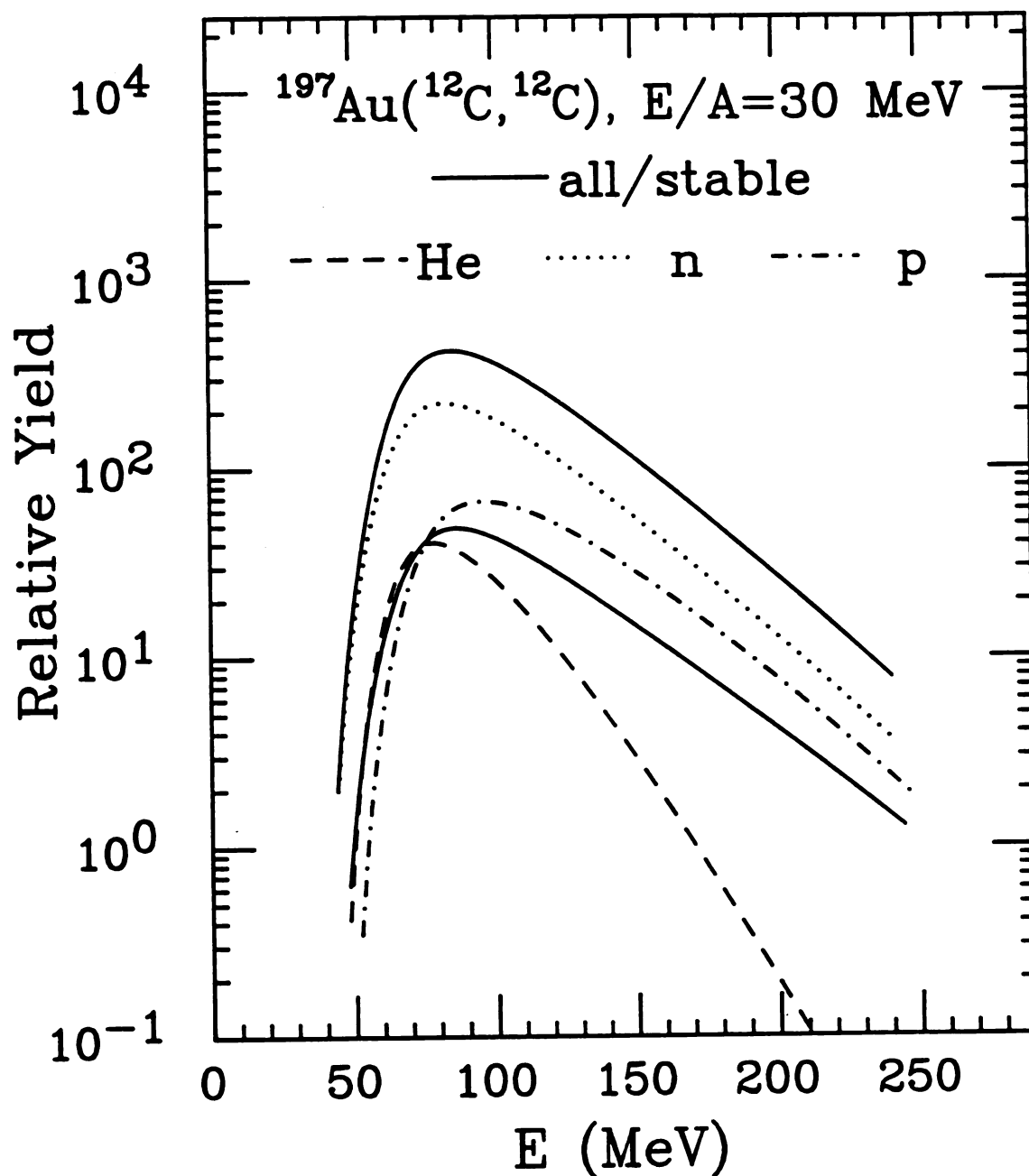


Figure VIII-14: The calculated energy spectrum for  $^{12}\text{C} + ^{197}\text{Au}$  reactions at  $E/A=30 \text{ MeV}$  at  $\theta=30^\circ$ , corresponding to the upper solid curve, is decomposed into the contributions from stable primaries (lower solid curve), neutron-unstable primary fragments (dotted curve), proton-unstable primary fragments (dot-dashed curve), and alpha-unstable primary fragments (dashed curve).

VIII.D. Summary :

The object of these calculations was to elucidate certain aspects of the transport phenomenon reflected in the competition between pre-equilibrium and equilibrium emission. The results of the calculations demonstrate the features expected from the decay of a localized region of excitation produced in a nuclear collision which evolves towards the equilibrated fusion-like system. It has been shown that the time scales for equilibration and statistical emission are comparable, and that many features of the data can result from this fact. The phenomena of incomplete momentum transfer, non-equilibrium emission, the evolution towards equilibrium-like emission for heavy fragments and fragments detected at backward angle, the energy and mass dependence of the fragment cross sections, and the kinematic effects of sequential decay are all qualitatively described in this framework.

The model may be extended by improving the descriptions of the dynamics of the collision process and of the emission mechanism itself. There is no rotation or angular momentum in the model, while the evidence is clear that these are important aspects of fragment emission (see Chapter IV). The linear evolution with time assumed here is much too simple to mimic what is probably a very complex evolution. The assumption of a hot source surrounded by a cold nucleus is also an extreme assumption. Because of the relation between light particle and fragment distributions discussed in Chapter IV, models calculating the time evolution of the one-body distributions in heavy ion collisions may yield better descriptions of the colliding systems. These may be incorporated in parametrized form into the present calculations.

In addition, the formulation for the instantaneous emission rate makes no allowance for in-medium, quantum mechanical, or geometrical and dynamical effects in the emission process. A more complete model for the emission mechanism may replace the present statistical ansatz.

## Chapter IX

### Summary and Conclusion

#### IX.A. Summary of present results :

The study of the emission of intermediate mass fragments promises to illuminate the more general question of how excited nuclear systems form and decay. The object of the present study was the characterization of relevant single particle inclusive and two-particle coincidence data at incident energies between  $E/A=15$  and 100 MeV and, from this, the identification of the statistical and dynamical aspects of nuclear reactions at intermediate energies.

The single particle inclusive cross sections were presented for four systems :  $^{12}\text{C} + \text{Ag}$  at  $E/A=15,30$  MeV,  $^{12}\text{C} + ^{197}\text{Au}$  at  $E/A=15,30$  MeV,  $^{14}\text{N} + \text{Ag}$  at  $E/A=35$  MeV, and  $^{32}\text{S} + \text{Ag}$  at  $E/A=22.5$  MeV. The energy spectra appear to be phase space dominated, showing no structure apart from a peaking at Coulombic energies and an exponential slope towards increasing energies. Though the spectra seem statistical in nature, a two source parametrization demonstrated that a significant fraction of the fragment cross sections can be described as "non-equilibrium", as

one component of the spectra has an average velocity larger than the center of mass velocity. The charge distributions are characterized by cross sections which decrease with increasing fragment charge. While the slope of the mass distributions have been offered as evidence of a critical phenomenon associated with the liquid-gas phase transition, the distributions from different systems differ in their slopes, and do not indicate a single critical parameter. Instead they indicate a projectile dependence of the emission rates, perhaps through a sensitivity to the entrance channel angular momentum. The isotopic distributions are peaked near the valley of  $\beta$  stability. They were described quite well by a Boltzman factor with the binding energies of the fragments and a modest temperature of  $T \approx 4$  MeV.

Using the  $^{32}\text{S} + \text{Ag}$  system at  $E/A=22.5$  MeV, the distributions of light particles detected in coincidence with intermediate mass fragments were investigated. The energy spectra of light particles detected in coincidence with intermediate mass fragments do not differ greatly from the inclusive cross sections. This observation is consistent with uncorrelated emission. The coincident light particles are, however, strongly correlated with the entrance channel reaction plane defined by the intermediate mass fragment and the beam axis. Furthermore, the emission pattern exhibits no distinct preference for the same or the opposite side of the beam axis as the coincident fragment. These angular correlations indicate that dynamical effects are strong and that the nuclear mean field remains a dominant factor in evolution of composite systems formed at intermediate bombarding energies.

The associated multiplicities of light particles and intermediate mass fragments was also investigated with the  $^{32}\text{S} + \text{Ag}$  system.

Intermediate mass fragments were found to be associated with the emission of approximately 10 nucleons, in the form of light particles, emitted at approximately half of the beam velocity. These particles carry away a significant fraction of the projectile momentum ( $\approx 0.2P_0$ ) and energy ( $\approx 160$  MeV out of 720 MeV), resulting in less than full momentum and energy transfer to the equilibrated fusion-like system. Intermediate mass fragments were found to be emitted with low multiplicities, with a total multiplicity for charges  $Z=3-24$  of approximately one. The associated multiplicities show little dependence on other emission and indicate that fragment emission is a stochastic, random process

The study of the velocity distributions of target residues in the  $^{32}\text{S} + \text{Ag}$  and the  $^{14}\text{N} + \text{Ag}$  systems provided information on the momentum and energy balance in these reactions. The distributions confirm that, in the events which dominate the production of intermediate mass fragments in the forward hemisphere, the momentum transfer to the equilibrated system is incomplete, and the fragment multiplicities are low. An indirect measurement of the undetected momentum and mass indicated that intermediate mass fragments are emitted in highly damped collisions, with 200-400 MeV of excitation in intrinsic degrees of freedom. Nonetheless, a substantial fraction of the projectile momentum is lost to pre-equilibrium emission of nuclei with an average velocity in the beam direction. Finally, the dependence of the residue angular distributions on the momentum of the coincident fragment indicate that emission of fragments at energies below the Coulomb barrier might be associated with additional particles emitted in the direction of the fragment. This can be interpreted as a result of a sizable contribution

from the sequential decay of a excited primary fragment into the detected intermediate mass fragment and one or more light particles.

While the experimental data provide many indications of non-equilibrium and dynamical effects, they also indicate that the emission mechanism is phase space dominated, and thus may be approximated by statistical methods. A comparison of data with a model calculation of statistical emission of intermediate mass fragments in both their ground and excited states suggests that fragments are emitted in excited states. The decay of particle unstable states produces characteristic structures in the fragment mass spectra and influences the isotopic distributions as well. The relative populations of excited states are also strongly influenced by sequential decay. Because the results of the calculations are sensitive to the precise nature of the branching ratios during sequential decay, the present calculations cannot determine to what extent the initial populations of the states can be approximated by purely statistical distributions among the asymptotic states.

A model calculation which incorporates statistical emission with a parametrization of the dynamical evolution of two colliding nuclei was presented. The time scale for statistical emission is found to be comparable to the equilibration time of the composite system, resulting in significant emission prior to equilibration. The model qualitatively reproduces certain features of the data, including non-compound emission, incomplete momentum transfer, the elemental yields, the energy dependence of the cross sections, and certain features of the energy spectra.

IX.B. Concluding remarks :

In spite of considerable progress in outlining the phenomenon of intermediate mass fragment emission, there is much room for contributions to the field, both experimental and theoretical.

Theoretical studies must concentrate on merging improved descriptions of the dynamical evolution of nuclear collisions and of the mechanism of fragment emission. Solutions to non-equilibrium transport equations promise to elucidate the dynamical features of the reactions. These calculate the one-body phase space densities during the collision. Since the coincidence data suggest that the collision dynamics affect intermediate mass fragment emission in much the same way as they affect nucleon emission, perhaps such models provide a satisfactory explanation of the collision dynamics.

Models of fragment emission may have to incorporate a dynamical description of the process. Fragments are, in a sense, complicated multiparticle correlations which must arise from the chaotic nucleon distributions in the emitting systems. At present the emission mechanism can only be approximated with statistical methods, and the new features which might reside in a microscopic understanding of the model remain the object of future study.

Progress in theory may be tied to additional experimental clues. Systematic studies of the target, projectile, and energy dependence of the inclusive and coincidence data are needed. Manifold coincidence studies, provided by large detector arrays, will provide a more precise picture of the dynamics of reactions producing fragments in both the forward and backward hemispheres. Studies of particle correlations at



small relative momenta promise to provide information on the spatial and temporal character of the emitting regions, in addition to information on the population of excited states. These studies may help investigators to understand the influence of impact parameter, fluctuations, temperature, collective motions, nuclear shapes, in-medium effects, and other statistical and dynamical aspects of nuclear collisions.

## APPENDICES

## Appendix A

### Kinematic bias in target velocities

Systematic errors in extracting information from the residue velocities can result from a biased sampling of the residue velocity distribution by a detector with a small angular acceptance. Consider a distribution in  $\vec{v}$  characterized by a mean velocity  $\vec{v}_0$  such that  $\vec{v} = \vec{v}_0 + \vec{v}'$ . For simplicity, we assume that the distribution of  $\vec{v}'$ ,  $f(\vec{v}')$ , depends only on  $v'$  so that  $f(\vec{v}') = f(v')$ .

By definition the average velocity for all particles is

$$\langle \vec{v} \rangle_{4\pi} = \vec{v}_0 . \quad (\text{A-1})$$

However, for a finite detector solid angle in the laboratory,  $\Omega$ , the measured average is given by:

$$\langle \vec{v} \rangle_{\Omega} = \frac{\int_{\Omega+} \vec{v} f(v') dv' d\Omega' + \int_{\Omega-} \vec{v} f(v') dv' d\Omega'}{\int_{\Omega+} f(v') dv' d\Omega' + \int_{\Omega-} f(v') dv' d\Omega'} , \quad (\text{A-2})$$

where  $\Omega+$  and  $\Omega-$  denote the solid angles corresponding to the two

kinematic solutions for values of  $\vec{v}'$ . In general, the measured average is different from  $\vec{v}_0$ .

As an illustration, we assume  $f(v') = \delta(v' - a)$ . If the detector is centered about  $\hat{v}_0$  and detects all particles emitted inside a cone of half angle  $\alpha$ , we can calculate the average velocity of the detected particles

$$\langle v \rangle_{\Omega} = \frac{1}{3} \sqrt{8v_0 a} \times \quad (A-3)$$

$$\frac{\left[ \frac{v_0^2 + a^2}{2 \cdot v_0 a} + \cos \theta \right]^{3/2} \Big|_{\theta=\theta_+}^{\theta=\theta_-} + \left[ \frac{v_0^2 + a^2}{2 \cdot v_0 a} + \cos \theta \right]^{3/2} \Big|_{\theta=\theta_-}^{\theta=\theta_+}}{(\cos \theta_+ - 1) - (\cos \theta_- + 1)},$$

with

$$\theta_{\pm} = \cos^{-1} \left\{ \frac{v_0}{a} \sin^2 \alpha \pm \cos \alpha \cdot \left[ 1 - \left( \frac{v_0}{a} \right)^2 \sin^2 \alpha \right]^{1/2} \right\}. \quad (A-4)$$

Here,  $\theta_+$  and  $\theta_-$  represent the angular limits of the solid angles of  $\Omega'$ ,  $\Omega_+$  and  $\Omega_-$ . For  $a=0.25v_0$ , the average emission angle in the laboratory is approximately  $16^\circ$ , similar to the one of the experimental distributions. For an acceptance angle of  $\alpha=6^\circ$ , the measured average velocity is  $\langle v \rangle \approx 1.1v_0$ .

## APPENDIX B

### Gamma ray efficiency calibration

The absolute efficiency,  $\epsilon_i^a$ , of a detector,  $i$ , at an energy,  $a$ , is determined from the coincidence rates with other detectors,  $j$ , which observe a coincident gamma ray of energy,  $b$  by the formula

$$\epsilon_i^a = \frac{\sum_j [ J_{ij}^{ab} - J_{ij}^{bb} (K_i^a/K_i^b) ] W_{ij}^{ab}}{\sum_j K_j^b \lambda_j^b} \quad (B-1)$$

where  $J_{ij}^{ab}$  represents rate for the coincident detection of gamma ray  $a$  in detector  $i$  with gamma ray  $b$  in detector  $j$ ;  $K_i^b$  is the single particle detection rate for gamma ray  $b$  in detector  $i$ ;  $\lambda_j^b$  is a term which corrects the efficiency for branching ratios and backgrounds; and  $W_{ij}^{ab}$  is the weighting determined by the angular correlation between the coincident gamma rays.

The first term in the numerator is the measured coincident rate for the two gamma rays. The second term is a correction for random coincidences. This correction is calculated from the rate of random

coincidences between two gamma rays of the same energy, corrected for the detection rates of the two gamma rays. The difference between these two terms is the estimated real coincidence rates.

The term  $\lambda_j^b$  is the product of two contributions. The first is the correction for background counts which would otherwise be included in the singles rate,  $K_j^b$ . The second factor, B, is the correction resulting from the specific branching in the decay scheme of the source. It is equal to the average number of gamma rays, a, which are emitted from the nucleus in coincidence with gamma ray, b. Both numbers, and thus  $\lambda$ , are less than one.

The term  $W_{ij}^{ab} = 1/\omega(a,b;\beta)$  where  $\omega$  is the angular correlation between the two gamma rays and  $\beta$  is the angle between the two gamma rays. This correlation is given by [GIL75]

$$\begin{aligned} \omega(\beta) = & \sum_k P_k(\cos\beta) \sum_{L_1, L_1'} (-1)^{L_1+L_1'} \delta_{L_1} \delta_{L_1'} R_K(L_1, L_1', J_2, J_1) \\ & \times \sum_{L_2, L_2'} \delta_{L_2} \delta_{L_2'} R_K(L_2, L_2', J_2, J_3) / \sum \delta_{L_1}^2 \sum \delta_{L_2}^2, \end{aligned} \quad (B-2)$$

where  $P_K$  is the  $k^{\text{th}}$  Legendre polynomial,  $L_i$  is the lowest multipole of the  $i^{\text{th}}$  transition,  $L_i'$  is the next highest multipole, and  $\delta_L$  is the mixing ratio defined by

$$\delta_L = \frac{\langle I_1 || L || I_2 \rangle}{\langle I_1 || L_0 || I_2 \rangle}, \quad (B-3)$$

and  $L_0$  is the lowest multipole. The angular momentum algebra is found in

$$R_K(L_1, L_2', J_2, J_1) = (-1)^{1+J_1-J_2+L'-L-K} \hat{J}_1 \hat{L} \hat{L}' \\ \times (L L' 1 -1 | K 0) \cdot W(J_1 J_1 L L' | K J_2), \quad (B-4)$$

where  $W$  is the Racah coefficient [RAC42] and  $\hat{L} = (2L+1)^{1/2}$ . In practice, the angular correlations are tabulated [TAY71] in the form

$$\omega(\beta) = \sum_k A_{2k} P_{2k}(\cos\beta), \quad (B-5)$$

where the  $A_{2k}$  are tabulated coefficients.

The efficiency calibration in the present experiment was executed with measurements with three sources,  $^{88}\text{Y}$ ,  $^{60}\text{Co}$ , and  $^{75}\text{Se}$ . The characteristics of sources are summarized in Table B-1.

Table B-1 : The properties of the sources used to provide absolute efficiency calibrations. The gamma ray source is given and the nucleus which emits the gamma ray is given in parenthesis, E is the transition energy,  $J_i^\pi$  is the initial and  $J_f^\pi$  is the final spin and parity of the transition, L is the multipole,  $\delta$  is the multipole mixing ratio, B is the number of partner gamma rays emitted in coincidence with each transition, and  $A_2$  and  $A_4$  are the angular correlation coefficients for the transition pairs.

Source	E (keV)	$J_i^{\pi}$	$J_f^{\pi}$	L	B	$A_2$	$A_4$
$^{60}\text{Co}$ ( $^{60}\text{Ni}$ )	1173	$4^+$	$2^+$	E2	1.	.10204	.00907
	1333	$2^+$	$0^+$	E2	1.		
<hr/>							
$^{88}\text{Y}$ ( $^{88}\text{Sr}$ )	898	$3^-$	$2^+$	E1	1.	-.07143	.0
	1836	$2^+$	$0^+$	E2	.92		
<hr/>							
$^{75}\text{Se}$ ( $^{75}\text{As}$ )	136	$\frac{5}{2}^+$	$\frac{3}{2}^-$	E1	.98	-.0328	.0
	264	$\frac{3}{2}^-$	$\frac{3}{2}^-$	M1, E2 ( $\delta = -.045$ )	.95		
	<hr/>						
	121	$\frac{5}{2}^+$	$\frac{5}{2}^-$	E1	1.0	-.413	.0
	279	$\frac{5}{2}^-$	$\frac{3}{2}^-$	M1, E2 ( $\delta = -.42$ )	.85		



## Appendix C

### Jacobian for relativistic transformation

The efficiency for detecting a gamma ray emitted from a nucleus which is moving in the laboratory inertial frame must be corrected for the relativistic transformation of the detector solid angles. The Jacobian of the transformation for the detection efficiencies is given by the ratio of the solid angle in the laboratory inertial frames,  $\Omega$ , and the solid angle in the inertial frame of the emitting nucleus:

$$|J| = \frac{d\Omega}{d\Omega^*} = \frac{d \cos \theta}{d \cos \theta^*} \quad , \quad (C-1)$$

where  $\theta$  and  $\theta^*$  are the angles between the directions of the gamma ray in the two inertial frames and the axis defined by the velocity of the emitting system,  $\vec{\beta}$ , and  $\Omega$  and  $\Omega^*$  are the solid angles subtended by the detectors in the two frames. For photons,  $p=E$ , and the Lorentz transformation [HAG73] between the two frames is

$$p_{||}^* = \gamma ( p_{||} - \beta E ) \quad \text{and} \quad (C-2)$$

$$E^* = \gamma (E - \beta p_{||}), \quad (C-3)$$

where  $\gamma^2 = (1 - \beta^2)^{-1}$  and  $p_{||} = E \cos \theta$  is the component of the momentum parallel to the velocity  $\beta$ . Thus

$$\cos \theta^* = \frac{p_{||}^*}{E^*} = \frac{\cos \theta - \beta}{1 - \beta \cos \theta} \quad \text{and} \quad (C-4)$$

$$\frac{d \cos \theta}{d \cos \theta^*} = \frac{(1 - \beta \cos \theta)^2}{(1 - \beta \cos \theta) + \beta (\cos \theta - \beta)} = \frac{(1 - \beta \cos \theta)^2}{(1 - \beta^2)} \quad (C-5)$$

so that

$$|J| = \gamma^2 (1 - \beta \cos \theta)^2. \quad (C-6)$$

## Appendix D

### Sequential decay

In the schematic statistical model described in Chapter VII, nuclei are assumed to be emitted in particle unstable states. These nuclei are then assumed to decay statistically by the emission of a light particle, n, p, d, t, or  $\alpha$ . Each nucleus is allowed to decay only by the particle decay channels listed in [AZJ86]. Thus, if proton and deuteron decay are specified, then only decay by these channels is calculated. If no decay channels are listed for a given state, then all energetically allowed decays are calculated.

The relative decay rates to final states are calculated for all allowed decay channels according to the statistical model [HAU52] [ST084]. The initial state  $|JM\rangle$  decays to a final state  $|jm\rangle|sm_s\rangle|\ell m_\ell\rangle$ , where  $J$  is the spin of the parent with projection  $M$ ,  $j$  is the spin of the daughter with projection  $m$ ,  $s$  is the spin of the emitted light particle with projection  $m_s$ , and  $\ell$  is the orbital angular momentum of emission with projection  $m_\ell$ . The relative branch to each final state is given by

$$r(\epsilon, J, j, s) \propto \sum_S \sum_{\ell} T_{\ell}(E) \times \sum_{m, m_s, m_{\ell}} |\langle jm, sm_s | S(M-m_{\ell}) \rangle \langle S(M-m_{\ell}), \ell m_{\ell} | JM \rangle|^2 \quad (D-1)$$

where  $E$  is the  $Q$  value of the decay and  $S$  is the channel spin resulting from the coupling of  $j$  and  $s$ . Eq. D-1 can be rewritten as

$$r(\epsilon, J, j, s) \propto \sum_S \sum_{\ell} T_{\ell}(E) \times \sum_{m_s, m} |\langle jm, sm_s | S(M-m_{\ell}) \rangle|^2 \times \sum_{m_{\ell}} |\langle S(M-m_{\ell}), \ell m_{\ell} | JM \rangle|^2 \quad (D-2)$$

By orthogonality

$$\sum_{m_s, m} |\langle jm, sm_s | S(M-m_{\ell}) \rangle|^2 = 1 \quad (D-3)$$

$$\sum_{m_{\ell}} |\langle S(M-m_{\ell}), \ell m_{\ell} | JM \rangle|^2 = 1 \quad (D-4)$$

With the restrictions on  $S$  and  $\ell$ , the final relation is

$$r(\epsilon, J, j, s) \propto \sum_{S=|j-s|}^{j+s} \sum_{\ell=|J-S|}^{J+S} T_{\ell}(E) . \quad (D-5)$$

Thus, all of the angular momentum dependence of the branching ratio is contained in the two summations.

The transmission coefficients,  $T_{\ell}$ , can be calculated in the WKB approximation [HAH86] for emission through a barrier to be

$$T_\ell = x \cdot \exp(-2\omega), \quad (D-6)$$

where

$$x = \left[ \frac{2\eta}{kR} + \frac{(\ell+0.5)^2}{k^2 R^2} - 1 \right] = \left( \frac{V_C + V_L - E}{E} \right)^{1/2}, \quad (D-7)$$

is a measure of the barrier from the Coulomb potential,  $V_C$ , and the effective centrifugal potential,  $V_L$ ; in addition,

$$\eta = 2\pi Z_1 Z_2 \frac{e^2}{hc} \left( \frac{\mu c^2}{2E} \right)^{1/2}, \quad k = \left( \frac{2\mu c^2 E}{\hbar^2 c} \right)^{1/2}, \quad (D-8)$$

$$R = (1.3 + 1.25 A^{1/3}) \text{ fm}, \text{ and} \quad (D-9)$$

$$\begin{aligned} -2\omega = & (2krx + \eta \left[ \pi + 2\sin^{-1} \left( \frac{\eta - kR}{(\eta^2 + (\ell+0.5)^2)^{1/2}} \right) \right] \\ & - (2\ell+1) \cdot \ln \left[ \frac{x(\ell+0.5) + \eta + (\ell+0.5)^2/(k^2 R^2)}{(\eta^2 + (\ell+0.5)^2)^{1/2}} \right] \end{aligned} \quad (D-10)$$

In these expressions,  $E$  is the transition energy,  $Z_1$  and  $Z_2$  are the charges of the daughter nuclei,  $A$  is the radius of the parent,  $\mu$  is the reduced mass of the daughter nuclei, and  $\ell$  is the partial wave of emission. Transmission coefficients calculated for partial waves,  $\ell=0-8$ , as a function of emission energy are shown in Figure D-1 for three decay channels of  $^{12}\text{C}$ :  $n$  (bottom),  $p$  (middle), and  $\alpha$  (top). The plots are truncated where the transition energy is greater than the barrier, at which point the transmission coefficients are taken to be 1.

MSU-86-457

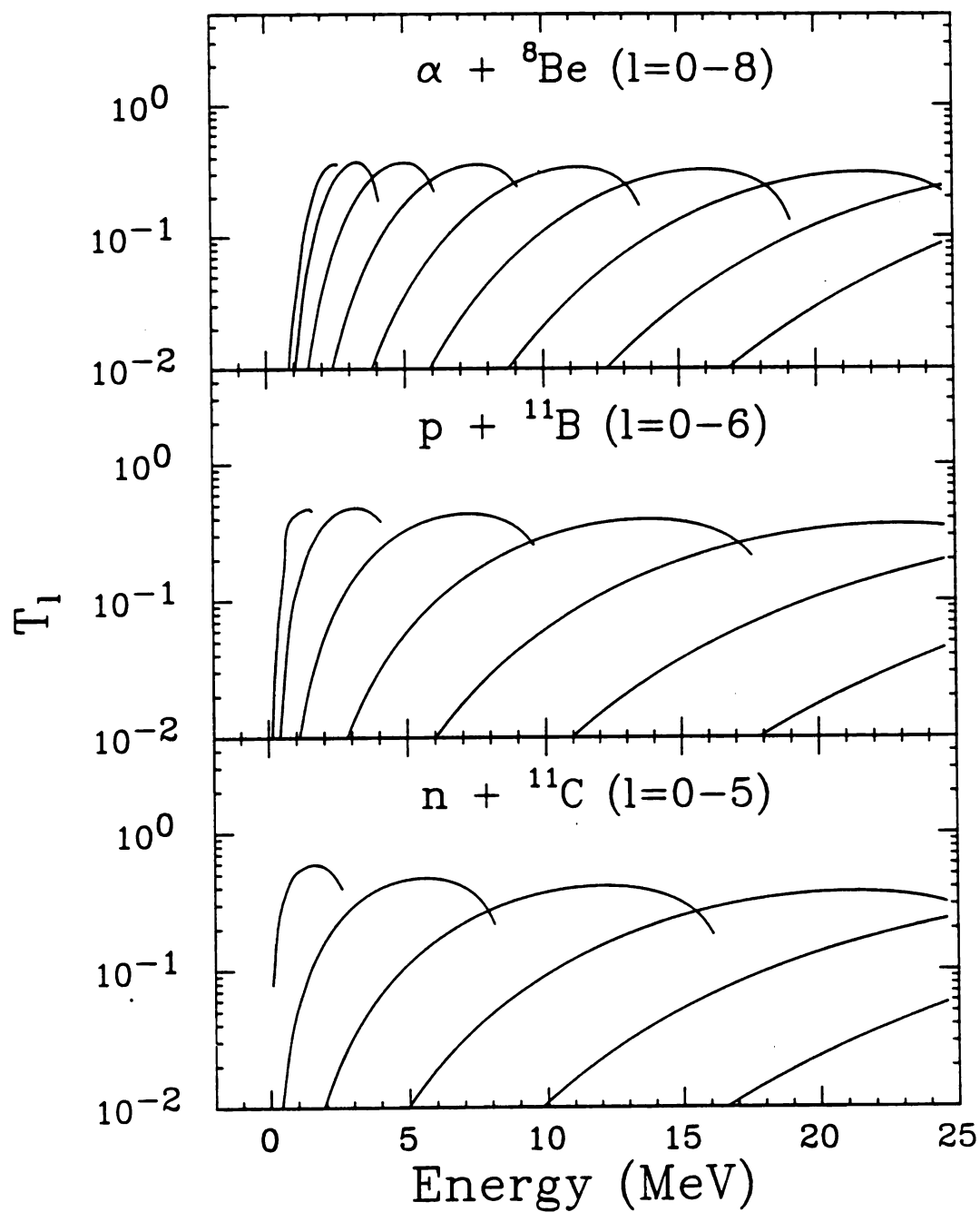


Figure D-1 : Transmission coefficients calculated as a function of energy with the form  $T_l = x \cdot \exp(-2\omega)$  for three decay channels of  ${}^{12}\text{C}$  : n(bottom), p(middle), and  $\alpha$ (top). The calculations are shown as solid curves for partial waves  $l=0$  to 8 (from left to right).

This formulation has the unfortunate property that the coefficients reach a maximum and then decline with increasing energy, and the coefficients do not approach unity. This can be avoided by dropping the pre-exponential term, so that

$$T_l = \exp(-2\omega). \quad (D-11)$$

Transmission coefficients calculated in this manner are shown in Figure D-2. This is the formulation of the transmission coefficients used in the calculations in Chapter VII.

Finally, results using a sharp cutoff approximation are investigated. In this approximation

$$T_l = \begin{cases} 1 & \text{if } x^2 < 0 \\ 10^{-9} & \text{if } x^2 > 0 \end{cases}, \quad (D-12)$$

where  $x^2$  is the sum of the Coulomb and the effective centrifugal potential barriers.

Figure D-3 depicts the mass distributions calculated with transmission coefficients calculated with Eq. D-6-10 for the case of emission from a nucleus,  $A=131$ ,  $Z=54$ , and  $T=5$  MeV. The histogram represents the distribution using Eq. D-11. The calculation using Eq. D-6 is represented by the open circles and using Eq. D-12 by solid squares. The mass distributions show little dependence on the form of the transmission coefficients.

The ratios of populations of levels in  ${}^4\text{He}$ ,  ${}^5\text{Li}$ ,  ${}^6\text{Li}$ , and  ${}^8\text{Be}$  are shown as functions of emission temperature in Figure D-4 for each of

MSU-86-458

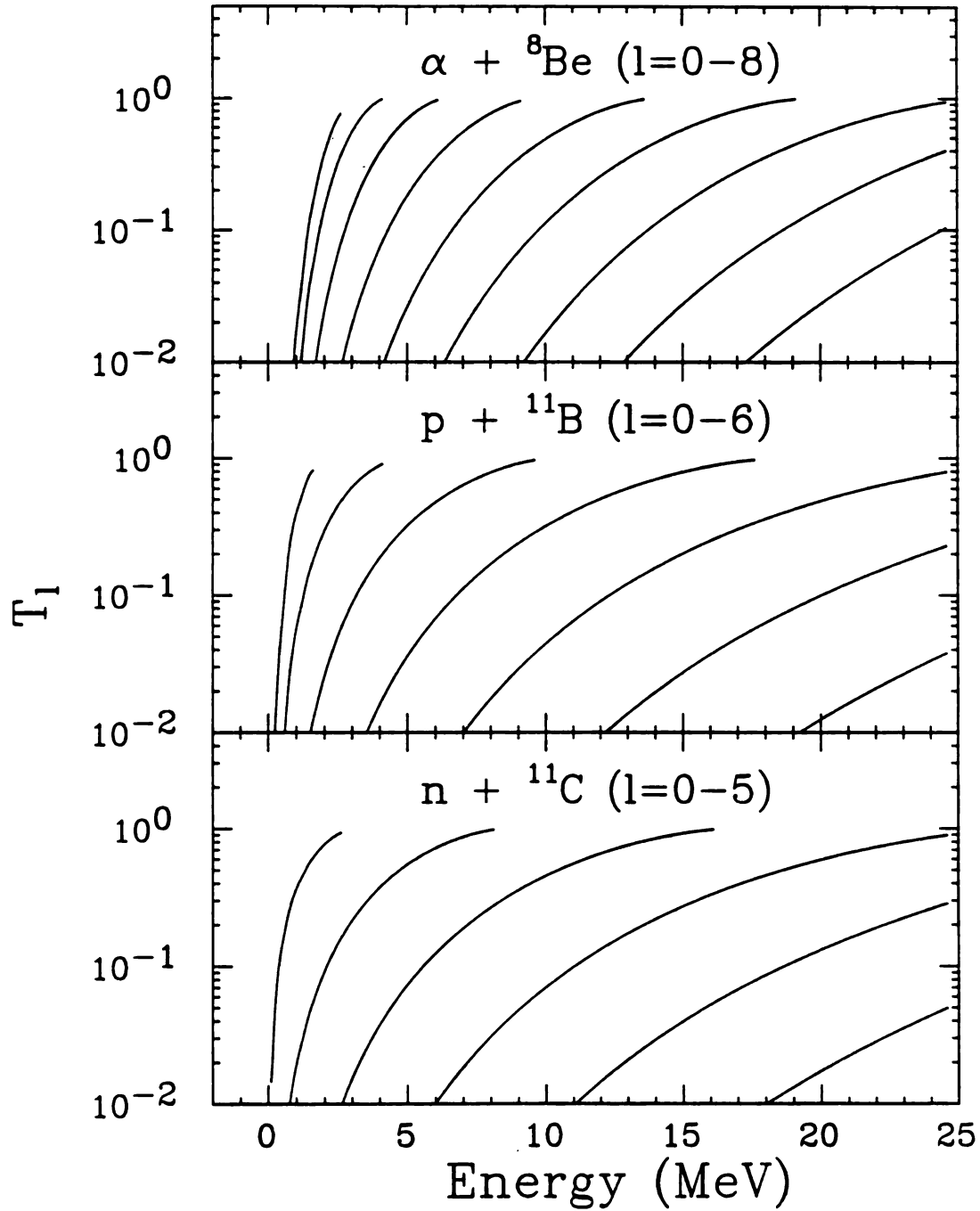


Figure D-2 : Transmission coefficients calculated as a function of energy with the form  $T_l = \exp(-2\omega)$  for three decay channels of  ${}^{12}\text{C}$  : n(bottom), p(middle), and  $\alpha$ (top). The calculations are shown as solid curves for partial waves  $l=0$  to 8 (from left to right).



MSU-86-459

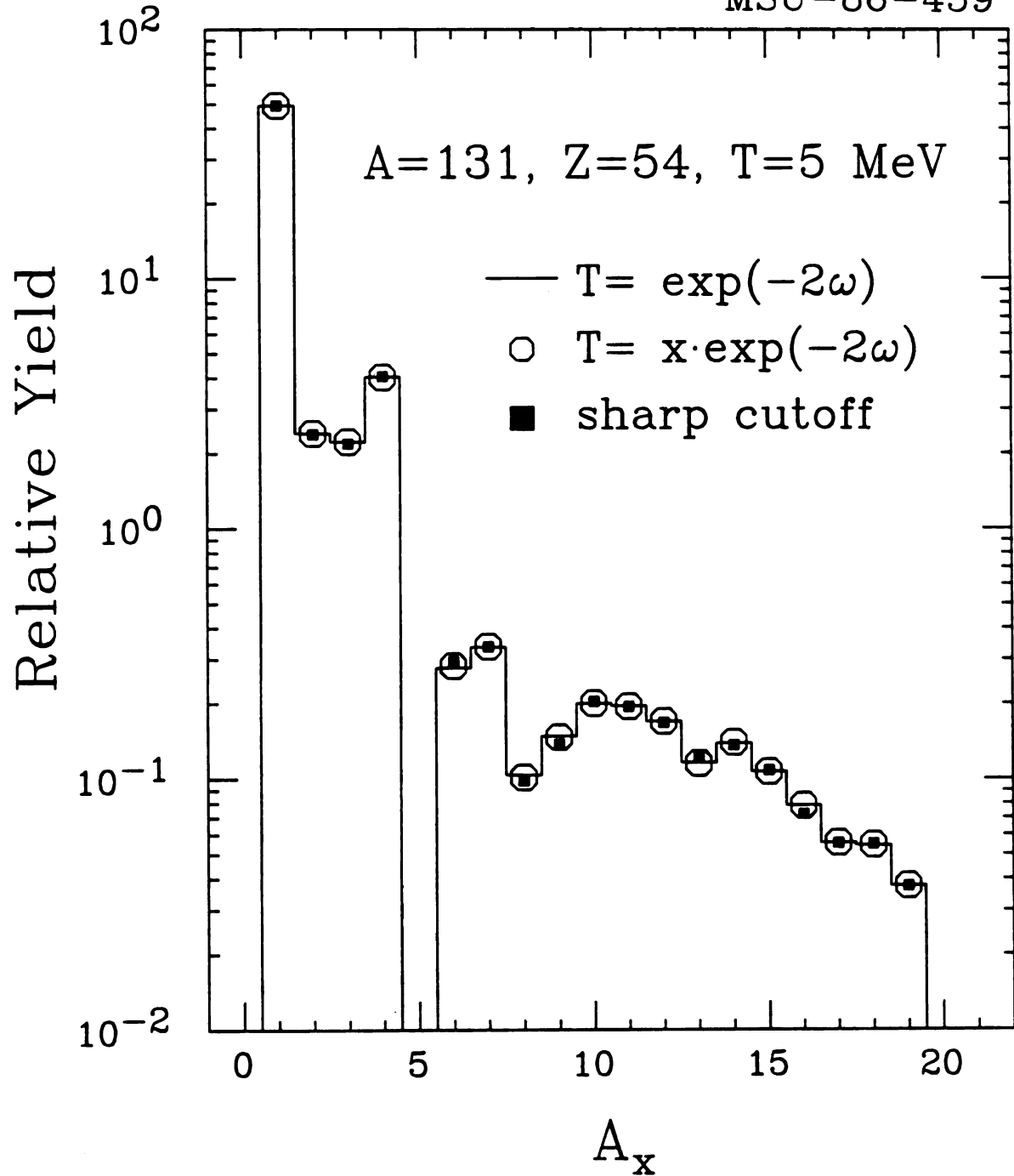


Figure D-3 : Final mass distributions calculated for the system  $A=131$ ,  $Z=54$ , and  $T=5 \text{ MeV}$  using three forms of the transmission coefficients :  $T_\ell = \exp(-2\omega)$  (histogram),  $T_\ell = x \cdot \exp(-2\omega)$  (open circles), and a sharp cutoff approximation (solid squares).

these calculations. The calculation used in the text, using Eq. D-11, is depicted by the solid line. The dashed line depicts the calculation using Eq. D-12. The dotted curves depict results using Eq. D-6. The comparison suggest that the calculations are not very sensitive to the precise formulation of the transmission coefficients.

It would be wrong to surmise from this that the decay calculations are insensitive to changes in the branching ratios. Instead, the effect on the branching ratios resulting by changing the transmission coefficients as above is insufficient to alter the final distributions significantly. Direct alterations in the branching ratios can produce significant effects. In order to demonstrate the possible effects, results of calculations using fixed branching ratios are shown in Figures D-5 and D-6. In these calculations, if the branching ratios are not specified in [AJZ86] then the particle branches are assumed to be equal for the allowed decay channels.

The effect of this assumption on the mass distribution is minimal. Figure D-5 shows the results using calculated branches as a histogram and the results using fixed branches as solid points. The variations are of the order of 10%. The general features of the mass distribution seem to be rather insensitive to these changes in the branching ratios.

The population of low lying bound states relative to the total ground state yield for states measured in the  $^{32}\text{S} + \text{Ag}$  reaction are shown as the hashed regions in Figure D-6. The solid curves represent the results of statistical calculations as presented in Figure VII-16, where the branching ratios for the available particle decay channels are calculated. The open points represent calculation with fixed branching ratios. Small differences are noticeable between the calculations for

MSU-86-460

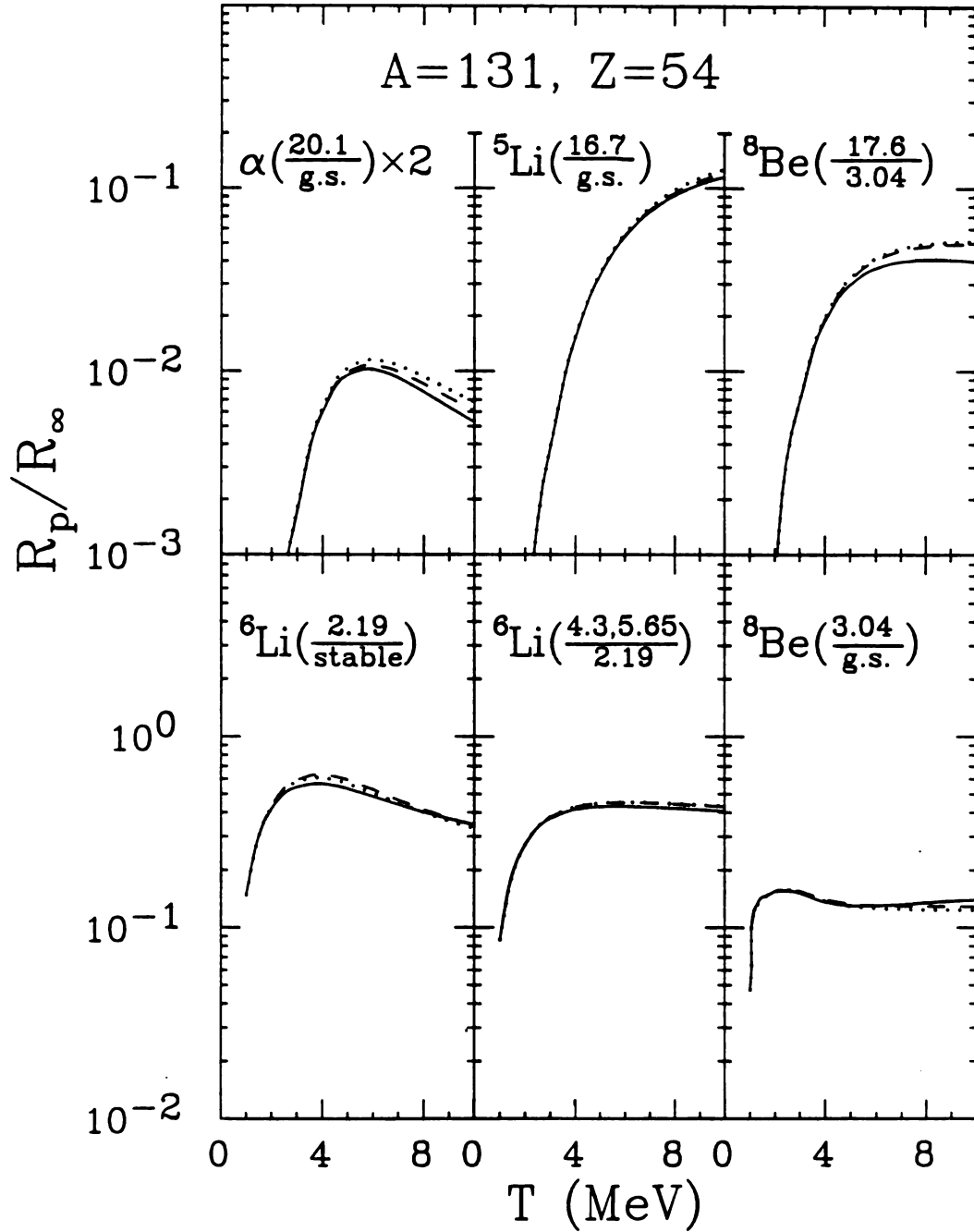


Figure D-4 : The ratios of populations of levels in  ${}^4\text{He}$ ,  ${}^5\text{Li}$ ,  ${}^6\text{Li}$ , and  ${}^8\text{Be}$  are shown as functions of emission temperature for calculations with different transmission coefficients :  $T_l = \exp(-2\omega)$  (solid curves),  $T_l = x \cdot \exp(-2\omega)$  (dotted curves), and a sharp cutoff approximation (dashed curves).

MSU-86-461

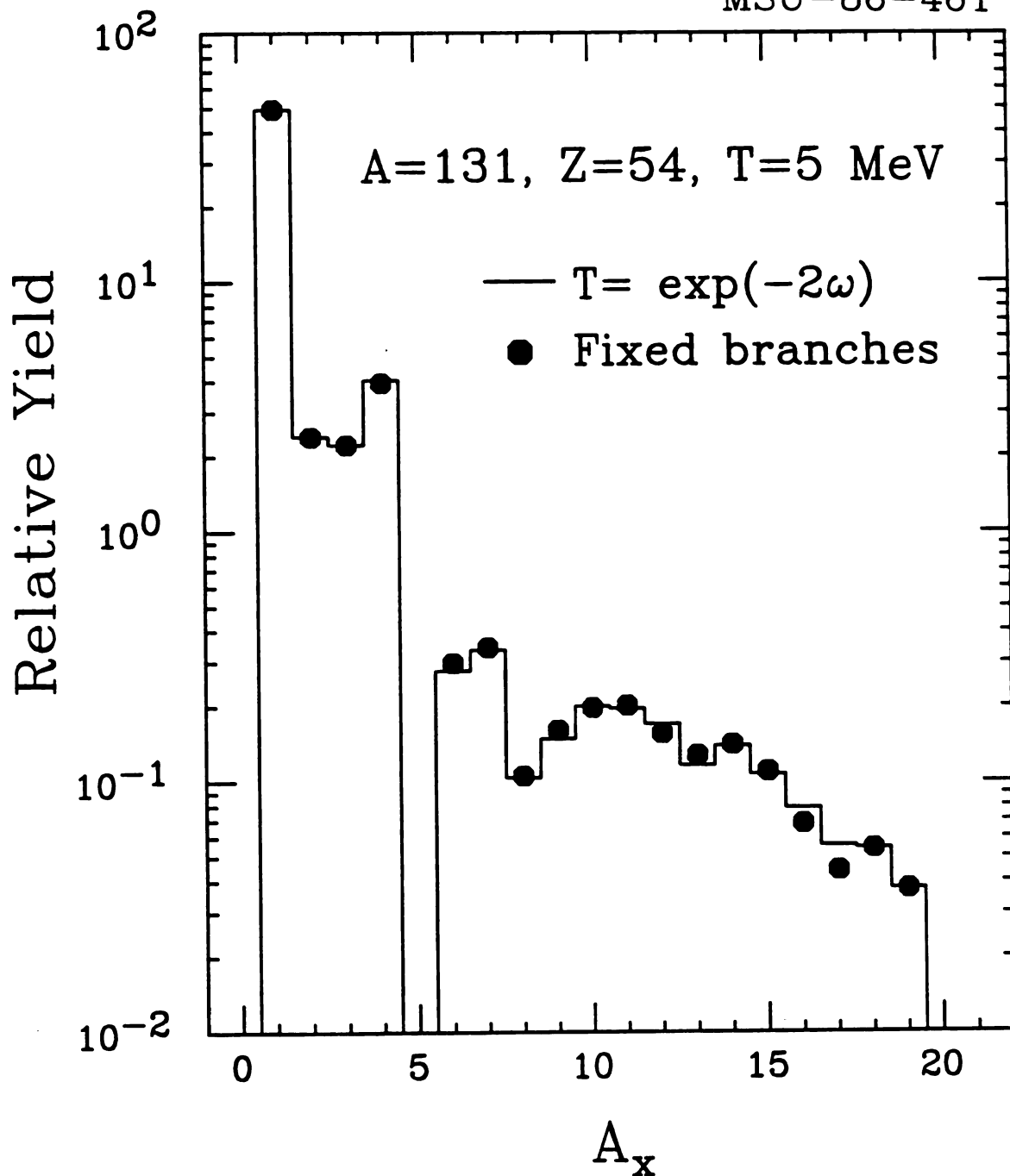


Figure D-5 : A comparison of the mass distributions calculated according to Eq. VII-1 using branching ratios calculated from transmission coefficients (histogram) and using branching ratios that are fixed to be equal for all allowed decay channels (solid points) for a system  $A=131$  and  $Z=54$  at  $T=5$  MeV.

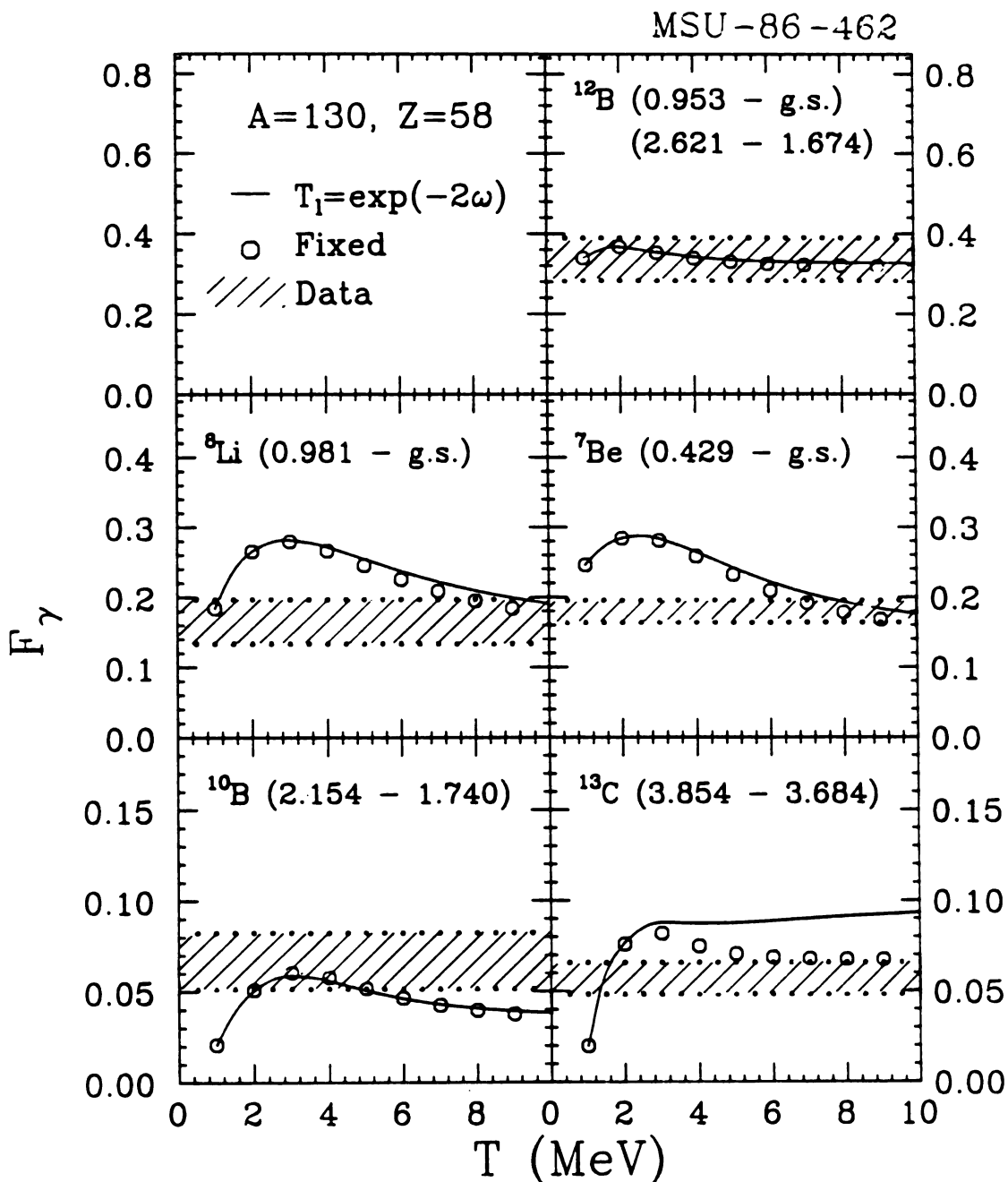


Figure D-6 : A comparison of the fractions,  $F_\gamma$ , of nuclei in their excited states as calculated according to Eq. VII-1 with branching ratios calculated according to statistical rules (solid curves) and branching ratios fixed to be equal for allowed channels for a system of  $A=130$  and  $Z=58$ . The fractions observed in  $^{32}\text{S}$  induced reactions on Ag at  $E/A=22.5$  MeV are indicated by the hashed regions.

all the state ratios; in the case of  $^{13}\text{C}$ , the change in the branching ratios results in a 25% suppression in the yield of the excited state relative to the ground state. This is the result of large differences in the  $\alpha/n$  branching ratios in  $^{17}\text{O}$  between the two calculations. The other ratios that are not affected here are not necessarily immune to problems with the branching ratios. Thus, while the calculations predict the general magnitude of the effects of sequential decay on these ratios, they cannot be expected to be in full agreement with the data simply as a result of uncertainties such as these.

## Appendix E

### Quantum Statistical Calculations

The quantum statistical model [ST083] [HAH86] describes the mass distribution in an infinite nuclear system in thermal and chemical equilibrium at a fixed temperature ( $T$ ), density ( $\rho$ ), and isospin ( $N/Z$ ). The distribution is calculated from the number of available states and their occupation for point like particles of mass,  $m_i$ , spin degeneracy,  $g_i=2s_i+1$ , where  $s_i$  is the spin, and chemical potential,  $\mu_i$ , in a volume

$$V = V_{\text{ext}} - \sum_i n_i V_i , \quad (\text{E-1})$$

where  $V_{\text{ext}} = (N+Z)/\rho$ . This is the total volume of the system less the volume excluded by the real volumes,  $V_i$ , of the nuclei.

The number of the  $i^{\text{th}}$  species of particle,  $n_i$ , is given by

$$n_i = \frac{1}{\exp(-\mu_i/T) - 1} + (g_i V / \lambda_i^3) \cdot F_{\text{BE}}(-\mu_i/T) \quad (\text{E-2})$$

for bosons and by

$$n_i = (g_i V / \lambda_i^3) (2/\pi^{1/2}) \cdot F_{FD}(\mu_i/T) \quad (E-3)$$

for fermions, where  $F_{BE}$  and  $F_{FD}$  are the Bose-Einstein and Fermi-Dirac integrals, respectively, and  $\lambda_i = h/(2\pi m_i T)^{1/2}$ , is the thermal wavelength. The chemical potential of each species is determined from the proton and neutron chemical potentials,  $\mu_p$  and  $\mu_n$ , by

$$\mu_i = Z_i \mu_p + N_i \mu_n + E_i, \quad (E-4)$$

where the binding energy,  $E_i$ , is given by

$$E_i = Z_i m_p c^2 + N_i m_n c^2 - m_i c^2. \quad (E-5)$$

$N_i$  and  $Z_i$  are the neutron and proton numbers of the source, and  $m_p$  and  $m_n$  are the masses of the proton and neutron.

Figures E-1 and E-2 demonstrate the dependence of the mass distributions on the temperature and density of the source. Figure E-1 shows the mass distribution for the quantum statistical breakup of a system with  $N/Z=77/54$  and a density,  $\rho/\rho_0 = .4$ , at temperatures of  $T=1, 3, 5$ , and  $10$  MeV. The primary distribution is indicated by the histogram and the final distribution, after the decay of unstable nuclei, by the solid points. At low temperatures, the system tends to divide itself into a small number of large fragments. As the temperature is increased, the mass distribution flattens and then falls with fragment mass, more steeply at higher temperatures.

Figure E-2 shows mass distributions of the same system at a temperature of  $T=5$  MeV at different densities. At high densities,



MSU-86-455

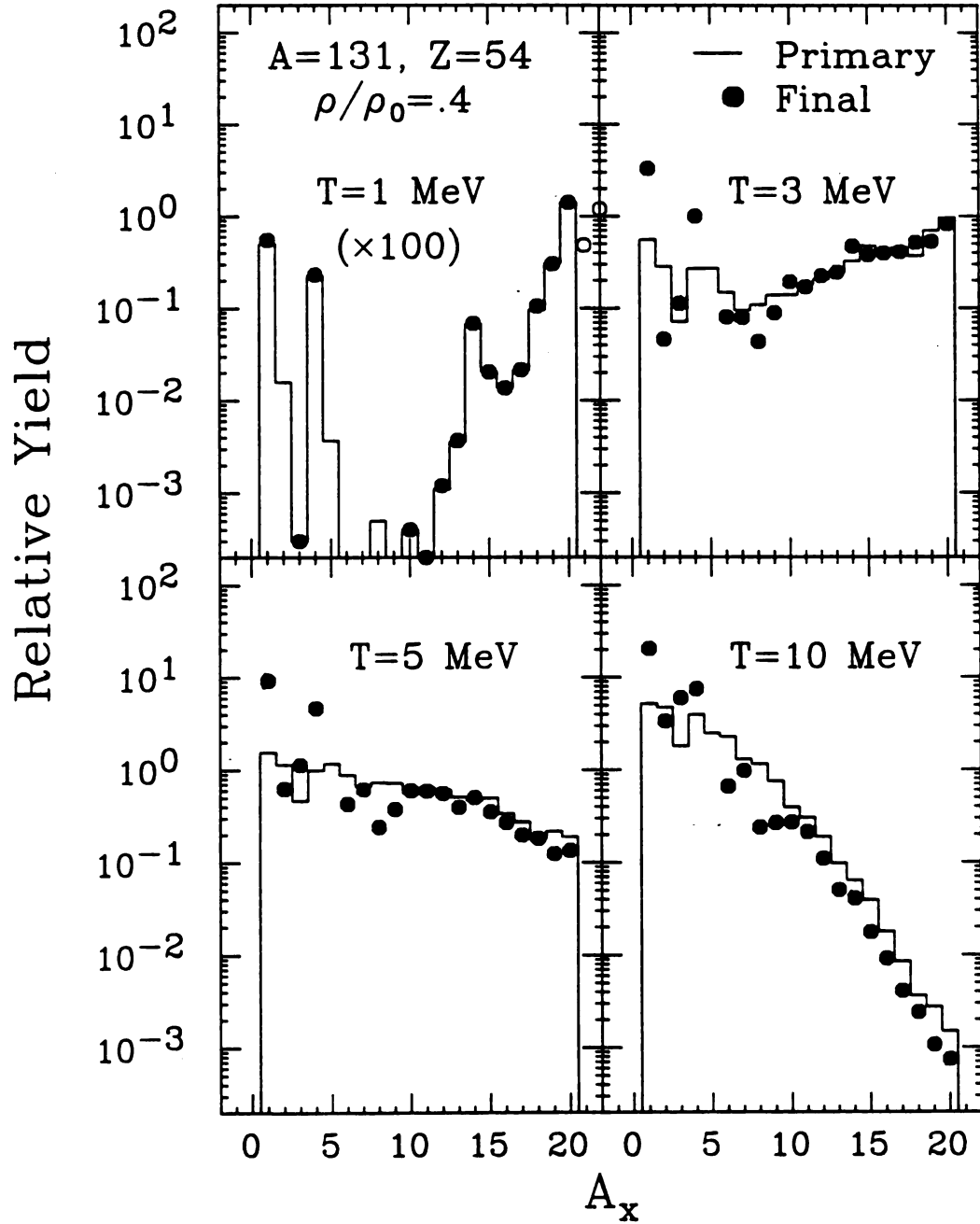


Figure E-1 : The primary and final mass distributions for the fragmentation of a  $A=131$ ,  $Z=54$  system at a density of  $\rho/\rho_0 = 0.4$  and at temperatures,  $T = 1, 3, 5$ , and  $10$  MeV, are shown as histograms and solid points, respectively.

MSU-86-456

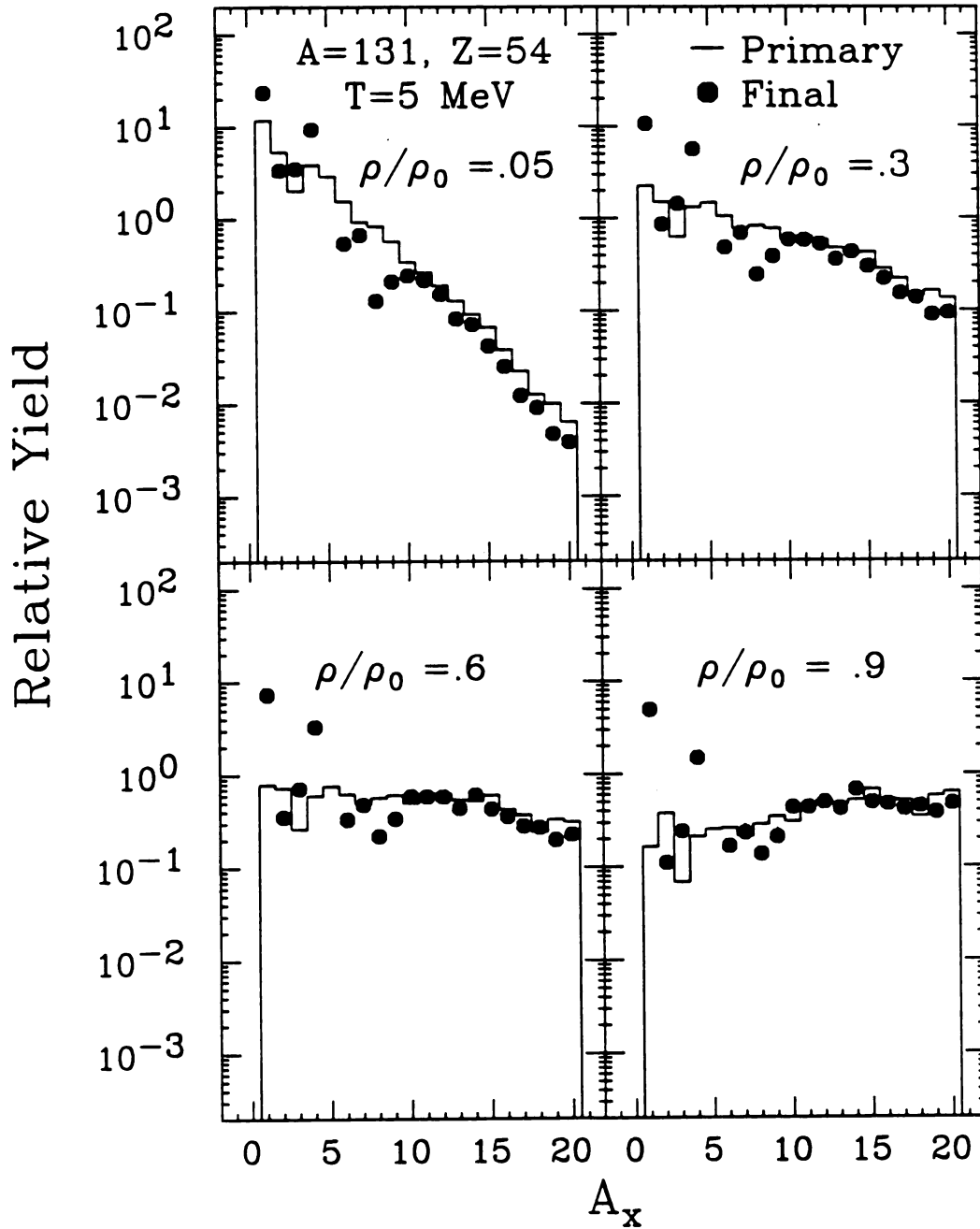


Figure E-2 : The primary and final mass distributions for the fragmentation of a  $A=131$ ,  $Z=54$  system at a temperature of  $T=5$  MeV and at densities,  $\rho/\rho_0 = .05, .3, .6$ , and  $.9$ , are shown as histograms and solid points, respectively.

$\rho/\rho_0=.9$ , the distribution rises with increasing fragment mass. As the density decreases, the relative yield of lighter fragments increases, and, by  $\rho/\rho_0=.05$ , the distribution falls steeply with increasing fragment mass.

At a fixed temperature, the effect of sequential decay on the relative populations of excited states will increase with increasing density. This results simply from the larger populations of the heavier parent nuclei relative to the primary populations of the daughters. At a fixed density, the effect of increasing temperature is mixed. The number of excited states in the primary distribution increases with temperature, but the relative population of the heavier, parent nuclei is diminished. As a result, the quantum statistical calculations of excited state populations are affected more gradually by increases in temperature as compared to results from Eq. VII-1.

There are a number of weaknesses in the quantum statistical model. The quantum statistical calculation is a nuclear matter calculation and neglects the effects of the nuclear surface and the long range Coulomb interaction. The energy spectra of fragments produced at lower incident energies,  $E/A \lesssim 100$  MeV, are distinctly peaked at energies approximately at the Coulomb barriers between the target-like system and the fragment. This indicates these are important aspects of the fragmentation process.

The fragment distributions become flatter with increasing excitation energy above  $E/A=15$  MeV. This trend runs counter to the expectations of the quantum statistical model, which predicts distributions which fall for steeply with increasing excitation. At high densities, the quantum statistical model becomes untenable [BERT83]. In

addition, in-medium effects may play a role in the fragment distributions. These are not included in the present model. At low densities, equilibrium may not be achieved.

## LIST OF REFERENCES

# LIST OF REFERENCES

## A

- [AIC84a] J. Aichelin, J. Hüfner, and R. Ibarra, Phys. Rev. C30 (1984) 107.
- [AIC84b] J. Aichelin and J. Hüfner, Phys. Lett. 136B (1984) 15.
- [AIC85a] J. Aichelin and G. Bertsch, Phys. Rev. C31 (1985) 1730.
- [AIC84c] J. Aichelin, Phys. Rev. Lett. 52 (1984) 2340.
- [AIC84d] J. Aichelin, Phys. Rev. C30 (1984) 718.
- [AJZ86] F. Ajzenberg-Selove, Nucl. Phys. A449 (1986) 1; Nucl. Phys. A443 (1985) 1; Nucl. Phys. A413 (1984) 1; Nucl. Phys. A392 (1983) 1; and Nucl. Phys. A375 (1982) 1.
- [ALE82] J.M. Alexander, D. Guerreau, and L.C. Vaz, Z. Phys. A305 (1982) 313.
- [ART77] A.G. Artukh, G.F. Gridnev, V.L. Mikheev, and V.V. Volkov, Nucl. Phys. A283 (1977) 350.
- [AUB82] R.L. Auble, J.B. Ball, F.E. Bertrand, R.L. Ferguson, C.B. Fulmer, I.Y. Lee, R.L. Robinson, G.R. Young, J.R. Wu, J.C. Wells, and H. Yamada, Phys. Rev. C25 (1982) 2504.
- [AWE79] T.C. Awes, C.K. Gelbke, B.B. Back, A.C. Mignerey, K.L. Wolf, P. Dyer, H. Breuer, and V.E. Viola, Jr., Phys. Lett. 87B (1979) 43.
- [AWE81a] T.C. Awes, G. Poggi, S. Saini, C.K. Gelbke, R. Legrain, and G.D. Westfall, Phys. Lett. 103B (1981) 417.
- [AWE81b] T.C. Awes, G. Poggi, C.K. Gelbke, B.B. Back, B.G. Glagola, H. Breuer, and V.E. Viola, Jr., Phys. Rev. C24 (1981) 89.
- [AWE82a] T.C. Awes, S. Saini, G. Poggi, C.K. Gelbke, D. Cha, R. Legrain, and G.D. Westfall, Phys. Rev. C25 (1982) 2361.

## B

- [BAB76] R. Babinet, L.G. Moretto, J. Galin, R. Jared, J. Moulton, and S.G. Thompson, Nucl. Phys. A258 (1976) 172.
- [BAR75] J. Barrette, P. Braun-Munzinger, and C.K. Gelbke, Nucl. Inst. Meth. 126 (1975) 181.
- [BAR78] J. Barrette, P. Braun-Munzinger, C.K. Gelbke, H.L. Harvey, H.E. Wegner, B. Zeidman, K.D. Hildenbrand, and U. Lynen, Nucl. Phys. A299 (1978) 147.
- [BARZ86] H.W. Barz, J.P. Bondorf, R. Donangelo, I.N. Mishustin, and H. Schultz, Nucl. Phys. A448 (1986) 753.
- [BAU85] W. Bauer, D.R. Dean, U. Mosel, and U. Post, Phys. Lett. 150B (1985) 53.
- [BAU86] W. Bauer, U. Post, D.R. Dean, and U. Mosel, Nucl. Phys. A452 (1986) 699.
- [BER84] M.A. Bernstein, W.A. Friedman, and W.G. Lynch, Phys. Rev. C29 (1984) 132; C30 (1984) 412E.
- [BER85] M.A. Bernstein, W.A. Friedman, W.G. Lynch, C.B. Chitwood, D.J. Fields, C.K. Gelbke, M.B. Tsang, T.C. Awes, R.L. Ferguson, F.E. Obenshain, F. Plasil, R.L. Robinson, and G.R. Young, Phys. Rev. Lett. 54 (1985) 402.
- [BERT83] G.F. Bertsch, Nucl. Phys. A400 (1983) 221c.
- [BERT81] G. Bertsch and J. Cugnon, Phys. Rev. C24 (1981) 2514.
- [BLO86] C. Bloch, W. Bennenson, E. Kashy, D.J. Morrissey, R.A. Blue, R.M. Ronningen, and H. Utsunomiya, Phys. Rev. C34 (1986) 850.
- [BOA84a] D.H. Boal, Phys. Rev. 30 (1984) 119.
- [BOA86] D.H. Boal and A.L. Goodman, Phys. Rev. C33 (1986) 1690.
- [BOH83] S. Bohrmann, J. Hüfner, and M.C. Nemes, Phys. Lett. 120B (1983) 59.
- [BON85b] J.P. Bondorf, R. Donangelo, I.N. Mishustin, C.J. Pethick, H. Schultz, and K. Sneppen, Nucl. Phys. A443 (1985) 321.
- [BON85c] J.P. Bondorf, R. Donangelo, I.N. Mishustin, and H. Schulz, Nucl. Phys. A444 (1985) 460.
- [BOR84] B. Borderie, M.F. Rivet, C. Cabot, D. Fabris, D. Gardes, H. Gauvin, F. Hanappe, and J. Peter, Z. Phys. A318 (1984) 315.

- [BOR85p] B. Borderie, M.F. Rivet, and D. Jacquet, Orsay preprint, IPNO-DRE-85-06.
- [BOU86s] R. Bougault, D. Horn, C.B. Chitwood, D.J. Fields, C.K. Gelbke, D.R. Klesch, W.G. Lynch, M.B. Tsang, K. Kwiatkowski, submitted for publication.
- [BRA78] P. Braun-Munzinger and J. Barrette, Nucl. Phys. A299 (1978) 161.
- [BRE79] A. Breskin, G. Charpak, S. Majewski, G. Melchart, G. Peterson, and F. Sauli, Nucl. Inst. Meth. 161 (1979) 19.
- [BRE84] A. Breskin, R. Chechik, P. Jacobs, I. Tserruya, and N. Zwang, Nucl. Inst. Meth. 221 (1984) 363.
- [BUE76] M. Buenerd, C.K. Gelbke, B.G. Harvey, D.L. Hendrie, J. Mahoney, A. Menchaca-Rocha, C. Olmer, and D.K. Scott, Phys. Rev. Lett. 37 (1976) 1191.

## C

- [CHAR85] R.J. Charity, M.A. McMahan, D.R. Bowman, Z.H. Liu, R.J. McDonald, G.J. Wozniak, S. Bradley, W.L. Kehoe, A.C. Mignerey, and M.N. Namboodiri, Phys. Rev. Lett. 56 (1986) 1354.
- [CHI83] C.B. Chitwood, D.J. Fields, C.K. Gelbke, W.G. Lynch, A.D. Panagiotou, M.B. Tsang, H. Utsunomiya, and W.A. Friedman, Phys. Lett. 131B (1983) 289.
- [CHI85] C.B. Chitwood, J. Aichelin, D.H. Boal, G. Bertsch, D.J. Fields, W.G. Lynch, M.B. Tsang, J.C. Shillcock, T.C. Awes, R.L. Ferguson, F.E. Obenshain, F. Plasil, R.L. Robinson, and G.R. Young, Phys. Rev. Lett. 54 (1985) 302.
- [CHI86a] C.B. Chitwood, C.K. Gelbke, J. Pochodzalla, Z. Chen, D.J. Fields, W.G. Lynch, R. Morse, M.B. Tsang, D.H. Boal, and J.C. Shillcock, Phys. Lett. 172B (1986) 27.
- [CHI86b] C.B. Chitwood, D.J. Fields, C.K. Gelbke, D.R. Klesch, W.G. Lynch, M.B. Tsang, T.C. Awes, R.L. Ferguson, F.E. Obenshain, F. Plasil, R.L. Robinson, and G.R. Young, Phys. Rev. C34 (1986) 858.
- [CUM85a] J.B. Cumming, Phys. Rev. C32 (1985) 1445.
- [CUR85t] M.J. Curtin, Michigan State University Ph.D. dissertation.



## D

- [DOS85] K.G.R. Doss, H.Å. Gustofsson, H.H. Gutbrod, B. Kolb, H. Löhner, B. Ludewigt, A.M. Poskanzer, T. Renner, H. Riedesel, H.G. Ritter, A. Warwick, and H. Wieman, Phys. Rev. C32 (1985) 116.

## F

- [FAI82] G. Fai and J. Randrup, Nucl. Phys. A381 (1982) 557.
- [FAI85] G. Fai, L.P. Csernai, J. Randrup, and H. Stöcker, Phys. Lett. 164B (1985) 265.
- [FAT85] M. Fatyga, K. Kwiatkowski, V.E. Viola, Jr., C.B. Chitwood, D.J. Fields, C.K. Gelbke, W.G. Lynch, J. Pochodzalla, M.B. Tsang, and M. Blann, Phys. Rev. Lett. 55 (1985) 1376.
- [FAT86pc] M. Fatyga, K. Kwiatkowski, V.E. Viola, Jr., W.G. Wilson, M.B. Tsang, J. Pochodzalla, W.G. Lynch, C.K. Gelbke, C.B. Chitwood, and D.J. Fields, in progress.
- [FIE84] D.J. Fields, W.G. Lynch, C.B. Chitwood, C.K. Gelbke, M.B. Tsang, H. Utsunomiya, and J. Aichelin, Phys. Rev. C30 (1984) 1912.
- [FIE86] D.J. Fields, W.G. Lynch, T.K. Nayak, M.B. Tsang, C.B. Chitwood, C.K. Gelbke, R. Morse, J. Wilczynski, T.C. Awes, R.L. Ferguson, F. Plasil, F.E. Obenshain, and G.R. Young, Phys. Rev. C34 (1986) 536.
- [FIE86p] D.J. Fields, C.K. Gelbke, W.G. Lynch, and J. Pochodzalla, MSU preprint MSUCL-576, accepted for publication in Phys. Lett.
- [FIN82] J.E. Finn, S. Agarwal, A. Bujak, J. Chuang, L.J. Gutay, A.S. Hirsch, R.W. Minich, N.T. Porile, R.P. Scharenberg, B.C. Stringfellow, and F. Turkot, Phys. Rev. Lett. 49 (1982) 1321.
- [FIS67] M.E. Fisher, Physics (N.Y.) 3 (1967) 255.
- [FOX86] D. Fox, D.A. Cebra, Z.M. Koenig, P. Ugorowski, and G.D. Westfall, Phys. Rev. C33 (1986) 1540.
- [FRA81] K.A. Frankel and J.D. Stevenson, Phys. Rev. C23 (1981) 1511.
- [FRI83a] W.A. Friedman and W.G. Lynch, Phys. Rev. C28 (1983) 16.
- [FRI83c] W.A. Friedman and W.G. Lynch, Phys. Rev. C28 (1983) 950.

## G

- [GA 84] C. Gale and S. Das Gupta, Phys. Rev. C29 (1984) 1339.
- [GALS84] S. Gales, E. Hourani, M. Hussonnois, J.P. Schapira, L. Stab, and M. Vergnes, Phys. Rev. Lett. 53 (1984) 759.
- [GAL75] J. Galin, L.G. Moretto, R. Babinet, R. Schmitt, R. Jared, and S.G. Thompson, Nucl. Phys. A255 (1975) 472.
- [GAL82] J. Galin, H. Oeschler, S. Song, B. Borderie, M.F. Rivet, I. Forest, R. Bimbot, D. Gardès, B. Gatty, H. Guillemot, M. Lefort, B. Tamain, and X. Tarrago, Phys. Rev. Lett. 48 (1982) 1787.
- [GAV83] A. Gavron, J.R. Beene, B. Cheynis, R.L. Ferguson, F.E. Obenshain, F. Plasil, G.R. Young, G.A. Pettitt, C.F. Maguire, D.G. Sarantites, M. Jääskeläinen, and K. Geoffroy-Young, Phys. Rev. C27 (1983) 450.
- [GEL78] C.K. Gelbke, C. Olmer, M. Buenerd, D.L. Hendrie, J. Mahoney, M.C. Mermaz, and D.K. Scott, Phys. Reports 42 (1978) 311.
- [GIL75] R.D. Gill, Gamma-Ray Angular Correlations, Academic Press (1975).
- [GOL74] A.S. Goldhaber, Phys. Lett. 53B (1974) 306.
- [GOL78] A.S. Goldhaber, Phys. Rev. C17 (1978) 2243.
- [GOO84] A.L. Goodman, J.I. Kapusta, and A.Z. Mekjian, Phys. Rev. C30 (1984) 851.
- [GOS77] J. Gosset, H.H. Gutbrod, W.G. Meyer, A.M. Poskanzer, A. Sandoval, R. Stock, and G.D. Westfall, Phys. Rev. C16 (1977) 629.
- [GRA85] S. Gralla, J. Albinski, R. Bock, A. Gobbi, N. Herrmann, K.D. Hildenbrand, J. Kuzminski, W.J.F. Müller, M. Petrovici, H. Stelzer, J. Töke, H.J. Wollersheim, A. Olmi, P.R. Maurenzig, and A.A. Stefanini, Phys. Rev. Lett. 54 (1985) 1898.
- [GRE80] R.E.L. Green and R.G. Korteling, Phys. Rev. C22 (1980) 1594.
- [GRO82] D.H.E. Gross, L. Satpathy, Meng Ta-chung, and M. Satpathy, Z. Phys. A309 (1982) 41.
- [GUS85] H.Å. Gustafsson, H.H. Gutbrod, B. Kolb, H. Löhner, B. Ludewigt, A.M. Poskanzer, T. Renner, H. Riedesel, H.G. Ritter, T. Siemiarczuk, J. Stepaniak, A. Warwick, and H. Weiman, Z. Phys. A321 (1985) 389.

## H

- [HAG73] R. Hagedorn, Relativistic Kinematics, Benjamin/Cummings, Reading, MA, 1973.
- [HAH86] D. Hahn and H. Stöcker, LBL preprint LBL-21386.
- [HAS85] B.E. Hasselquist, G.M. Crawley, B.V. Jacak, Z.M. Koenig, G.D. Westfall, J.E. Yurkon, R.S. Tickle, J.P. Dufour, and T.J.M. Symons, Phys. Rev. C32 (1985) 145.
- [HAU52] W. Hauser and H. Feshbach, Phys. Rev. 87 (1952) 366.
- [HIR84] A.S. Hirsch, A. Bujak, J.E. Finn, L.J. Gutay, R.W. Minich, N.T. Porile, R.P. Scharenberg, B.C. Stringfellow, and F. Turkot, Phys. Rev. C29 (1984) 508.
- [HYD71] E.K. Hyde, G.W. Butler, and A.M. Poskanzer, Phys. Rev. C4 (1971) 1759.

## J

- [JAC83] B.V. Jacak, G.D. Westfall, C.K. Gelbke, L.H. Harwood, W.G. Lynch, D.K. Scott, H. Stöcker, M.B. Tsang, and T.J.M. Symons, Phys. Rev. 51 (1983) 1846.
- [JAC85] B.V. Jacak, D. Fox, and G.D. Westfall, Phys. Rev. C31 (1985) 704.
- [JAQ83] H.R. Jaquaman, A.Z. Mekjian, and L. Zamick, Phys. Rev. C27 (1983) 2782.
- [JAQ84] H.R. Jaquaman, A.Z. Mekjian, and L. Zamick, Phys. Rev. C29 (1984) 2067.
- [JACQ84] D. Jacquet, E. Duek, J.M. Alexander, B. Borderie, J. Galin, D. Gardès, D. Guerreau, M. Lefort, F. Monnet, M.F. Rivet, and X. Tarrago, Phys. Rev. Lett. 53 (1984) 2226.
- [JAK82] B. Jakobsson, G. Jönsson, B. Lindkvist, and A. Oskarsson, Z. Phys. A307 (1982) 293.
- [JEN86] B.K. Jennings, D.H. Boal, and J.C. Shillcock, Phys. Rev. C33 (1986) 1303.

## K

- [KAU80] S.B. Kaufman, E.P. Steinberg, B.D. Wilkins, and D.J. Henderson, Phys. Rev. C22 (1980) 1897.
- [KIA70] C.S. Kiang, Phys. Rev. Lett. 24 (1970) 47.

- [KRI85] P. Kristiansson, L. Carlén, H.Å. Gustafsson, B. Jakobsson, A. Oskarsson, H. Ryde, J.P. Bondorf, O.B. Nielsen, G. Løvholden, T.F. Thorsteinsen, D.Heuer, and H. Nifenecker, Phys. Lett. 155B (1985) 31.
- [KRU85] H. Kruse, B.V. Jacak, J.J. Molitoris, G.D. Westfall, and H. Stöcker, Phys. Rev. C31 (1985) 1770.
- [KUD84] H. Kudo, K.J. Moody, and G.T. Seaborg, Phys. Rev. C30 (1984) 1561.
- [KWI83] K. Kwiatkowski, S.H. Zhou, T.E. Ward, V.E. Viola, Jr., H. Breuer, G.J. Matthews, A. Gökmen, and A.C. Mignerey, Phys. Rev. Lett. 50 (1983) 1648.
- [KWI86] K. Kwiatkowski, J. Boshkin, H. Karwowski, M. Fatyga, and V.E. Viola, Jr. , Phys. Lett. 171B (1986) 41.

## L

- [LOC82] D.K. Lock, R. Vandenbosch, and A. Lazzarini, Nucl. Phys. A384 (1982) 241.
- [LOC85] D.K. Lock, R. Vandenbosch, and J. Randrup, Phys. Rev. C31 (1985) 1268.
- [LYN82] W.G. Lynch, L.W. Richardson, M.B. Tsang, R.E. Ellis, C.K. Gelbke, and R.E. Worner, Phys. Let. 108B (1982) 274.
- [LYN83] W.G. Lynch, C.B. Chitwood, M.B. Tsang, D.J. Fields, D.R. Klesch, C.K. Gelbke, G.R. Young, T.C. Awes, R.L. Ferguson, F.E. Obenshain, F. Plasil, R.L. Robinson, and A.D. Panagiotou, Phys. Rev. Lett. 51 (1983) 1850.

## M

- [MAC85b] H. Machner, Phys. Rev. C31 (1985) 1271.
- [MAR69] P. Marmier and E. Sheldon, Physics of Nuclei and Particles, 1 p.38, Academic Press (1969).
- [MAR85] J.B. Marston and S.E. Koonin, Phys. Rev. Lett. 54 (1985) 1139.
- [MAS81] N. Masuda, K. Inoue, and Y. Ito, Phys. Rev. C23 (1981) 1543.
- [MEK78] A.Z. Mekjian, Phys. Rev. C17 (1978) 1051.
- [MEY80] W.G. Meyer, H.H. Gutbrod, Ch. Lukner, and A. Sandoval, Phys. Rev. C22 (1980) 179.

- [McM85] M.A. McMahan, L.G. Moretto, M.L. Padgett, G.J. Wozniak, L.G. Sobotka, and M.G. Mustafa, Phys. Rev. Lett. 54 (1985) 1995.
- [MIG80] A.C. Mignerey, V.E. Viola, Jr., H. Breuer, K.L. Wolf, B.G. Glagola, J.R. Birkelund, D. Hilscher, J.R. Huizenga, W.W. Schröder, and W.W. Wilcke, Phys. Rev. Lett. 45 (1980) 509.
- [MIN82] R.W. Minich, S. Agarwal, A. Bujak, J. Chuang, J.E. Finn, L.J. Gutay, A.S. Hirsch, N.T. Porile, R.P. Scharenberg, B.C. Stringfellow, and F. Turkot, Phys. Lett. 118B (1982) 458.
- [MIT85] W. Mittig, A. Cunsolo, A. Foti, J.P. Wieleczko, F. Auger, B. Berthier, J.M. Pascaud, J. Quebert, and E. Plagnol, Phys. Lett. 154B (1985) 259.
- [MOR72] L.G. Moretto, Phys. Lett. 40B (1972) 185.
- [MOR75a] L.G. Moretto, Nucl. Phys. A247 (1975) 211.
- [MOR75b] L.G. Moretto, S.K. Kataria, R.C. Jared, R. Schmitt, and S.G. Thompson, Nucl. Phys. A255 (1975) 491.
- [MOR76] L.G. Moretto, J. Galin, R. Babinet, Z. Fraenkel, R. Schmitt, R. Jared, and S.G. Thompson, Nucl. Phys. A259 (1976) 173.
- [MORR79] D.J. Morrissey, L.F. Oliveira, J.O. Rasmussen, G.T. Seaborg, Y. Yariv, and Z. Fraenkel, Phys. Rev. Lett. 43 (1979) 1139.
- [MORR84] D.J. Morrissey, W. Bennenson, E. Kashy, B. Sherrill, A.D. Panagiotou, R.A. Blue, R.M. Ronningen, J. Van der Plicht, and H. Utsunomiya, Phys. Lett. 148B (1984) 423.
- [MORR85] D.J. Morrissey, W. Bennenson, E. Kashy, C. Bloch, M. Lowe, R.A. Blue, R.M. Ronningen, B. Sherrill, H. Utsunomiya, and I. Kelson, Phys. Rev. C32 (1985) 877.
- [MUR84] M.J. Murphy, S. Gil, M.N. Harakeh, A. Ray, A.G. Seamster, R. Vandenbosch, and T.C. Awes, Phys. Rev. Lett. 53 (1984) 1543.
- [MUR86] M.J. Murphy, D. Leach, A. Ray, A. Seamster, and R. Vandenbosch, Phys. Rev. C33 (1986) 165.

## O

- [ONO86] A.D. Onofrio, B. Delaunay, J. Delaunay, H. Dumont, A. Brondi, R. Moro, M. Romano, F. Terrasi, J.F. Bruandet, and J. Gomez del Campo, Saclay preprint Sch-704 1986.

## P

- [PAN84] A.D. Panagiotou, M.W. Curtin, H. Toki, and P.J. Siemens, Phys. Rev. Lett. 52 (1984) 496.

- [POC85a] J. Pochodzalla, W.A. Friedman, C.K. Gelbke, W.G. Lynch, M. Maier, D. Ardouin, H. Delagrange, H. Doubre, C. Grégoire, A. Kyanowski, W. Mittig, A. Péghaire, J. Peter, F. Saint-Laurent, Y.P. Viyogi, B. Zwieglinski, G. Bizard, F. Lefèbvres, B. Tamain, and J. Québert, Phys. Rev. Lett. 55 (1985) 177.
- [POC85b] J. Pochodzalla, W.A. Friedman, C.K. Gelbke, W.G. Lynch, M. Maier, D. Ardouin, H. Delagrange, H. Doubre, C. Grégoire, A. Kyanowski, W. Mittig, A. Péghaire, J. Péter, F. Saint-Laurent, Y.P. Viyogi, B. Zwieglinski, G. Bizard, F. Lefèbvres, B. Tamain, and J. Québert, Phys. Lett. 161B (1985) 256.
- [POC85c] J. Pochodzalla, W.A. Friedman, C.K. Gelbke, W.G. Lynch, M. Maier, D. Ardouin, H. Delagrange, H. Doubre, C. Grégoire, A. Kyanowski, W. Mittig, A. Péghaire, J. Péter, F. Saint-Laurent, Y.P. Viyogi, B. Zwieglinski, G. Bizard, F. Lefèbvres, B. Tamain, and J. Québert, Phys. Lett. 161B (1985) 275.
- [POC86a] J. Pochodzalla, C.B. Chitwood, D.J. Fields, C.K. Gelbke, W.G. Lynch, M.B. Tsang, D.H. Boal, and J.C. Shillcock, Phys. Lett. 174B (1986) 36.
- [POC86b] J. Pochodzalla, C.K. Gelbke, C.B. Chitwood, D.J. Fields, W.G. Lynch, M.B. Tsang, and W.A. Friedman, Phys. Lett. 175B (1986) 275.
- [POC86p] J. Pochodzalla, C.K. Gelbke, W.G. Lynch, M. Maier, D. Ardouin, H. Delagrange, H. Doubre, C. Grégoire, A. Kyanowski, W. Mittig, A. Péghaire, J. Péter, F. Saint-Laurent, B. Zwieglinski, G. Bizard, F. Lefèbvres, B. Tamain, and J. Québert, Y.P. Viyogi, W.A. Friedman, D.H. Boal, MSU preprint, MSUCL-569, 1986.
- [POE85] D.N. Poenaru, M. Iuascu, A. Sandulescu, and W. Greiner, Phys. Rev. C32 (1985) 572.
- [POR85] N.T. Porile, A. Bujak, J.E. Finn, L.J. Gutay, A.S. Hirsch, R.W. Minich, G. Paderewski, R.P. Scharenberg, B.C. Stringfellow, and F. Turkot, Phys. Lett. 156B (1985) 177.
- [POS71] A.M. Poskanzer, G.W. Butler, and E.K. Hyde, Phys. Rev. C3 (1971) 882.

## R

- [RAC42] G. Racah, Phys. Rev. 62 (1942) 438.
- [RAN81] J. Randrup and S.E. Koonin, Nucl. Phys. A356 (1981) 223.

- [ROE83] G. Röpke, Phys. Lett. 121B (1983) 223.
- [ROE85] G. Röpke, H. Schulz, L.N. Andronenko, A.A. Kotov, W. Neubert, and E.N. Volin, Phys. Rev. C31 (1985) 1556.

## S

- [SIE83] P.J. Siemens, Nature 305 (1983) 410.
- [SOB83] L.G. Sobotka, M.L. Padgett, G.J. Wozniak, G. Guarino, A.J. Pacheco, L.G. Moretto, Y. Chan, R.G. Stokstad, I. Tserruya, and S. Wald, Phys. Rev. Lett. 51 (1983) 2187.
- [SOB84] L.G. Sobotka, M.A. McMahan, R.J. MacDonald, C. Signarbieux, G.J. Wozniak, M.L. Padgett, J.H. Gu, Z.H. Liu, Z.Q. Yao, and L.G. Moretto, Phys. Rev. Lett. 53 (1984) 2004.
- [SOB85] L.G. Sobotka and L.G. Moretto, Phys. Rev. C31 (1985) 668.
- [STE67] R. Stein, Nucl. Phys. 87 (1967) 854.
- [STOC83] H. Stöcker, G. Buchwald, G. Graebner, P. Subramanian, J.A. Maruhn, W. Greiner, B.V. Jacak, and G.D. Westfall, Nucl. Phys. A400 (1983) 63c.
- [STR84] R.W. Stoenner, P.E. Haustein, and J.B. Cumming, Phys. Rev. Lett. 53 (1984) 341.
- [STO84] R.G. Stokstad, Treatise on Heavy-Ion Science, 3, Plenum Press, New York (1984) 83.

## T

- [TAN80] I. Tanihata, M.C. Lemaire, S. Nagamiya, and Schnetzer, Phys. Lett. 97B (1980) 363.
- [TAN81] I. Tanihata, S. Nagamiya, Schnetzer, and H. Steiner, Phys. Lett. 100B (1981) 121.
- [TAY71] W.H. Taylor, B. Singh, F.S. Prato, and R. McPherson, Nucl. Data. A9 (1971) 1.
- [TRA86pc] W. Trautman, private communication.
- [TRO85p] R. Trockel, K.D. Hildenbrand, U. Lynen, W.F.J. Mueller, H.J. Rabe, H. Sann, H. Stelzer, R. Wada, N. Brummund, R. Glasow, K.H. Kampert, R. Santo, D. Pelte, J. Pochodzalla, and E. Eckert, GSI preprint, GSI-85-45, Sept. 1985.
- [TSA83] M.B. Tsang, D. Ardouin, C.K. Gelbke, W.G. Lynch, Z.R. Xu, B.B. Back, R. Betts, S. Saini, P.A. Baisden, and M.A. McMahan, Phys. Rev. C28 (1985) 747.

- [TSA84a] M.B. Tsang, D.R. Klesch, C.B. Chitwood, D.J. Fields, C.K. Gelbke, W.G. Lynch, H. Utsunomiya, K. Kwiatkowski, V.E. Viola, and M. Fatyga, Phys. Lett. 134B (1984) 169.
- [TSA84b] M.B. Tsang, C.B. Chitwood, D.J. Fields, C.K. Gelbke, D.R. Klesch, W.G. Lynch, K. Kwiatkowski, and V.E. Viola, Phys. Rev. Lett. 52 (1984) 1967.
- [TSA84c] M.B. Tsang, W.G. Lynch, C.B. Chitwood, D.J. Fields, D.R. Klesch, C.K. Gelbke, G.R. Young, T.C. Awes, R.L. Ferguson, F.E. Obenshain, F. Plasil, and R.L. Robinson, Phys. Lett. 148B (1984) 265.
- [TSA86] M.B. Tsang, R.M. Ronningen, G. Bertsch, Z. Chen, C.B. Chitwood, D.J. Fields, C.K. Gelbke, W.G. Lynch, T. Nayak, J. Pochodzalla, and T. Shea, Phys. Rev. Lett. 57 (1986) 559.

## V

- [VIC85] A. Vicentini, G. Jacucci, V.R. Pandharipande, Phys. Rev. C31 (1985) 1783.
- [VIO85] V.E. Viola, Jr., K. Kwiatkowski, and M. Walker, Phys. Rev. C31 (1985) 1550.
- [VIY79] Y.P. Viyogi, T.J.M. Symons, P. Doll, D.E. Greiner, H.H. Heckman, D.L. Hendrie, P.J. Lindstrom, J. Mohoney, D.K. Scott, K. Van Bibber, G.D. Westfall, H. Wieman, H.J. Crawford, C. McParland, and C.K. Gelbke, Phys. Rev. Lett. 42 (1979) 33.

## W

- [WAR82] A.I. Warwick, A. Baden, H.H. Gutbrod, M.R. Maier, J. Peter, H.G. Ritter, H. Stelzer, H.H. Weiman, F. Weik, M. Freedman, D.J. Henderson, S.B. Kaufman, E.P. Steinberg, and B.O. Wilkins, Phys. Rev. Lett. 48 (1982) 1719.
- [WAR83] A.I. Warwick, H.H. Weiman, H.H. Gutbrod, M.R. Maier, J. Peter, H.G. Ritter, H. Stelzer, F. Weik, M. Freedman, D.J. Henderson, S.B. Kaufman, E.P. Steinberg, and B.D. Wilkins, Phys. Rev. 27 (1983) 1083.
- [WEI37] V. Weisskopf, Phys. Rev. 22 (1937) 295.
- [WES76] G.D. Westfall, J. Gosset, P.J. Johansen, A.M. Poskanzer, W.G. Meyer, H.H. Gutbrod, A. Sandoval, and R. Stock, Phys. Rev. Lett. 37 (1976) 1202.
- [WES78] G.D. Westfall, R.G. Sextro, A.M. Poskanzer, A.M. Zebelman, G.W. Butler, and E.K. Hyde, Phys. Rev. C17 (1978) 1368.



- [WES82] G.D. Westfall, B.V. Jacak, N. Anantaraman, M.W. Curtin, G.M. Crawley, C.K. Gelbke, B. Hasselquist, W.G. Lynch, D.K. Scott, M.B. Tsang, M.J. Murphy, T.J.M. Symons, R. Legrain, and T.J. Majors, Phys. Lett. 116B (1982) 118.
- [WOZ72] G.J. Wozniak, H.L. Harvey, K.H. Wilson, and J. Cerny, Phys. Rev. Lett. 28 (1972) 1278.

## X

- [XU87] H. Xu, D.J. Fields, W.G. Lynch, M.B. Tsang, C.K. Gelbke, D. Hahn, M.R. Maier, D.J. Morrissey, J. Pochodzalla, H. Stocker, D.G. Sarantites, L.G. Sobotka, M.L. Halbert, and D.C. Hensley, Phys. Lett. 182B (1987) 155.

## Z

- [ZAR81] F. Zarbakhsh, A.L. Sagle, F. Brochard, T.A. Mulera, V. Perez-Mendez, R. Talaga, I. Tanihata, J.B. Carroll, K.S. Ganezer, G. Igo, J. Oostens, D. Woodward, and R. Sutter, Phys. Rev. Lett. 46 (1981) 1268.
- [ZEI80] U. Littmark and J.F. Zeigler, The Stopping and Ranges of Ions in Matter ; Handbook of Range Distributions for Energetic Ions in All Elements, 6 Pergamon Press, New York (1980).